NEURON-MICROGLIA CROSSTALK IN FTLD-*GRN* MODELS

Marvin Reich

Dissertation at the
Graduate School of Systemic Neurosciences
Ludwig-Maximilians-Universität München

May, 2024

Dedicated to my mother, who taught me to always be curious and to follow my dreams.

ABBREVIATIONS

AD	Alzheimer's disease
AAV	Adenovirus-associated virus
ASO	Antisense oligonucleotide
BBB	Blood-brain barrier
BDNF	Brain-derived neurotrophic factor
BMDM	Bone marrow-derived macrophages
C	Complement
C9orf72	Chromosome 9 open reading frame 72
CBD	Corticobasal degeneration
CHMP2B	Charged multivesicular body protein 2B
CNS	Central nervous system
CSF	Cerebrospinal fluid
CTS	Cathepsin
CXCL3	Fractalkine
DAM	Disease-/damage-associated microglia
DEG	Differentially expressed gene
FTD	Frontotemporal dementia
bvFTD	*Behavioral variant FTD*
FTLD	Frontotemporal lobar degeneration
FUS	Fused in sarcoma
GCase	Glucocerebrosidase
GRN	Granulin
GWAS	Genome-wide association study
HET	Heterozygous
IBA1	Ionized calcium-binding adapter molecule 1
KD	Knockdown
KO	Knockout
LAMP1	Lysosomal-associated membrane protein 1
LC/MS	Liquid chromatography coupled to mass spectrometry
LGMN	Legumain
LLPS	Liquid-liquid phase separation
LOF	Loss-of-function
MAP6	Microtubule-associated protein 6
MAPT	Microtubule-associated protein tau
MEF	Mouse embryonic fibroblast
MFG	Middle frontal gyrus
MND	Motor neuron disease
NCL	Neuronal ceroid lipofuscinosis
NfL	Neurofilament light-chain
NLS	Nuclear localization sequence
NMDA	N-methyl-D-aspartate

NPTX2	Neuronal pentraxin 2
PD	Parkinson's disease
PET	Positron emission tomography
PGRN	Progranulin
PPA	Primary progressive aphasia
PSP	Progressive supranuclear palsy
PTV	Protein transport vehicle
SOD1	Superoxide dismutase 1
SPPL2A	Signal peptide peptidase-like 2A
STMN2	Stathmin-2
TAM	Tyro3, Axl and Mer
TBK1	TANK-binding kinase 1
TDP-43	Transactive response DNA-binding protein of 43 kDa
pTDP-43	*Phosphorylated TDP-43*
TfR	Transferrin receptor
TMEM106B	Transmembrane protein 106B
TNF	Tumor necrosis factor
TREM2	Triggering receptor expressed on myeloid cells 2
TSPO	Translocator protein
UPS	Ubiquitin-proteasome system
UBQLN2	Ubiquilin 2
VCP	Valosin containing protein
WT	Wildtype

CONTENTS

1. ABSTRACT

Frontotemporal dementia (FTD) is a devastating neurodegenerative disease affecting more than a million people worldwide. Progranulin (PGRN) haploinsufficiency is the primary genetic cause of a subtype of frontotemporal lobar degeneration (FTLD-*GRN*) presenting with behavioral changes and TDP-43 pathology. FTLD-*GRN*, due to its monogenic nature, facilitates studies to better understand the molecular determinants of FTD and to develop novel treatment strategies. Nevertheless, to date, the pathobiology of FTLD-*GRN* is still only partially understood and there is no disease-modifying treatment available.

Several treatment strategies for FTLD-*GRN* are already in clinical development, all aiming to raise PGRN levels in the brain. However, none of them proved efficacy on TDP-43 pathology, behavioral phenotypes, or neurodegeneration. In this study, a novel treatment approach was established by applying a protein replacement approach using recombinant PGRN engineered for transferrin receptor-mediated blood-brain-barrier transcytosis, combined with a liver-targeting adenovirus-associated virus (AAV) gene therapy approach (AAV(L):bPGRN). The AAV(L):bPGRN treatment was tested in two preclinical FTLD-*GRN* models, namely *Grn* knockout (KO), and double KO (DKO) mice, in which both *Grn* and the FTLD-*GRN* risk factor *Tmem106b* are knocked out. The recently described DKO model not only exacerbates the phenotypes of *Grn* KO mice, such as neuroinflammation, lipidome alterations, and autophagic and lysosomal dysfunction. Additionally, DKO mice have a reduced life span, strong neurodegeneration, motor impairment, as well as TDP-43 pathology, a hallmark of FTLD-*GRN*. Using this AAV-based approach, all of the phenotypes in *Grn* KO and DKO mice could be ameliorated or fully reversed. The PGRN replacement strategy was further translated to a human induced pluripotent stem cell (hiPSC)-based model, in which microglia, derived from newly generated DKO hiPSCs, were co-cultured with wildtype neurons. The phenotypes observed in this *in vitro* hiPSC model, such as neuronal degeneration, TDP-43 pathology, and lysosomal dysfunction were all successfully rescued as well. These findings strongly support both PGRN replacement therapy as a promising treatment approach, as well as the DKO mouse model and hiPSC models as useful tools to study FTLD-*GRN*.

The second project addresses a related major open question in the FTD field, which is how loss of PGRN, a lysosomal protein primarily expressed in microglia, eventually leads to TDP-43 pathology in neurons, subsequently resulting in neurodegeneration. The lysosomal protease legumain (LGMN) appears to be a perfect link, as it is critical for the correct maturation of several other lysosomal proteases and was previously shown to be able to process PGRN, as well as TDP-43, into disease-associated fragments. Here, LGMN levels and activity were shown to be increased in both FTLD-*GRN* patient brains and in multiple FTLD-*GRN* models, including hiPSC-derived microglia and, age-independently, in

Abstract

Grn KO mice. *In vitro*, LGMN maturation was slowed down in the presence of full-length PGRN, but matured LGMN rapidly processed PGRN, showing a reciprocal regulation that could be disrupted in FTLD-*GRN*. Given the predominantly microglial expression of LGMN, a pathomechanism was proposed, in which excess LGMN in *GRN* KO microglia could be transferred to neurons resulting in TDP-43 processing and aggregation, as observed in FTLD-*GRN*. To test whether LGMN transfer from microglia to neurons could be possible, neuronal uptake and activation of LGMN from conditioned media by neurons was shown, causing increased TDP-43 processing, which could be ameliorated by LGMN inhibition. AAV-mediated overexpression of LGMN in mouse brain also resulted in increased TDP-43 processing and the accumulation of insoluble phosphorylated TDP-43, as well as motor impairment and neurodegeneration, similarly to the DKO mice. Therefore, LGMN is proved to be an important link between PGRN haploinsufficiency and TDP-43 pathology in FTLD-*GRN*.

In summary, the two studies presented in this thesis address major gaps in the FTD field, establishing LGMN as a link between the loss of PGRN and TDP-43 pathology, and also provide support for PGRN replacement as a disease-modifying therapeutic approach for FTLD-*GRN*.

2. INTRODUCTION

2.1. FRONTOTEMPORAL DEMENTIA – A MULTIFACTORIAL DISEASE

In our ageing society, more and more people are at risk to suffer from neurodegenerative diseases, as age is the main risk factor for developing dementia[6,7]. After early-onset Alzheimer's disease (AD), frontotemporal dementia (FTD) is the second most prevalent form of presenile dementia, currently affecting around 1.5 million people worldwide (prevalence 15-22 per 100'000 people)[8,9]. Despite many years of intensive research, there is no disease modifying treatment available due to a lack of understanding of the underlying mechanisms, but also because of the heterogeneity of the disease[10].

Originally, the disease was described by the Czech psychiatrist Arnold Pick as an early-onset form of dementia with atrophy in the frontal and temporal lobes and the presence of so-called Pick bodies[11], intracellular neuronal aggregates of the protein tau, characterized by Alois Alzheimer after microscopical examination[12]. The next major advances in FTD research did not happen until around 1970, when larger cohorts of non-AD dementia patients were assembled and characterized[13]. Marek-Marcel Mesulam described primary progressive aphasia (PPA), a disease variant that is characterized by gradual language impairment[14]. FTD was also further sub-categorized into a spectrum of syndromes, of which the most common is the behavioral variant (bvFTD)[15,16], which presents clinically with personality changes, such as apathy, unusual social behavior, language impairment, and overeating[17-19]. The pathological spectrum of bvFTD includes neurodegeneration[11,17], neuroinflammation[20,21], and can present with motor dysfunction[22,23]. These can partially overlap with other neurodegenerative diseases that belong to the FTD spectrum, such as motor neuron disease (MND)[24], corticobasal degeneration (CBD)[25], and progressive supranuclear palsy (PSP)[25]. However, the degeneration of the frontal and temporal cortical lobes (frontotemporal lobar degeneration (FTLD)) is characteristic for FTD[17,26]. The most common type of MND that also strongly overlaps with FTD symptomatically, pathologically and genetically is amyotrophic lateral sclerosis (ALS)[27,28]. Because of this overlap, the two diseases are sometimes referred to as the FTD-ALS spectrum[29,30]. Nevertheless, ALS patients present much more frequently with motor impairments resulting from the loss of upper and lower motor neurons, which is typical for the disease, while FTD patients usually have psychiatric symptoms and dementia[28,30]. The degree of overlap of symptoms and pathologies across all of these diseases complicates the diagnosis and often the correct identification is only possible after neuropathological assessment[30,31].

2.1.1. TDP-43 PATHOLOGY IS A HALLMARK OF MANY FTD, ALS AND AD CASES

Post mortem, extensive research has been performed to dissect disease subgroups based on specific protein aggregation patterns, employing immunohistochemistry, immunoblotting, and electron microscopy techniques. ALS cases predominantly present with intracellular aggregates of transactive response DNA-binding protein of 43 kDa (TDP-43), and much more rarely with fused in sarcoma (FUS) or superoxide dismutase 1 (SOD1) aggregates (Fig. 1A)[32]. On the other hand, FTD primarily presents with intracellular aggregates of TDP-43 (FTLD-TDP)[33] and of the cytoskeletal protein tau (FTLD-tau)[34,35], while fewer FTD cases have aggregated FUS (FTLD-FUS) or aggregates of the ubiquitin-proteasome system (UPS)[36,37].
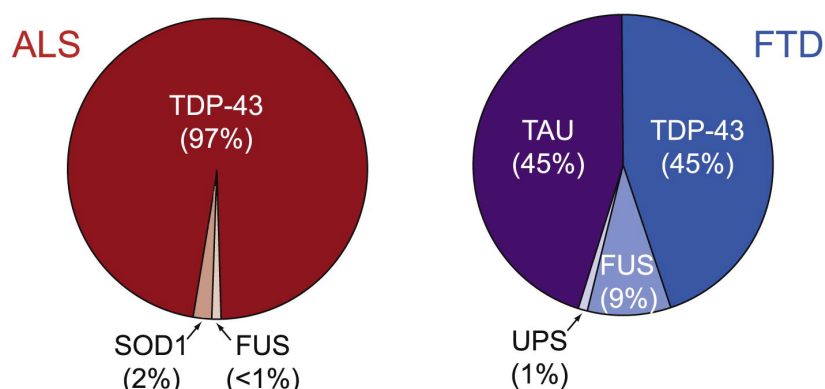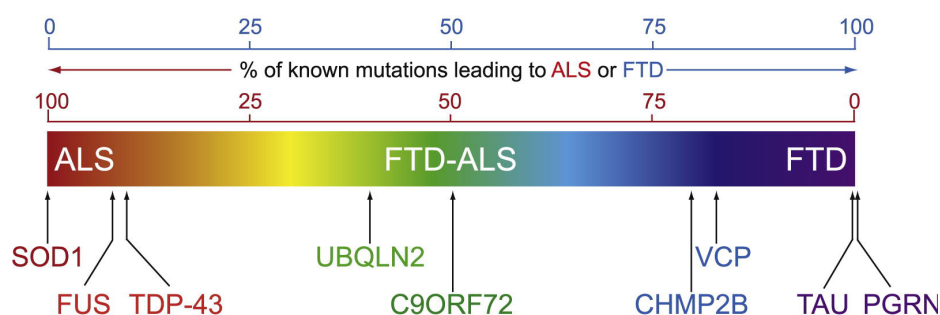
FIGURE 1: GENETIC AND NEUROPATHOLOGICAL CONTRIBUTIONS TO THE FTD/ALS SPECTRUM. (A) PERCENTAGE DISTRIBUTION OF THE HISTOPATHOLOGICAL HALLMARKS TDP-43, FUS, SOD1, AND TAU INCLUSIONS, AND AGGREGATES OF THE UBIQUITIN-PROTEASOME SYSTEM (UPS) AGGREGATING IN FTD AND ALS. (B) PERCENTAGE DISTRIBUTION OF DISEASE-CAUSING MUTATIONS ACROSS THE FTD/ALS SPECTRUM. SOD1-MUTATIONS EXCLUSIVELY CAUSE ALS, TDP-43 AND FUS PRIMARILY ALS, WHILE MUTATIONS IN UBQLN2 AND C9ORF72 CAN RESULT IN BOTH FTD AND ALS. TAU AND PGRN ARE EXCLUSIVELY ASSOCIATED WITH FTD. *ADAPTED FROM LING ET AL.[5] (REPRINTED WITH PERMISSION FROM ELSEVIER).*

Many disease-causing mutations in the TARDP gene coding for TDP-43 have been identified, especially for ALS but also for FTD[38-40]. The protein is ubiquitously expressed and, subcellularly, it mainly localizes to the nucleus, where it is critical for the regulation of transcription, splicing events, and RNA stability[41-43]. Under stress or disease conditions,

TDP-43 translocates more to the cytosol where several post-translational modifications occur. These include phosphorylation at several sites, C- and N-terminal truncation, as well as ubiquitylation[33,44-46]. While also playing a role in protein homeostasis, all of these can be identified by immunoblot in the insoluble fraction of brain homogenates of FTD or ALS patients, suggesting a link with the pathology[47,48].

With increasing amounts of cytosolic TDP-43, aggregates begin to form that can be visualized by immunohistochemistry[33]. The shape and localization of these aggregates and their associated neuronal dystrophy are highly specific and are used in the classification of FTLD-TDP subgroups (FTLD-TDP types A-D)[31,49]. Type A patients, commonly diagnosed with bvFTD or the non-fluent variant of PPA, have compact cortical and some hippocampal neuronal cytoplasmic inclusions, short dystrophic neurites, as well as sparse nuclear and glial cytoplasmic inclusions. Type B is characterized by smaller neuronal cytoplasmic TDP-43 aggregates and pre-aggregates in deeper cortical layers and also in motor neurons, as well as glial cytoplasmic inclusions. Neuronal inclusions and dystrophic neurites are uncommon for this type, which is associated with patients having both FTD and ALS symptoms. Type C, which is often found in semantic variant PPA patients, shows long dystrophic neurites and compact neuronal cytoplasmic inclusion in the hippocampus, but almost none in the cortex. Glial or nuclear inclusions are also rare. Type D is uniquely found in patients with a mutation in the valosin containing protein gene (*VCP*) and characterized by short dystrophic neurons and neuronal nuclear inclusions[31,49].

Through the cryo-electron microscopy of FTLD-TDP and ALS patient brain extracts, the amyloid-like filamentous structure of TDP-43 aggregates was resolved, and it was found to be the same in ALS and FTLD-TDP[50]. A common aggregation mechanism across the disease spectrum is therefore likely. However, further analysis revealed that filaments of type A FTLD-TDP patients are structurally distinct[51], hinting to a potentially different processing and aggregation in this subgroup. Why and how TDP-43 aggregates form still remains an open question. A likely scenario is liquid-liquid phase separation (LLPS), where sequestration of the protein in condensates leads to the formation of aggregation seeds[52-55]. This process can be enhanced by post-translational modifications, such as acetylation or phosphorylation, and hindered by RNA binding to the protein [53,56-58].

2.1.1.1. PATHOLOGICAL CONSEQUENCES OF TDP-43 AGGREGATION

Whether the aggregation of TDP-43 results in a toxic gain- or loss-of-function is still under debate, however, increasing evidence speaks for a combination of both[47]. Intensive research *in vitro* and *in vivo* has shown that the injection of TDP-43 aggregates in mouse brains, its supplementation in neuronal cultures or its increased expression is neurotoxic[44,59]. Likewise, the artificial induction of TDP-43 aggregation through the

deletion of its nuclear localization sequence (NLS) or by the introduction of disease-causing mutations was shown to induce cell death in various models[38,60,61]. Nevertheless, other studies have also shown loss-of-function effects by using models with reduced or depleted TDP-43 levels[62-64]. Due to the role of TDP-43 in the nuclear splicing machinery, its knockdown (KD) in neurons impairs the maturation of several of its target gene transcripts, such as *UNC13A* or *STMN2*, and leads to the splicing in of cryptic exons, with either additional or missing RNA stretches[64]. These RNAs can sometimes be translated into cryptic peptides, which can even be detected in the CSF of FTD patients[65]. As an example, TDP-43 loss drastically reduces the levels of stathmin-2 (STMN2), a protein involved in axonal maintenance, as its mis-spliced mRNA is degraded, which in turn causes axonal loss[66]. Another example is that of neuronal pentraxin-2 (NPTX2), which was shown to be increased – resulting in neurodegeneration – since its expression is regulated by TDP-43 binding to its 3' untranslated region[67].

Understanding the molecular mechanisms leading to TDP-43 mislocalization and aggregation and their pathological consequences is critical for the development of potential therapeutics. This is not only relevant to ALS and FTD, but also AD, as 30-50% of AD cases present with TDP-43 co-pathology[68].

2.1.2. FTD IS A DISEASE WITH A STRONG GENETIC COMPONENT

Despite being a highly heterogenous disease, FTD, in a large fraction of all cases, has a strong genetic component. Depending on the study, almost half of all patients have a family history of FTD and 10% of the cases are autosomal dominant[69]. Most genetic cases of FTD/ALS are caused by either hexanucleotide repeats in the chromosome 9 open reading frame 72 (*C9orf72*) or by mutations in the *MAPT* or the granulin (*GRN*) gene (Fig. 1B)[70-77]. *C9orf72* mutations can lead to either FTD or ALS, always present with dipeptide repeat inclusions and can further present with TDP-43 pathology[31,72,77]. In contrast, *MAPT* mutations highly selectively cause FTLD-tau with tau inclusions[73,75,76]. Similarly, *GRN* mutations primarily result in FTLD-TDP type A[78]. Interestingly, *GRN* mutations have also been found as a risk factor for AD and Parkinson's disease (PD), respectively[79-81].

Much rarer mutations occur in the genes encoding valosin containing protein (*VCP*), charged multivesicular body protein 2B (*CHMP2B*)[82,83] and TANK-binding kinase 1 (*TBK1*)[84-86]. Lastly, mutations in the *TARDP* gene, encoding TDP-43, *FUS*, or in the gene encoding ubiquilin 2 (*UBQLN2*) are most commonly causing ALS, but have also been described for FTD or ALS/FTD [87-90]. All of these proteins are part of the endolysosomal system, suggesting a critical role of the endolysosomal compartment in the pathogenesis of FTD.

2.2. THE ROLE OF PROGRANULIN IN FTLD-TDP

As mentioned before, loss-of-function (LOF) mutations in the *GRN* gene almost always lead to FTLD-TDP[78]. These patients are therefore particularly valuable to investigate potential causes of TDP-43 pathology, the downstream pathomechanisms and the development of treatment strategies. The first mutations were discovered in 2006[71,74], and since then numerous additional mutations were identified, mostly leading to a reduction in the protein levels of progranulin (PGRN) by different mechanisms[71,74,91-93]. These include DNA deletions, missplicing, mutations in the START codon or the introduction of premature STOP codons, leading to nonsense-mediated mRNA decay, all preventing the synthesis of the protein. Additionally, mutations can impair the trafficking of PGRN down the secretory pathway[91-93]. The reduction caused by LOF mutations can even be detected in patient plasma and is used for diagnosis[94-96]. Resulting from the heterozygous LOF mutations are haploinsufficiency of the protein and subsequently bvFTD[71,74]. Homozygous mutations are ultra-rare and cause the lysosomal storage disorder neuronal ceroid lipofuscinosis (NCL), an aggressive form of childhood dementia[97,98].

2.2.1. PROGRANULIN – A PROTEIN WITH MANY FUNCTIONS

The *GRN* gene is located on chromosome 17 and encodes for the 593 amino acid-long protein PGRN[99]. It is expressed throughout the whole body, primarily in cells of the hematopoietic lineage[100]. In the central nervous system (CNS), it was shown to be primarily expressed in microglia and neurons, with considerably higher levels in microglia[100,101]. PGRN consists of seven granulin domains and one slightly shorter para-granulin domain[99]. It also comprises a signal sequence for translocation into the secretory pathway where it is matured by heavy glycosylation, resulting in secretion as a 90 kDa protein, instead of the calculated 68.5 kDa (Fig. 2)[102]. Originally, PGRN was described as a growth factor in several tissues, and increased levels are associated with wound healing and, in the brain, with neurite outgrowth[103-105]. Additionally, PGRN levels were also found to be increased in several cancers[105,106]. It was also shown to be anti-inflammatory in a murine model of arthritis[107]. In the CNS, PGRN has been described as a neurotrophic factor[108]. Once secreted, the protein can further be taken up by cells again and trafficked to the lysosome. Transport into the cell and to the lysosome is mediated either by binding to sortilin or by co-transport with prosaposin *via* the mannose-6-phosphate receptor (Fig. 2)[109,110].
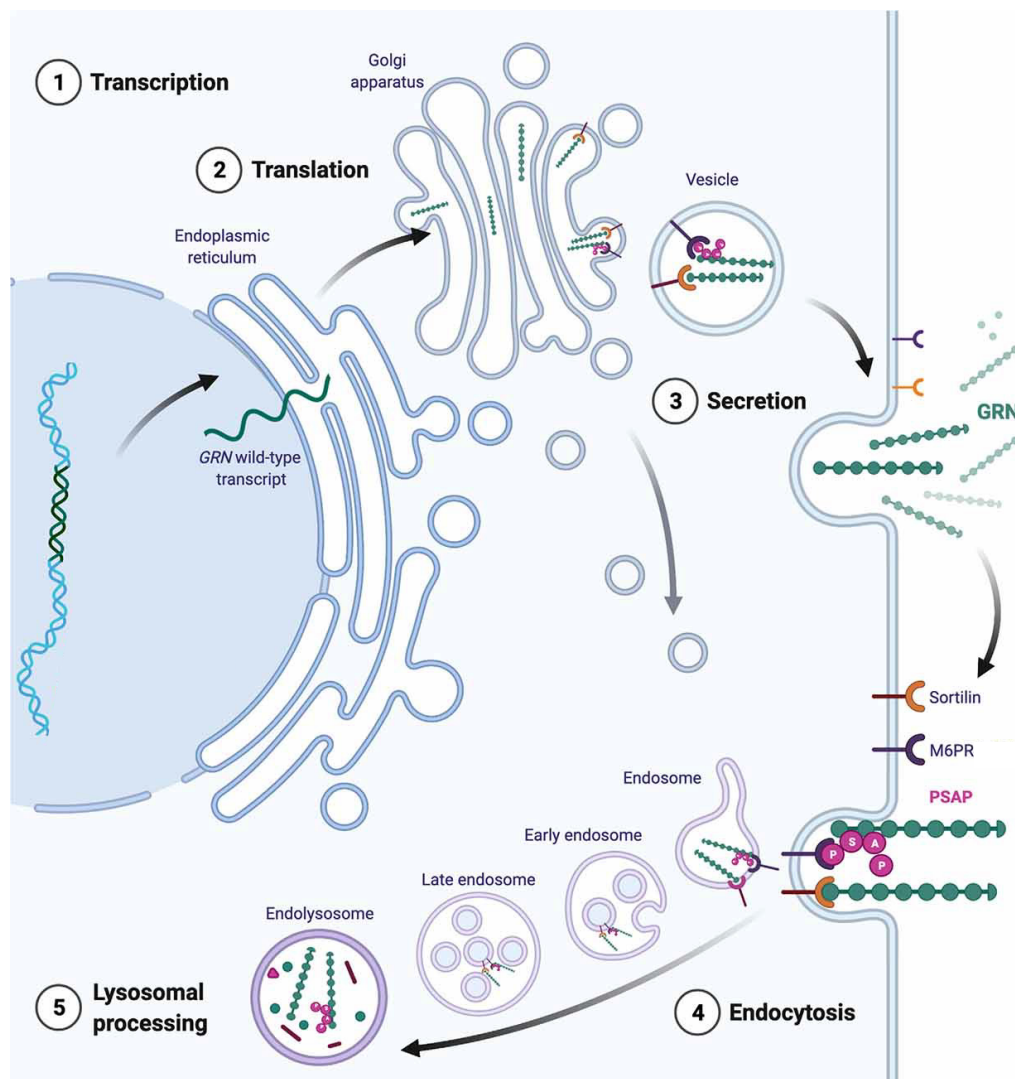
FIGURE 2: PGRN SECRETION AND UPTAKE PATHWAYS.
AFTER HAVING UNDERGONE GLYCOSYLATION IN THE ENDOPLASMIC RETICULUM AND GOLGI APPARATUS, PGRN IS DIRECTED TO THE SECRETORY PATHWAY AND RELEASED INTO THE EXTRACELLULAR SPACE. IT CAN THEN BE INTERNALIZED AGAIN AND ENTER THE ENDOLYSOSOMAL COMPARTMENT, EITHER BY BINDING TO SORTILIN OR BY CO-TRANSPORT WITH PROSAPOSIN (PSAP) *VIA* THE MANNOSE-6-PHOSPHATE RECEPTOR (M6PR). IN THE LYSOSOME, PGRN IS AT LAST PROCESSED INTO SINGLE GRANULINS. *ADAPTED FROM TERRYN ET AL.[2] (REPRINTED UNDER A CC BY LICENCE FROM FRONTIERS).*

Within the lysosome, progranulin is rapidly processed into highly stable single and multi-granulins[111-113]. This process can be mediated by cathepsin L (CTSL)[112,114]. More recently the cathepsins B, K, S, V, E, and G, as well as legumain (LGMN), all present in the endolysosomal compartment, were shown to cleave PGRN *in vitro*[115]. Outside of the cell, PGRN was also shown to be cleaved by elastase and metalloproteinase-12[116,117]. However, as partially inhibiting PGRN transport to the lysosome *via* sortilin depletion results in an increase of PGRN levels and reduced levels of granulin peptides, the lysosome seems to be the primary location of intracellular PGRN processing[118]. The function of the different granulins is not understood yet, however, some evidence hints towards a pro-inflammatory role that might even promote TDP-43 pathology[119-121]. On the other hand,

a recent preprint claims that overexpression of the granulins A and F in the brains of *Grn* knockout (KO) mice leads to a rescue of the pathological phenotypes[122].

2.2.2. PROGRANULIN REGULATES LYSOSOMAL FUNCTION

Multiple transport mechanisms of PGRN to the lysosome, its lysosomal processing into granulins, and the lysosomal storage disorder NCL which results from homozygous LOF mutations in the *GRN* gene, all indicate a central role of PGRN in lysosomal biology.

In fact, PGRN is not only processed by different cathepsins, but it has also been shown to act as a chaperone for CTSD during its autocatalytic maturation[123,124]. *Grn* KO mouse and FTLD-*GRN* patient brains have increased CTSD protein levels and activity, and this has also been observed for CTSB and CTSL[125-127]. Other studies report decreased CTSD activity in patient-derived fibroblasts and human induced pluripotent stem cell (hiPSC)-derived cortical neurons, implying a potential cell type-specific regulation[128,129]. Additionally, the levels of the lysosome-associated membrane protein 1 (LAMP1) increase with age in *Grn* KO mice[126,130]. This might be a compensatory cellular response to maintain lysosomal function, as PGRN was shown to regulate lysosomal acidification which is impaired upon loss of PGRN[131,132]. In another study, Galectin-3, a protein recruited to damaged membranes, strongly co-localized with lysosomes upon *GRN* KO, a process that could be reversed by addition of PGRN[133,134]. In hiPSC-derived *GRN* KO neurons and *Grn* KO mouse brains, the lysosomal proteome was drastically altered, including upregulation of cathepsins, proteins involved in autophagy as well as v-ATPases, which mediate lysosomal acidification, and impaired lysosomal protein degradation[132].

In summary, PGRN is critical for lysosomal homeostasis and its depletion impairs multiple facets of their physiology, which might in turn trigger further downstream pathological changes.

2.2.2.1. REGULATION OF LIPID HOMEOSTASIS BY PROGRANULIN

As the lysosome is a primary location of lipid metabolism, it makes sense to assume a role of PGRN in lysosomal lipid homeostasis[135]. The interaction of PGRN with pro-saposin as part of its lysosomal targeting already suggests an involvement in lipid processing, as the saposins that are derived from prosaposin also mediate glycosphingolipid degradation[136-138].

PGRN can also bind to, and thereby stabilize glucocerebrosidase (GCase), the enzyme that primarily metabolizes the glycosphingolipid glucosylceramide[139,140]. LOF mutations in GCase can cause Gaucher disease, another lysosomal storage disorder, and GCase is further associated with PD[141,142]. Fittingly, GCase activity is reduced in *Grn* KO mouse and

FTLD-*GRN* patient brains[133,140,143]. Glucosylsphingosine, another substrate of GCase, was also shown to be strongly elevated in *Grn* KO mice cerebrospinal fluid (CSF) and brains, but only showed a trending increase in FTLD-*GRN* patient CSF[133].

The same study reported overall decreased levels of multiple bis(monoacylglycero)phosphate (BMP) species upon PGRN loss, which was also confirmed in patients[133,144]. This phenotype is described as causative for the reduced GCase activity, as their negatively charged heads could electrostatically sequester the positively charged GCase to membranes within the lysosome and thereby restrict the access to its substrate glucosylsphingosine[133]. Nevertheless, the reduction in BMP levels is still surprising, as these are usually increased in lysosomal storage disorders[145].

2.2.2.2. THE ENDOLYSOSOMAL PROTEIN TMEM106B IS A RISK FACTOR FOR FTLD-*GRN*

The significance of lysosomal biology in FTLD-*GRN* was further reinforced by the identification of transmembrane protein 106B (*TMEM106B*) as a strong risk gene for FTLD-TDP, and in particular for FTLD-*GRN*, in a genome-wide association study (GWAS), which was confirmed in a case-control study[146-148]. The more common allele rs1990622[T] increases the risk to develop FTD, while the minor allele rs1990622[C] is protective. Interestingly, another coding variant, rs3173615, introduces a T185S replacement, which also decreases disease risk, most likely due to an enhanced degradation of TMEM106B[146,149]. Independently, *TMEM106B* was also identified as a risk factor for multiple other conditions, including neurodegenerative diseases such as AD, PD, ALS and FTLD with C9orf72 repeat expansions[150-153].

TMEM106B is a type 2 transmembrane protein that is localized in the endolysosomal compartment (Fig. 3)[154,155]. It is heavily N-glycosylated in its luminal domain and can be regulated through cleavage by lysosomal proteases, forming an N-terminal fragment without the luminal domain, and further cleaved down to an unstable intracellular domain by signal peptide peptidase-like 2a (SPPL2a)[154,155].

TMEM106B has several critical roles in endolysosomal organization and trafficking. Upon overexpression of the protein, several studies showed enlarged lysosomes as well as cytotoxicity[154-158]. Knockdown of TMEM106B in primary neurons caused enhanced retrograde lysosomal transport and dendritic spine degeneration[159]. TMEM106B is therefore essential for the appropriate dendritic transport of lysosomes, a process mediated by its interaction with microtubule-associated protein 6 (MAP6)[159]. Its critical role in lysosomal transport was also shown *in vivo*, as *Tmem106b* KO mice exhibit axonal swellings in Purkinje cells, consisting of heavily enlarged lysosomes, and subsequently Purkinje cell loss[160,161]. The direct involvement of TMEM106B in lysosomal function and protein degradation was shown by one study through increased lysosomal protease

levels, and by another study through raised levels of the autophagy markers p62 and LC3 upon *Tmem106b* KO[160,162].
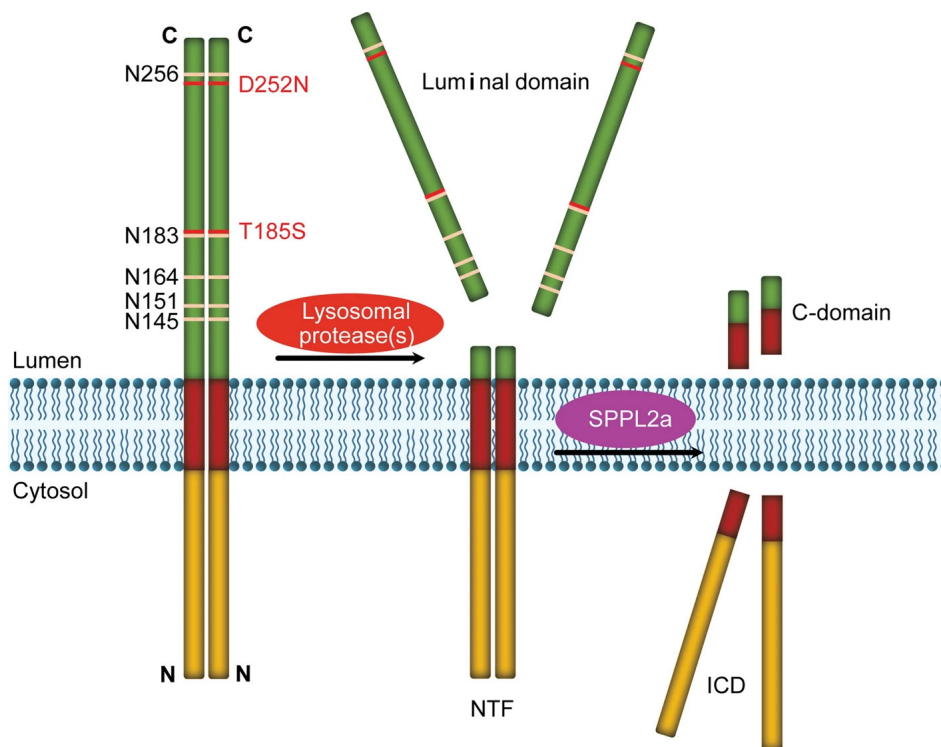
FIGURE 3: SCHEMATIC SHOWING THE STRUCTURE AND PROCESSING OF TMEM106B.
TMEM106B IS A LYSOSOMAL TYPE 2 TRANSMEMBRANE PROTEIN WITH SEVERAL N-GLYCOSYLATION SITES IN ITS LUMINAL DOMAIN. IT IS CLEAVED BY LYSOSOMAL PROTEASES INTO AN N-TERMINAL FRAGMENT (NTF) AND A LUMINAL DOMAIN. FURTHER PROCESSING BY SPPL2A RELEASES FROM THE MEMBRANE AN UNSTABLE INTRACELLULAR DOMAIN (ICD) AND A SHORT C-TERMINAL FRAGMENT. *ADAPTED FROM FENG ET AL.[4] (REPRINTED WITH PERMISSION FROM SPRINGER NATURE).*

Recently, C-terminal fragments of TMEM106B, cleaved at amino acid 120, were shown to form stable amyloid fibrils in aged individual as well as FTLD-*GRN* patient brains[163-165]. The functional consequences of this fibrillar accumulation remain to be investigated, however, early results indicate that the amount of sarkosyl-insoluble TMEM106B fragments correlates with urea-insoluble phosphorylated TDP-43 (pTDP-43), especially in FTLD type A[166]. The same study also confirmed that patients expressing the protective T185S variant had prolonged survival and reduced levels of TMEM106B fragments, providing a potential reason for the protective effect of this variant[166].

2.2.2.3. PGRN AND TMEM106B HAVE AN INTRICATE RELATIONSHIP

As *TMEM106B* is a risk factor for FTLD-*GRN*, the question of how TMEM106B and PGRN interact seems obvious, yet the answer is not as straight forward. When looking at expression levels, FTLD-*GRN* patients have higher *TMEM106B* mRNA and protein levels[125,146,156]. Likewise, TMEM106B levels are increased in aged *Grn* KO mice, but also in

other conditions of lysosomal dysfunction, as in *Ctsd* KO mice or upon inhibition of lysosomal degradation *via* bafilomycin treatment[125,154]. On the other hand, overexpression or reduction of TMEM106B levels *in vitro* does not change PGRN levels[154-156]. On the contrary, TMEM106B overexpression in another study even reduced processing of PGRN into granulins, most likely due to the induction of lysosomal dysfunction[111]. In *Tmem106b* KO mice, PGRN levels are increased[160]. However, in patients carrying the TMEM106B risk allele, plasma PGRN levels were found to be reduced[94,146,167].

A study that combined *Grn* KO in mice with the overexpression of neuronal Tmem106b showed increased lysosomal dysfunction as well as lipofuscin accumulation, a phenotype that is also present in patients[128,168]. Combinatorial KO of both *Grn* and *Tmem106b* strongly exacerbated the phenotypes present in *Grn* KO mice in three independent studies[162,169,170]. These animals present with a drastically reduced life span of four to five months, severe neurodegeneration, neuroinflammation, motor impairments, autophagic defects, as well as myelination deficits[162,169-171].

In conclusion, the functions of PGRN and TMEM106B are closely entangled. They can reciprocally influence their protein levels and activity, however, to date they haven't been shown to directly interact with each other. Their co-dependent effect on each other could potentially be explained by their respective strong influence on lysosomal homeostasis.

2.2.2.4. LEGUMAIN – A UNIQUE LYSOSOMAL PROTEASE

As described above, the loss of PGRN has a strong effect on lysosomal homeostasis, especially also through dysregulated cathepsin maturation and activity[126]. Another protein with critical regulatory roles in the lysosome is legumain (LGMN).

The cysteine protease LGMN is also known as asparaginyl endopeptidase (AEP), as it is the only protease in humans that cleaves at the C-terminus of asparagine residues[172]. LGMN is expressed as an inactive pro-LGMN that is stable at neutral pH[172]. With decreasing pH, LGMN undergoes autocatalytic N- and C-terminal processing to form the mature form of the protein that is most active at pH 4[172-174]. Consequently, pro-LGMN and mature LGMN show distinct localizations in the cell and mature LGMN co-localizes with the lysosomal marker LAMP1[173]. The stability of LGMN is heavily impaired upon increase of pH after its maturation[172].

Within the lysosome, LGMN has been shown to have a central role in the maturation of several lysosomal proteases. In *Lgmn* KO mice, CTSL cannot complete its maturation[175]. Another study showed not only the impaired maturation of CTSL, but also that of CTSH and CTSB in the kidney of *Lgmn* KO mice[176]. Further observations include weight loss and enlarged lysosomes upon *Lgmn* KO[176].

In neurodegenerative diseases, LGMN was shown to play a role in the processing of the amyloid precursor protein, tau, and alpha-synuclein in *in vitro* cleavage assays[177-179]. A more robust link between tau processing by LGMN and tauopathies was established through *in vivo* studies, where the genetic ablation or pharmacological inhibition of LGMN rescued multiple phenotypes in the P301S tau mouse model[178,180].

In the context of FTLD-*GRN*, LGMN was shown to process PGRN *in vitro* amongst other proteases and LGMN activity, while decreased in the inferior occipital cortex (a control region in FTD), was relatively increased within the affected middle frontal gyrus (MFG) in FTLD-*GRN* patient brains[115]. Compared to non-demented individuals, however, there was no increase in LGMN activity in the MFG[115]. Importantly, LGMN is capable of cleaving TDP-43 *in vitro* and liquid chromatography coupled to mass spectrometry (LC/MS) analysis of patient-derived brain material and of various cellular models revealed C-terminal asparagine residues in TDP-43 fragments, strongly supporting the pathological involvement of LGMN in TDP-43 processing[181]. In addition, almost no fragments of TDP-43 could be detected in *Lgmn* KO mouse brains by immunoblot analysis[181].

Taken together, the central role of LGMN in the lysosome together with its capability to process both PGRN, as well as TDP-43 into disease-relevant fragments, presents LGMN as a potential link between PGRN-deficiency and TDP-43 pathology.

2.3. MICROGLIA AND THEIR CRITICAL ROLE IN FTLD-*GRN*

Microglia were initially described by Pío del Río-Hortega more than a hundred years ago and named based on their small size and supportive function[182]. Despite their early discovery, microglia were often neglected in the context of neurodegeneration. However, when large-scale GWAS led to the discovery that immune pathways are centrally involved in neurodegeneration, the field of neuroimmunology, with a special focus on microglia, received increasing attention[183-186].

Known as the tissue-resident innate immune cells of the brain, microglia constantly surveille their surroundings in the adult brain for potential infiltrates or injuries by sensing changes in the extracellular composition, but also *via* direct cell contact (Fig. 4)[187-190]. However, they already have critical functions during development. After migration to the brain from the yolk sac, microglia support the appropriate development of neuronal circuits[191,192]. Developing neurons express complement (C)1q and C3 at synapses in an activity-dependent manner, and microglia prune inactive synapses *via* phagocytosis[192,193]. This process has been shown to be essential to refine brain circuitry during development, but it also continues to be active throughout the lifespan[194,195]. Similarly, microglia recognize dying neurons through neuronal ATP release and a lack of fractalkine (CX3CL1) expression. These environmental changes can be sensed *via* the microglial fractalkine

receptor, P2Y purinergic receptors for ATP, or also Tyro3, Axl and Mer (TAM) receptor signaling[194,196,197]. Among their other roles, microglia also release brain-derived neurotrophic factor (BDNF) to support neurogenesis and neuronal survival in development and adulthood[198,199].
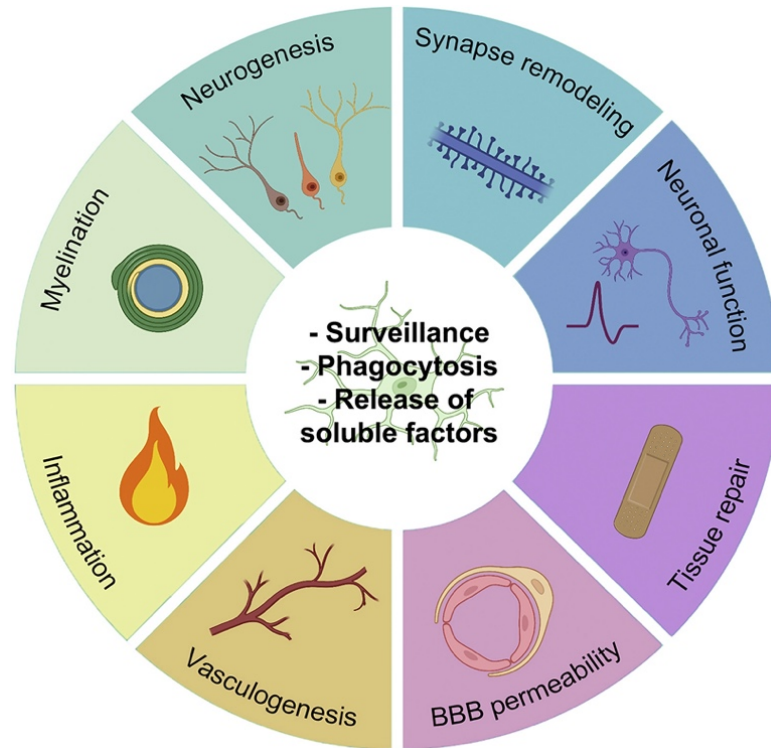
FIGURE 4: OVERVIEW OF MICROGLIAL FUNCTIONS.
BY EXECUTING THEIR FUNDAMENTAL FUNCTIONS OF SURVEILLANCE, PHAGOCYTOSIS AND THE RELEASE OF SOLUBLE FACTORS, MICROGLIA ARE INVOLVED IN MANY PROCESSES IN THE BRAIN. THESE INCLUDE MYELINATION, NEUROGENESIS, SYNAPSE REMODELING, MODULATION OF NEURONAL ACTIVITY, TISSUE REPAIR, BBB MAINTENANCE AND REPAIR, VASCULOGENESIS, AND INFLAMMATION. *(REPRINTED FROM PAOLICELLI ET AL.[1] WITH PERMISSION FROM ELSEVIER).*

In addition to their roles in the regulation of neural plasticity, neuronal homeostasis, and tissue surveillance, microglia further support correct myelination through the removal of aberrant myelination, as well as regulating the general pool of oligodendrocyte precursor cells[200,201]. Moreover, vascularization in both the brain and the eye are also regulated by microglia[202-204]. In the adult brain microglia ensure blood-brain barrier (BBB) integrity by creating an anti-inflammatory milieu through cytokine release in homeostasis, but also by the physical closure of lesions that are sensed *via* their purinergic receptors[205,206].

2.3.1. MICROGLIA AT THE CENTER OF NEURODEGENERATION

As microglia constantly surveil their environment looking for potential changes, they are also rapidly responding to any abnormality. This reactivity was originally described as a morphological transition from highly ramified homeostatic cells, to 'activated', more ameboid cells in disease conditions[12]. Nowadays, microglia are seen as highly dynamic

cells that respond uniquely to different challenges by adopting different transcriptomic, proteomic and metabolomic signatures[1]. A microglia state shared by many neurodegenerative diseases, is that of disease- or damage-associated microglia (DAM), originally described by Keren-Shaul *et al.* in an amyloid pathology model using single-cell RNA sequencing[207]. This microglial population emerges from the homeostatic microglia, induced by upregulation of triggering receptor expressed on myeloid cells 2 (TREM2)[207]. Since then, similar signatures have been identified in different disease models, as well as in patients, and during normal ageing[208-211]. Reactive microglia can have beneficial functions, like neurotrophic support, phagocytosis of pathological aggregates and of apoptotic or degenerating cells[212,213]. However, they can also create a pro-inflammatory neurotoxic milieu through the release of cytokines and complement components[212,214,215]. This pro-inflammatory environment can further stimulate other cells, such as astrocytes, to adopt a neurotoxic phenotype[216]. The beneficial and detrimental roles of microglia in the context of neurodegenerative diseases have been extensively discussed by the community and are still under debate[217-222]. The consensus is, however, that microglia play a central role in the dynamics of neurodegeneration[1]. This is further supported by genetics, since multiple GWAS studies have identified mutations in microglial genes as factors in a variety of neurological diseases[183-186].

2.3.2. THE ROLE OF MICROGLIA IN FTLD-*GRN*

Besides the fact, that PGRN is primarily expressed by microglia in the CNS and shows only low expression levels in astrocytes and neurons, there are multiple other reasons why microglia play a critical role in FTLD-*GRN*[126,223]. To start, different studies have shown increased numbers of ionized calcium-binding adapter molecule 1 (IBA1)-positive microglia, as well as increased expression of the microglial phagocytic activation marker CD68 in FTLD-*GRN* patient brains compared to C9orf72 mutation carriers and healthy controls[224,225]. FTLD-*GRN* patients also show an increased intensity of the neuroinflammation and microglial activation marker translocator protein (TSPO) in positron-emission-tomography (PET), compared to sporadic FTLD[226,227]. By applying a combination of single-nucleus RNA sequencing and Nanostring transcriptomics of thalamus and frontal cortex of FTLD-*GRN* patients and controls, Marsan *et al.* could show dramatic changes in microglial gene expression, especially in the thalamus[223]. Differentially expressed genes (DEGs) include the general microglial markers *TMEM119* and *CXCR1*, as well as the activation markers *CD68*, *C1QA/B/*C and *C3*[223].

Additionally, by using *Grn* KO mice, several other publications also showed microglial activation in disease. Transcriptional analysis revealed a characteristic gene signature, similar to the DAM state, but also comprising a number of differentially expressed lysosomal genes[169,223,226,228,229]. Many of these markers could be confirmed by

immunofluorescence staining[228]. Single-cell RNA sequencing further indicates an age-dependent increase in microglia numbers[228]. This increase, as well as the phagocytic activity marker Cd68 and several other microglial activation markers, such as ApoE, Clec7a, and Trem2 were also reported in other studies[133,226]. Götzl *et al.* further confirmed the increase in TSPO PET intensity, as observed in FTLD-*GRN* patients, in *Grn* KO mice[226].

Functionally, loss of PGRN in mice was shown to increase the pro-inflammatory cytokines tumor necrosis factor (TNF) and IL-6 in microglia[230]. Microglia *in vivo* as well as primary *Grn* KO microglia were shown to have increased levels of the complement proteins C1qa, C3, and C3b[229]. Consequently, primary *Grn* KO microglia excessively prune synapses of co-cultured primary neurons and synaptosomes from aged *Grn* KO mice, contain high levels of C1q and C3[229]. In another study, media transfer from *Grn* KO primary microglia to primary neurons resulted in TDP-43 mislocalization to the cytosol and cytotoxicity[228]. Interestingly, all of these phenotypes could be rescued by genetic ablation of C1q, C3, or both, arguing in support of a central role of complement-mediated neuron-microglia crosstalk in the pathogenesis of FTLD-*GRN*[228,229].

On a side note, microglial activation in FTLD-*GRN* is not necessarily entirely pathogenic, as genetic ablation of Trem2, the protein necessary for the DAM state transition, on top of a *Grn* KO mouse background, resulted in drastically worsened neurodegeneration, as quantified *via* neurofilament light-chain (NfL) measurements in the CSF[231].

2.4. THERAPEUTIC APPROACHES FOR FTLD-*GRN*

To date, there is no disease-modifying treatment available in the clinic for either FTD or FTLD-*GRN* patients. However, research efforts are under way both to deepen the molecular understanding of the disease, as well as to translate these findings into potential drug candidates. There are several promising approaches in preclinical and clinical development for FTLD-*GRN*, all attempting to raise PGRN levels in order to rescue the disease-causing haploinsufficiency of the protein (Fig. 5).

Clinically, the most advanced along the trial pipeline is an anti-sortilin antibody in phase III[232,233]. This molecule aims at preventing the sortilin-mediated uptake of extracellular PGRN and its subsequent trafficking to the lysosome, thereby increasing extracellular levels. This approach was able to normalize plasma and CSF PGRN levels in FTLD-*GRN* patients to the levels of non-mutation-carriers[232,233]. However, as discussed, PGRN executes many functions within the lysosome and prevention of lysosomal transport might have an overall negative effect on disease outcome.
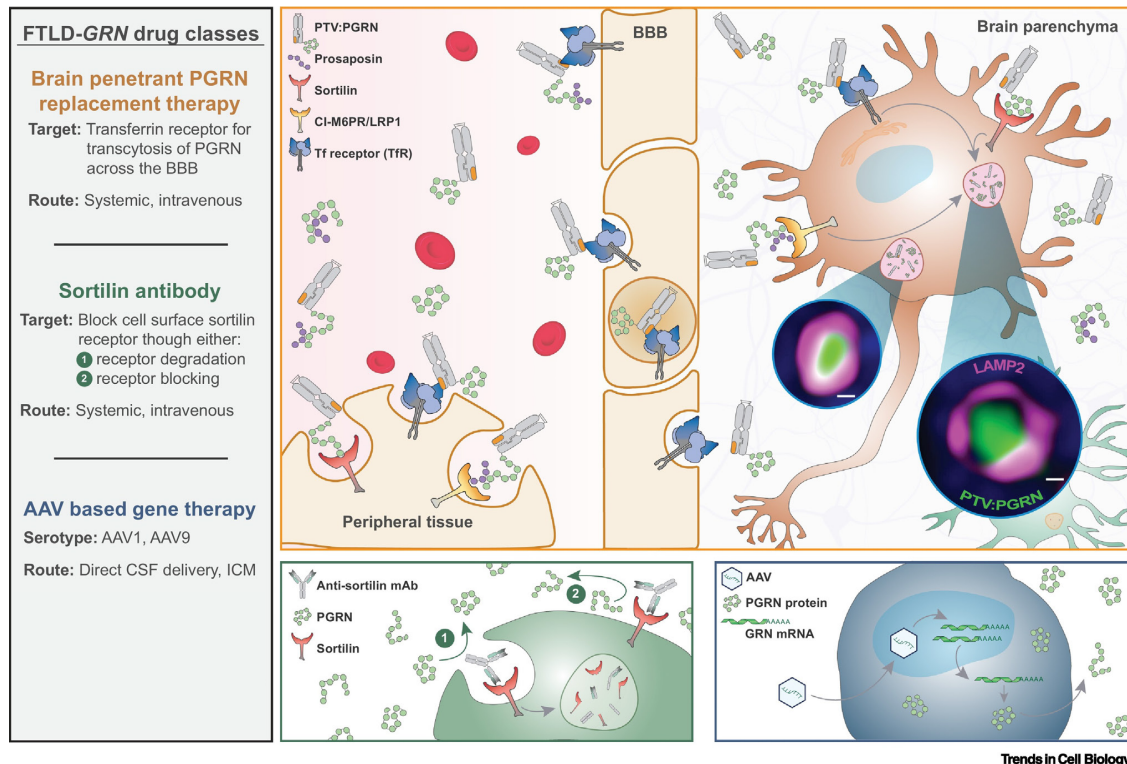
FIGURE 5: OVERVIEW OF THE THERAPEUTIC APPROACHES FOR FTLD-*GRN* CURRENTLY IN CLINICAL DEVELOPMENT.
OVERVIEW OF THE THREE THERAPEUTIC APPROACHES FOR FTLD-GRN THAT ARE CURRENTLY IN CLINICAL DEVELOPMENT. PTV:PGRN (IN ORANGE) IS A PROTEIN REPLACEMENT THERAPY USING PGRN ENGINEERED TO BIND THE TRANSFERRIN RECEPTOR (TFR) FOR RECEPTOR-MEDIATED TRANSCYTOSIS THROUGH THE BBB AND ENHANCED DELIVERY TO THE BRAIN. AN ANTI-SORTILIN ANTIBODY (IN GREEN) PREVENTS SORTILIN-MEDIATED TRANSPORT OF PGRN INTO THE CELL AND TO THE LYSOSOME, THUS INCREASING EXTRACELLULAR PGRN LEVELS. AAV-BASED GENE THERAPY APPROACHES (IN BLUE) ENABLE LOCAL EXPRESSION AND SECRETION OF PGRN IN THE BRAIN. *ADAPTED FROM SIMON ET AL.[3] (REPRINTED UNDER A CC BY NC ND LICENCE FROM ELSEVIER).*

Another promising approach is adenovirus-associated virus (AAV)-mediated gene therapy. Two approaches are currently in clinical development and both aim for *cisterna magna* injection of an AAV expressing PGRN[234,235]. In *Grn* KO mice, both approaches strongly increased CSF PGRN levels and ameliorated pathological phenotypes[234,235]. AAV-mediated delivery was also recently shown to work when expressing single granulins[122]. In non-human primates, only expression by ependymal cells was shown as well as increased CSF and plasma PGRN levels[235]. A possible concern with this approach is the limited brain biodistribution of both the virus and the expressed PGRN, which was reported to be problematic in larger animals[236-238]. The virus only transduces the outer cortical layers, and thus PGRN can only be secreted and taken up locally in these brain regions. In fact, a recent mouse study employing an AAV-based approach to increase PGRN levels *via* direct CNS delivery could rescue the pathology in the spinal cord, but did not show an effect on brain pathology in an FTLD-*GRN* mouse model[239]. A *cisterna magna* injection also risks injuring the brain or the viral capsid itself could raise immune reactions[236,240].

Lastly, a recombinant brain-penetrant PGRN replacement therapy is also in clinical development[133]. The molecule PTV:PGRN consists of recombinant PGRN fused to a protein transport vehicle (PTV), a modified Fc fragment that can bind to the transferrin receptor (TfR), thus enabling receptor-mediated transcytosis through the BBB. Under physiological conditions, the BBB is only weakly permeable to large molecules, but PTV:PGRN was shown to have a roughly five-fold-increased brain penetrance compared to a non-TfR-binding PGRN control[133,241]. Using primary bone marrow-derived macrophages (BMDMs), hiPSC-derived microglia, as well as *Grn* KO mice, a study showed, after PTV:PGRN administration, rescue of lysosomal defects, lipid aberrations, and gliosis[133]. A potential concern is the prevention of endogenous transferrin binding to its receptors, which was, however, not observed in a previous study applying the transport vehicle technology[242].

In conclusion, the molecules in development for the treatment of FTLD-*GRN* have great potential. However, none of the studies has conclusively addressed the effect of treatment on FTLD-*GRN* hallmarks such as TDP-43 pathology, defects in protein degradation, behavioral changes, and neurodegeneration.

2.5. AIMS OF THE STUDY

Despite many years of research, there is no disease-modifying treatment available for FTD. The first project presented in this thesis addresses gaps in the field through the following questions:

Is PGRN replacement therapy a feasible approach to treat FTLD-*GRN*?

- Is it possible to apply a gene therapy approach for peripheral expression of brain-penetrant PGRN to raise PGRN levels in the brain?

- Does this approach rescue disease-relevant phenotypes, such as TDP-43 pathology, neurodegeneration and behavior phenotypes, in the *Grn x Tmem106b* double knockout mouse model?

- Can FTLD-*GRN* pathology be modeled *in vitro* using hiPSC-derived *GRN x TMEM106B* double knockout neuron-microglia co-cultures and can these phenotypes be rescued with PGRN replacement?

LOF mutations in *GRN*, a gene primarily expressed by microglia, eventually lead to TDP-43 pathology primarily in neurons. This spatial paradox is addressed in the second project in this thesis:

How does the loss of PGRN cause TDP-43 pathology in FTLD-*GRN*?

- Does the loss of PGRN result in the increase of a specific lysosomal protease, which can also cleave TDP-43 and whose activity can be regulated by PGRN itself?

- Can this lysosomal protease be transferred from microglia to neurons?

- Does this transfer subsequently cause TDP-43 pathology in neurons?

Introduction

3. RESEARCH ARTICLES

3.1. RESCUE OF FTLD-ASSOCIATED TDP-43 PATHOLOGY AND NEURODEGENERATION BY PERIPHERAL AAV-MEDIATED EXPRESSION OF BRAIN-PENETRANT PROGRANULIN

Research article 1:
(Reich, Simon *et al*.) "Rescue of FTLD-associated TDP-43 pathology and neurodegeneration by peripheral AAV-mediated expression of brain-penetrant progranulin" – revised version submitted to Science Translational Medicine

Access to preprint:
https://www.biorxiv.org/content/10.1101/2023.07.14.549089v1

Authors:
Marvin Reich*, Matthew J. Simon*, Beate Polke, Georg Werner, Christian Schrader, Iñaki Paris, Sophie Robinson, Sonnet S. Davis, Gabrielly Lunkes de Melo, Lennart Schlaphoff, Lena Spieth, Stefan Berghoff, Todd Logan, Brigitte Nuscher, Katrin Buschmann, Dieter Edbauer, Mikael Simons, Jung H. Suh, Thomas Sandmann, Mihalis S. Kariolis, Sarah L. DeVos, Joseph W. Lewcock, Dominik Paquet[#], Anja Capell[#], Gilbert Di Paolo[#], Christian Haass[#]

The author of this thesis is one of the first authors of this manuscript.

Author contributions:
Conceptualization: MR, MJS, MSK, SLD, JWL, AC, GDP, CH
Methodology: MR, MJS, IP, GW, SR, SSD, GL, LSc, LSp, SB, TL, MS, MSK, JHS, TS, SLD, JWL, DP, AC, GDP, CH
Investigation: MR, MJS, BP, CS, IP, GW, SR, SSD, GL, LSc, LSp, SB, BN, KB, JHS, TS
Visualization: MR, MJS, IP, JHS, TS
Funding acquisition: DP, CH
Project administration: DE, MS, JWL, DP, AC, GDP, CH
Supervision: MR, MJS, GW, SR, JHS, TS, LSc, LSp, SB, DP, AC
Writing – original draft: MR, MJS, GDP, CH

My author contributions in detail:
I planned and executed the DKO mouse treatment study – this included coordination of the mouse cohort, performing *i.v.* tail vein injections for AAV-delivery, blood collections from the facial vein and longitudinal rotarod measurements. I executed the flipping test, hindlimb clasping test and organ collection with the help of GW. For all *post mortem* analyses, I planned the experiments. I further post-processed the brains for cryosectioning

which I performed with the help of LSc and subsequently established and performed immunofluorescence stainings. I imaged the sections partially with the help of IP. For biochemical analyses, I pulverized the tissues and subsequently performed western blot analysis with the help of CS, a student under my supervision. I also planned and coordinated the ELISA and SIMOA experiments that were performed by KB and BN. I performed the preliminary Nanostring that made us decide to perform bulk RNA sequencing. In general, I led the communication with our collaborator Denali Therapeutics regarding this study including study design, material exchange, and experimental coordination. For the RNA sequencing and lipidomics analysis specifically, I worked closely with TS and JHS on data interpretation and presentation.

For the hiPSC experiments, I cloned the required constructs and performed genome editing of the *TMEM106B KO* and DKO cell lines, including genotyping and quality controls. I performed the initial characterization of microglia, neurons, and co-cultures derived from these cells and established a series of pathological readouts. Under my supervision, BP, a master's student, performed the treatment of these cultures with PTV:PGRN followed by biochemical analysis. I performed the immunofluorescence stainings and imaging for this study.

For all experiments performed with DKO cells or animals, I interpreted and quantified the results (besides the imaging) and prepared the figures for this manuscript. For the other figures, I received help from MJS. I wrote the first draft of this manuscript with the help of CH, MJS and GDP and incorporated the comments from all authors for the final version.

Rescue of FTLD-associated TDP-43 pathology and neurodegeneration by peripheral AAV-mediated expression of brain-penetrant progranulin

Authors: Marvin Reich[1,2,3,†], Matthew J. Simon[4,†], Beate Polke[5,‡], Georg Werner[5], Christian Schrader[5,§], Iñaki Paris[5], Sophie Robinson[2,3,5], Sonnet S. Davis[4], Gabrielly Lunkes de Melo[4], Lennart Schlaphoff[1,2,6], Lena Spieth[1,6,7], Stefan Berghoff[1,6,7], Todd Logan[4,∥], Brigitte Nuscher[5], Katrin Buschmann[5], Dieter Edbauer[1,8], Mikael Simons[1,3,6,8], Jung H. Suh[4], Thomas Sandmann[4], Mihalis S. Kariolis[4], Sarah L. DeVos[4], Joseph W. Lewcock[4], Dominik Paquet[3,8,*], Anja Capell[5,*], Gilbert Di Paolo[4,*], Christian Haass[1, 5, 8,*]

Affiliations:

[1] German Center for Neurodegenerative Diseases (DZNE) Munich, Munich, Germany.
[2] Graduate School of Systemic Neurosciences (GSN), Ludwig-Maximilian University of Munich; Munich, Germany.
[3] Institute for Stroke and Dementia Research, University Hospital, Ludwig-Maximilian University of Munich; Munich, Germany.
[4] Denali Therapeutics, Inc.; South San Francisco, CA, USA.
[5] Metabolic Biochemistry, Biomedical Centre (BMC), Faculty of Medicine, Ludwig-Maximilian University of Munich; Munich, Germany.
[6] Institute of Neuronal Cell Biology, Technical University Munich; Munich, Germany.
[7] Max Planck Institute for Multidisciplinary Sciences; Göttingen, Germany.
[8] Munich Cluster for Systems Neurology (Synergy); Munich, Germany.
* Correspondence: christian.haass@dzne.de
                    dipaolo@dnli.com
                    anja.capell@mail03.med.uni-muenchen.de
                    dominik.paquet@med.uni-muenchen.de
[†] Equal contribution
[‡] Present address: Roche Pharma Research and Early Development, Neuroscience and Rare Diseases Discovery and Translational Area, Roche Innovation Center Basel, F. Hoffmann-La Roche Ltd; Basel, Switzerland
[§] Present address: Department of Neurology and Neurological Sciences, Stanford University School of Medicine; Stanford, CA, USA.
[∥] Present address: BioMarin Pharmaceutical Inc.; San Rafael, CA, USA

One sentence summary:
Peripheral AAV-mediated delivery of brain-penetrant PGRN rescues TDP-43 pathology, neurodegeneration and motor phenotypes in FTLD-*GRN* models.

1

23

Abstract:

Progranulin (PGRN) haploinsufficiency is a major risk factor for frontotemporal lobar degeneration with TDP-43 pathology (FTLD-*GRN*). Multiple therapeutic strategies are in clinical development to restore PGRN levels in the CNS, including gene therapy. However, a limitation of current gene therapy approaches aimed to alleviate FTLD-associated pathologies may be their inefficient brain exposure and biodistribution. We therefore developed an adeno-associated virus (AAV) targeting the liver (L) to achieve sustained peripheral expression of a transferrin receptor (TfR) binding, brain-penetrant (b) PGRN variant (AAV(L):bPGRN) in two mouse models of FTLD-*GRN*, namely *Grn* knockout and *GrnxTmem106b* double knockout mice. This therapeutic strategy avoids potential safety and biodistribution issues of CNS-administered AAVs while maintaining sustained levels of PGRN in the brain following a single dose. AAV(L):bPGRN treatment reduced several FTLD-*GRN* associated disease pathologies including severe motor function deficits, aberrant TDP-43 solubility and phosphorylation, dysfunctional protein degradation, lipid metabolism, gliosis and neurodegeneration in the brain. Translatability of our findings was confirmed in a novel human *in vitro* model using co-cultured human induced pluripotent stem cell (hiPSC)-derived microglia lacking PGRN and TMEM106B and wild-type hiPSC-derived neurons. As in mice, aberrant TDP-43, lysosomal dysfunction and neuronal loss were ameliorated after treatment with exogenous TfR-binding protein transport vehicle fused to PGRN (PTV:PGRN). Together, our studies suggest that peripherally administered brain-penetrant PGRN replacement strategies can ameliorate FTLD-*GRN* relevant phenotypes including TDP-43 pathology, neurodegeneration and behavioral deficits. Our data provide preclinical proof of concept for the use of this AAV platform for treatment of FTLD-*GRN* and potentially other CNS disorders.

45

50

55

60

2

24

Main text:

65   **INTRODUCTION**

Haploinsufficiency of progranulin (PGRN) caused by heterozygous loss-of-function (LoF) mutations in the *GRN* gene dramatically enhances the risk for FTLD-TDP (*1-3*). As in all TDP-43 proteinopathies, FTLD with PGRN deficiency (FTLD-*GRN*) displays aggregation, pathological processing and abnormal phosphorylation of TDP-43 (*4, 5*). FTLD-*GRN* patients present with

70   severe clinical symptoms associated with underlying neurodegeneration primarily in the cortex (*5, 6*), resulting in enhanced neurofilament light chain (NfL) levels in blood and cerebrospinal fluid (CSF) (*7-9*), as well as pronounced neuroinflammation and dysfunction of the endo-lysosomal system (*5, 10, 11*). PGRN deficiency is hypothesized to contribute to these pathologies through its established role in lysosomal function (*11-14*), microglia homeostasis (*15-17*) and inflammatory

75   signaling (*11, 18, 19*) (reviewed in (*4, 5, 20, 21*)). PGRN or its proteolytic derivatives, the granulin peptides, are localized within the endo-lysosomal system (*22, 23*) and are implicated in the regulation of lysosomal proteases (*11, 12, 24-27*), lysosomal pH (*14, 28, 29*) as well as lipid hydrolases, such as glucocerebrosidase (GCase) (*29-34*). Loss of PGRN in mice causes an age-dependent increase in lysosomal enzymes, lysosomal membrane proteins, hyperactivated microglia

80   and saposin D, indicating deficits in endolysosomal and autophagic protein degradation (*11-19, 25, 29-33, 35, 36*). Lysosomal phenotypes further include deficiency of endolysosomal anionic phospholipid bis(monoacylglycero)phosphate (BMP) and secondary storage of sphingolipids, such as GCase substrates and gangliosides (*29, 33, 37*). Consistent with its critical role in the lysosome, homozygous LoF mutations in *GRN* cause the fatal lysosomal storage disease (LSD) termed

85   neuronal ceroid lipofuscinosis (NCL) in humans (*38, 39*).

$Grn^{+/-}$ (*Grn* HET) mice present with no robust disease-relevant phenotypes (*12, 40*). In contrast, $Grn^{-/-}$ (*Grn* KO) mice recapitulate lysosomal and inflammatory FTLD-*GRN* pathologies but exhibit only minor TDP-43 pathology even at advanced ages (*12, 16, 19*). Furthermore, behavioral phenotypes in *Grn* HET and *Grn* KO mice are subtle and have limited relevance to

90   FTLD-*GRN* clinical phenotypes (*40, 41*). We and others recently developed a mouse model that addressed some of the limitations of the *Grn* KO model by introducing an additional KO of *Tmem106b (42-44)*, a genetic risk factor for FTLD-*GRN* (*45*). TMEM106B is involved in endo-lysosomal degradation and trafficking (*46-50*) and has been shown to undergo processing and give rise to a C-terminal fragment prone to forming fibrils which are observed in the brain of FTLD-

3

25

95   *GRN* patients and aged individuals (*51-53*). The *Tmem106b* and *Grn* double KO (DKO) generally exacerbates phenotypes observed in the single KOs, including lysosomal and autophagic dysfunction, neuroinflammation, and myelin loss (*42-44, 54*). Importantly, unlike the *Grn* KO, it exhibits much more robust accumulation of insoluble and hyperphosphorylated TDP-43, and motor impairment at an age of 4 months (*42-44*). Thus, this model reproduces key biochemical, cell

100   biological as well as disease-relevant motor and neurodegeneration phenotypes of FTLD-*GRN*.

To date, there is no disease-modifying treatment for FTLD-*GRN*, although several therapeutic approaches are currently being tested in the clinic (reviewed in (*20, 55*)). Given that it is a monogenic disease, correcting the PGRN deficiency with a protein replacement therapy may offer an effective therapeutic approach to slow or halt disease progression and reduce pathology.

105   While adeno-associated virus (AAV)-based therapies are under clinical investigation (*56-58*), they typically rely on direct CNS administration, which may introduce safety concerns as well as result in limited or uneven biodistribution of the AAV (*56-58*) (reviewed in (*59*)). Thus, the number of cells expressing PGRN and PGRN exposure in cells far from the injection site might be insufficient. Consistent with this, a recent study suggests that AAV1 and 9 administered to the CSF can reduce

110   disease phenotypes in the spinal cord, but not in the brain of an FTLD-*GRN* mouse model, limiting their use for neurodegenerative diseases with widespread brain pathologies, such as FTLD-*GRN* (*60*). As an alternative, we recently fused human recombinant PGRN to a transport vehicle (PTV:PGRN), enabling transferrin receptor (TfR)-mediated transcytosis across the blood-brain barrier (BBB) and delivery throughout the whole CNS (*29*). Using PTV:PGRN, multiple FTLD-

115   related pathologies in *Grn* KO mice and human microglia – lipid/lysosomal abnormalities, microglial/astrocytic hyperactivation – were rescued (*29*). However, due to the limited pathology of the *Grn* KO mouse model, TDP-43 pathology, motor deficits and neurodegeneration could not be investigated.

Here, we developed an advanced gene therapy approach by using a liver-targeting (L)

120   adeno-associated virus expressing brain-penetrant (b) PGRN (AAV(L):bPGRN). This strategy combines a TfR-mediated, brain-penetrant PGRN biologic with AAV-targeted delivery to the liver, enabling brain-wide PGRN delivery with a single peripheral administration treatment paradigm without requiring direct CNS injection. We tested the AAV(L):bPGRN approach in *Grn* KO mice as well as in our recently described DKO mouse model lacking both *Grn* and *Tmem106b* to study

125   whether PGRN replacement could rescue TDP-43 pathology, motor impairment, exacerbated

26

neuroinflammation, neuronal loss, impaired protein degradation, and lipidomic and transcriptomic changes in the brain. To complement our *in vivo* efforts, we generated a hiPSC-derived FTLD-model by co-culturing *GRN* and *TMEM106B* DKO human iPSC-derived microglia (iMG) with WT human iPSC-derived neurons (iN). This model recapitulates multiple *in vivo* phenotypes, including

130   microglial hyperactivation, lysosomal abnormalities, aberrant TDP-43 processing and phosphorylation, as well as neurodegeneration. Strikingly, our replacement strategy significantly reduced all phenotypes observed in the DKO mice and human iPSC model, despite the phenotypic severity and constitutive loss of TMEM106B.

Our study provides compelling evidence that brain-penetrant PGRN replacement therapies

135   such as AAV(L):bPGRN or PTV:PGRN can have an impact on the central pathologies of FTLD-*GRN* in the brain, namely TDP-43 pathology and neurodegeneration, in both mouse and human FTLD models.

RESULTS

140   **AAV(L):bPGRN allows safe and robust expression and brain delivery**

We generated AAV(L):bPGRN, a liver-targeting AAV8 encoding a fusion protein (8D3:PGRN) consisting of a single chain fragment variable (scFv) antibody recognizing mouse transferrin receptor (TfR; 8D3) fused to human PGRN (hPGRN). AAV(L):bPGRN infects hepatocytes in the liver where it stably expresses 8D3:PGRN after a single peripheral administration to provide

145   sustained expression and secretion of the fusion protein into systemic circulation (Fig. 1A). As a proof-of-principle, we first confirmed AAV(L):bPGRN treatment drives stable expression of 8D3:PGRN in *Grn* KO mice. We infected 4-5-month-old WT and *Grn* KO mice with AAV(L):bPGRN and monitored hPGRN levels in liver, brain and plasma for 31 weeks (Fig. 1B). In the liver of AAV(L):bPGRN treated mice, hPGRN levels of 5 µg/mg above background were

150   observed 9 weeks after dosing, suggesting robust liver targeting of AAV(L):bPGRN (Fig. 1C). Furthermore, one week after injection, hPGRN was detectable in plasma and after 4 weeks, expression stabilized at an average of 3 µg/ml (Fig. 1D), demonstrating that the liver expressed AAV(L):bPGRN is secreted into circulation. Finally, robust levels of hPGRN were detected in the brain of mice at both 9 and 31 weeks after injection, supporting efficient blood-brain-barrier

155   transcytosis of the fusion protein (Fig. 1E).

5

As high levels of AAV infection have been linked to adverse effects, including hepatotoxicity (*61*), and TfR is highly expressed on immature red blood cells (RBCs) we evaluated serum chemistry (including alanine transaminase (ALT) and aspartate aminotransferase (AST)) and hematology (including circulating reticulocytes), and performed histopathologic analysis of

160   key organs from *Grn* KO mice treated with AAV(L):bPGRN after 31 weeks (Fig. S1, Table S1). No significant microscopic findings were noted in the assessed tissues, including brain, liver, heart, and sciatic nerve (Table S1). No treatment-related findings were identified in serum. Minimal and non-adverse changes were observed in hematology, including slight decrease in red blood cell size (mean corpuscular volume (MCV)) and hemoglobin (mean corpuscular hemoglobin (MCH))

165   levels, accompanied by a slight increase in RBC and reticulocyte counts (Fig. S1A-D). Thus, a single injection of AAV(L):bPGRN in mice allows for sustained brain delivery of hPGRN without any significant deleterious side-effects.

6

28
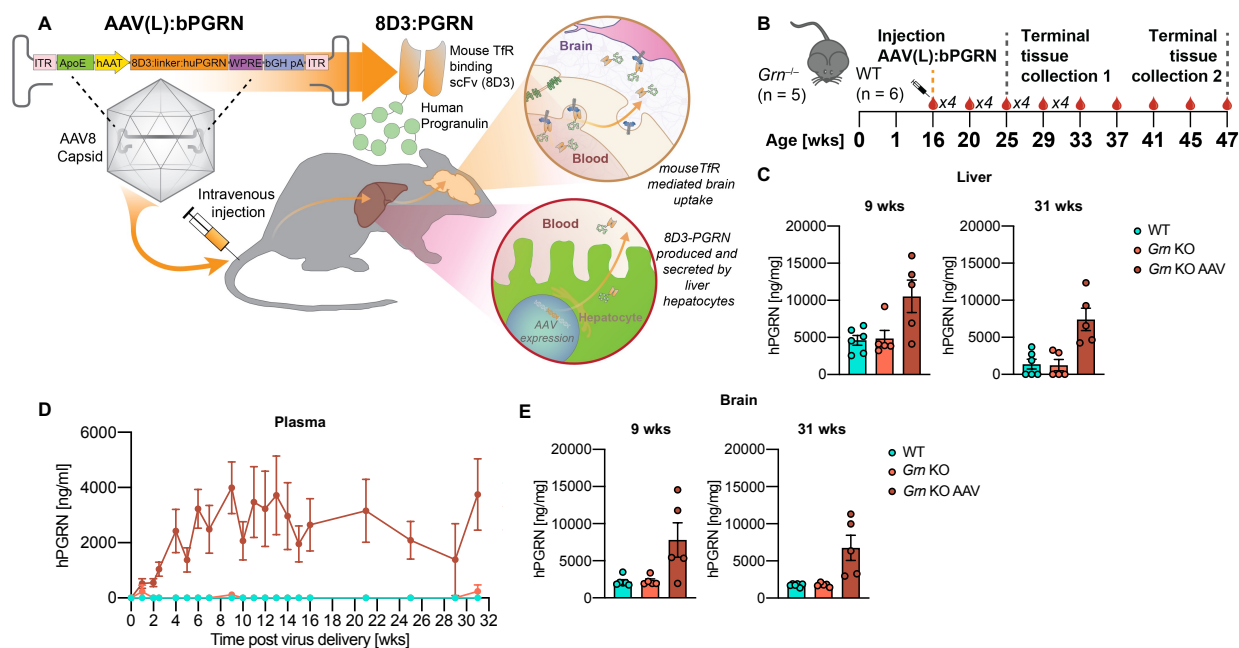
Fig. 1: AAV-expressed PGRN is delivered to the brain and shows no side effects in *Grn* KO mice. (**A**) Graphical summary of treatment paradigm. Intravenously administered AAV expresses brain-penetrant (b) human progranulin (PGRN) in the liver (L) (AAV(L):bPGRN). PGRN is fused to a single chain fragment variable (scFv) antibody recognizing mouse transferrin receptor (TfR; 8D3). 8D3:PGRN is expressed by liver hepatocytes, released into the vasculature and can cross the blood-brain-barrier *via* transferrin receptor-binding. (**B**) Schematic of AAV treatment and sample collection in the *Grn* KO AAV treatment study. Directly after treatment, blood was sampled weekly (x4 = 4 times in 4 weeks (wks)), from 16 weeks after treatment on every 4 weeks. (**C-E**) hPGRN levels in liver (C), plasma (D) and brain (E) following AAV(L):bPGRN treatment in mice. For tissues, 9-week samples are depicted on the left and 31-week on the right. For all figures, error bars represent standard error of the mean (SEM). n=5-6/group.

7

AAV(L):bPGRN is stably expressed in DKO mice and ameliorates motor defects

We next examined the effects of AAV(L):bPGRN mediated PGRN replacement in DKO mice. Previously, we demonstrated that DKO mice not only exacerbate the FTLD-related pathologies observed in *Grn* KO mice, but additionally exhibit motor impairment, and pronounced abnormal phosphorylation and deposition of insoluble TDP-43 (*42-44*). To determine whether restoring PGRN is sufficient to prevent these phenotypes, DKO mice were injected at 6 weeks of age, prior to development of robust pathologies. A predetermined treatment duration until an age of 15 weeks was established due to the severity of the DKO phenotypes (Fig. 2A) (*42*). As early as 4 weeks after AAV delivery, stable levels of hPGRN of around 4 µg/ml were observed in plasma of treated WT and DKO mice (Fig. 2B). Robust hPGRN protein levels were also detected in liver and brain of treated mice (Fig. 2C,D), without affecting endogenous expression of mPGRN (Fig. S2A-C).

Given that motor impairment is a common symptom observed in FTLD-*GRN* patients and in DKO mice (*62-64*), our initial objective was to evaluate whether the administration of AAV expressing 8D3:PGRN could alleviate these phenotypes. Therefore, we conducted a longitudinal assessment of rotarod performance, commencing three days after AAV injection. While initially, all mice performed at a comparable level, WT animals increased time on the rotarod over 15 weeks regardless of treatment. In contrast, performance of both DKO and AAV-treated DKO mice decreased over time (Fig. 2E). However, AAV treatment significantly slowed the rate of decline in DKO mice, and in contrast to untreated DKO mice, AAV treated DKO mice never failed the test (rotarod time <3 s). To further assess motor function, we performed a flipping test at 15 weeks, evaluating righting ability. In this paradigm, saline-treated DKO mice could be flipped over, while most AAV-treated DKO mice could not be flipped or raised themselves immediately (Fig. 2F, Fig. S3A, Movie S1-4). We further conducted the hind limb clasping test (*42, 65*) and found that treated DKO mice showed significantly reduced hind limb clasping compared to untreated DKO mice, with some mice not exhibiting any clasping phenotype (score = 0) (Fig. 2G, Fig. S3B). In conclusion, AVV driven expression of 8D3:PGRN substantially lowered severe motor neuron deficits in the DKO mice.

8

30
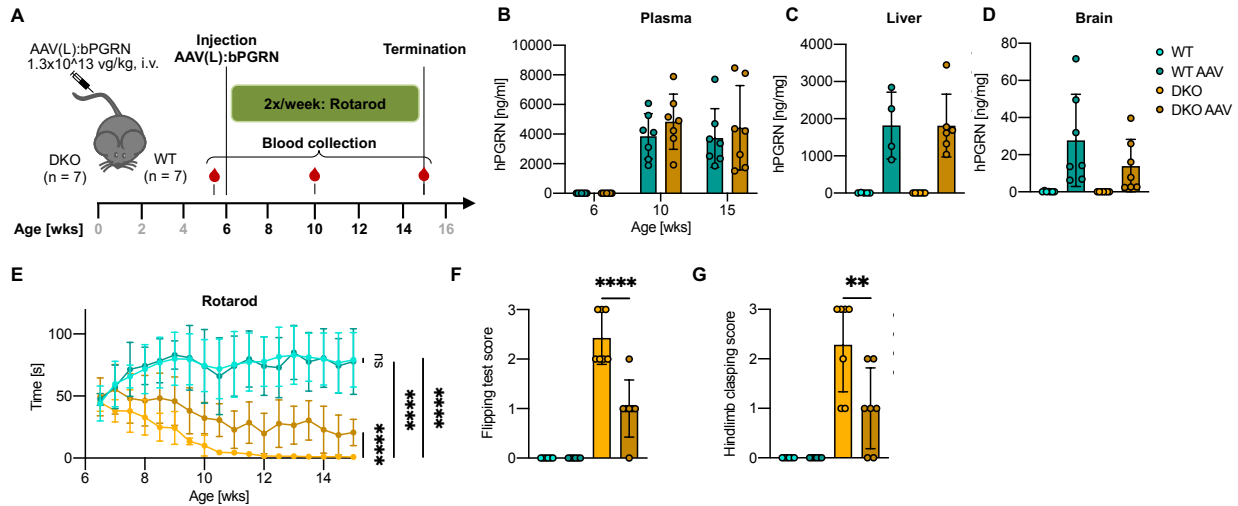
Fig. 2: AAV-expressed PGRN is delivered to the brain and ameliorates behavioral abnormalities in DKO mice. (**A**) Schematics of AAV treatment and sample collection in the *Grn* x *Tmem106b* double knockout (DKO) AAV(L):bPGRN treatment study. (**B-D**) hPGRN levels in plasma (left, n=7/group; 6, 10 and 15-week-old), liver (middle, n=4-6/group; 15-week-old) and brain (right, n=7/group; 15-week-old) following AAV(L):bPGRN treatment in mice as assessed by ELISA. (**E**) Longitudinal assessment of rotarod performance following treatment. (**F**) Quantification of the flipping test based on a scoring system (n=7/group). (**G**) Quantification of the hind limb clasping test based on a scoring system (n=7/group).

Data is depicted as mean ± standard deviation (SD), data points represent individual animals. For E, overall comparison was performed by two-way ANOVA with Tukey's multiple comparison. Individual groups in E were compared using two-tailed student's t-test. For F and G, one-way ANOVA with Tukey's multiple comparison was performed. ns $p > 0.05$, **$p < 0.01$, ****$p < 0.0001$.

9

AAV(L):bPGRN reduces proteolysis defects, TDP-43 pathology and neurodegeneration

Based on the correction of functional motor deficits, we hypothesized AAV(L):bPGRN treatment may also correct the endolysosomal and autophagic protein degradation defects observed in the DKO mice (*42-44*). These mice present with an increase in ubiquitinated proteins in the brain (Fig. 3A,B), indicating defects in proteolysis by the ubiquitin/proteasome pathway. Moreover, the lysosomal sphingolipid-activator protein prosaposin, its functionally active cleavage product saposin D, and the autophagosome cargo protein p62 are all upregulated, suggesting endo-lysosomal and autophagy dysregulation (Fig. 3A,B) (*66, 67*). The accumulation of insoluble p62 and both LC3 I and its lipid modified form LC3 II, key players in the autophagy pathway (*67*), indicates the formation of pathological autophagic aggregates (Fig. 3A,B) (*68*). Immunofluorescence detection of p62 confirmed the presence of these aggregates (Fig. 3C,D). Strikingly, all these protein degradation-related phenotypes were significantly reduced in treated DKO mice compared to untreated animals (Fig. 3A-D).

DKO mice also exhibit TDP-43 pathology (*42-44*), a hallmark of FTLD-*GRN* that is observed in patients' brains (*69, 70*), but is not robustly replicated in *Grn* KO mice (*11, 19*). This includes insoluble TDP-43 deposits, abnormal processing and phosphorylation of the protein (*42-44, 71*). Upon analyzing solubility, processing and phosphorylation of TDP-43 by sequential extraction and subsequent biochemical analysis, we only observed mild changes in protein levels and processing of TDP-43 in the high salt- and RIPA-soluble fraction (Fig. S4A-D). However, protein levels of insoluble TDP-43 (urea fraction) were consistently increased in DKO mice compared to WT mice, and this phenotype was completely reversed following AAV treatment (Fig. 3E,F). Additionally, we found a drastic increase of the pathological insoluble and phosphorylated TDP-43 (pSer409/410) in DKO mice compared to WT which was reduced by 70% in AAV(L):bPGRN-treated DKO mice (Fig. 3E,F). Because TDP-43 pathology is generally associated with neurodegeneration, we measured plasma neurofilament light chain (NfL) levels, a clinical marker for neurodegeneration (*7, 8*), before and during treatment. Initially, plasma NfL levels were comparable between WT and DKO mice. However, while NfL levels rose over time in DKO mice, they were significantly lower in treated DKO animals as early as 4 weeks after treatment and even decreased after 9 weeks (Fig. 3G). At 12 months of age, *Grn* KO mice only showed a mild increase in plasma NfL, but substantial increase of NfL in the CSF which was also rescued upon treatment with AAV(L):bPGRN (Fig. S4E).

32

Together, these findings demonstrate a robust reduction of TDP-43 pathology, associated with a rescue of the impaired protein degradation machinery, motor phenotypes, and reduced neurodegeneration following treatment with AAV(L):bPGRN.

255
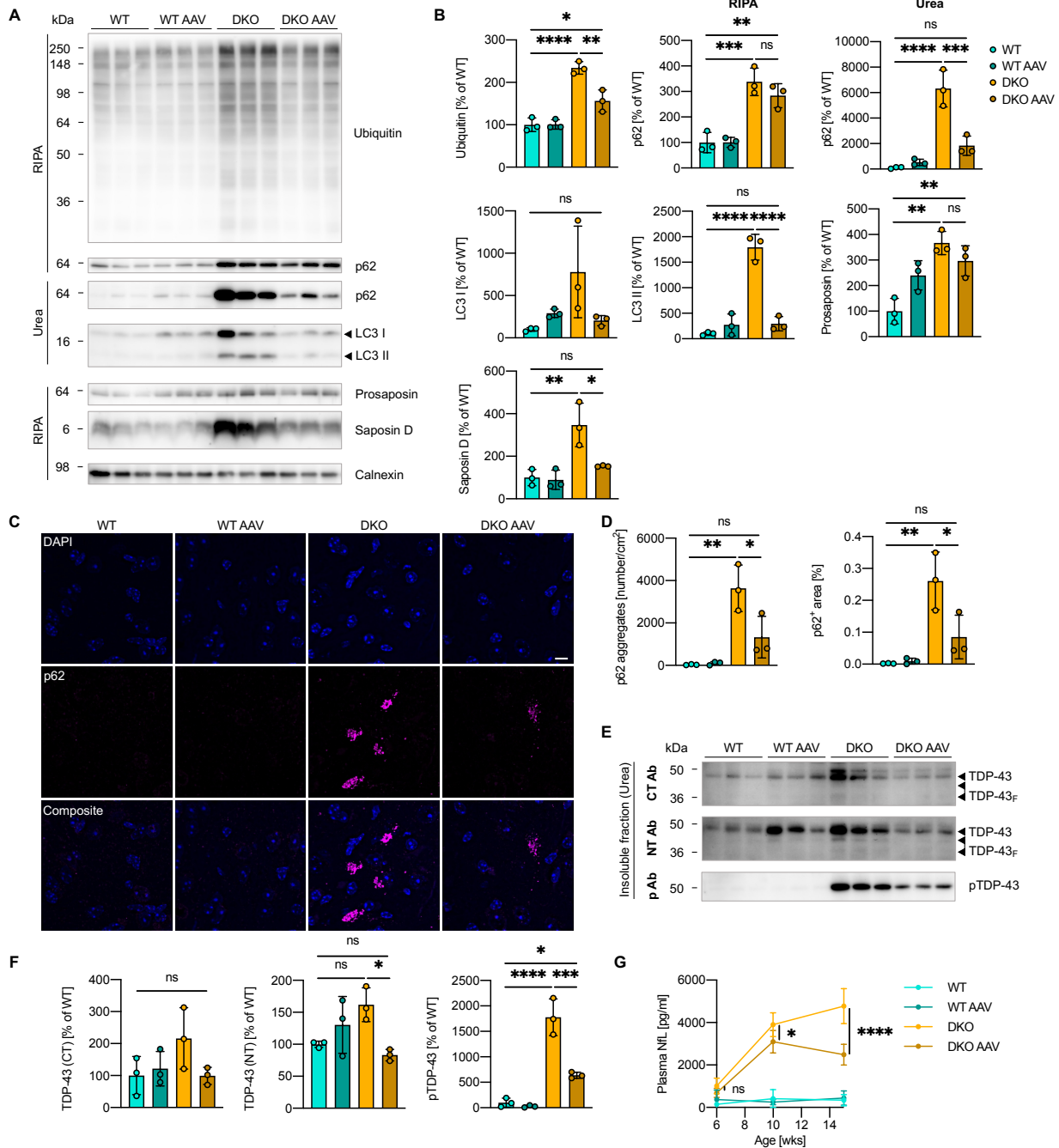
Fig. 3: AAV-mediated delivery of 8D3:PGRN reduces protein degradation defects, TDP-43 pathology and NfL levels in DKO mice. (**A**) Western blot showing the protein levels of Ubiquitin, p62, prosaposin and saposin D in the RIPA fraction and the protein levels of p62 and LC3 I and II in the urea fraction in the brain of WT and DKO mice after treatment (n=3/group). (**B**) Quantification of the protein levels in A normalized to the mean of WT (n=3/group). (**C**) Representative immunofluorescence images of the thalamus of WT and DKO mice after treatment showing Map2+, Iba1+ and p62+ cells (scalebar = 10 μm). (**D**) Quantification of the number of p62

12

34

aggregates and p62$^+$ area in whole brain hemispheres (n=3/group). (**E**) Western blot showing the protein levels of RIPA-insoluble TDP-43 in the urea soluble fraction of the brain of WT and DKO mice after treatment using antibodies directed against the C- and N-terminus as well as to the phosphorylation site Ser409/410 (n=3/group). (**F**) Quantification of the protein levels in E normalized to mean of WT (n=3/group). (**G**) Plasma NfL levels of mice before treatment (6 weeks) and 4 and 9 weeks after treatment (n=7/group).

Data is depicted as mean ± SD, data points represent individual animals. For statistical analysis, one-way ANOVA with Tukey's multiple comparison was performed. ns $p > 0.05$, *$p < 0.05$, **$p < 0.01$, ***$p < 0.001$, ****$p < 0.0001$.

13

AAV(L):bPGRN reduces gliosis *in vivo*

275 Previous studies demonstrated that gliosis and neuroinflammation are hallmark pathologies not only in *Grn* KO (*12, 16, 19*) and the DKO mouse models (*42-44*), but also in FTLD-*GRN* patients (*5, 72*). To investigate if these pathological phenotypes could also be rescued by AAV(L):bPGRN treatment, we examined the transcriptional profile of *Grn* KO and DKO mice following AAV(L):bPGRN treatment. In 12-month-old *Grn* KO mice, bulk brain RNA sequencing analysis

280 demonstrated mild transcriptional changes consistent with previous reports (*12, 15, 16, 19, 29*), which in turn were partially corrected with AAV(L):bPGRN (Fig. S5A). In 4-month-old DKO animals however, these changes were drastically exacerbated, consistent with previous reports (*42-44*). Projected into two dimensions via multi-dimensional scaling, samples from WT animals (with or without AAV treatment) clustered together, indicating globally similar gene expression profiles,

285 but DKO samples segregated according to genotype and treatment (Fig 4A). AAV treatment of DKO animals shifted the corresponding samples toward those of WT animals, indicating partial correction of the transcriptional differences. We next completed gene-level differential expression analysis. We found that in DKO mice, 481 genes were up- and 304 genes downregulated compared to WT animals (Fig. S6A). Following AAV(L):bPGRN treatment, 51 genes were down- and 171

290 genes upregulated again in DKO mice (Fig. 4B). Pathway analysis revealed that the most impacted genes include established markers for disease-associated microglia (DAM) and lysosomal dysfunction (Fig. 4C) (*12, 73*). Interestingly, while the expression of many of these markers was fully corrected with AAV(L):bPGRN, some genes only showed partial response to treatment (ex:*Serpina3n*), suggesting *Tmem106b*-specific effects that are not responsive to PGRN

295 replacement. Others, like *Ccl2*, showed an AAV response, regardless of genotype. As both DKO and treatment strongly modulated the abundance of known cell type markers such as *Gfap* (astrocytes) and *Itgax* (microglia) (Fig. 4B), we next determined changes in cell type composition (*74*) (Fig. S6B,C). Both, microglia and astrocyte markers were greatly increased in the DKO mice and showed a marked reduction with AAV treatment. In contrast, DKO brains had a reduction in

300 neuronal cell type markers that are elevated with AAV treatment. Interestingly, different established oligodendrocyte markers displayed different gene expression changes across genotypes and treatments, perhaps reflecting differential responses in cellular subtypes. To confirm the significant reduction in gene expression associated with microglia and astrocyte activation following PGRN replacement, we further assessed the expression of Gfap, Iba1 and Cd68 by

14

36

305 immunohistochemistry (Fig. 4D,E). In DKO mice, both the total number of microglia and Cd68$^+$ reactive microglia, as well as astrocytes, were significantly elevated. Consistent with the RNA sequencing data, PGRN replacement resulted in a significant reduction of astrocytes. While the number of microglia was only slightly reduced, the proportion of Cd68$^+$ microglia was substantially decreased (Fig. 4D,E). We further assessed the levels of Trem2, a microglial surface receptor that

310 is critical for the transition to reactive microglia (*73, 75, 76*). The markedly elevated levels of Trem2 in plasma, liver and brain of DKO mice were all effectively decreased after PGRN replacement (Fig. 4F), consistent with a reduced microglial response to the pathological challenges after treatment-related amelioration. In *Grn* KO mice, comparable elevations of Cd68, Iba1 and Trem2 were also responsive to AAV(L):PGRN treatment, supporting the link between PGRN and

315 glial function (Fig. S5B-D).

15
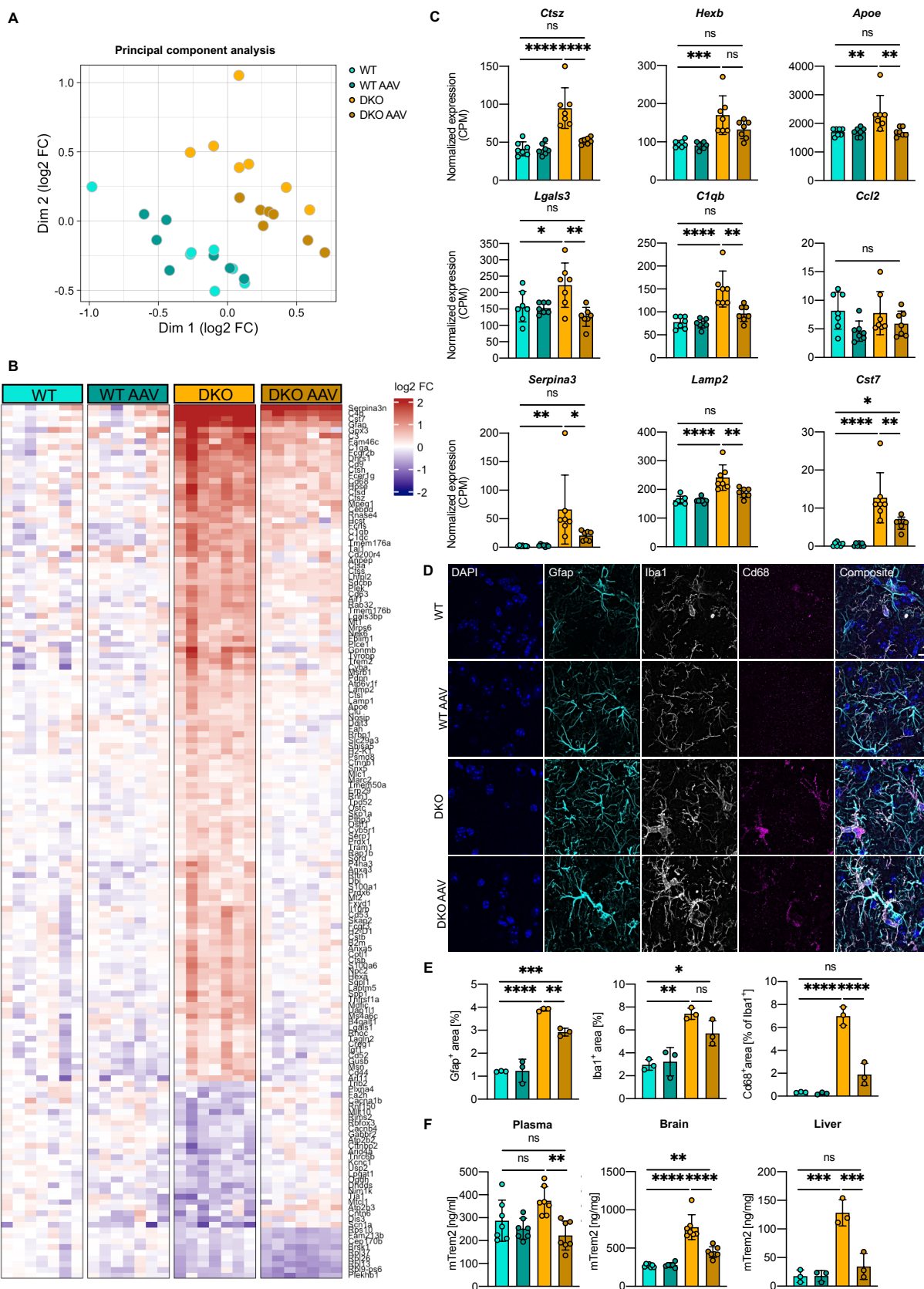
Fig. 4: AAV-mediated delivery of 8D3:PGRN normalizes astrogliosis and microgliosis in

16

DKO mice. (**A**) UMAP depiction of full transcript profile comparing untreated and AAV(L):bPGRN-treated WT and DKO mice (n=7/group). (**B**) Heatmap showing the top 222
320   differentially expressed genes in DKO mice and correction with AAV(L):bPGRN with a false discovery rate (FDR) < 5% and at least a 20% change comparing WT and DKO as well as DKO AAV and DKO. Plotted values are log2 transformed fold changes (FC) (n=7/group). (**C**) Transcriptional changes in genes linked to lysosomal function (n=7/group). (**D**) Representative immunofluorescence images of the thalamus of WT and DKO mice after treatment showing Iba1$^+$,
325   Gfap$^+$ and Cd68$^+$ cells (scalebar = 10 µm). (**E**) Quantification of the Gfap$^+$, Iba1$^+$ and Iba$^+$/Cd68$^+$ area in whole brain hemispheres (n=3/group). (**F**) mTrem2 levels in plasma (left, n=7/group), brain (middle, n=5-7/group) and liver (right, n=3/group) of WT and DKO mice after treatment at the end of the study as assessed by ELISA.

C, E, F: Data is depicted as mean ± SD, data points represent individual animals. For statistical
330   analysis, one-way ANOVA with Tukey's multiple comparison was performed. ns $p > 0.05$, $*p < 0.05$, $**p < 0.01$, $***p < 0.001$, $****p < 0.0001$.

17

AAV(L):bPGRN rescues lipid biomarkers of FTLD-*GRN*

Previously, *Grn* KO mice were found to exhibit robust alterations of lipid metabolism and lysosomal function (*29*). Here, we sought to determine if AAV(L):bPGRN can restore lipid changes. We first confirmed that 12-month-old *Grn* KO mice exhibit dysregulation of the phospholipid BMP and the glycosphingolipid glucosylsphingosine. Similar to recombinant PGRN replacement (*29*), AAV(L):bPGRN treatment restored these lipids back to baseline levels (Fig. S7A,B). Next, due to the established role of Tmem106b in the endolysosomal pathway (*46-50*), we hypothesized that the lipid profile of DKO mouse brain may be similarly or even more dysregulated. To assess this, we performed targeted lipidomic assessment of DKO and WT mouse brain with or without AAV(L):bPGRN treatment (Fig. 5). Unsupervised principal component analysis (PCA) of 203 lipids detected showed clear separation between WT and DKO mice along the principal component (PC) 1 axis. Lipid profiles of AAV(L):bPGRN-treated DKO mice shifted closer to WT conditions indicating a partial correction (Fig. 5A). Univariate analysis of lipid alterations in DKO mice brain relative to WT identified 27 significantly dysregulated lipids including several lipid classes such as gangliosides (GM1, GM2, GM3, GD3), glycerophospholipids (BMP, lysophosphatidylglycerol (LPG), phosphatidylinositol (PI)), sterols (cholesteryl ester, CE) and sphingolipids (S1P, Cer) (Fig. 5B,C). Of these, 19 lipids were responsive to AAV(L):bPGRN treatment with varying sensitivity (Fig. 5B-E). AAV(L):bPGRN treatment broadly increased BMP species of varying acyl-chain compositions back to WT levels (Fig. 5F). AAV(L):bPGRN treatment significantly lowered levels of galactosylsphingosine, which accumulates when galactosyl ceramidase (Galc) is impaired. The broad upregulation of gangliosides in *Grn* KO mice such as GM3, was also observed in DKO mice and further exacerbated by additional increase of GM2 and GM1 species and partially rescued upon treatment (Fig. 5G). The more robust ganglioside accumulating phenotype of DKO mice relative to *Grn* KO alone (Fig. S7) and only partial rescue upon AAV(L):bPGRN treatment suggests that TMEM106B may have a more dominant influence over lysosomal ganglioside catabolism. Also unique to DKO, there was an increase in myelin-associated lipids, CE and galactosylceramide (GalCer). Accumulation of these lipids potentially reflects the significantly altered myelin homeostasis in the DKO brain (Fig. 5H) (*42, 77, 78*). Taken together, these data highlight that DKO mice have severe lipid dysregulation that is largely corrected with PGRN replacement using AAV(L):bPGRN.

18

40
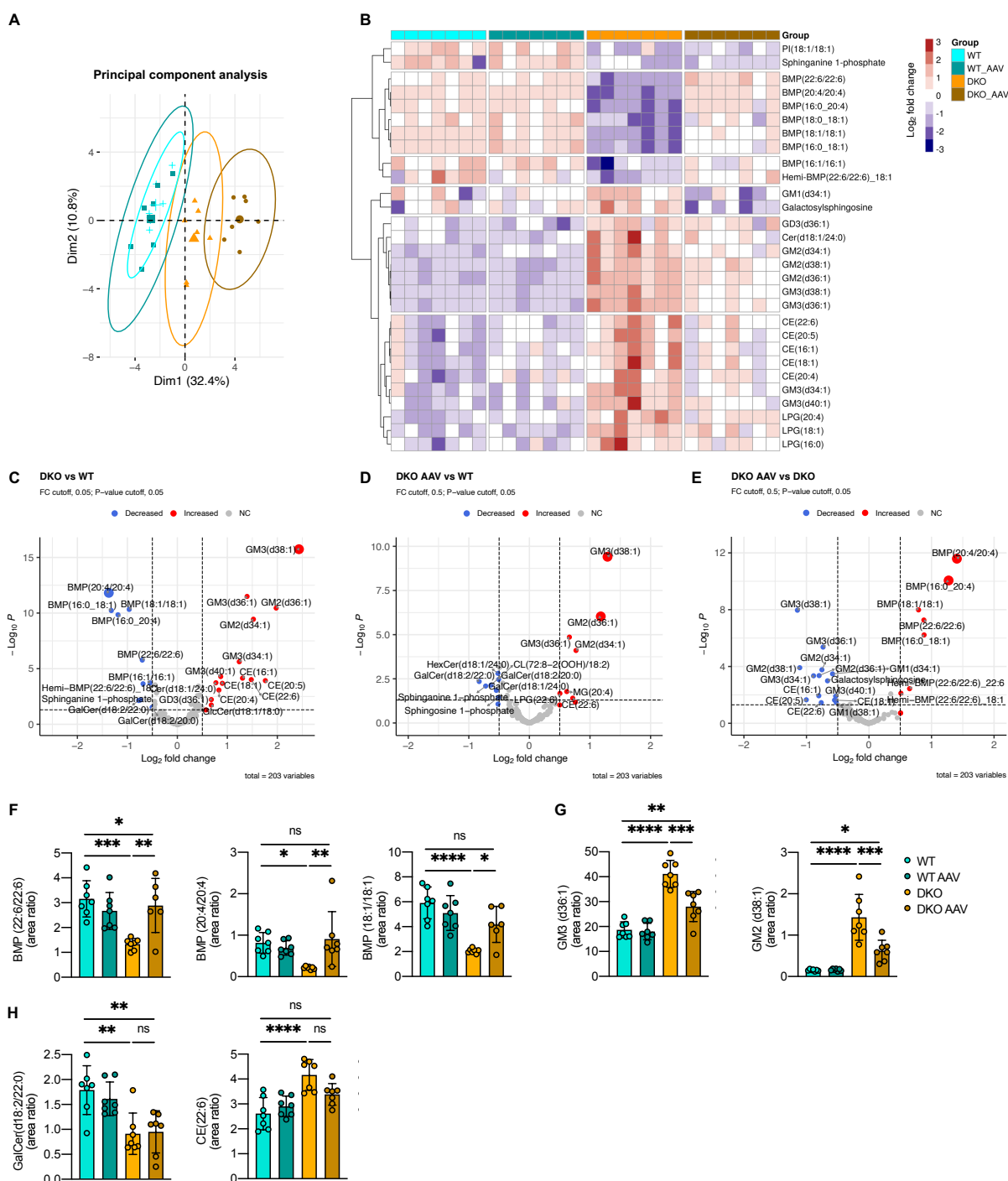
Fig. 5: AAV-mediated delivery of 8D3:PGRN restores lipid profile of DKO mice. (**A**) Principal component analysis of global lipid changes comparing untreated and AAV(L):bPGRN-treated WT and DKO mice. (**B**) Heatmap depiction of differentially regulated lipids in DKO mice and correction with AAV(L):bPGRN treatment. Columns represent individual animals. Plotted values are log2 transformed. (**C-E**) Volcano plot depictions of major lipid changes that are genotype dependent (**C**) or treatment dependent comparing AAV-treated DKO mice (DKO AAV) to WT

370 mice (D) or DKO mice (E). FDR cutoff: <5%, change cutoff: >20%. (**F-H**) Bar plots of treatment

response of BMPs (F), gangliosides (G) and changes in myelin associated lipids (H). n=7/group.

Data is depicted as mean ± SD ns $p > 0.05$, *$p < 0.05$, **$p < 0.01$, ***$p < 0.001$, ****$p < 0.0001$.

20

42

PTV:PGRN rescues FTLD-like pathology in human neurons and microglia

375   To test whether our findings can be translated to human cells and to enable investigation of cell-autonomous versus non-autonomous effects, we extended our experiments to human induced pluripotent stem cells (hiPSC). First, we generated a DKO hiPSC line by knocking out *TMEM106B* in our recently described *GRN* KO cell line using an established CRISPR/Cas9 editing workflow (Fig. S8) (*79, 80*). To establish a hiPSC-based FTLD model, we co-cultured DKO hiPSC-derived

380   microglia (iMG) with WT hiPSC-derived neurons (iN) (Fig. 6A). Crosstalk between these two cell types is expected as microglia express the highest PGRN levels of all brain cell types, whereas TDP-43 pathology is mostly observed in neurons (*71*). Upon co-culture of DKO iMG together with WT iN we observed a significant increase in TDP-43 processing and phosphorylation (Fig. 6B,C), resulting in pronounced disruption of the neuronal network as shown by a reduction in MAP2$^+$ area

385   (Fig. 6D,E). Lastly, we replicated our recently reported finding in *GRN* KO monocultured iMG showing dysfunctional lysosomes (*29, 32*). We found a strong elevation of the protein expression levels and catalytic activities of the lysosomal proteases cathepsin B, D and L (CTSB, CTSD, CTSL) in the co-cultures (Fig. 6F-H). As the *in vivo* mechanism of action of AAV(L):bPGRN cannot be replicated in a cell culture system, we applied PTV:PGRN (*29*) to the co-culture model

390   to confirm therapeutic effects of PGRN replacement on TDP-43 pathology and neurodegeneration in a human system. Following a 5-day co-culture, we treated the cells with either PTV:PGRN, an inactive human IgG control (IgG) or PBS as control every second day until collection after 2 weeks (Fig. 6A). The cultures treated with PTV:PGRN showed partially normalized levels of PGRN, with fully reversed aberrant TDP-43 processing and disruption of the neuritic network (Fig. 6B-E).

395   Moreover, the increased levels of pTDP-43 and lysosomal proteases as well as their increased activity were also reduced (Fig. 6B,C,F-H).

    Taken together, PGRN replacement in a human model successfully alleviates disease associated phenotypes and supports the applicability of our newly developed hiPSC-derived FTLD model for developing therapeutic approaches.

400
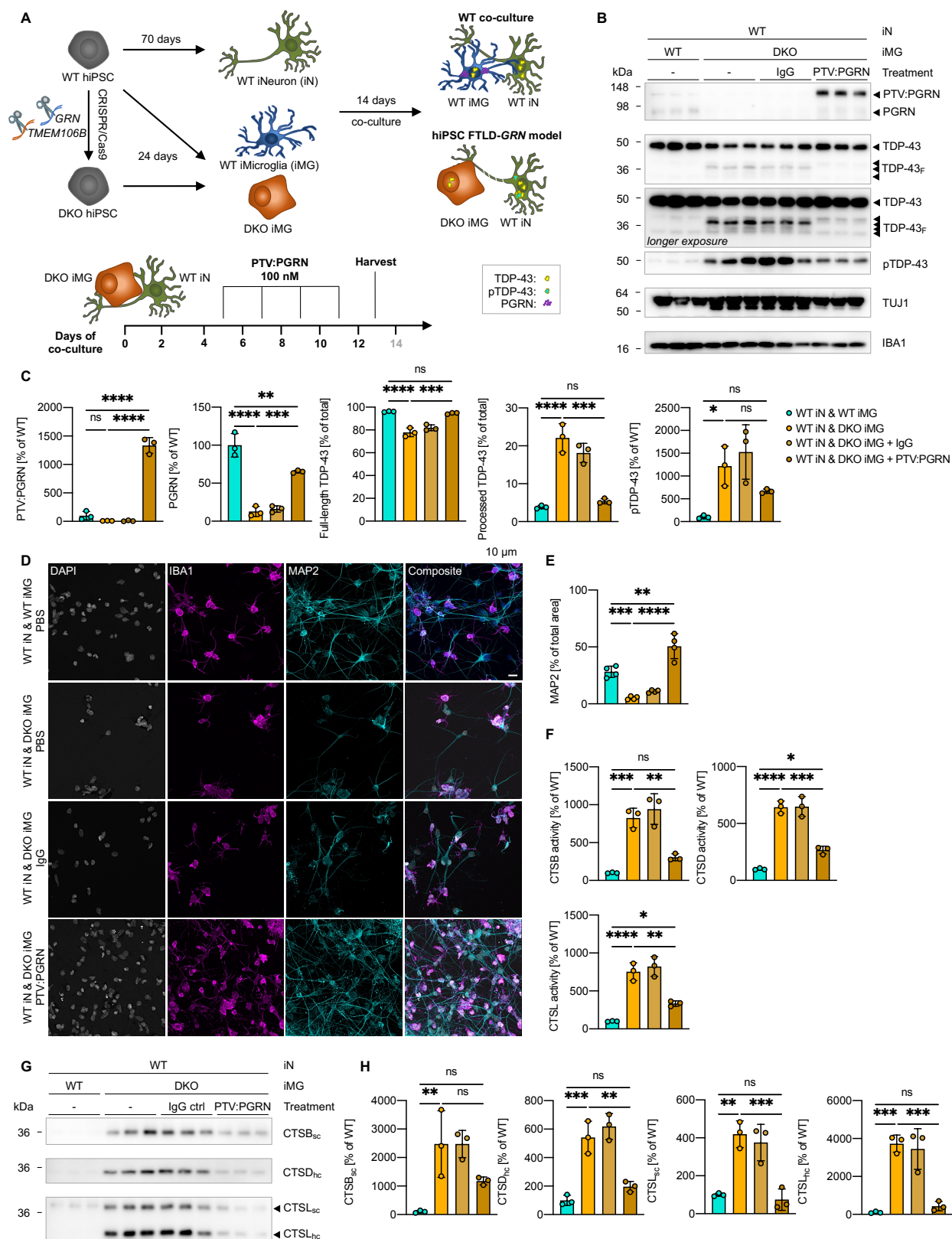
Fig. 6: PTV:PGRN rescues FTLD-*GRN* core pathologies in hiPSC-derived DKO microglia in co-culture with neurons. (A) Graphical description of DKO hiPSC generation and differentiation,

hiPSC-based co-culture FTLD-*GRN* model and treatment paradigm for PTV:PGRN treatment study. (**B**) Western blot showing the protein levels of PTV:PGRN and hPGRN, TDP-43 (NT Ab),

405   pTDP-43, TUJ1 and IBA1 in untreated iMG / iN co-cultures as well as inactive control human IgG- and PTV:PGRN-treated cultures (n=3/biological replicates). (**C**) Quantification of the protein levels in B normalized to the mean of the WT iN / WT iMG co-culture (n=3/biological replicates). (**D**) Representative immunofluorescence images showing IBA1$^+$ and MAP2$^+$ cells (scalebar = 10 μm). (**E**) Quantification of the MAP2$^+$ area (n=4/replicates). (**F**) *In vitro* activity of the lysosomal

410   proteases cathepsin B (top left), cathepsin D (top right) and cathepsin L (bottom) normalized to the mean of the WT iN / WT iMG co-culture (n=3/biological replicates). (**G**) Western blot showing the protein levels of cathepsin B, D and L (n=3/biological replicates). (**H**) Quantification of the protein levels in G normalized to the WT iN / WT iMG co-culture (n=3/biological replicates).

Data is depicted as mean ± SD, data points represent individual samples. For statistical analysis,

415   one-way ANOVA with Tukey's multiple comparison was performed. ns $p > 0.05$, *$p < 0.05$, **$p < 0.01$, ***$p < 0.001$, ****$p < 0.0001$.

23

DISCUSSION

Currently, there are several candidate therapeutic approaches for FTLD-*GRN* in clinical trials or preclinical development, all aiming to raise PGRN protein levels (reviewed in (*20, 55*)). These include an anti-sortilin antibody to increase circulating PGRN levels *via* inhibition of cellular uptake (*81-83*), AAV-based gene therapy approaches (*84-86*), a recombinant brain-penetrant PGRN biologic (*29*), as well as small molecules and transcriptional regulators (*87*). Here, we tested an innovative approach for a PGRN replacement therapy using a second-generation gene therapy approach in two different mouse models for FTLD-*GRN*, namely *Grn* KO and *GrnxTmem106b* DKO mice, that combines the dosing advantages of AAV approaches with the biodistribution improvements allowed by TfR-mediated transcytosis at the BBB and brain delivery of recombinant fusion proteins.

Despite several decades of research, mouse models reproducing TDP-43 pathology associated with FTLD-*GRN* without overexpression have been a major limitation in the field. Since *Grn* HET mice do not show any robust biochemical, pathological or behavioral phenotypes (*11, 40*), we took advantage of our recently developed model, which employs KO of *Grn* in combination with a KO of *Tmem106b (42)*. This model was previously shown to reproduce abnormal phosphorylation and deposition of insoluble TDP-43, which are a central pathological hallmark of FTLD-*GRN*. This mouse model also exhibits profound motor phenotypes, in addition to exacerbating the phenotypes seen in *Grn* KO mice including deficits in protein degradation, lipid and transcriptome alterations, gliosis, and neurodegeneration (*42-44*).

In our study, a single injection paradigm resulted in successful AAV-mediated expression of a TfR-binding PGRN biologic (8D3:PGRN) in the periphery (*i.e.,* liver), which was robustly and sustainably delivered to the brain. This resulted in amelioration of the TDP-43 phenotypes within the brain. Furthermore, levels of endolysosomal lipid BMP, which was recently described as a pathway biomarker downregulated in *Grn* KO mice (*29, 33*), were fully restored. Levels of GM3 and GM2, which were upregulated in DKO mice were ameliorated as well, suggesting that the secondary storage of gangliosides observed in *Grn* KO mice is also responsive to PGRN replacement, despite the loss of *Tmem106b (29, 33)*. Autophagic and lysosomal protein dysregulation was ameliorated as well. Transcriptomic and immunohistochemical analyses further indicated that microglia and astrocyte reactive states were significantly dampened. Altogether, these beneficial treatment effects were associated with a longitudinal decrease of plasma NfL, a

46

biomarker for neurodegeneration which is commonly used in clinical practice (*8*). Lastly, the severe

450   motor phenotypes in DKO mice, which started shortly after treatment, were substantially reduced. In contrast to other therapeutic strategies, which enhance circulating levels of PGRN by inhibiting cellular uptake (*e.g.*, the anti-sortilin antibody Latozinemab) (*83*), our approach increases both extracellular and intracellular PGRN. The latter is believed to be critical, as PGRN or its proteolytically generated granulins exert crucial functions within the endolysosomal pathway,

455   which may be compromised by inhibition of cellular uptake of PGRN (*22, 88*).

We also verified the PGRN replacement strategy in a novel human iPSC-derived cellular model consisting of WT neurons co-cultured with *GRN/TMEM106B* DKO microglia. This model is based on the observation that *GRN* is predominantly expressed in microglia, whereas TDP-43 pathology primarily occurs in neurons (*71, 89, 90*). Microglial/neuronal crosstalk is in line with

460   recent findings showing that complement factors secreted by *Grn* KO mouse microglia increase cell death and aberrant TDP-43 in mouse cortical neurons (*19*). Thus, we expected non-cell autonomous effects on neurons caused by loss of PGRN in microglia, which we indeed observed in our human co-culture system. Upon treatment with PTV:PGRN, disease-relevant abnormal posttranslational modification of TDP-43 and lysosomal dysfunction as well as neuronal loss were

465   strongly ameliorated in the co-cultures, demonstrating applicability of this human model system to test efficacy of PGRN replacement.

Our toxicological evaluation of serum chemistry and hematology, as well as histopathological analysis did not show any significant adverse events and demonstrated that application of the brain-penetrant biologic AAV(L):bPGRN appears safe in mice at least for 31

470   weeks of treatment. This is of foremost importance, since mice intraventricularly injected with AAVs expressing PGRN showed neuroinflammation (*56*). Another caveat with protein replacement therapy is the impermeability of the BBB for AAVs or larger proteins, such as PGRN. Therefore, current therapeutic approaches investigated in the clinic rely on lumbar or cisterna magna CSF injection (*86*), which can cause injury to the medulla (*57*), and, despite direct delivery

475   into the CNS, exhibit biodistribution limited to regions adjacent to CSF (*58*). This was also shown recently where direct CNS delivery of AAV1 and 9 expressing PGRN in a mouse model of FTLD-*GRN* resulted in amelioration of phenotypes in the spinal cord, but not in the brain (*60*).

Due to the severity of the DKO phenotypes, we employed a preventive subchronic treatment paradigm shortly before pathologies occur, while treating *Grn* KO animals in a chronic treatment

480 paradigm. As genetic testing combined with measurements of plasma PGRN and NfL levels may allow for diagnosis of asymptomatic *GRN* mutation carriers before they convert to the clinical stage of the disease, prevention trials with PGRN replacement therapies may potentially be applied before clinical symptoms arise. Taken together, our findings strongly support the application of brain-penetrant PGRN as replacement therapy in FTLD-*GRN* patients. Furthermore, since our

485 approach ameliorates lysosome-related deficits within the brain, similar brain penetrant therapeutics approaches may be developed for other lysosomal disorders with a neuronopathic component.

A limitation of our study is that by definition, the effect of PGRN replacement on TMEM106B fibrils (*51-53*) or of molecules aiming to increase PGRN levels, could not be

490 addressed using this model due to the full loss of PGRN and TMEM106B. Another limitation of our and other models for TDP-43 pathology is the sparse TDP-43 mis-localization and nuclear clearance (*19, 42*). However, the biochemical TDP-43 phenotypes closely resemble those observed in patients (*71*).

495 **MATERIALS AND METHODS**

Animal experiments and mouse brain tissue

All animal experiments were performed either according to German animal welfare law and approved by the government of upper Bavaria (Vet_02-17-106) or by the Denali Therapeutics Institutional Animal Care and Use Committee. Mice were kept under standard housing conditions;

500 standard pellet food and water was provided *ad libitum*. AAV was applied intravenously *via* tail vain injection (max. 200 µl). For tissue collection, mice were anesthetized with either Ketamine/Xylazine or tribromoethanol. Whole blood was either terminally collected via cardiac puncture or during the study via facial vein puncture and transferred into EDTA-coated tubes before centrifugation at 12,700 rpm for 7 min at 4°C. The plasma fraction was used for analysis. In cases

505 where CSF was drawn, it was obtained by cisterna magna puncture and spun down at 12,700 rpm for 7 min at 4°C to minimize blood contamination. Mice were transcardiacally perfused with chilled PBS before organ collection. Tissues and fluids were stored at -80°C until further use.

26

48

Generation and maintenance of WT and *GRNxTMEM106B* DKO iPSC lines

Experiments using hiPSC were performed following all relevant local guidelines and regulations. The iPSC line A18944 was purchased from Thermo Fisher (A18945). For the generation of *GRNxTMEM106B* DKO iPSC lines, our previously described *GRN* KO iPSC line was used (*32*). Cells were kept in Essential 8 Flex media (Thermo Fisher, A2858501) on vitronectin-coated (Thermo Fisher, A3349401) cell culture dishes at 37°C, 95% humidity and 5% CO_2. Cells were detached as colonies at 70% confluency using PBS with 0.5 mM EDTA and passaged subsequently.

CRISPR/Cas9 genome editing

Human iPSC were edited as previously described (*80, 91*) with modifications. In brief, CRISPOR (http://crispor.tefor.net) (*92*) was used to design gRNAs and for the determination of putative off-target loci. To cover most of the coding region of the *TMEM106B* gene locus, exon 2 was targeted close to *de novo* STOP codons in alternate reading frames.

Cells were cultured as single cells on Geltrex (Thermo Fisher Scientific, A1110501) in StemFlex™ media (Thermo Fisher Scientific, A3349401) supplemented with ROCK inhibitor (Selleck-chem, S1049) for two days prior to electroporation. They were harvested using Accutase (Thermo Fisher Scientific, A1110501) and resuspended in 20 µl P3 nucleofector solution (Lonza) before addition to a pre-incubated ribonucleoprotein complex of gRNA (60 pmol) and Cas9 (30 pmol, Integrated DNA Technologies) protein. Using a Nucleofector (Lonza) with program CA-137, cells were electroporated and grown on Geltrex in StemFlex™ media with ROCK inhibitor until colonies appeared. Single colonies were picked and expanded upon Sanger sequencing verification of successful KO. Successful editing was further confirmed by Western blot. Quality controls were performed to confirm the absence of off-target effects (by PCR for the 10 most likely hits based on MIT and CFD scores on CRISPOR), the absence of loss of heterozygosity (nearby SNP sequencing), pluripotency of the novel cell line (immunofluorescence staining for OCT4, NANOG, SSEA4 and TRA160) and chromosomal integrity by molecular karyotyping (LIFE & BRAIN GmbH).

Differentiation of human iPSC-derived Microglia (iMG)

Cells were differentiated into iMG following the protocol initially presented by Abud et al. (*93*), with the modifications we recently published (*32*). On day 24 of differentiation, cells were used for co-cultures with iN.

540   *Differentiation of human iPSC-derived Neurons (iN)*

Cells were differentiated into cortical neurons (iN) according to our recently published protocol, following a dual-SMAD inhibition approach (*94*). On day 60 of differentiation, iN were used for co-cultures with iMG.

Co-culture of iMG and iN and PTV:PGRN treatment

545   For co-cultures, iMG and iN were cultured together at a 1:8 ratio. The required amount of iMG were collected and spun down as for passaging before resuspending in 50% of the required iN media, supplemented with double the concentration of the cytokines needed for iMG identity, namely hIL34 (Peprotech, 200-34), hM-CSF (Peprotech, 300-25) and hTGF-ß (Peprotech, 100-21). 50% of the media was removed from the iN and the fresh media containing the iMG added.

550   From then on, 50% media without doubling the cytokine concentration was replaced every other day before cell processing for experiments on day 14 of co-culture.

To test the efficacy of PTV:PGRN in our model, cells were treated with either PBS or 100 nM inactive human IgG as a control, or 100 nM PTV:PGRN (*29*) starting on day 5 of co-culture every other day until collection.

555

Design and generation of AAV(L):bPGRN

The mature protein expressed by AAV(L):bPGRN was designed by genetically fusing a mouse TfR binding scFv (8D3) to the N-terminus of full-length human PGRN. A human influenza hemagglutinin (HA) tag and 2x Gly4Ser linker were included between the scFv and PGRN to

560   provide an additional handle for detection (HA tag) and to impart flexibility between the two proteins. Mature PGRN was used for the fusion protein, with N- and C-terminal breakpoints of T18 and L593, respectively; numbering as outlined in UniProt P28799. The fusion protein was cloned into a plasmid under an ApoE/AAT1 promoter, with a terminal WPRE to enhance expression, and flanking AAV2 ITRs. After generating the viral cis plasmid, recombinant AAV8 was generated

565   and characterized by Signagen. The virus was titered by rtPCR quantification of genome copies. Endotoxin quantification was also performed and measured at less than 0.05 u/ml. Virus was delivered to animals as described above at a dose of 1.3×10^{13} vg/kg,

50

Motor function assessment of DKO mice

570   All motor tests were performed blinded.

Rotarod test

Motor function was assessed using a rotarod (TSE Systems, 3376O4R), accelerating from 4-40 rpm within 300 s as previously described (*42*). Mice were trained twice within one week before longitudinal assessment twice per week. The average of three consecutive tests was calculated for 575   each recording day.

Flipping test

Mice were recorded while being slightly poked to assess balance. Mice were scored based on showing no change in balance (0), trembling (1), flipping over and standing up within 3 seconds (2), or flipping over and not standing up within 3 seconds (3).

580   *Hind limb clasping test*

Mice were recorded while being lifted by their tail as previously described (*65*). They were scored based on no cramping of the hind limbs (0), cramping for less than 25% (1), more than 25% (2) or more than 50% of the recording time.

585   **Toxicity assessment**

Assessment of toxicity was based on body weight, serum chemistry, hematology, necropsy and microscopic evaluation of select organs. Whole blood and serum were collected for complete blood count (CBC) and serum chemistry, respectively. Samples were evaluated at Quality Veterinary Laboratories (QVL). A complete necropsy was performed by qualified staff, and brain, heart, lung, 590   liver, kidney, spleen, small and large intestine, prostate, testes, femur/tibia (including bone marrow) and sciatic nerve were collected into 10% buffered formalin. For tissue histopathology, tissues were processed to H&E-stained slides at Cureline Biopathology. Histology slides were reviewed by a board-certified veterinary pathologist, and instances of abnormal tissue observations were recorded.

595

Gene profiling of total brain

Total RNA was extracted from frozen brain powder using the Qiagen RNeasy plus kit (Qiagen, 74034). Quality and quantity were assessed with a 4200 TapeStation System (Agilent). Next generation sequencing libraries were generated using the QuantSeq 3' mRNA-seq Library Prep Kit FWD for Illumina sequencing with the UMI second strand synthesis module (Lexogen). Library concentration and quality were assessed with the 4200 TapeStation system (Agilent). The libraries were pooled in equimolar ratios for sequencing on an Illumina NovaSeq 6000 instrument. Raw sequencing data (FASTQ files) were processed with skewer (version 0.2.2) (*95*) to trim sequencing adapters. Unique molecular identifiers (UMIs) were extracted from each read with the umi2index tool (Lexogen). Quality control of the trimmed reads was performed using FastQC (version 0.11.5) (*96*). Reads were aligned to the mouse reference genome (version GRCm38_p6) with STAR (version 2.7.1a) (*97*), using an index created with the –sjdbOverhang=50 argument. Splice junctions from Gencode gene models (release M17) were provided via the –sjdbGTFfile argument. Alignments were obtained with the following parameters: –readFilesCommand zcat –outFilterType BySJout –outFilterMultimapNmax 20 –alignSJoverhangMin 8 –alignSJDBoverhangMin 1 – outFilterMismatchNmax 999 –outFilterMismatchNoverLmax 0.6 –alignIntronMin 20 – alignIntronMax 1000000 –alignMatesGapMax 1000000 –quantMode GeneCounts – outSAMunmapped Within –outSAMattributes NH HI AS nM MD XS –outSAMstrandField intronMotif –outSAMtype BAM SortedByCoordinate –outBAMcompression 6. Reads sharing the same UMI and genomic coordinate were deduplicated using the collapse_UMI_bam tool (Lexogen). Post-alignment quality control reports were generated using MultiQC (version 1.0) (*98*). The raw gene expression matrix was constructed from the 'forward' column of STAR's ReadsPerGene.out.tab output files using R (version 4.3). Gene symbols and biotype information were extracted from the Gencode GTF file. For downstream analysis, library size factors were determined using TMM normalization (*99*) across all genes annotated as protein_coding with the edgeR R package (version 3.42.4) (*100*). Exploratory and differential expression analysis was performed with the edgeR and limma (version 3.56.2) (*101*) R packages. Multidimensional scaling was performed based on the top 500 most variable genes with the plotMDS function, after removing batch effects with removeBatchEffect function. For differential expression analysis, a linear model with fixed effects for experimental group, sex and batch covariates was fit to all protein-coding genes with the voomLmFit function, including sample weights. Contrasts of interest were extracted

30

52

with the eBayes function with robust priors (e.g., by setting robust=TRUE). Genes with a false discovery rate (fdr) of less than 5% and a fold change of at least 20% were considered to display a significant genotype or treatment effect. Significant genotype x treatment interactions were called by applying a 15% fdr threshold. To visualize genes whose expression was perturbed in the double-knock out samples and also showed correction after AAV treatment, their normalized, batch-corrected expression was plotted with the ComplexHeatmap R package (version 2.16.0) (*102*). We found that in the DKO mice, *Grn* expression was still detected by our 3' mRNA sequencing approach, but protein PGRN was absent confirming successful knockout as previously described (*11, 15, 42*).

Lipid analysis by liquid chromatography-mass spectrometry (LCMS)

Lipidomic analyses were largely performed as previously described (*29*). Approximately 20 mg tissue were homogenized for 30 sec at 25 Hz at 4°C in 400 µl of LC-MS grade methanol containing 2 µl internal standard mix solution. Homogenized samples were centrifuged at 21,000 g for 20 min at 4°C. Cleared methanolic supernatants were kept at -20°C for 1 h. Samples were centrifuged at 21,000 g for 10 min at 4°C and supernatants dried under a constant stream of N_2. Dried samples were stored at -80°C until analysis. For analysis and separation of glucosylceramides and galactosylceramides, 50 µl of above extracts were dried under constant stream of N_2 for 4 h and resuspended in 200 µl of 92.5/5/2.5 LCMS grade acetonitrile/isopropanol/water fortified with 5 mM ammonium formate and 0.5% formic acid.

Samples extracted above were analyzed using three different lipidomics assays, namely 1) lipidomics positive, 2) lipidomics negative and 3) glycosphingolipid positive panels. All of these assays were performed using the Agilent 1290 Infinity UPLC system coupled to Sciex 6500+ QTRAP mass spectrometer. All data acquisition was performed in multiple reaction monitoring mode (MRM) with the collision energy (CE) values reported in Table S2 and S3. Lipids were quantified using a mixture of non-endogenous internal standards as reported in Table S2 and S3. All quantification was performed using MultiQuant 3.02 software (Sciex). Chromatography and mass spectrometer settings used are described below:

Lipidomics positive: Mobile phase A consisted of 60:40 acetonitrile/water (v/v) with 10 mM ammonium formate + 0.1% formic acid; mobile phase B consisted of 90:10 isopropyl alcohol/acetonitrile (v/v) with 10 mM ammonium formate + 0.1% formic acid. Source settings for

31

53

positive mode were as follows: curtain gas at 40 psi; collision gas was set at medium; ion spray voltage at 5500 V; temperature at 250°C; ion source Gas 1 at 55 psi; ion source Gas 2 at 60 psi; entrance potential at 10 V; and collision cell exit potential at 12.5 V.

Lipidomics negative: Mobile phase composition was same as in positive mode with the exception that 10 mM ammonium acetate and 0.1% acetic acid were used as fortificants. Source settings were as follows: curtain gas at 30 psi; collision gas was set at medium; ion spray voltage at -4500 V; temperature at 600°C; ion source Gas 1 at 55 psi; ion source Gas 2 at 60 psi; entrance potential at -10 V and collision cell exit potential at -15.0 V.

Lipidomics analysis in positive and negative ionization modes were initiated with 5 µl of sample injection using a BEH C18 1.7 µm, 2.1×100 mm column (Waters) as stationary phase with 0.25 mL/min flowrate and column temperature set at 55°C. The gradient was programmed as follows: 0.0-8.0 min from 45% B to 99% B, 8.0-9.0 min at 99% B, 9.0-9.1 min to 45% B, and 9.1-10.0 min at 45% B.

Glucosylsphingolipid panel in positive mode: Mobile phase A consisted of 92.5/5/2.5 ACN/IPA/H2O with 5 mM ammonium formate and 0.5% formic acid. Mobile phase B consisted of 92.5/5/2.5 H2O/IPA/ACN with 5 mM ammonium formate and 0.5% formic acid. For each analysis, 5 µL of sample was injected on a HALO HILIC 2.0 µm, 3.0 × 150 mm column (Advanced Materials Technology, PN 91813-701) using a flow rate of 0.48 mL/min at 45°C. Mobile phase A consisted of 92.5/5/2.5 ACN/IPA/H2O with 5 mM ammonium formate and 0.5% formic acid. Mobile phase B consisted of 92.5/5/2.5 H2O/IPA/ACN with 5 mM ammonium formate and 0.5% formic acid. The gradient was programmed as follows: 0.0–2 min at 100% B, 2.1 min at 95% B, 4.5 min at 85% B, hold to 6.0 min at 85% B, drop to 0% B at 6.1 min and hold to 7.0 min, ramp back to 100% at 7.1 min and hold to 8.5 min. Glucosylceramide and galactosylceramide were identified based on their retention times and MRM properties of commercially available reference standards (Avanti Polar Lipids, Birmingham, AL, USA). Table S4 shows specific analytes and internal standards used in this assay.

Integrated areas of endogenous lipids were divided by areas of spiked in stable isotope internal standards. Specific pairings of endogenous lipid to class level internal standards are described in Table S2-4. For all analysis, raw area ratio data was log2 transformed and filtered to retain variables that are present in at least 70% of samples. Missing values were imputed using the kNN method using the 5 nearest donor variables. Unwanted variations in the dataset were adjusted for using the RUV4 method. Genotype, treatment and genotype-:treatment interaction effects on lipids were

32

54

assessed using a robust linear model with sex, batch, and RUV4 regression factors as covariates in the model. Top contrast results were visualized using heatmaps, boxplots or volcano plots. Bar plots of mean differences of selected analytes were created using GraphPad Prism. All analyses were performed using R statistical software (version 4.0.2; R Core Team 2020).

695

Protein analysis and Western blotting

Mouse hemispheres were mechanically pulverized before sequential protein extraction as previously described (*11*).

Initially, brain samples were lysed in high salt lysis buffer (0.5 M NaCl, 10 mM Tris pH 7.7, 5 mM
700   EDTA, 1mM DTT, 10% sucrose) and incubated on ice for 15 min followed by centrifugation. The supernatant was used as high salt fraction, the pellet was resuspended in RIPA lysis buffer (150 mM NaCl, 20 mM Tris pH 7.4, 2.5 mM EDTA, 0.1% (w/v) SDS, 1% (v/v) NP-40, 0.25% Na-deoxycholate) and incubated on ice for 15 min followed by centrifugation. The supernatant was used as RIPA fraction, the pellet was resuspended in urea lysis buffer (30 mM Tris pH 8.5, 7 M
705   urea, 2 M thiourea, 4% CHAPS) and processed as before generating the urea fraction as supernatant after centrifugation. All lysis buffers were supplemented with PhosStop™ phosphatase inhibitor cocktail (Roche, 04906837001), protease inhibitor cocktail (Merck, P8340) and Benzonase® (EMD Millipore, 70746-4).

Material from hiPSC was lysed in RIPA lysis buffer for 20 min on ice before centrifugation. Protein
710   concentration was determined using BCA protein assay (Thermo Fisher Scientific, 23225). Equal amounts of protein were diluted in Laemmli buffer and separated by SDS-PAGE before transfer onto polyvinylidene difluoride or nitrocellulose membranes (both GE Healthcare Science). After primary antibody incubation (Progranulin (clone 8H10, (*11*)), Calnexin (Stressgen, SPA-860), Ubiquitin (Cellsignaling, 3936), p62 (MBL, PM045), LC3 (Novusbio, NB100-2220), Saposin D
715   ((*103*)), TDP-43 NT (Proteintech, 10782-2-AP), TDP-43 CT (Proteintech, 12892-1-AP), pTDP-43 (Proteintech, 80007-1-RR), b-Actin (Sigma-Aldrich, A5316), Progranulin (Thermo Fisher Scientific, 40-3400), TUJ1 (Biolegend, 801201), IBA1 (Gentex, GTX100042), Cathepsin B (Santa Cruz, Sc-13985), Cathepsin D (R&D Systems, AF1029), Cathepsin L (R&D Systems, AF1515), TMEM106B (clone 344, (*104*)), GAPDH (Invitrogen, AM4300)) followed by incubation with
720   HRP-conjugated secondary antibodies, detection using ECL Plus substrate (Thermo Fisher

33

Scientific) and imaged using an Amersham ImageQuant 800 system (Cytiva). Images were quantified using the MultiGaugeV3.0 software (Fujifilm Life Science).

Lysosomal protease activity assays

725   Cells were lysed under mild conditions (50 mM Na-citrate pH 5.0, 0.8% (v/v) NP-40) for 15 min on ice before centrifugation and lysosomal protease activities performed as previously described (*12*). Activity assays for cathepsin B (Abnova, KA0766), cathepsin D (Abnova, KA0767) and cathepsin L (Abnova, KA0770) were performed according to the manufacturer's instructions using samples with normalized protein concentrations. Fluorescence generated by cleavage of the
730   quenched substrate was measured using a Fluoroskan Ascent FL plate reader.

ELISA-based quantification of mTrem2

For the analysis of total cellular and soluble Trem2, samples were homogenized in either high salt lysis buffer or CST lysis buffer (Cell Signaling Technologies (CST), 9803) with protease and
735   phosphatase inhibitors. Trem2 measurements were made using the Mesoscale Discovery (MSD) platform as previously described (*29, 105*) using a biotinylated anti-mTrem2 polyclonal antibody (R&D Systems BAF1729) as capture antibody and a sulfo-tagged detection antibody (sheep anti-mouse Trem2, AF1729 R&D Systems). MSD plates were developed using 2x MSD read buffer T, followed by detection using an MSD Meso Sector S600 reader. MSD values were converted to
740   absolute quantities of Trem2 by interpolating from a 4-parameter logistic curve fit to the mouse Trem2-His protein standard using Graphpad Prism software. For the same samples BCA protein analysis was performed and Trem2 levels were normalized using the protein concentrations.

ELISA-based quantification of mPGRN and hPGRN

745   For the analysis of total cellular and soluble PGRN in DKO mice, samples were homogenized in high salt lysis buffer with protease and phosphatase inhibitors. PGRN measurements were made using the Mesoscale Discovery (MSD) platform as previously described (*106*) using either a biotinylated anti-hPGRN antibody (R&D Systems, BAF2420) or anti-mPGRN antibody (R&D Systems, BAF2557) at 0.2 µg/mL as capture antibody and for detection rabbit anti-hPGRN

34

56

750   (Thermo Fisher Scientific, 40-3400) or a rat anti-mPGRN (R&D Systems, MAB25571) antibody at 0.25 µg/mL followed by sulfo-tagged secondary antibodies (anti-rabbit and anti-rat respectively). MSD plates were developed using 2x MSD read buffer T, followed by detection using an MSD Meso Sector S600 reader. MSD values were converted to absolute quantities of PGRN by interpolating from a 6-parameter logistic curve fit to the recombinant protein standard

755   (Workbench v4 software (MSD)).

Human PGRN levels in *Grn* KO mice were measured using the DuoSet ELISA kit (R&D DY2420) as previously described (*29*). Concentrations were calculated by interpolating values against an 8 point standard curve using Graphpad Prism.

760   **Neurofilament light-chain analysis**

Plasma and CSF neurofilament light chain (NfL) levels were analyzed as previously described (*29*) using the Quanterix Simoa Neurofilament Light Advantage kit. Plasma was diluted 20x in sample diluent and CSF was diluted 100x in sample diluent. Sample NfL concentrations were measured using the NfL analysis protocol on the Quanterix SR-X instrument and interpolated against a

765   calibration curve provided with the Quanterix assay kit.

Immunofluorescence labeling of mouse brain tissue

For the analysis of DKO mouse brains, tissue was postfixed with 4% paraformaldehyde (PFA) for 24 h directly after tissue extraction, cryoprotected in 30% sucrose for 3 nights and subsequently

770   embedded in Tissue-Tek OCT cryo-embedding matrix prior to freezing the tissue on dry ice. Brain samples were cut into 16 µm sections (CryoStar NX70 HOMVP, Thermo Fisher Scientific) and stored at -80°C. Immunofluorescence staining was performed on sections that were adjusted to RT for 30 min and washed with PBS to remove excess embedding matrix. Sections were transferred to citrate buffer (0.01 M, pH 6.0) for antigen retrieval. Tissue permeabilization was performed by

775   incubating sections with 0.5% Triton-X-100 in PBS for 10 min. Blocking was performed using a mixed blocking solution (2.5% bovine serum albumin, 2.5% fish gelatin, 2.5% fetal calf serum in PBS). Primary antibodies (Map2 (1:500, Novusbio, NB300-213), Iba1 (1:400, Synaptic Systems, 234004), Gfap (1:500, Thermo Fisher Scientific, 13-0300) Cd68 (1:500, abcam, ab125212), p62 (1:200, MBL, PM045)) were diluted in antibody diluent (0.625% bovine serum albumin, 0.625%

35

780   fish gelatin, 0.625% fetal calf serum in PBS) and incubated for 24 h at 4°C, followed by incubation with fluorophore-coupled secondary antibodies (Thermo Fisher Scientific), for 1 h at RT. Afterwards, sections were incubated with DAPI (1:1000, Thermo Fisher Scientific, 62248) for 10 min and mounted with ProLong™ Gold Antifade mounting solution (Invitrogen, P36930).

For the analysis of *Grn* KO mouse brains, samples were processed as previously described (*29*),
785   tissue was postfixed with 4% PFA for 24 h directly after tissue perfusion and extraction, cryoprotected in 30% sucrose overnight before section at 40 µm thickness using a freezing microtome. Immunofluorescence staining was performed on free floating sections. Blocking and antibody washes were performed using a mixed blocking solution (1% BSA + 5% Normal Donkey Serum + 0.3% Triton-X-100 in PBS). Primary antibodies (Cd68 (1:500, BioRad MCA1957), Iba1
790   (1:400, Novus NB100-1028), and Gfap (1:500, Novus NBP1-05198) were used and incubated for 24 h at 4°C, followed by incubation with fluorophore-coupled secondary antibodies (Thermo Fisher Scientific), for 2-4 h at RT. Afterwards, sections were incubated with DAPI (1:5000, Thermo Fisher Scientific, 62248) for 10 min and mounted with ProLong™ Gold Antifade mounting solution (Invitrogen, P36930).

795

Immunofluorescence labeling of hiPSC cultures

Cells were fixed by replacing the culture media with 4% PFA (Thermo Fisher Scientific, J19943.K2) and incubating at 37°C, 95% humidity and 5% CO_2 for 15 min, before storage at 4°C in PBS until further processing as previously described (*107*). After two initial PBS washes, cells
800   were permeabilized using 0.1% Triton-X-100 in PBS, before blocking in SuperBlock™ blocking buffer (Thermo Fisher Scientific, 37515). Primary antibodies (MAP2 (1:1000, abcam, ab92434), IBA1 (1:400, Invitrogen, PA5-27436)) were diluted in SuperBlock™ and samples incubated at 4°C for 24 h followed by incubation with fluorophore-coupled secondary antibodies (Thermo Fisher Scientific) for 90 min at RT. Cells were incubated with DAPI for 10 min and mounted with
805   ProLong™ Gold Antifade mounting solution.

Image acquisition

For quantification, full brain hemispheres were imaged at 20x using a Zeiss Axio Scan.Z1 digital slide scanner or a Leica DMI-8 epifluorescence microscope with a DFC9000GT camera and a 20x

36

58

810   objective (HC PL FL L 20x/0.40 CORR PH1). Image mosaics were merged using the Leica LAS X software suite. Analysis was completed using Zeiss Zen Blue 3.2 software or ImageJ. Image pre-processing to eliminate illumination gradient aberrations using a difference of gaussian filters with the CLIJ2 plugin (*108*) was performed. Regional ROIs were drawn, and a rolling ball thresholding approach was used to determine the area of each marker relative to total regional area. 1-3 sections

815   were analyzed per brain and average percent coverage values were calculated across images. Representative images were acquired on a Zeiss spinning disc microscope using a 40x/1.3 n.A. oil immersion objective or on a Zeiss LSM800 Axio Observer 7 confocal microscope with a 63x (63x/1.4 Oil) or a 40x (40x/1.3 Oil) objective. Post-processing was performed in ImageJ.

820   **Statistical analysis**

All non-sequencing or lipidomics data was analyzed using either a Student's t-test, one-way analysis of variance 1555 (ANOVA), or two-way ANOVA with multiple comparisons when indicated. Data was plotted and statistical tests were performed using GraphPad Prism. All studies and sample analyses were performed blinded and in randomized order. Studies with multiple assays

825   were designed to be powered for the most variable analyte based on previous data. Exclusion of mice only occurred if confounding health concerns were identified during the study. Data was only excluded in circumstances when extreme outliers were identified (ROUT, $Q = 0.5\%$). All heatmaps were generated in R using the Complex Heatmap package. Data represented as mean $\pm$ SEM or mean $\pm$ SD for *in vitro* and *in vivo* graphs. N is defined as the number of independent experiments

830   or biological replicates in an *in vitro* study and as the number of mice in an *in vivo* study.

Author Contributions

Conceptualization: MR, MJS, MSK, SLD, JWL, AC, GDP, CH

Methodology: MR, MJS, IP, GW, SR, SSD, GL, LSc, LSp, SB, TL, MS, MSK, JHS, TS, SLD, JWL, DP, AC, GDP, CH

Investigation: MR, MJS, BP, CS, IP, GW, SR, SSD, GL, LSc, LSp, SB, BN, KB, JHS, TS

Visualization: MR, MJS, IP, JHS, TS

Funding acquisition: DP, CH

Project administration: DE, MS, JWL, DP, AC, GDP, CH

Supervision: MR, MJS, GW, SR, JHS, TS, LSc, LSp, SB, DP, AC

Writing – original draft: MR, MJS, GDP, CH

Writing – review & editing: MR, MJS, BP, GW, IP, LSp, TL, MS, JHS, TS, MSK, SLD, JWL, DP, AC, GDP, CH

865 **Competing interests**

CH collaborates with Denali Therapeutics and is a member of the advisory board of AviadoBio. DP is a scientific advisor of ISAR Bioscience. MJS, SSD, GL, JHS, TS, MSK, SLD, JWD and GDP are full-time employees and/or shareholders of Denali Therapeutics.

870 **Data and materials availability**

The bulk RNA sequencing data and lipidomics data will be made available in an online repository.

Supplementary information:

875   Fig. S1: AAV-expressed 8D3:PGRN has minimal effects on red blood cells in *Grn* KO mice

Fig. S2: AAV-mediated delivery of 8D3:PGRN does not alter endogenous PGRN levels in WT mice

Fig. S3: AAV-expressed 8D3:PGRN ameliorates behavioral abnormalities in DKO mice

Fig. S4: AAV-mediated delivery of 8D3:PGRN reduces TDP-43 pathology in DKO and NfL in
880   *Grn* KO mice

Fig. S5: AAV-mediated delivery of 8D3:PGRN normalizes astrogliosis and microgliosis in *Grn* KO mice

Fig. S6: AAV-mediated delivery of 8D3:PGRN partially restores genetic cell type composition within the brain

885   Fig. S7: AAV-mediated delivery of 8D3:PGRN restores lipid profile of *Grn* KO mice

Fig. S8: Generation of *TMEM106BxGRN* DKO hiPSC

TableS1: Summary of histopathological findings in Grn KO mice treated with AAV(L):bPGRN

Table S2: Lipidomics in positive mode acquisition parameters

Table S3: Lipidomics in negative mode acquisition parameters

890   Table S4: Glucosylsphingolipid in positive mode acquisition parameters

Extra files:

MovieS1_flipping_test_WT.mov

MovieS2_flipping_test_WT_AAV.mov

895   MovieS3_ flipping_test_DKO.mov

MovieS4_flipping_test_DKO_AAV.mov

Fig4_RNAseq_data.xlsx

Fig5_LCMS_data.xlsx

FigS5_RNAseq_data.xlsx

900   FigS7_LCMS_data.xslx

References:

1. M. Stevens, C. M. van Duijn, W. Kamphorst, P. de Knijff, P. Heutink, W. A. van Gool, P. Scheltens, R. Ravid, B. A. Oostra, M. F. Niermeijer, J. C. van Swieten, Familial aggregation in frontotemporal dementia. *Neurology* **50**, 1541-1545 (1998).

2. M. Baker, I. R. Mackenzie, S. M. Pickering-Brown, J. Gass, R. Rademakers, C. Lindholm, J. Snowden, J. Adamson, A. D. Sadovnick, S. Rollinson, A. Cannon, E. Dwosh, D. Neary, S. Melquist, A. Richardson, D. Dickson, Z. Berger, J. Eriksen, T. Robinson, C. Zehr, C. A. Dickey, R. Crook, E. McGowan, D. Mann, B. Boeve, H. Feldman, M. Hutton, Mutations in progranulin cause tau-negative frontotemporal dementia linked to chromosome 17. *Nature* **442**, 916-919 (2006).

3. M. Cruts, I. Gijselinck, J. van der Zee, S. Engelborghs, H. Wils, D. Pirici, R. Rademakers, R. Vandenberghe, B. Dermaut, J. J. Martin, C. van Duijn, K. Peeters, R. Sciot, P. Santens, T. De Pooter, M. Mattheijssens, M. Van den Broeck, I. Cuijt, K. Vennekens, P. P. De Deyn, S. Kumar-Singh, C. Van Broeckhoven, Null mutations in progranulin cause ubiquitin-positive frontotemporal dementia linked to chromosome 17q21. *Nature* **442**, 920-924 (2006).

4. A. W. Kao, A. McKay, P. P. Singh, A. Brunet, E. J. Huang, Progranulin, lysosomal regulation and neurodegenerative disease. *Nature Reviews Neuroscience* **18**, 325-333 (2017).

5. I. R. Mackenzie, A. Baborie, S. Pickering-Brown, D. Du Plessis, E. Jaros, R. H. Perry, D. Neary, J. S. Snowden, D. M. Mann, Heterogeneity of ubiquitin pathology in frontotemporal lobar degeneration: classification and relation to clinical phenotype. *Acta Neuropathol* **112**, 539-549 (2006).

6. I. R. Mackenzie, The neuropathology and clinical phenotype of FTD with progranulin mutations. *Acta Neuropathol* **114**, 49-54 (2007).

7. L. H. Meeter, E. G. Dopper, L. C. Jiskoot, R. Sanchez-Valle, C. Graff, L. Benussi, R. Ghidoni, Y. A. Pijnenburg, B. Borroni, D. Galimberti, R. J. Laforce, M. Masellis, R. Vandenberghe, I. L. Ber, M. Otto, R. van Minkelen, J. M. Papma, S. A. Rombouts, M. Balasa, L. Öijerstedt, V. Jelic, K. M. Dick, D. M. Cash, S. R. Harding, M. Jorge Cardoso, S. Ourselin, M. N. Rossor, A. Padovani, E. Scarpini, C. Fenoglio, M. C. Tartaglia, F. Lamari, C. Barro, J. Kuhle, J. D. Rohrer, C. E. Teunissen, J. C. van Swieten, Neurofilament light chain: a biomarker for genetic frontotemporal dementia. *Ann Clin Transl Neurol* **3**, 623-636 (2016).

8. J. D. Rohrer, I. O. Woollacott, K. M. Dick, E. Brotherhood, E. Gordon, A. Fellows, J. Toombs, R. Druyeh, M. J. Cardoso, S. Ourselin, J. M. Nicholas, N. Norgren, S. Mead, U. Andreasson, K. Blennow, J. M. Schott, N. C. Fox, J. D. Warren, H. Zetterberg, Serum neurofilament light chain protein is a measure of disease intensity in frontotemporal dementia. *Neurology* **87**, 1329-1336 (2016).

9. H. Zetterberg, J. Jacobsson, L. Rosengren, K. Blennow, P. M. Andersen, Cerebrospinal fluid neurofilament light levels in amyotrophic lateral sclerosis: impact of SOD1 genotype. *Eur J Neurol* **14**, 1329-1333 (2007).

10. M. E. Ward, R. Chen, H. Y. Huang, C. Ludwig, M. Telpoukhovskaia, A. Taubes, H. Boudin, S. S. Minami, M. Reichert, P. Albrecht, J. M. Gelfand, A. Cruz-Herranz, C. Cordano, M. V. Alavi, S. Leslie, W. W. Seeley, B. L. Miller, E. Bigio, M. M. Mesulam, M. S. Bogyo, I. R. Mackenzie, J. F. Staropoli, S. L. Cotman, E. J. Huang, L. Gan, A. J. Green, Individuals with progranulin haploinsufficiency exhibit features of neuronal ceroid lipofuscinosis. *Sci Transl Med* **9**, (2017).

41

11.   J. K. Götzl, K. Mori, M. Damme, K. Fellerer, S. Tahirovic, G. Kleinberger, J. Janssens, J. van der Zee, C. M. Lang, E. Kremmer, J. J. Martin, S. Engelborghs, H. A. Kretzschmar, T. Arzberger, C. Van Broeckhoven, C. Haass, A. Capell, Common pathobiochemical hallmarks of progranulin-associated frontotemporal lobar degeneration and neuronal ceroid lipofuscinosis. *Acta Neuropathol* **127**, 845-860 (2014).

12.   J. K. Götzl, A. V. Colombo, K. Fellerer, A. Reifschneider, G. Werner, S. Tahirovic, C. Haass, A. Capell, Early lysosomal maturation deficits in microglia triggers enhanced lysosomal activity in other brain cells of progranulin knockout mice. *Mol Neurodegener* **13**, 48 (2018).

13.   Y. Tanaka, J. K. Chambers, T. Matsuwaki, K. Yamanouchi, M. Nishihara, Possible involvement of lysosomal dysfunction in pathological changes of the brain in aged progranulin-deficient mice. *Acta Neuropathol Commun* **2**, 78 (2014).

14.   Y. Tanaka, G. Suzuki, T. Matsuwaki, M. Hosokawa, G. Serrano, T. G. Beach, K. Yamanouchi, M. Hasegawa, M. Nishihara, Progranulin regulates lysosomal function and biogenesis through acidification of lysosomes. *Hum Mol Genet* **26**, 969-988 (2017).

15.   J. K. Götzl, M. Brendel, G. Werner, S. Parhizkar, L. Sebastian Monasor, G. Kleinberger, A. V. Colombo, M. Deussing, M. Wagner, J. Winkelmann, J. Diehl-Schmid, J. Levin, K. Fellerer, A. Reifschneider, S. Bultmann, P. Bartenstein, A. Rominger, S. Tahirovic, S. T. Smith, C. Madore, O. Butovsky, A. Capell, C. Haass, Opposite microglial activation stages upon loss of PGRN or TREM2 result in reduced cerebral glucose metabolism. *EMBO Mol Med* **11**, (2019).

16.   H. Lui, J. Zhang, S. R. Makinson, M. K. Cahill, K. W. Kelley, H. Y. Huang, Y. Shang, M. C. Oldham, L. H. Martens, F. Gao, G. Coppola, S. A. Sloan, C. L. Hsieh, C. C. Kim, E. H. Bigio, S. Weintraub, M. M. Mesulam, R. Rademakers, I. R. Mackenzie, W. W. Seeley, A. Karydas, B. L. Miller, B. Borroni, R. Ghidoni, R. V. Farese, Jr., J. T. Paz, B. A. Barres, E. J. Huang, Progranulin Deficiency Promotes Circuit-Specific Synaptic Pruning by Microglia via Complement Activation. *Cell* **165**, 921-935 (2016).

17.   M. Huang, E. Modeste, E. Dammer, P. Merino, G. Taylor, D. M. Duong, Q. Deng, C. J. Holler, M. Gearing, D. Dickson, N. T. Seyfried, T. Kukar, Network analysis of the progranulin-deficient mouse brain proteome reveals pathogenic mechanisms shared in human frontotemporal dementia caused by GRN mutations. *Acta Neuropathol Commun* **8**, 163 (2020).

18.   J. Marschallinger, T. Iram, M. Zardeneta, S. E. Lee, B. Lehallier, M. S. Haney, J. V. Pluvinage, V. Mathur, O. Hahn, D. W. Morgens, J. Kim, J. Tevini, T. K. Felder, H. Wolinski, C. R. Bertozzi, M. C. Bassik, L. Aigner, T. Wyss-Coray, Lipid-droplet-accumulating microglia represent a dysfunctional and proinflammatory state in the aging brain. *Nat Neurosci* **23**, 194-208 (2020).

19.   J. Zhang, D. Velmeshev, K. Hashimoto, Y. H. Huang, J. W. Hofmann, X. Shi, J. Chen, A. M. Leidal, J. G. Dishart, M. K. Cahill, K. W. Kelley, S. A. Liddelow, W. W. Seeley, B. L. Miller, T. C. Walther, R. V. Farese, Jr., J. P. Taylor, E. M. Ullian, B. Huang, J. Debnath, T. Wittmann, A. R. Kriegstein, E. J. Huang, Neurotoxic microglia promote TDP-43 proteinopathy in progranulin deficiency. *Nature* **588**, 459-465 (2020).

20.   M. J. Simon, T. Logan, S. L. DeVos, G. Di Paolo, Lysosomal functions of progranulin and implications for treatment of frontotemporal dementia. *Trends Cell Biol* **33**, 324-339 (2023).

950
955
960
965
970
975
980
985
990

42

64

21. D. H. Paushter, H. Du, T. Feng, F. Hu, The lysosomal function of progranulin, a guardian against neurodegeneration. *Acta Neuropathol* **136**, 1-17 (2018).

22. C. J. Holler, G. Taylor, Q. Deng, T. Kukar, Intracellular Proteolysis of Progranulin Generates Stable, Lysosomal Granulins that Are Haploinsufficient in Patients with Frontotemporal Dementia Caused by GRN Mutations. *eNeuro* **4**, (2017).

23. S. Mohan, P. J. Sampognaro, A. R. Argouarch, J. C. Maynard, M. Welch, A. Patwardhan, E. C. Courtney, J. Zhang, A. Mason, K. H. Li, E. J. Huang, W. W. Seeley, B. L. Miller, A. Burlingame, M. P. Jacobson, A. W. Kao, Processing of progranulin into granulins involves multiple lysosomal proteases and is affected in frontotemporal lobar degeneration. *Mol Neurodegener* **16**, 51 (2021).

24. X. Zhou, D. H. Paushter, T. Feng, C. M. Pardon, C. S. Mendoza, F. Hu, Regulation of cathepsin D activity by the FTLD protein progranulin. *Acta Neuropathologica* **134**, 151-153 (2017).

25. S. Beel, M. Moisse, M. Damme, L. De Muynck, W. Robberecht, L. Van Den Bosch, P. Saftig, P. Van Damme, Progranulin functions as a cathepsin D chaperone to stimulate axonal outgrowth in vivo. *Hum Mol Genet* **26**, 2850-2863 (2017).

26. V. J. Butler, W. A. Cortopassi, S. Gururaj, A. L. Wang, O. M. Pierce, M. P. Jacobson, A. W. Kao, Multi-Granulin Domain Peptides Bind to Pro-Cathepsin D and Stimulate Its Enzymatic Activity More Effectively Than Progranulin in Vitro. *Biochemistry* **58**, 2670-2674 (2019).

27. C. W. Lee, J. N. Stankowski, J. Chew, C. N. Cook, Y. W. Lam, S. Almeida, Y. Carlomagno, K. F. Lau, M. Prudencio, F. B. Gao, M. Bogyo, D. W. Dickson, L. Petrucelli, The lysosomal protein cathepsin L is a progranulin protease. *Mol Neurodegener* **12**, 55 (2017).

28. S. Hasan, M. S. Fernandopulle, S. W. Humble, A. M. Frankenfield, H. Li, R. Prestil, K. R. Johnson, B. J. Ryan, R. Wade-Martins, M. E. Ward, L. Hao, Multi-modal Proteomic Characterization of Lysosomal Function and Proteostasis in Progranulin-Deficient Neurons. *bioRxiv*, (2023).

29. T. Logan, M. J. Simon, A. Rana, G. M. Cherf, A. Srivastava, S. S. Davis, R. L. Y. Low, C. L. Chiu, M. Fang, F. Huang, A. Bhalla, C. Llapashtica, R. Prorok, M. E. Pizzo, M. E. K. Calvert, E. W. Sun, J. Hsiao-Nakamoto, Y. Rajendra, K. W. Lexa, D. B. Srivastava, B. van Lengerich, J. Wang, Y. Robles-Colmenares, D. J. Kim, J. Duque, M. Lenser, T. K. Earr, H. Nguyen, R. Chau, B. Tsogtbaatar, R. Ravi, L. L. Skuja, H. Solanoy, H. J. Rosen, B. F. Boeve, A. L. Boxer, H. W. Heuer, M. S. Dennis, M. S. Kariolis, K. M. Monroe, L. Przybyla, P. E. Sanchez, R. Meisner, D. Diaz, K. R. Henne, R. J. Watts, A. G. Henry, K. Gunasekaran, G. Astarita, J. H. Suh, J. W. Lewcock, S. L. DeVos, G. Di Paolo, Rescue of a lysosomal storage disorder caused by Grn loss of function with a brain penetrant progranulin biologic. *Cell* **184**, 4651-4668.e4625 (2021).

30. X. Zhou, D. H. Paushter, M. D. Pagan, D. Kim, M. Nunez Santos, R. L. Lieberman, H. S. Overkleeft, Y. Sun, M. B. Smolka, F. Hu, Progranulin deficiency leads to reduced glucocerebrosidase activity. *PLoS One* **14**, e0212382 (2019).

31. B. M. Evers, C. Rodriguez-Navas, R. J. Tesla, J. Prange-Kiel, C. R. Wasser, K. S. Yoo, J. McDonald, B. Cenik, T. A. Ravenscroft, F. Plattner, R. Rademakers, G. Yu, C. L. White, 3rd, J. Herz, Lipidomic and Transcriptomic Basis of Lysosomal Dysfunction in Progranulin Deficiency. *Cell Rep* **20**, 2565-2574 (2017).

1035   32.   A. Reifschneider, S. Robinson, B. van Lengerich, J. Gnörich, T. Logan, S. Heindl, M. A.
               Vogt, E. Weidinger, L. Riedl, K. Wind, A. Zatcepin, I. Pesämaa, S. Haberl, B. Nuscher, G.
               Kleinberger, J. Klimmt, J. K. Götzl, A. Liesz, K. Bürger, M. Brendel, J. Levin, J. Diehl-Schmid,
               J. Suh, G. Di Paolo, J. W. Lewcock, K. M. Monroe, D. Paquet, A. Capell, C. Haass, Loss of
               TREM2 rescues hyperactivation of microglia, but not lysosomal deficits and neurotoxicity
1040   in models of progranulin deficiency. *Embo j* **41**, e109108 (2022).
        33.   S. Boland, S. Swarup, Y. A. Ambaw, P. C. Malia, R. C. Richards, A. W. Fischer, S. Singh, G.
               Aggarwal, S. Spina, A. L. Nana, L. T. Grinberg, W. W. Seeley, M. A. Surma, C. Klose, J. A.
               Paulo, A. D. Nguyen, J. W. Harper, T. C. Walther, R. V. Farese, Deficiency of the
               frontotemporal dementia gene GRN results in gangliosidosis. *Nature Communications*
1045   **13**, 5924 (2022).
        34.   A. E. Arrant, J. R. Roth, N. R. Boyle, S. N. Kashyap, M. Q. Hoffmann, C. F. Murchison, E. M.
               Ramos, A. L. Nana, S. Spina, L. T. Grinberg, B. L. Miller, W. W. Seeley, E. D. Roberson,
               Impaired β-glucocerebrosidase activity and processing in frontotemporal dementia due
               to progranulin mutations. *Acta Neuropathol Commun* **7**, 218 (2019).
1050   35.   J. K. Götzl, C. M. Lang, C. Haass, A. Capell, Impaired protein degradation in FTLD and
               related disorders. *Ageing Res Rev* **32**, 122-139 (2016).
        36.   M. C. Chang, K. Srinivasan, B. A. Friedman, E. Suto, Z. Modrusan, W. P. Lee, J. S.
               Kaminker, D. V. Hansen, M. Sheng, Progranulin deficiency causes impairment of
               autophagy and TDP-43 accumulation. *J Exp Med* **214**, 2611-2628 (2017).
1055   37.   C. Valdez, D. Ysselstein, T. J. Young, J. Zheng, D. Krainc, Progranulin mutations result in
               impaired processing of prosaposin and reduced glucocerebrosidase activity. *Hum Mol
               Genet* **29**, 716-726 (2020).
        38.   K. R. Smith, J. Damiano, S. Franceschetti, S. Carpenter, L. Canafoglia, M. Morbin, G. Rossi,
               D. Pareyson, S. E. Mole, J. F. Staropoli, K. B. Sims, J. Lewis, W. L. Lin, D. W. Dickson, H. H.
1060   Dahl, M. Bahlo, S. F. Berkovic, Strikingly different clinicopathological phenotypes
               determined by progranulin-mutation dosage. *Am J Hum Genet* **90**, 1102-1107 (2012).
        39.   L. Canafoglia, M. Morbin, V. Scaioli, D. Pareyson, L. D'Incerti, V. Fugnanesi, F. Tagliavini,
               S. F. Berkovic, S. Franceschetti, Recurrent generalized seizures, visual loss, and palinopsia
               as phenotypic features of neuronal ceroid lipofuscinosis due to progranulin gene
1065   mutation. *Epilepsia* **55**, e56-59 (2014).
        40.   A. J. Filiano, L. H. Martens, A. H. Young, B. A. Warmus, P. Zhou, G. Diaz-Ramirez, J. Jiao, Z.
               Zhang, E. J. Huang, F. B. Gao, R. V. Farese, Jr., E. D. Roberson, Dissociation of
               frontotemporal dementia-related deficits and neuroinflammation in progranulin
               haploinsufficient mice. *J Neurosci* **33**, 5352-5361 (2013).
1070   41.   Y. Kayasuga, S. Chiba, M. Suzuki, T. Kikusui, T. Matsuwaki, K. Yamanouchi, H. Kotaki, R.
               Horai, Y. Iwakura, M. Nishihara, Alteration of behavioural phenotype in mice by targeted
               disruption of the progranulin gene. *Behav Brain Res* **185**, 110-118 (2007).
        42.   G. Werner, M. Damme, M. Schludi, J. Gnörich, K. Wind, K. Fellerer, B. Wefers, W. Wurst,
               D. Edbauer, M. Brendel, C. Haass, A. Capell, Loss of TMEM106B potentiates lysosomal
1075   and FTLD-like pathology in progranulin-deficient mice. *EMBO Rep* **21**, e50241 (2020).
        43.   T. Feng, S. Mai, J. M. Roscoe, R. R. Sheng, M. Ullah, J. Zhang, Katz, II, H. Yu, W. Xiong, F.
               Hu, Loss of TMEM106B and PGRN leads to severe lysosomal abnormalities and
               neurodegeneration in mice. *EMBO Rep* **21**, e50219 (2020).

66

44. X. Zhou, M. Brooks, P. Jiang, S. Koga, A. R. Zuberi, M. C. Baker, T. M. Parsons, M. Castanedes-Casey, V. Phillips, A. L. Librero, A. Kurti, J. D. Fryer, G. Bu, C. Lutz, D. W. Dickson, R. Rademakers, Loss of Tmem106b exacerbates FTLD pathologies and causes motor deficits in progranulin-deficient mice. *EMBO Rep* **21**, e50197 (2020).

45. V. M. Van Deerlin, P. M. Sleiman, M. Martinez-Lage, A. Chen-Plotkin, L. S. Wang, N. R. Graff-Radford, D. W. Dickson, R. Rademakers, B. F. Boeve, M. Grossman, S. E. Arnold, D. M. Mann, S. M. Pickering-Brown, H. Seelaar, P. Heutink, J. C. van Swieten, J. R. Murrell, B. Ghetti, S. Spina, J. Grafman, J. Hodges, M. G. Spillantini, S. Gilman, A. P. Lieberman, J. A. Kaye, R. L. Woltjer, E. H. Bigio, M. Mesulam, S. Al-Sarraj, C. Troakes, R. N. Rosenberg, C. L. White, 3rd, I. Ferrer, A. Lladó, M. Neumann, H. A. Kretzschmar, C. M. Hulette, K. A. Welsh-Bohmer, B. L. Miller, A. Alzualde, A. Lopez de Munain, A. C. McKee, M. Gearing, A. I. Levey, J. J. Lah, J. Hardy, J. D. Rohrer, T. Lashley, I. R. Mackenzie, H. H. Feldman, R. L. Hamilton, S. T. Dekosky, J. van der Zee, S. Kumar-Singh, C. Van Broeckhoven, R. Mayeux, J. P. Vonsattel, J. C. Troncoso, J. J. Kril, J. B. Kwok, G. M. Halliday, T. D. Bird, P. G. Ince, P. J. Shaw, N. J. Cairns, J. C. Morris, C. A. McLean, C. DeCarli, W. G. Ellis, S. H. Freeman, M. P. Frosch, J. H. Growdon, D. P. Perl, M. Sano, D. A. Bennett, J. A. Schneider, T. G. Beach, E. M. Reiman, B. K. Woodruff, J. Cummings, H. V. Vinters, C. A. Miller, H. C. Chui, I. Alafuzoff, P. Hartikainen, D. Seilhean, D. Galasko, E. Masliah, C. W. Cotman, M. T. Tuñón, M. C. Martínez, D. G. Munoz, S. L. Carroll, D. Marson, P. F. Riederer, N. Bogdanovic, G. D. Schellenberg, H. Hakonarson, J. Q. Trojanowski, V. M. Lee, Common variants at 7p21 are associated with frontotemporal lobar degeneration with TDP-43 inclusions. *Nat Genet* **42**, 234-239 (2010).

46. P. Lüningschrör, G. Werner, S. Stroobants, S. Kakuta, B. Dombert, D. Sinske, R. Wanner, R. Lüllmann-Rauch, B. Wefers, W. Wurst, R. D'Hooge, Y. Uchiyama, M. Sendtner, C. Haass, P. Saftig, B. Knöll, A. Capell, M. Damme, The FTLD Risk Factor TMEM106B Regulates the Transport of Lysosomes at the Axon Initial Segment of Motoneurons. *Cell Rep* **30**, 3506-3519.e3506 (2020).

47. C. M. Lang, K. Fellerer, B. M. Schwenk, P. H. Kuhn, E. Kremmer, D. Edbauer, A. Capell, C. Haass, Membrane orientation and subcellular localization of transmembrane protein 106B (TMEM106B), a major risk factor for frontotemporal lobar degeneration. *J Biol Chem* **287**, 19355-19365 (2012).

48. J. Perneel, R. Rademakers, Identification of TMEM106B amyloid fibrils provides an updated view of TMEM106B biology in health and disease. *Acta Neuropathol* **144**, 807-819 (2022).

49. M. Stagi, Z. A. Klein, T. J. Gould, J. Bewersdorf, S. M. Strittmatter, Lysosome size, motility and stress response regulated by fronto-temporal dementia modifier TMEM106B. *Mol Cell Neurosci* **61**, 226-240 (2014).

50. O. A. Brady, Y. Zheng, K. Murphy, M. Huang, F. Hu, The frontotemporal lobar degeneration risk factor, TMEM106B, regulates lysosomal morphology and function. *Hum Mol Genet* **22**, 685-695 (2013).

51. A. Chang, X. Xiang, J. Wang, C. Lee, T. Arakhamia, M. Simjanoska, C. Wang, Y. Carlomagno, G. Zhang, S. Dhingra, M. Thierry, J. Perneel, B. Heeman, L. M. Forgrave, M. DeTure, M. L. DeMarco, C. N. Cook, R. Rademakers, D. W. Dickson, L. Petrucelli, M. H. B. Stowell, I. R. A. Mackenzie, A. W. P. Fitzpatrick, Homotypic fibrillization of TMEM106B across diverse neurodegenerative diseases. *Cell* **185**, 1346-1355.e1315 (2022).

45

52. Y. X. Jiang, Q. Cao, M. R. Sawaya, R. Abskharon, P. Ge, M. DeTure, D. W. Dickson, J. Y. Fu, R. R. Ogorzalek Loo, J. A. Loo, D. S. Eisenberg, Amyloid fibrils in FTLD-TDP are composed of TMEM106B and not TDP-43. *Nature* **605**, 304-309 (2022).

53. M. Schweighauser, D. Arseni, M. Bacioglu, M. Huang, S. Lövestam, Y. Shi, Y. Yang, W. Zhang, A. Kotecha, H. J. Garringer, R. Vidal, G. I. Hallinan, K. L. Newell, A. Tarutani, S. Murayama, M. Miyazaki, Y. Saito, M. Yoshida, K. Hasegawa, T. Lashley, T. Revesz, G. G. Kovacs, J. van Swieten, M. Takao, M. Hasegawa, B. Ghetti, M. G. Spillantini, B. Ryskeldi-Falcon, A. G. Murzin, M. Goedert, S. H. W. Scheres, Age-dependent formation of TMEM106B amyloid filaments in human brains. *Nature* **605**, 310-314 (2022).

54. X. Zhou, A. M. Nicholson, Y. Ren, M. Brooks, P. Jiang, A. Zuberi, H. N. Phuoc, R. B. Perkerson, B. Matchett, T. M. Parsons, N. A. Finch, W. Lin, W. Qiao, M. Castanedes-Casey, V. Phillips, A. L. Librero, Y. Asmann, G. Bu, M. E. Murray, C. Lutz, D. W. Dickson, R. Rademakers, Loss of TMEM106B leads to myelination deficits: implications for frontotemporal dementia treatment strategies. *Brain* **143**, 1905-1919 (2020).

55. H. Rhinn, N. Tatton, S. McCaughey, M. Kurnellas, A. Rosenthal, Progranulin as a therapeutic target in neurodegenerative diseases. *Trends Pharmacol Sci* **43**, 641-652 (2022).

56. D. A. Amado, J. M. Rieders, F. Diatta, P. Hernandez-Con, A. Singer, J. T. Mak, J. Zhang, E. Lancaster, B. L. Davidson, A. S. Chen-Plotkin, AAV-Mediated Progranulin Delivery to a Mouse Model of Progranulin Deficiency Causes T Cell-Mediated Toxicity. *Mol Ther* **27**, 465-478 (2019).

57. L. Samaranch, J. Bringas, P. Pivirotto, W. S. Sebastian, J. Forsayeth, K. Bankiewicz, Cerebellomedullary Cistern Delivery for AAV-Based Gene Therapy: A Technical Note for Nonhuman Primates. *Hum Gene Ther Methods* **27**, 13-16 (2016).

58. W. A. Liguore, J. S. Domire, D. Button, Y. Wang, B. D. Dufour, S. Srinivasan, J. L. McBride, AAV-PHP.B Administration Results in a Differential Pattern of CNS Biodistribution in Non-human Primates Compared with Mice. *Mol Ther* **27**, 2018-2037 (2019).

59. D. J. Wolak, R. G. Thorne, Diffusion of macromolecules in the brain: implications for drug delivery. *Mol Pharm* **10**, 1492-1504 (2013).

60. T. Feng, G. Minevich, P. Liu, H. X. Qin, G. Wozniak, J. Pham, K. Pham, A. Korgaonkar, M. Kurnellas, N. A. Defranoux, H. Long, A. Mitra, F. Hu, AAV-GRN partially corrects motor deficits and ALS/FTLD-related pathology in Tmem106b-/-Grn-/- mice. *iScience*, (in press).

61. H. C. J. Ertl, Immunogenicity and toxicity of AAV gene therapy. *Front Immunol* **13**, 975803 (2022).

62. I. Le Ber, A. Camuzat, D. Hannequin, F. Pasquier, E. Guedj, A. Rovelet-Lecrux, V. Hahn-Barma, J. van der Zee, F. Clot, S. Bakchine, M. Puel, M. Ghanim, L. Lacomblez, J. Mikol, V. Deramecourt, P. Lejeune, V. de la Sayette, S. Belliard, M. Vercelletto, C. Meyrignac, C. Van Broeckhoven, J. C. Lambert, P. Verpillat, D. Campion, M. O. Habert, B. Dubois, A. Brice, Phenotype variability in progranulin mutation carriers: a clinical, neuropsychological, imaging and genetic study. *Brain* **131**, 732-746 (2008).

63. J. R. Burrell, M. C. Kiernan, S. Vucic, J. R. Hodges, Motor Neuron dysfunction in frontotemporal dementia. *Brain* **134**, 2582-2594 (2011).

64. D. De Silva, S. Hsieh, J. Caga, F. V. Leslie, M. C. Kiernan, J. R. Hodges, E. Mioshi, J. R. Burrell, Motor function and behaviour across the ALS-FTD spectrum. *Acta Neurol Scand* **133**, 367-372 (2016).

46

68

65.   S. J. Guyenet, S. A. Furrer, V. M. Damian, T. D. Baughan, A. R. La Spada, G. A. Garden, A simple composite phenotype scoring system for evaluating mouse models of cerebellar ataxia. *J Vis Exp*, (2010).

66.   J. Adams, M. Feuerborn, J. A. Molina, A. R. Wilden, B. Adhikari, T. Budden, S. Y. Lee, Autophagy–lysosome pathway alterations and alpha-synuclein up-regulation in the subtype of neuronal ceroid lipofuscinosis, CLN5 disease. *Scientific Reports* **9**, 151 (2019).

67.   S. Pankiv, T. H. Clausen, T. Lamark, A. Brech, J.-A. Bruun, H. Outzen, A. Øvervatn, G. Bjørkøy, T. Johansen, p62/SQSTM1 Binds Directly to Atg8/LC3 to Facilitate Degradation of Ubiquitinated Protein Aggregates by Autophagy*. *Journal of Biological Chemistry* **282**, 24131-24145 (2007).

68.   G. Bjørkøy, T. Lamark, A. Brech, H. Outzen, M. Perander, A. Overvatn, H. Stenmark, T. Johansen, p62/SQSTM1 forms protein aggregates degraded by autophagy and has a protective effect on huntingtin-induced cell death. *J Cell Biol* **171**, 603-614 (2005).

69.   M. Neumann, D. M. Sampathu, L. K. Kwong, A. C. Truax, M. C. Micsenyi, T. T. Chou, J. Bruce, T. Schuck, M. Grossman, C. M. Clark, L. F. McCluskey, B. L. Miller, E. Masliah, I. R. Mackenzie, H. Feldman, W. Feiden, H. A. Kretzschmar, J. Q. Trojanowski, V. M. Lee, Ubiquitinated TDP-43 in frontotemporal lobar degeneration and amyotrophic lateral sclerosis. *Science* **314**, 130-133 (2006).

70.   M. Neumann, P. Frick, F. Paron, J. Kosten, E. Buratti, I. R. Mackenzie, Antibody against TDP-43 phosphorylated at serine 375 suggests conformational differences of TDP-43 aggregates among FTLD-TDP subtypes. *Acta Neuropathol* **140**, 645-658 (2020).

71.   M. Neumann, Molecular Neuropathology of TDP-43 Proteinopathies. *International Journal of Molecular Sciences* **10**, 232-246 (2009).

72.   S. Lemprière, Neuroinflammation predicts cognitive decline in FTD. *Nature Reviews Neurology* **19**, 258-258 (2023).

73.   H. Keren-Shaul, A. Spinrad, A. Weiner, O. Matcovitch-Natan, R. Dvir-Szternfeld, T. K. Ulland, E. David, K. Baruch, D. Lara-Astaiso, B. Toth, S. Itzkovitz, M. Colonna, M. Schwartz, I. Amit, A Unique Microglia Type Associated with Restricting Development of Alzheimer's Disease. *Cell* **169**, 1276-1290.e1217 (2017).

74.   A. T. McKenzie, M. Wang, M. E. Hauberg, J. F. Fullard, A. Kozlenkov, A. Keenan, Y. L. Hurd, S. Dracheva, P. Casaccia, P. Roussos, B. Zhang, Brain Cell Type Specific Gene Expression and Co-expression Network Architectures. *Scientific Reports* **8**, 8868 (2018).

75.   S. Krasemann, C. Madore, R. Cialic, C. Baufeld, N. Calcagno, R. El Fatimy, L. Beckers, E. O'Loughlin, Y. Xu, Z. Fanek, D. J. Greco, S. T. Smith, G. Tweet, Z. Humulock, T. Zrzavy, P. Conde-Sanroman, M. Gacias, Z. Weng, H. Chen, E. Tjon, F. Mazaheri, K. Hartmann, A. Madi, J. D. Ulrich, M. Glatzel, A. Worthmann, J. Heeren, B. Budnik, C. Lemere, T. Ikezu, F. L. Heppner, V. Litvak, D. M. Holtzman, H. Lassmann, H. L. Weiner, J. Ochando, C. Haass, O. Butovsky, The TREM2-APOE Pathway Drives the Transcriptional Phenotype of Dysfunctional Microglia in Neurodegenerative Diseases. *Immunity* **47**, 566-581.e569 (2017).

76.   A. A. Nugent, K. Lin, B. van Lengerich, S. Lianoglou, L. Przybyla, S. S. Davis, C. Llapashtica, J. Wang, D. J. Kim, D. Xia, A. Lucas, S. Baskaran, P. C. G. Haddick, M. Lenser, T. K. Earr, J. Shi, J. C. Dugas, B. J. Andreone, T. Logan, H. O. Solanoy, H. Chen, A. Srivastava, S. B. Poda, P. E. Sanchez, R. J. Watts, T. Sandmann, G. Astarita, J. W. Lewcock, K. M. Monroe, G. Di

Paolo, TREM2 Regulates Microglial Cholesterol Metabolism upon Chronic Phagocytic Challenge. *Neuron* **105**, 837-854.e839 (2020).

1215   77.   Y. Wu, W. Shao, T. W. Todd, J. Tong, M. Yue, S. Koga, M. Castanedes-Casey, A. L. Librero, C. W. Lee, I. R. Mackenzie, D. W. Dickson, Y.-J. Zhang, L. Petrucelli, M. Prudencio, Microglial lysosome dysfunction contributes to white matter pathology and TDP-43 proteinopathy in GRN-associated FTD. *Cell Reports* **36**, (2021).

78.   T. Feng, L. Luan, Katz, II, M. Ullah, V. M. Van Deerlin, J. Q. Trojanowski, E. B. Lee, F. Hu, 1220   TMEM106B deficiency impairs cerebellar myelination and synaptic integrity with Purkinje cell loss. *Acta Neuropathol Commun* **10**, 33 (2022).

79.   D. Paquet, D. Kwart, A. Chen, A. Sproul, S. Jacob, S. Teo, K. M. Olsen, A. Gregg, S. Noggle, M. Tessier-Lavigne, Efficient introduction of specific homozygous and heterozygous mutations using CRISPR/Cas9. *Nature* **533**, 125-129 (2016).

1225   80.   D. Kwart, D. Paquet, S. Teo, M. Tessier-Lavigne, Precise and efficient scarless genome editing in stem cells using CORRECT. *Nat Protoc* **12**, 329-354 (2017).

81.   W. C. Lee, S. Almeida, M. Prudencio, T. R. Caulfield, Y. J. Zhang, W. M. Tay, P. O. Bauer, J. Chew, H. Sasaguri, K. R. Jansen-West, T. F. Gendron, C. T. Stetler, N. Finch, I. R. Mackenzie, R. Rademakers, F. B. Gao, L. Petrucelli, Targeted manipulation of the sortilin-1230   progranulin axis rescues progranulin haploinsufficiency. *Hum Mol Genet* **23**, 1467-1478 (2014).

82.   S. Miyakawa, H. Sakuma, D. Warude, S. Asanuma, N. Arimura, T. Yoshihara, D. Tavares, A. Hata, K. Ida, Y. Hori, Y. Okuzono, S. Yamamoto, K. Iida, H. Shimizu, S. Kondo, S. Sato, Anti-sortilin1 Antibody Up-Regulates Progranulin via Sortilin1 Down-Regulation. *Front* 1235   *Neurosci* **14**, 586107 (2020).

83.   M. Kurnellas, A. Mitra, T. Schwabe, R. Paul, A. E. Arrant, E. D. Roberson, M. Ward, F. Yeh, H. Long, A. Rosenthal, Latozinemab, a novel progranulin-elevating therapy for frontotemporal dementia. *J Transl Med* **21**, 387 (2023).

84.   A. E. Arrant, A. J. Filiano, D. E. Unger, A. H. Young, E. D. Roberson, Restoring neuronal 1240   progranulin reverses deficits in a mouse model of frontotemporal dementia. *Brain* **140**, 1447-1465 (2017).

85.   A. E. Arrant, V. C. Onyilo, D. E. Unger, E. D. Roberson, Progranulin Gene Therapy Improves Lysosomal Dysfunction and Microglial Pathology Associated with Frontotemporal Dementia and Neuronal Ceroid Lipofuscinosis. *J Neurosci* **38**, 2341-2358 1245   (2018).

86.   C. Hinderer, R. Miller, C. Dyer, J. Johansson, P. Bell, E. Buza, J. M. Wilson, Adeno-associated virus serotype 1-based gene therapy for FTD caused by GRN mutations. *Ann Clin Transl Neurol* **7**, 1843-1853 (2020).

87.   P. A. Ljubenkov, L. Edwards, L. Iaccarino, R. La Joie, J. C. Rojas, M. Koestler, B. Harris, B. F. 1250   Boeve, B. Borroni, J. C. van Swieten, M. Grossman, F. Pasquier, G. B. Frisoni, C. J. Mummery, R. Vandenberghe, I. Le Ber, D. Hannequin, S. M. McGinnis, S. Auriacombe, M. Onofrj, I. J. Goodman, H. J. Riordan, G. Wisniewski, J. Hesterman, K. Marek, B. A. Haynes, H. Patzke, G. Koenig, D. Hilt, H. Moebius, A. L. Boxer, Effect of the Histone Deacetylase Inhibitor FRM-0334 on Progranulin Levels in Patients With Progranulin Gene 1255   Haploinsufficiency: A Randomized Clinical Trial. *JAMA Netw Open* **4**, e2125584 (2021).

88.   X. Zhou, D. H. Paushter, T. Feng, L. Sun, T. Reinheckel, F. Hu, Lysosomal processing of progranulin. *Mol Neurodegener* **12**, 62 (2017).

70

89. Y. Zhang, Steven A. Sloan, Laura E. Clarke, C. Caneda, Colton A. Plaza, Paul D. Blumenthal, H. Vogel, Gary K. Steinberg, Michael S. B. Edwards, G. Li, John A. Duncan, III, Samuel H. Cheshier, Lawrence M. Shuer, Edward F. Chang, Gerald A. Grant, Melanie G. H. Gephart, Ben A. Barres, Purification and Characterization of Progenitor and Mature Human Astrocytes Reveals Transcriptional and Functional Differences with Mouse. *Neuron* **89**, 37-53 (2016).

90. Z. Ye, C. Kenian, A. S. Steven, L. B. Mariko, R. S. Anja, O. Sean, Keeffe, P. P. Hemali, G. Paolo, C. Christine, R. Nadine, D. Shuyun, A. L. Shane, Z. Chaolin, D. Richard, M. Tom, A. B. Ben, W. Jia Qian, An RNA-Sequencing Transcriptome and Splicing Database of Glia, Neurons, and Vascular Cells of the Cerebral Cortex. *The Journal of Neuroscience* **34**, 11929 (2014).

91. I. Weisheit, J. A. Kroeger, R. Malik, B. Wefers, P. Lichtner, W. Wurst, M. Dichgans, D. Paquet, Simple and reliable detection of CRISPR-induced on-target effects by qgPCR and SNP genotyping. *Nat Protoc* **16**, 1714-1739 (2021).

92. J. P. Concordet, M. Haeussler, CRISPOR: intuitive guide selection for CRISPR/Cas9 genome editing experiments and screens. *Nucleic Acids Res* **46**, W242-w245 (2018).

93. E. M. Abud, R. N. Ramirez, E. S. Martinez, L. M. Healy, C. H. H. Nguyen, S. A. Newman, A. V. Yeromin, V. M. Scarfone, S. E. Marsh, C. Fimbres, C. A. Caraway, G. M. Fote, A. M. Madany, A. Agrawal, R. Kayed, K. H. Gylys, M. D. Cahalan, B. J. Cummings, J. P. Antel, A. Mortazavi, M. J. Carson, W. W. Poon, M. Blurton-Jones, iPSC-Derived Human Microglia-like Cells to Study Neurological Diseases. *Neuron* **94**, 278-293.e279 (2017).

94. A. Dannert, J. Klimmt, C. Cardoso Gonçalves, D. Crusius, D. Paquet, Reproducible and scalable differentiation of highly pure cortical neurons from human induced pluripotent stem cells. *STAR Protoc* **4**, 102266 (2023).

95. H. Jiang, R. Lei, S.-W. Ding, S. Zhu, Skewer: a fast and accurate adapter trimmer for next-generation sequencing paired-end reads. *BMC Bioinformatics* **15**, 182 (2014).

96. S. Andrews, J. Gilley, M. P. Coleman, Difference Tracker: ImageJ plugins for fully automated analysis of multiple axonal transport parameters. *J Neurosci Methods* **193**, 281-287 (2010).

97. A. Dobin, C. A. Davis, F. Schlesinger, J. Drenkow, C. Zaleski, S. Jha, P. Batut, M. Chaisson, T. R. Gingeras, STAR: ultrafast universal RNA-seq aligner. *Bioinformatics* **29**, 15-21 (2013).

98. P. Ewels, M. Magnusson, S. Lundin, M. Käller, MultiQC: summarize analysis results for multiple tools and samples in a single report. *Bioinformatics* **32**, 3047-3048 (2016).

99. M. D. Robinson, A. Oshlack, A scaling normalization method for differential expression analysis of RNA-seq data. *Genome Biology* **11**, R25 (2010).

100. M. D. Robinson, D. J. McCarthy, G. K. Smyth, edgeR: a Bioconductor package for differential expression analysis of digital gene expression data. *Bioinformatics* **26**, 139-140 (2010).

101. C. W. Law, Y. Chen, W. Shi, G. K. Smyth, voom: precision weights unlock linear model analysis tools for RNA-seq read counts. *Genome Biology* **15**, R29 (2014).

102. Z. Gu, R. Eils, M. Schlesner, Complex heatmaps reveal patterns and correlations in multidimensional genomic data. *Bioinformatics* **32**, 2847-2849 (2016).

103. A. Klein, M. Henseler, C. Klein, K. Suzuki, K. Harzer, K. Sandhoff, Sphingolipid activator protein D (sap-D) stimulates the lysosomal degradation of ceramide in vivo. *Biochem Biophys Res Commun* **200**, 1440-1448 (1994).

49

104.   B. M. Schwenk, C. M. Lang, S. Hogl, S. Tahirovic, D. Orozco, K. Rentzsch, S. F. Lichtenthaler, C. C. Hoogenraad, A. Capell, C. Haass, D. Edbauer, The FTLD risk factor TMEM106B and MAP6 control dendritic trafficking of lysosomes. *Embo j* **33**, 450-467 (2014).

105.   G. Kleinberger, M. Brendel, E. Mracsko, B. Wefers, L. Groeneweg, X. Xiang, C. Focke, M. Deußing, M. Suárez-Calvet, F. Mazaheri, S. Parhizkar, N. Pettkus, W. Wurst, R. Feederle, P. Bartenstein, T. Mueggler, T. Arzberger, I. Knuesel, A. Rominger, C. Haass, The FTD-like syndrome causing TREM2 T66M mutation impairs microglia function, brain perfusion, and glucose metabolism. *Embo j* **36**, 1837-1853 (2017).

106.   A. Capell, S. Liebscher, K. Fellerer, N. Brouwers, M. Willem, S. Lammich, I. Gijselinck, T. Bittner, A. M. Carlson, F. Sasse, B. Kunze, H. Steinmetz, R. Jansen, D. Dormann, K. Sleegers, M. Cruts, J. Herms, C. Van Broeckhoven, C. Haass, Rescue of progranulin deficiency associated with frontotemporal lobar degeneration by alkalizing reagents and inhibition of vacuolar ATPase. *J Neurosci* **31**, 1885-1894 (2011).

107.   M. Reich, I. Paris, M. Ebeling, N. Dahm, C. Schweitzer, D. Reinhardt, R. Schmucki, M. Prasad, F. Köchl, M. Leist, S. A. Cowley, J. D. Zhang, C. Patsch, S. Gutbier, M. Britschgi, Alzheimer's Risk Gene TREM2 Determines Functional Properties of New Type of Human iPSC-Derived Microglia. *Front Immunol* **11**, 617860 (2020).

108.   R. Haase, L. A. Royer, P. Steinbach, D. Schmidt, A. Dibrov, U. Schmidt, M. Weigert, N. Maghelli, P. Tomancak, F. Jug, E. W. Myers, CLIJ: GPU-accelerated image processing for everyone. *Nature Methods* **17**, 5-6 (2020).

1305

1310

1315

1320

1325

Supplementary Materials for

Rescue of FTLD-associated TDP-43 pathology and neurodegeneration by peripheral AAV-mediated expression of brain-penetrant progranulin

Marvin Reich[1,2,3,†], Matthew J. Simon[4,†], Beate Polke[5,‡], Georg Werner[5], Christian Schrader[5,§], Iñaki Paris[5], Sophie Robinson[2,3,5], Sonnet S. Davis[4], Gabrielly Lunkes de Melo[4], Lennart Schlaphoff[1,2,6], Lena Spieth[1,6,7], Stefan Berghoff[1,6,7], Todd Logan[4,‖], Brigitte Nuscher[5], Katrin Buschmann[5], Dieter Edbauer[1,8], Mikael Simons[1,3,6,8], Jung H. Suh[4], Thomas Sandmann[4], Mihalis S. Kariolis[4], Sarah L. DeVos[4], Joseph W. Lewcock[4], Dominik Paquet[3,8,*], Anja Capell[5,*], Gilbert Di Paolo[4,*], Christian Haass[1, 5, 8,*]

Fig. S1: AAV-expressed 8D3:PGRN has minimal effects on red blood cells in *Grn* KO mice. Quantification of blood cell measurements including number of red blood cells (RBC) (**A**), number of reticulocytes (**B**), mean corpuscular volume (MCV) (**C**) and mean corpuscular hemoglobin (MCH) (**D**) in 12-month-old *Grn* KO mice following 31 weeks of AAV(L):bPGRN treatment. Data is depicted as mean ± SEM, data points represent individual samples. For statistical analysis, one-way ANOVA with Tukey's multiple comparison was performed. $*p < 0.05$, $**p < 0.01$.
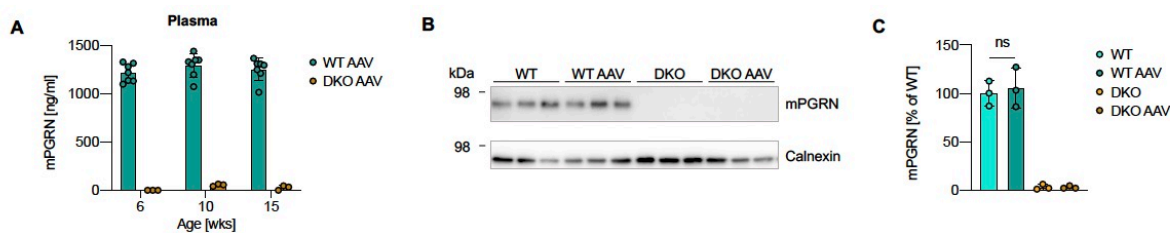
Fig. S2: AAV-mediated delivery of 8D3:PGRN does not alter endogenous PGRN levels in WT mice. (**A**) mPGRN levels in plasma following AAV(L):bPGRN treatment in WT and DKO mice as assessed by ELISA (n=3-7/group). (**B**) mPGRN levels in brain following treatment as assessed by Western blot (n=3/group). (**C**) Quantification of mPGRN levels in B normalized to WT (n=3/group).

Data is depicted as mean ± SD, data points represent individual animals. For statistical analysis, one-way ANOVA with Tukey's multiple comparison was performed. ns $p > 0.05$.
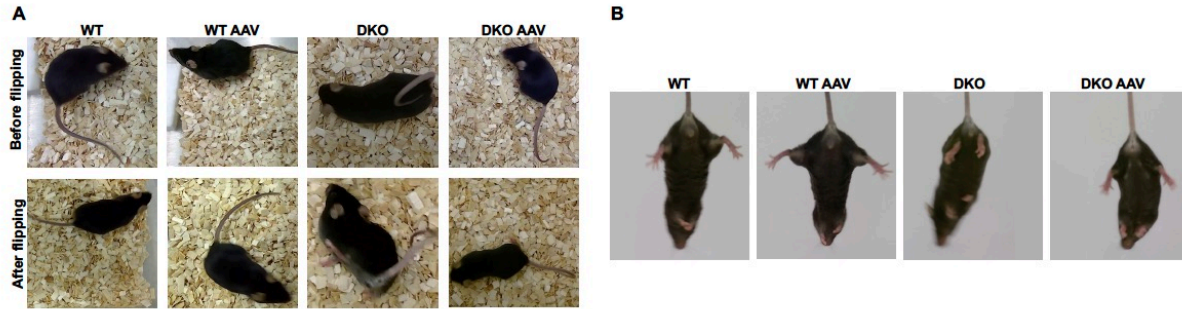
Fig. S3: AAV-expressed 8D3:PGRN ameliorates behavioral abnormalities in DKO mice. (A) Representative images of 15-week-old mice 9 weeks after AAV(L):bPGRN treatment before and after flipping. (**B**) Representative images of hind limb clasping test showing 15-week-old mice 9 weeks after treatment.

76
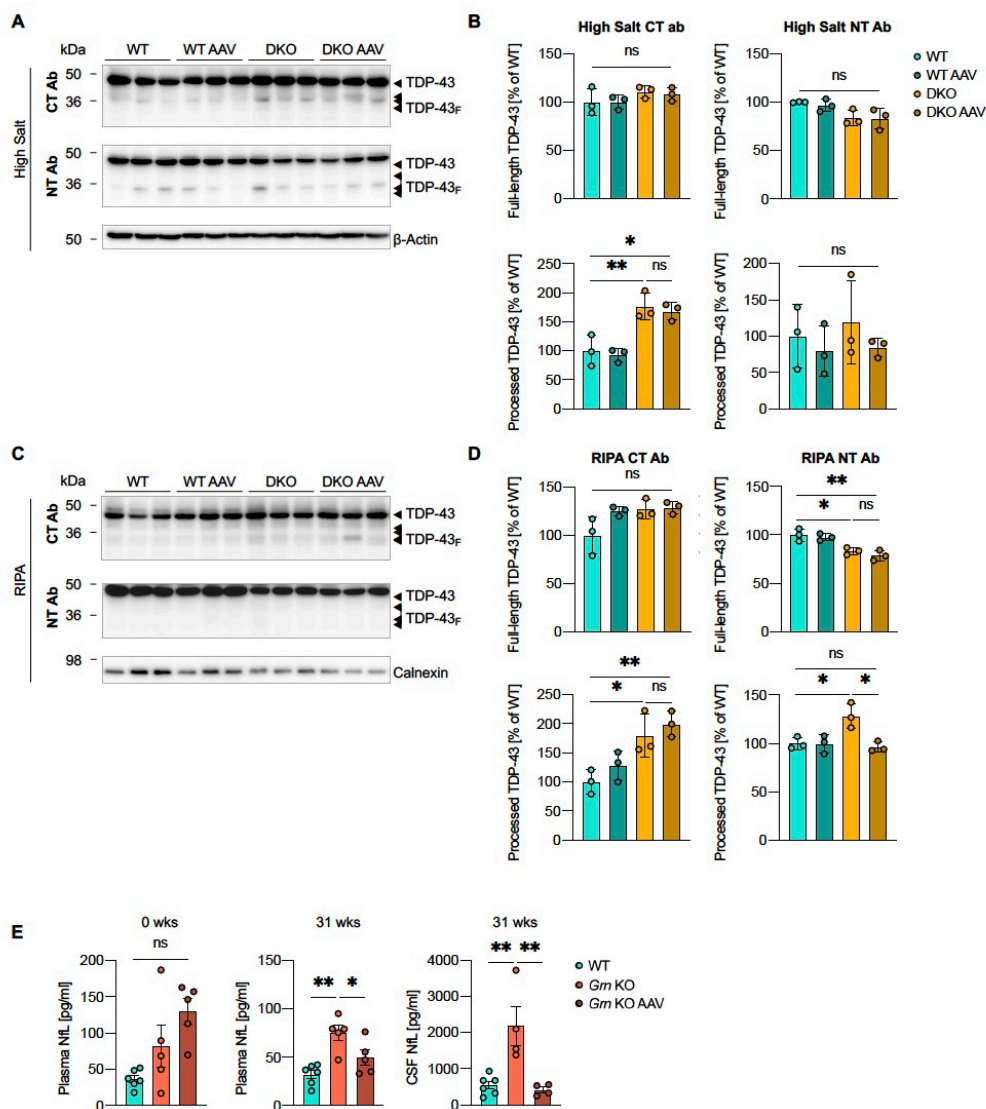
Fig. S4: AAV-mediated delivery of 8D3:PGRN reduces TDP-43 pathology in DKO and NfL in *Grn* KO mice. (**A,C**) Western blot showing the protein levels of TDP-43 in the high salt (A) and RIPA (B) fractions of brains of untreated and AAV(L):bPGRN-treated WT and DKO mice by using antibodies either directed against the C- terminus or the N-terminus (n=3/group). (**B,D**) Quantification of the protein levels in A (B) and C (D) normalized to WT (n=3/group). (**E**) NfL levels in plasma and CSF of *Grn* KO animals following AAV(L):bPGRN treatment. n=5-6/group. Data is depicted as mean ± SD (B,D) or mean ± SEM (E), data points represent individual animals. For statistical analysis, one-way ANOVA with Tukey's multiple comparison was performed. ns p > 0.05, *p < 0.05, **p < 0.01.

77

Fig. S5: AAV-mediated delivery of 8D3:PGRN normalizes astrogliosis and microgliosis in **Grn KO mice.** (**A**) Heatmap depiction of transcriptional changes in 12-month-old *Grn* KO mice following 31 weeks of AAV(L):bPGRN treatment. Columns represent individual animals. Plotted values are log2 transformed. (**B**) Representative immunofluorescence images of the thalamus
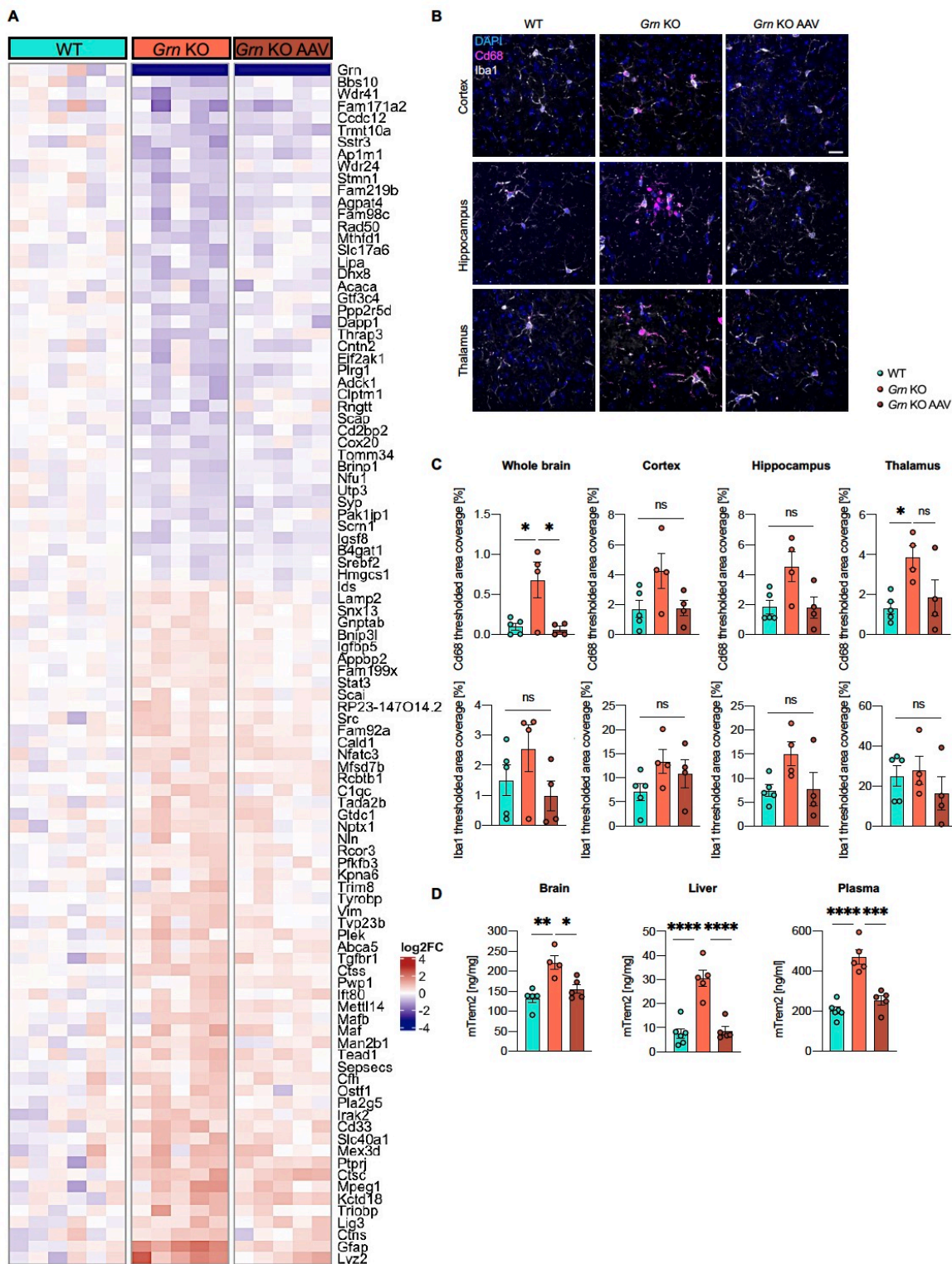
showing Iba1$^+$ and Cd68$^+$ cells (scalebar = 20 µm). (**C**) Regional quantification of Cd68 and Iba1 in whole hemispheres (left), cortex (middle left), hippocampus (middle right) and thalamus (right). (**D**) ELISA-quantified mTrem2 levels in brain (left), liver (middle) and plasma (right) in 12-month-old *Grn* KO mice following 31 weeks of AAV(L):bPGRN treatment. n=5-6/group. Data is depicted as mean ± SEM ns p > 0.05, *p < 0.05, **p < 0.01, ***p < 0.001, ****p < 0.0001.
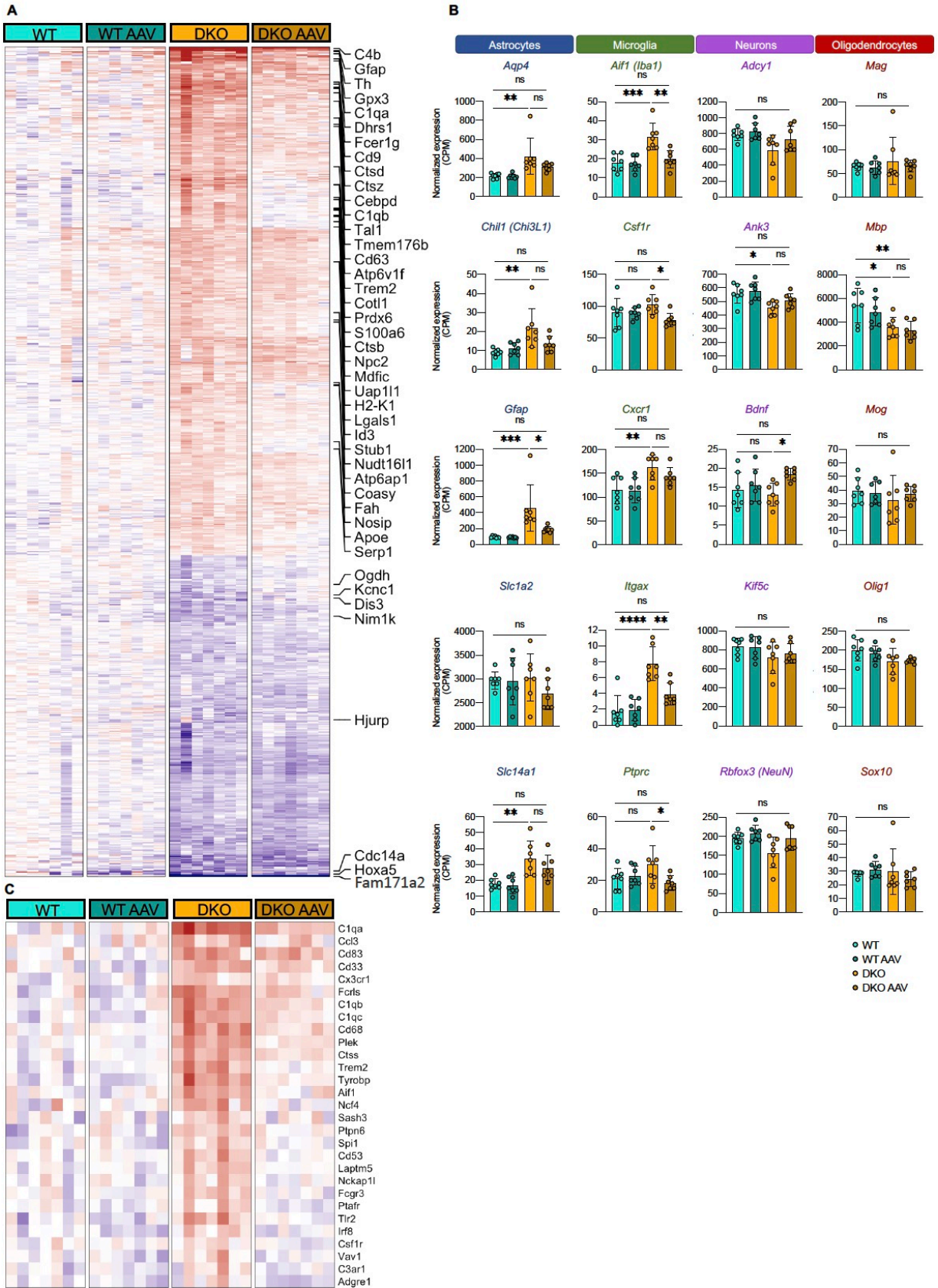
Fig. S6: AAV-mediated delivery of 8D3:PGRN partially restores genetic cell type

composition within the brain. (**A**) Heatmap depiction of the top 785 differentially expressed genes in DKO mice and correction with AAV(L):bPGRN with a false discovery rate (FDR) < 5% and at least a 20% change comparing WT and DKO. Plotted values are log2 transformed. (**B**) Expression of astrocyte (blue), microglia (green), neurons (purple) and oligodendrocyte (red) markers in the treated and untreated WT and DKO mice. (**C**) Heatmap depiction of the top 29 differentially expressed microglia-specific genes in DKO mice and correction with AAV(L):bPGRN with a false discovery rate (FDR) < 5% and at least a 20% change comparing WT and DKO. Plotted values are log2 transformed. n=7/group. Data is depicted as mean ± SD. ns $p > 0.05$, *$p < 0.05$, **$p < 0.01$, ***$p < 0.001$, ****$p < 0.0001$.
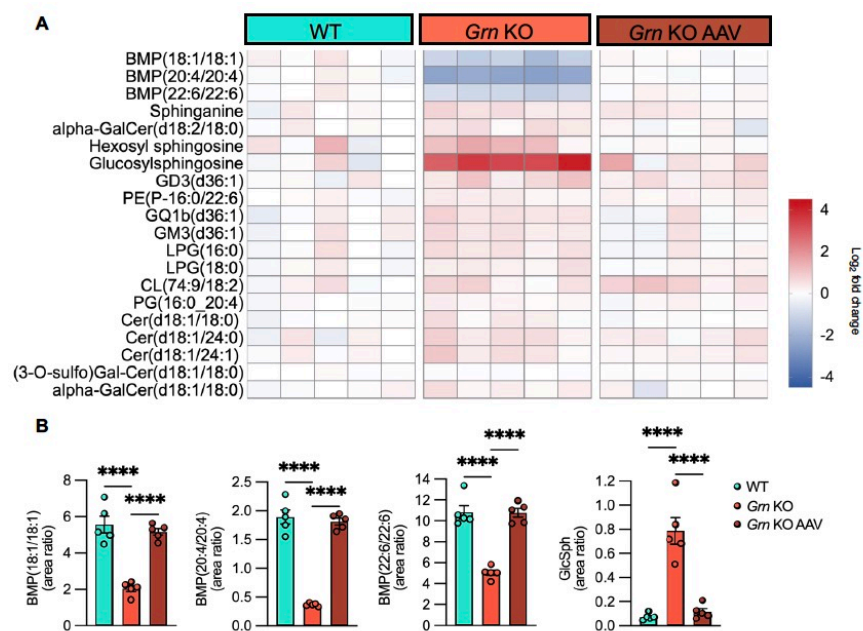
Fig. S7: AAV-mediated delivery of 8D3:PGRN restores lipid profile of *Grn* KO mice. (A) Heatmap depiction of differentially regulated lipids in *Grn* KO mice and correction with AAV(L):bPGRN treatment. Columns represent individual animals. Plotted values are log2 transformed. FDR cutoff: <5%, change cutoff: >20%. **(B)** Bar plots of treatment response of BMPs and gangliosides. n=5/group. Data is depicted as mean ± SEM. ****p < 0.0001.

82
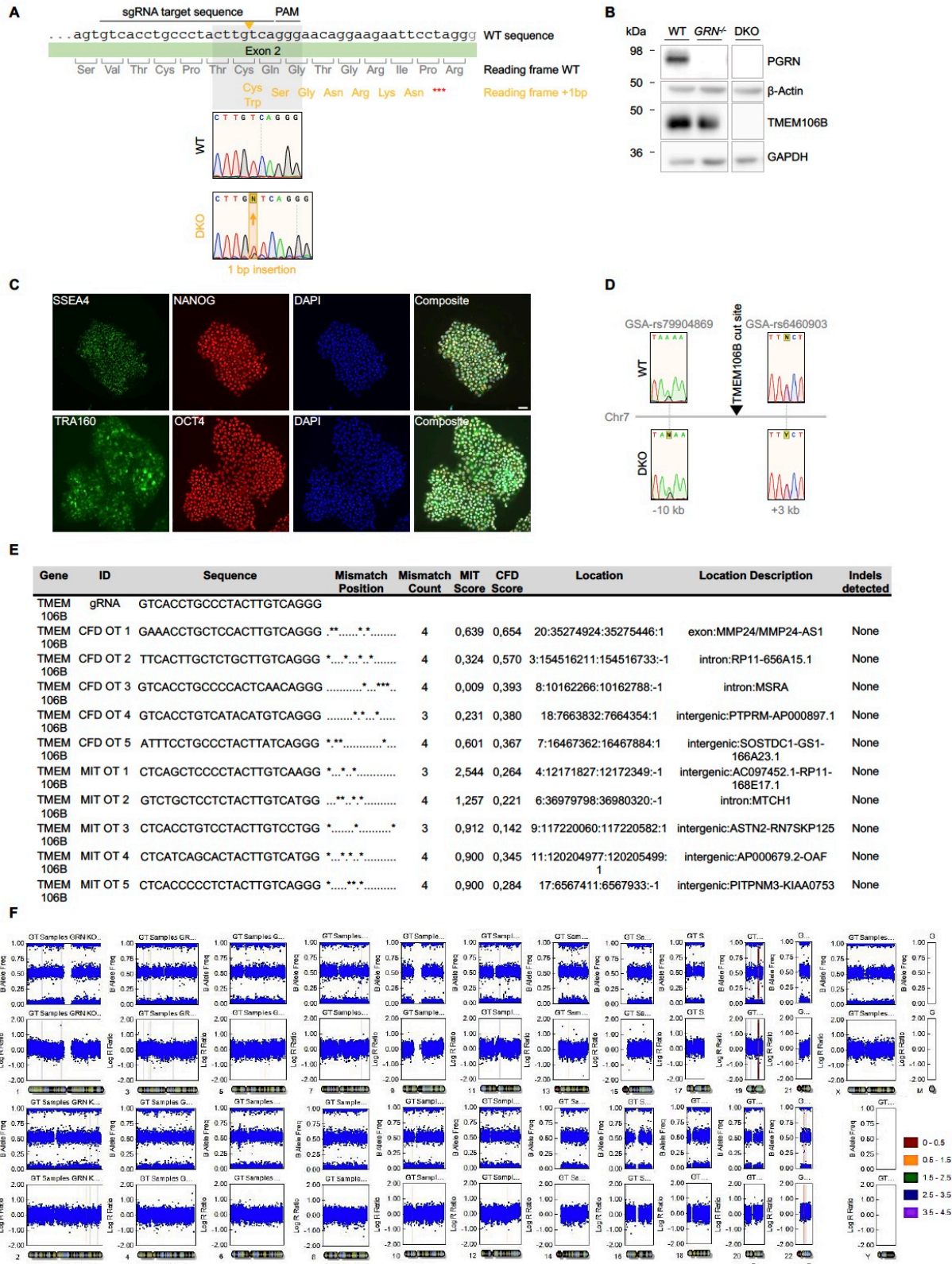
Fig. S8: Generation of *TMEM106BxGRN* DKO hiPSC. (A) Schematic overview of the edited locus on exon 2 of the TMEM106B gene. Indicated are the sgRNA target sequence, the protospacer

adjacent motif (PAM), reading frame with WT and DKO amino acid sequence and Sanger sequencing traces of WT and DKO lines. (**B**) Western blot confirming loss of TMEM106B and hPGRN in edited hiPSC in comparison to WT. (**C**) Immunofluorescence images showing expression of pluripotency markers SSEA4, NANOG, TRA160 and OCT4 (scalebar = 50 µm) in edited iPSCs. (**D**) Sanger sequencing of heterozygous SNPs on both sides of the edited locus in WT and DKO confirm that no loss of heterozygosity was induced by CRISPR editing. (**E**) Overview of the most likely off-targets as assessed using CRISPOR. Sanger sequencing of the PCR-amplified off-target sequences showed no deviation from the WT sequence. (**F**) Karyogram of DKO cell line indicating integrity of all chromosomes after editing, as assessed by molecular karyotyping.

84

TableS1: Summary of histopathological findings in Grn KO mice treated with AAV(L):bPGRN

Tissue	Microscopic findings			Comments
	WT	**Grn KO**	**Grn KO AAV**	
Brain	0	0	0	
Heart	0	0	0	
Lung	4	5	2	*Mild infiltrates in all groups*
Liver	0	0	0	
Kidney	5	3	3	*Mild infiltrates in all groups*
Spleen	0	0	0	
Intestine	0	0	0	
Prostate	0	0	0	
Testes	0	0	0	
Bone marrow	0	0	0	
Sciatic nerve	0	0	0	

Table S2: Lipidomics in positive mode acquisition parameters

Name	Internal Standard	Q1 m/z	Q3 m/z	CE (V)
1-O-Palmitoyl-Cer(d18:1/18:0)	Cer(d18:1/16:0(d7))	786.8	502.5	35
24-Hydroxycholesterol	24-Hydroxcholesterol-d7	385.3	367.3	30
24-Hydroxycholesterol(d7)	IS	392.3	367.3	30
3-O-SulfoLacCer(d18:1/18:0)	LacCer(d18:1/17:0)	970.8	548.5	61
4-beta-Hydroxycholesterol	Cholesterol(d7)	420.3	385.3	15
7-keto-Cholesterol	Cholesterol(d7)	401.3	383.3	15
CE HETE	CE(18:1(d7))	706.6	369.2	25
CE HODE	CE(18:1(d7))	682.6	369.2	25
CE HpODE	CE(18:1(d7))	698.6	369.2	25
CE oxoHETE	CE(18:1(d7))	704.6	369.2	25
CE oxoODE	CE(18:1(d7))	680.6	369.2	25
CE(16:1)	CE(18:1(d7))	640.6	369.3	26
CE(18:1(d7))	IS	675.2	369.4	26
CE(18:1)	CE(18:1(d7))	668.6	369.3	26
CE(18:2)	CE(18:1(d7))	666.6	369.3	26
CE(20:4)	CE(18:1(d7))	690.6	369.3	26
CE(20:5)	CE(18:1(d7))	688.6	369.3	26
CE(22:6)	CE(18:1(d7))	714.6	369.3	26
Cer(d18:0/16:0)	Cer(d18:1/16:0(d7))	540.6	284.3	40
Cer(d18:0/18:0)	Cer(d18:1/16:0(d7))	568.7	284.3	40
Cer(d18:0/24:0)	Cer(d18:1/16:0(d7))	652.9	284.3	40
Cer(d18:0/24:1)	Cer(d18:1/16:0(d7))	650.9	284.4	40
Cer(d18:1/16:0(d7))	IS	545.5	271.4	40
Cer(d18:1/16:0)	Cer(d18:1/16:0(d7))	538.5	264.3	40
Cer(d18:1/18:0)	Cer(d18:1/16:0(d7))	566.6	264.3	40
Cer(d18:1/24:0)	Cer(d18:1/16:0(d7))	650.6	264.3	40
Cer(d18:1/24:1)	Cer(d18:1/16:0(d7))	648.6	264.3	40
Cholesterol	Cholesterol(d7)	369.3	369.3	10
Cholesterol(d7)	IS	376.2	376.2	10
Cholesteryl hexoside	CE(18:1(d7))	566.6	369.3	17
Coenzyme Q10	TG(15:0/18:1(d7)/15:0)	863.3	197.2	35

86

DG(15:0/18:1(d7))	IS	605.6	346.5	30
DG(16:0_18:1)	DG(15:0/18:1(d7))	612.4	313.3	30
DG(16:0_20:4)	DG(15:0/18:1(d7))	634.5	313.3	30
DG(18:0_18:1)	DG(15:0/18:1(d7))	640.4	341.3	30
DG(18:0_20:4)	DG(15:0/18:1(d7))	662.5	341.3	30
DG(18:0_22:6)	DG(15:0/18:1(d7))	686.6	341.3	30
DG(18:1_20:4)	DG(15:0/18:1(d7))	660.5	339.3	30
DG(18:1/18:1)	DG(15:0/18:1(d7))	638.4	339.3	30
GB3(d18:1/16:0)	GB3(d18:1/18:0(d3))	1025	520.5	40
GB3(d18:1/18:0(d3))	IS	1056	551.6	40
GB3(d18:1/18:0)	GB3(d18:1/18:0(d3))	1053	548.6	40
GB3(d18:1/24:0)	GB3(d18:1/18:0(d3))	1137	632.6	40
GB3(d18:1/24:1)	GB3(d18:1/18:0(d3))	1135	630.6	40
GlcCer(d18:1(d5)/18:0)	IS	733.6	269.3	45
GlcCer(d18:1/16:0(d3))	IS	703.7	264.3	51
Glucosylsphingosine(d5)	IS	467.2	269.3	16
HexCer(d18:1/12:0)	GlcCer(d18:1(d5)/18:0)	644.5	264.3	40
HexCer(d18:1/16:0)	GlcCer(d18:1(d5)/18:0)	700.6	264.3	40
HexCer(d18:1/18:0)	GlcCer(d18:1(d5)/18:0)	728.6	264.3	40
HexCer(d18:1/22:0)	GlcCer(d18:1(d5)/18:0)	784.7	264.4	40
HexCer(d18:1/24:0)	GlcCer(d18:1(d5)/18:0)	812.7	264.3	40
HexCer(d18:1/24:1)	GlcCer(d18:1(d5)/18:0)	810.7	264.3	40
Hexosylsphingosine	Glucosylsphingosine(d5)	462.3	264.2	16
LacCer(d18:1/16:0)	LacCer(d18:1/17:0)	862.6	264.3	40
LacCer(d18:1/17:0)	IS	876.6	264.3	40
LacCer(d18:1/18:0)	LacCer(d18:1/17:0)	890.7	264.3	40
LacCer(d18:1/24:0)	LacCer(d18:1/17:0)	974.8	264.3	40
LacCer(d18:1/24:1)	LacCer(d18:1/17:0)	972.7	264.3	40
Lactosylsphingosine	Glucosylsphingosine(d5)	624.4	264.3	16
LPC(16:0)	LPC(18:1(d7))	496.3	184.1	40
LPC(16:1)	LPC(18:1(d7))	494.5	184.1	40
LPC(18:0)	LPC(18:1(d7))	524.3	184.1	40

87

LPC(18:1(d7))	IS	529.3	184.1	40
LPC(18:1)	LPC(18:1(d7))	522.3	184.1	40
LPC(20:4)	LPC(18:1(d7))	544.3	184.1	40
LPC(22:6)	LPC(18:1(d7))	568.3	184.1	40
LPC(24:0)	LPC(18:1(d7))	608.5	184.1	40
LPC(24:1)	LPC(18:1(d7))	606.5	184.1	40
LPC(26:0)	LPC(18:1(d7))	636.5	104.1	40
LPC(26:1)	LPC(18:1(d7))	634.5	104.1	40
lyso-GB3	lyso-GB3-d7	786.6	264.3	46
lyso-GB3-d7	IS	793.5	271.3	46
lyso-GB4	GB3(d18:1/18:0(d3))	990.6	264.3	52
MG(16:0)	MG(18:1(d7))	348.3	239.3	22
MG(16:1)	MG(18:1(d7))	346.3	237.3	22
MG(18:0)	MG(18:1(d7))	376.3	267.3	22
MG(18:1(d7))	IS	381.3	272.5	22
MG(18:1)	MG(18:1(d7))	374.3	265.3	22
MG(20:4)	MG(18:1(d7))	396.3	287.3	22
N-Oleoylethanolamine	LPC(18:1(d7))	326.3	62.1	23
N-Palmitoyl-O-phosphocholineserine	LPC(18:1(d7))	509.5	184.1	40
Palmitoylethanolamine	LPC(18:1(d7))	300.3	62.1	23
PC(15:0/18:1(d7))	IS	754.6	184.1	40
PC(16:0/5:0(CHO))	PC(15:0/18:1(d7))	594.5	184.1	40
PC(16:0/9:0(CHO))	PC(15:0/18:1(d7))	650.4	184.1	40
PC(16:0/9:0(COOH))	PC(15:0/18:1(d7))	666.4	184.1	40
PC(18:0/20:4(OH[S]))	PC(15:0/18:1(d7))	826.6	184.1	40
PC(18:0/20:4(OOH[S]))	PC(15:0/18:1(d7))	842.6	184.1	40
PC(34:1)	PC(15:0/18:1(d7))	760.6	184.1	40
PC(36:1)	PC(15:0/18:1(d7))	788.6	184.1	40
PC(36:2)	PC(15:0/18:1(d7))	786.6	184.1	40
PC(36:4)	PC(15:0/18:1(d7))	782.6	184.1	40
PC(38:4)	PC(15:0/18:1(d7))	810.6	184.1	40
PC(38:6)	PC(15:0/18:1(d7))	806.6	184.1	40

88

PC(40:5)	PC(15:0/18:1(d7))	836.6	184.1	40
PC(40:6)	PC(15:0/18:1(d7))	834.6	184.1	40
PC(O-16:0/0:0)	LPC(18:1(d7))	482.3	184.1	40
PC(O-16:0/2:0)	LPC(18:1(d7))	524.3	184.2	40
PC(O-18:0/2:0)	LPC(18:1(d7))	552.5	184.1	40
PE(15:0/18:1(d7))	IS	711.6	570.5	40
PE(18:0/20:4(OH[S]))	PE(15:0/18:1(d7))	784.5	643.4	40
PE(18:0/20:4(OOH[S]))	PE(15:0/18:1(d7))	800.5	659.4	40
PE(34:1)	PE(15:0/18:1(d7))	718.6	577.6	40
PE(36:1)	PE(15:0/18:1(d7))	746.6	605.5	40
PE(36:2)	PE(15:0/18:1(d7))	744.6	603.5	40
PE(36:4)	PE(15:0/18:1(d7))	740.6	599.5	40
PE(38:4)	PE(15:0/18:1(d7))	768.6	627.5	40
PE(38:5)	PE(15:0/18:1(d7))	766.6	625.5	40
PE(38:6)	PE(15:0/18:1(d7))	764.6	623.5	40
PE(40:4)	PE(15:0/18:1(d7))	796.6	655.5	40
PE(40:5)	PE(15:0/18:1(d7))	794.6	635.5	40
PE(40:6)	PE(15:0/18:1(d7))	792.6	651.5	40
PE(40:7)	PE(15:0/18:1(d7))	790.6	649.5	40
Sitosteryl hexoside	CE(18:1(d7))	594.6	397.4	17
SM(d18:1(d9)/18:1)	IS	738.7	184.1	40
SM(d18:1/16:0)	SM(d18:1(d9)/18:1)	703.6	184.1	40
SM(d18:1/18:0)	SM(d18:1(d9)/18:1)	731.6	184.1	40
SM(d18:1/24:0)	SM(d18:1(d9)/18:1)	815.7	184.1	40
SM(d18:1/24:1)	SM(d18:1(d9)/18:1)	813.7	184.1	40
Sphinganine	Sphingosine(d17:1)	302.2	284.3	20
Sphinganine 1-phosphate	Sphingosine 1-phosphate-d7	382.3	284.3	18
Sphingosine	Sphingosine(d17:1)	300.2	264.3	20
Sphingosine 1-phosphate	Sphingosine 1-phosphate-d7	380.3	264.3	25
Sphingosine 1-phosphate-d7	IS	387.3	271.3	25
Sphingosine 1-phosphocholine	LPC(18:1(d7))	465.5	184.1	40
Sphingosine(d17:1)	IS	286.2	250.3	20

TG(15:0/18:1(d7)/15:0)	IS	829.8	570.8	40
TG(18:0_36:2)	TG(15:0/18:1(d7)/15:0)	904.7	603.4	40
TG(18:1_34:2)	TG(15:0/18:1(d7)/15:0)	874.7	575.4	40
TG(18:1_34:3)	TG(15:0/18:1(d7)/15:0)	872.7	573.4	40
TG(20:4_32:1)	TG(15:0/18:1(d7)/15:0)	870.6	549.3	40
TG(20:4_34:2)	TG(15:0/18:1(d7)/15:0)	896.6	575.3	40
TG(20:4_34:3)	TG(15:0/18:1(d7)/15:0)	894.6	573.3	40
TG(20:4_36:0)	TG(15:0/18:1(d7)/15:0)	928.8	607.5	40
TG(20:4_36:2)	TG(15:0/18:1(d7)/15:0)	924.7	603.4	40
TG(20:4_36:3)	TG(15:0/18:1(d7)/15:0)	922.7	601.4	40
TG(22:6_36:2)	TG(15:0/18:1(d7)/15:0)	948.7	603.4	40
TG(22:6_38:1)	TG(15:0/18:1(d7)/15:0)	978.7	633.4	40
TG(22:6_38:2)	TG(15:0/18:1(d7)/15:0)	976.7	631.4	40

Note: IS - Internal standard

90

Table S3: Lipidomics in negative mode acquisition parameters

Name	Internal Standard	Q1 m/z	Q3 m/z	CE (V)
(3-O-sulfo)GalCer(d18:1/16:0)	(3-O-sulfo)GalCer(d18:1/18:0(d3))	778.5	97	-150
(3-O-sulfo)GalCer(d18:1/18:0(2OH)	(3-O-sulfo)GalCer(d18:1/18:0(d3))	822.6	97	-150
(3-O-sulfo)GalCer(d18:1/18:0(d3))	IS	809.6	97	-150
(3-O-sulfo)GalCer(d18:1/18:0)	(3-O-sulfo)GalCer(d18:1/18:0(d3))	806.6	97	-150
(3-O-sulfo)GalCer(d18:1/24:0(2OH))	(3-O-sulfo)GalCer(d18:1/18:0(d3))	906.7	97	-150
(3-O-sulfo)GalCer(d18:1/24:0)	(3-O-sulfo)GalCer(d18:1/18:0(d3))	890.7	97	-150
(3-O-sulfo)GalCer(d18:1/24:1(2OH))	(3-O-sulfo)GalCer(d18:1/18:0(d3))	904.7	97	-150
(3-O-sulfo)GalCer(d18:1/24:1)	(3-O-sulfo)GalCer(d18:1/18:0(d3))	888.7	97	-150
Arachidonic acid	Arachidonic acid-d8	303.2	303.2	-10
Arachidonic acid_MRM	Arachidonic acid-d8_MRM	303.2	259.1	-19
Arachidonic acid-d8	IS	311.3	311.3	-10
Arachidonic acid-d8_MRM	IS	311.3	267.1	-19
BMP(14:0/14:0)	IS	665.3	227.2	-50
BMP(16:0_18:1)	BMP(14:0/14:0)	747.5	255.4	-50
BMP(16:0_20:4)	BMP(14:0/14:0)	769.5	255.4	-50
BMP(16:0_22:6)	BMP(14:0/14:0)	795.5	255.4	-50
BMP(16:1/16:1)	BMP(14:0/14:0)	717.5	253.1	-50
BMP(18:0_18:1)	BMP(14:0/14:0)	775.5	281.4	-50
BMP(18:0_20:4)	BMP(14:0/14:0)	797.5	283.4	-50
BMP(18:0_22:6)	BMP(14:0/14:0)	823.5	283.4	-50
BMP(18:1/18:1)	BMP(14:0/14:0)	773.5	281.3	-50

91

BMP(20:4/20:4)	BMP(14:0/14:0)	817.5	303.3	-50
BMP(22:6/22:6)	BMP(14:0/14:0)	865.5	327.3	-50
Cholesterol sulfate	(3-O-sulfo)GalCer(d18:1/18:0(d3))	465.3	96.7	-80
CL(14:0/14:0/14:0/14:0)	IS	619.5	227.2	-50
CL(72:6/18:2)	CL(14:0/14:0/14:0/14:0)	725.7	279.2	-50
CL(72:7/18:2)	CL(14:0/14:0/14:0/14:0)	724.7	279.2	-50
CL(72:8-2(OOH)/18:2)	CL(14:0/14:0/14:0/14:0)	755.7	279.2	-50
CL(72:8/18:2)	CL(14:0/14:0/14:0/14:0)	723.7	279.3	-50
CL(74:9/18:2)	CL(14:0/14:0/14:0/14:0)	736.7	279.2	-50
DHA	Arachidonic acid-d8_MRM	327.2	229.1	-19
EPA	Arachidonic acid-d8_MRM	301.3	257.1	-19
FAHFA(18:1/9-O-18:0)	PG(15:0/18:1(d7))	563.6	281	-50
GD1a/b(d36:1)	GM3(d18:1/18:0(d5))	917.5	290.1	-65
GD3(d34:1)	GM3(d18:1/18:0(d5))	720.9	290.1	-65
GD3(d36:1)	GM3(d18:1/18:0(d5))	734.9	290.1	-65
GM3(d18:1/18:0(d5))	IS	1184.8	290.1	-65
GM3(d34:1)	GM3(d18:1/18:0(d5))	1151.7	290.1	-65
GM3(d36:1)	GM3(d18:1/18:0(d5))	1179.8	290.1	-65
GQ1b(d36:1)	GM3(d18:1/18:0(d5))	1208.6	290.1	-65
Hemi-BMP(14:0/14:0)_14:0	IS	875.5	227.3	-50
Hemi-BMP(18:1/18:1)_16:0	Hemi-BMP(14:0/14:0)_14:0	1011.7	281.3	-50
Hemi-BMP(18:1/18:1)_18:0	Hemi-BMP(14:0/14:0)_14:0	1039.7	281.3	-50
Hemi-BMP(18:1/18:1)_18:1	Hemi-BMP(14:0/14:0)_14:0	1037.7	281.3	-50
Hemi-BMP(20:4/20:4)_16:0	Hemi-BMP(14:0/14:0)_14:0	1056.8	303.3	-50
Hemi-BMP(20:4/20:4)_18:0	Hemi-BMP(14:0/14:0)_14:0	1185.8	303.3	-50
Hemi-BMP(20:4/20:4)_18:1	Hemi-BMP(14:0/14:0)_14:0	1183.8	303.3	-50
Hemi-BMP(20:4/20:4)_20:4	Hemi-BMP(14:0/14:0)_14:0	1104.8	303.3	-50

92

Hemi-BMP(22:6/22:6)_16:0	Hemi-BMP(14:0/14:0)_14:0	1103.7	327.3	-50
Hemi-BMP(22:6/22:6)_18:0	Hemi-BMP(14:0/14:0)_14:0	1131.7	327.3	-50
Hemi-BMP(22:6/22:6)_18:1	Hemi-BMP(14:0/14:0)_14:0	1129.7	327.3	-50
Hemi-BMP(22:6/22:6)_22:6	Hemi-BMP(14:0/14:0)_14:0	1175.7	327.3	-50
Linoleic acid	Arachidonic acid-d8	279.2	279.2	-38
Linolenic acid	Arachidonic acid-d8	277.2	277.2	-10
LPE(16:0)	LPE(18:1(d7))	452.2	255.3	-50
LPE(18:0)	LPE(18:1(d7))	480.31	283.3	-50
LPE(18:1(d7))	IS	485.3	288.3	-50
LPG(16:0)	LPE(18:1(d7))	483.3	255.3	-50
LPG(18:0)	LPE(18:1(d7))	511.3	283.3	-50
LPG(18:1)	LPE(18:1(d7))	509.3	281.3	-50
LPG(20:4)	LPE(18:1(d7))	531.3	303.3	-50
LPG(22:6)	LPE(18:1(d7))	555.3	327.3	-50
LPI(16:0)	LPE(18:1(d7))	571.3	241.1	-50
LPI(18:0)	LPE(18:1(d7))	599.3	241.1	-50
Oleic acid	Arachidonic acid-d8	281.2	281.2	-10
PA(15:0/18:1(d7))	IS	666.52	241.3	-50
PA(16:0_18:1)	PA(15:0/18:1(d7))	673.5	255.3	-50
PA(18:0_18:1)	PA(15:0/18:1(d7))	701.5	283.3	-50
PA(18:0_20:4)	PA(15:0/18:1(d7))	723.5	283.3	-50
PA(18:0_22:6)	PA(15:0/18:1(d7))	747.5	283.3	-50
PA(18:1/18:1)	PA(15:0/18:1(d7))	699.5	281.3	-50
Palmitic acid	Arachidonic acid-d8	255.1	255.1	-10
Palmitoleic acid	Arachidonic acid-d8	253.1	253.1	-10
PE(15:0/18:1(d7))	IS	709.6	241.3	-50
PE(O-16:0/20:4)	PE(15:0/18:1(d7))	724.5	303.2	-50
PE(O-16:0/22:6)	PE(15:0/18:1(d7))	748.5	327.2	-50
PE(O-18:0/20:4)	PE(15:0/18:1(d7))	752.6	303.2	-50
PE(O-18:0/22:6)	PE(15:0/18:1(d7))	776.6	327.2	-50

PE(P-16:0/20:4)	PE(15:0/18:1(d7))	722.6	303.3	-50
PE(P-16:0/20:5)	PE(15:0/18:1(d7))	720.6	301.3	-50
PE(P-16:0/22:4)	PE(15:0/18:1(d7))	750.6	331.3	-50
PE(P-16:0/22:6)	PE(15:0/18:1(d7))	746.6	327.3	-50
PE(P-18:0/18:1)	PE(15:0/18:1(d7))	728.6	281.3	-50
PE(P-18:0/18:2)	PE(15:0/18:1(d7))	726.6	279.2	-50
PE(P-18:0/20:4)	PE(15:0/18:1(d7))	750.6	303.3	-50
PE(P-18:0/20:5)	PE(15:0/18:1(d7))	748.6	301.3	-50
PE(P-18:0/22:6)	PE(15:0/18:1(d7))	774.6	327.3	-50
PE(P-18:1/20:4)	PE(15:0/18:1(d7))	748.5	303.3	-50
PE(P-18:1/22:6)	PE(15:0/18:1(d7))	772.5	327.3	-50
PEth(16:0_18:1)	PE(15:0/18:1(d7))	772.5	255.1	-50
PEth(18:1/18:1)	PE(15:0/18:1(d7))	773.6	281.2	-50
PG(15:0/18:1(d7))	IS	740.55	241.3	-50
PG(16:0_18:1)	PG(15:0/18:1(d7))	747.5	255.3	-50
PG(16:0_20:4)	PG(15:0/18:1(d7))	769.5	255.3	-50
PG(16:0_22:6)	PG(15:0/18:1(d7))	795.5	255.3	-50
PG(18:0_18:1)	PG(15:0/18:1(d7))	775.5	281.3	-50
PG(18:0_20:4)	PG(15:0/18:1(d7))	797.5	283.3	-50
PG(18:0_22:6)	PG(15:0/18:1(d7))	823.5	283.3	-50
PG(18:1/18:1)	PG(15:0/18:1(d7))	773.4	281.4	-50
PI(15:0/18:1(d7))	IS	828.6	241.3	-50
PI(16:0_18:1)	PI(15:0/18:1(d7))	835.6	255.3	-50
PI(16:0_20:4)	PI(15:0/18:1(d7))	857.6	255.3	-50
PI(16:0_22:6)	PI(15:0/18:1(d7))	881.6	255.3	-50
PI(18:0_18:1)	PI(15:0/18:1(d7))	863.6	283.3	-50
PI(18:0_20:4)	PI(15:0/18:1(d7))	885.6	283.3	-50
PI(18:0_22:6)	PI(15:0/18:1(d7))	909.6	283.3	-50
PI(18:1/18:1)	PI(15:0/18:1(d7))	861.6	281.3	-50
PI(20:4/20:4)	PI(15:0/18:1(d7))	905.6	303.3	-50
PS(15:0/18:1(d7))	IS	753.55	241.3	-50
PS(16:0_18:1)	PS(15:0/18:1(d7))	760.6	255.3	-50

94

PS(16:0_20:4)	PS(15:0/18:1(d7))	782.6	255.3	-50
PS(16:0_22:6)	PS(15:0/18:1(d7))	806.6	255.3	-50
PS(18:0_18:1)	PS(15:0/18:1(d7))	788.6	283.3	-50
PS(18:0_20:4)	PS(15:0/18:1(d7))	810.6	283.3	-50
PS(18:0_22:6)	PS(15:0/18:1(d7))	834.6	283.3	-50
PS(18:1/18:1)	PS(15:0/18:1(d7))	786.6	281.3	-50
PS(22:6/22:6)	PS(15:0/18:1(d7))	878.5	327.3	-50
Stearic acid	Arachidonic acid-d8	283.2	283.2	-10

Note: IS - Internal standard

Table S4: Glucosylsphingolipid in positive mode acquisition parameters

Name	Internal Standard	Q1 m/z	Q3 m/z	CE (V)
alpha-GalCer(d18:1/16:0)	GalCer(d18:1/15:0)	700.6	264.3	32
alpha-GalCer(d18:1/18:0)	GalCer(d18:1/15:0)	728.6	264.3	32
alpha-GalCer(d18:1/20:0)	GalCer(d18:1/15:0)	756.6	264.3	32
alpha-GalCer(d18:1/22:0)	GalCer(d18:1/15:0)	784.7	264.3	32
alpha-GalCer(d18:1/22:1)	GalCer(d18:1/15:0)	782.7	264.3	32
alpha-GalCer(d18:1/24:0)	GalCer(d18:1/15:0)	812.7	264.3	32
alpha-GalCer(d18:1/24:1)	GalCer(d18:1/15:0)	810.7	264.3	32
alpha-GalCer(d18:2/18:0)	GalCer(d18:1/15:0)	726.6	262.3	32
alpha-GalCer(d18:2/20:0)	GalCer(d18:1/15:0)	754.6	262.3	32
alpha-GalCer(d18:2/22:0)	GalCer(d18:1/15:0)	782.7	262.3	32
Cholesteryl galactoside	GlcCer(d18:1(d5)/18:0)	566.6	369.3	13
Cholesteryl glucoside	GlcCer(d18:1(d5)/18:0)	566.6	369.3	13
Galactosylsphingosine	Glucosylsphingosine(d5)	462.2	282.3	18
GalCer(d18:1/15:0)	IS	686.3	264.3	32
GalCer(d18:1/16:0)	GalCer(d18:1/15:0)	700.6	264.3	32
GalCer(d18:1/18:0)	GalCer(d18:1/15:0)	728.6	264.3	32
GalCer(d18:1/20:0)	GalCer(d18:1/15:0)	756.6	264.3	32
GalCer(d18:1/22:0)	GalCer(d18:1/15:0)	784.7	264.3	32
GalCer(d18:1/22:1)	GalCer(d18:1/15:0)	782.7	264.3	32
GalCer(d18:1/24:0)	GalCer(d18:1/15:0)	812.7	264.3	32
GalCer(d18:1/24:1)	GalCer(d18:1/15:0)	810.7	264.3	32
GalCer(d18:2/18:0)	GalCer(d18:1/15:0)	726.6	262.3	32
GalCer(d18:2/20:0)	GalCer(d18:1/15:0)	754.6	262.3	32
GalCer(d18:2/22:0)	GalCer(d18:1/15:0)	782.7	262.3	32
GlcCer(d18:1(d5)/18:0)	IS	733.6	269.3	32
GlcCer(d18:1/16:0(d3))	IS	703.6	264.3	32
GlcCer(d18:1/16:0)	GlcCer(d18:1/16:0(d3))	700.6	264.3	32
GlcCer(d18:1/18:0)	GlcCer(d18:1(d5)/18:0)	728.6	264.3	32
GlcCer(d18:1/20:0)	GlcCer(d18:1(d5)/18:0)	756.6	264.3	32

96

GlcCer(d18:1/22:0)	GlcCer(d18:1(d5)/18:0)	784.7	264.3	32
GlcCer(d18:1/22:1)	GlcCer(d18:1(d5)/18:0)	782.7	264.3	32
GlcCer(d18:1/24:0)	GlcCer(d18:1(d5)/18:0)	812.7	264.3	32
GlcCer(d18:1/24:1)	GlcCer(d18:1(d5)/18:0)	810.7	264.3	32
GlcCer(d18:2/18:0)	GlcCer(d18:1(d5)/18:0)	726.6	262.3	32
GlcCer(d18:2/20:0)	GlcCer(d18:1(d5)/18:0)	754.6	262.3	32
GlcCer(d18:2/22:0)	GlcCer(d18:1(d5)/18:0)	782.7	262.3	32
Glucosylsphingosine	Glucosylsphingosine(d5)	462.2	282.3	18
Glucosylsphingosine(d5)	IS	467.2	287.3	18
Sitosteryl galactoside	GlcCer(d18:1(d5)/18:0)	594.6	397.4	13
Sitosteryl glucoside	GlcCer(d18:1(d5)/18:0)	594.6	397.4	13

Note: IS - Internal standard

98

3.2. ENHANCED LEGUMAIN ACTIVITY LINKS PROGRANULIN DEFICIENCY TO TDP-43 PATHOLOGY IN FRONTOTEMPORAL LOBAR DEGENERATION

Research article 2:

(Robinson, Reich, Mühlhofer *et al.*) "Enhanced legumain activity links progranulin deficiency to TDP-43 pathology in frontotemporal lobar degeneration" – in revision at Nature Neuroscience

Access to preprint:

https://www.biorxiv.org/content/10.1101/2024.01.16.575687v1

Authors:

Sophie Robinson*, Marvin Reich*, Maria-Teresa Mühlhofer*, Katrin Buschmann, Eline Wauters, Quirin Mühlhofer, Georg Werner, Andrea Ahles, Stefan Engelhardt, Claudia Krenner, Björn Bartels, Simon Gutbier, Anika Reifschneider, Henrick Riemenschneider, Thomas Reinheckel, Dieter Edbauer, Matthew J. Simon, Mihalis S. Kariolis, Todd Logan, Gilbert Di Paolo, Christine Van Broeckhoven, Markus Damme, Dominik Paquet, Christian Haass[#], Anja Capell[#]

The author of this thesis is one of the first authors of this manuscript.

Author contributions:

Conceptualization: AC, CH

Methodology: AC, MR, MTM, SR, KB, EW, QM, GW, AA, CK, BB, SG, AR, HR, MJS

Investigation: AC, MR, MTM, SR, KB, EW, QM, GW, AA, CK, BB, SG, AR, HR, MJS

Visualization: AC, MR, MTM, SR

Funding acquisition: AC, CH, DP

Project administration: AC, CH, SE, BB, SG, TR, DE, MJS, MSK, TL, GDP, CVB, MD, DP

Supervision: AC, CH, SE, BB, SG, TR, DE, MJS, MSK, TL, GDP, CVB, MD, DP

Writing – original draft: AC, CH, MR, MTM, SR

My author contributions in detail:

For this study, I performed and analyzed the overexpression of legumain in HeLa cells. This includes the transfection of HeLa cells, as well as the analysis by western blot and activity assays. I also performed and analyzed the media transfer experiments from HeLa overexpressing legumain to primary neurons. This includes the isolation and culturing of primary hippocampal mouse neurons, as well as their treatments with HeLa supernatants after legumain transfection, followed by analysis by western blot, activity assays and immunofluorescence. I further initiated and coordinated the collaboration with Roche, where we obtained a selective legumain inhibitor. With this inhibitor, I performed a

treatment study in hiPSC-derived microglia/neuron co-cultures, analyzing the effect of treatment on TDP-43 pathology and legumain activity by western blot and activity assays. For the overexpression of human legumain in *Grn* KO mice, I performed *i.v.* tail vein injections of the AAV. Additionally, I analyzed the PTV:PGRN-treated mouse brain samples that were generated at Denali by western blot and activity assay. For all these experiments except the legumain-AAV study, I also performed the data analysis, interpretation and visualization. I wrote parts of the initial draft of the manuscript together with AC, MTM, SR and CH and incorporated suggestions from other authors with AC and MTM.

Enhanced legumain activity links progranulin deficiency to TDP-43 pathology in frontotemporal lobar degeneration

Sophie Robinson[1,2,3#], Marvin Reich[2,3,4#], Maria-Teresa Mühlhofer[3,4#], Katrin Buschmann[1], Eline Wauters[5,6], Quirin Mühlhofer[1], Georg Werner[1], Andrea Ahles[7], Stefan Engelhardt[7], Claudia Krenner[1], Björn Bartels[8], Simon Gutbier[8], Anika Reifschneider[1], Henrick Riemenschneider[4], Thomas Reinheckel[9], Dieter Edbauer[4,10], Matthew J. Simon[11], Mihalis S. Kariolis[11], Todd Logan[11], Gilbert Di Paolo[11], Christine Van Broeckhoven[5,6], Markus Damme[12], Dominik Paquet[2,10], Christian Haass[1,4,10+], Anja Capell[1,4+]

[1]Biomedical Center (BMC), Division of Metabolic Biochemistry Faculty of Medicine, Ludwig-Maximilians-Universität München, 81377 Munich, Germany

[2]Institute for Stroke and Dementia Research (ISD), University Hospital, Ludwig-Maximilians-Universität München, Munich, Germany.

[3]Graduate School of Systemic Neurosciences (GSN), Ludwig-Maximilians-Universität München, Munich, Germany.

[4]German Center for Neurodegenerative Diseases (DZNE), Munich, Germany

[5]Neurodegenerative Brain Diseases Group, Center for Molecular Neurology, VIB, Antwerp, Belgium.

[6]Department of Biomedical Sciences, University of Antwerp, Antwerp, Belgium.

[7]Institute of Pharmacology and Toxicology, Technical University of Munich, Munich, Germany.

[8]Roche Pharma Research and Early Development, Therapeutic Modalities, Roche Innovation Center Basel, F. Hoffmann-La Roche Ltd, Basel, Switzerland.

[9]Institute of Molecular Medicine and Cell Research, University of Freiburg, Freiburg, Germany

[10]Munich Cluster for Systems Neurology (SyNergy), Munich, Germany.

[11]Denali Therapeutics Inc., South San Francisco, USA

[12]Institute of Biochemistry, Kiel University, Kiel, Germany.

[#]Contributed equally

[+]Correspondence:

anja.capell@mail03.med.uni-muenchen.de

christian.haass@mail03.med.uni-muenchen.de

Key words: AEP, Frontotemporal dementia, LGMN, lysosomes, microglia, neurodegeneration, progranulin, TDP-43.

Loss-of-function mutations in *GRN* are a major cause of frontotemporal lobar degeneration (FTLD) with TDP-43-positive inclusions. Progranulin (PGRN) loss leads to lysosomal dysfunction, microglial hyperactivation, and TDP-43 deposition, yet the underlying pathomechanism remains unknown. We demonstrate that PGRN slows the maturation and limits the proteolytic activity of the lysosomal protease legumain (LGMN). Accordingly, LGMN activity is strongly elevated in *Grn* knockout (ko) mice, in human induced pluripotent stem cell-derived *GRN* ko microglia, and in FTLD-*GRN* patients' brain. Secreted microglial LGMN is internalized by neurons, where it mediates pathological processing of TDP-43, which is prevented by selective LGMN inhibition. In contrast, AAV-mediated overexpression of LGMN in mouse brains promotes TDP-43 processing, the aggregation of phosphorylated TDP-43 and increases plasma neurofilament light chain (NfL), a marker for neuronal loss. Our findings identify LGMN as a link between PGRN haploinsufficiency and TDP-43 pathology in FTLD-*GRN* and suggest LGMN as a therapeutic target.

Main

Frontotemporal lobar degeneration (FTLD) is a non-curable, rare, early-onset neurodegenerative disorder[1]. Up to 50% of FTLD patients develop TAR DNA binding protein 43 (TDP-43) pathology, which is characterized by aberrant TDP-43 processing, cytosolic deposition, abnormal phosphorylation and nuclear clearance[2,3]. Heterozygous loss-of-function (LOF) mutations in the *GRN* gene are a major cause of FTLD (FTLD-*GRN*) with TDP-43 pathology[4,5], whereas homozygous LOF mutations result in neuronal ceroid lipofuscinosis (NCL)[6,7], a lysosomal storage disorder. In the brain, progranulin (PGRN), a secreted growth factor-like protein, is critical for neuronal survival[8] and diminishes inflammatory processes and hyperactivation of microglia upon CNS damage[9]. As a result, loss of PGRN in mice leads to inflammation and the transition of microglia to a disease associated microglia (DAM) population[10-12]. Microglial dysregulation upon PGRN loss may be associated with its function within lysosomes[13]. NCL cases caused by loss of PGRN and PGRN-deficient mouse models

102   2

exhibit multiple endo-lysosomal and autophagic phenotypes, such as dysregulation of lysosomal proteases and pH[14-20], lipid dyshomeostasis, and lipofuscin accumulation[13,16,21-25]. PGRN is either secreted or transported to lysosomes *via* multiple pathways, including sortilin and prosaposin/cation-independent mannose-6-phosphate receptor[26]. Upon increased acidification of the endo-lysosomal pathway, PGRN is proteolytically processed into granulin peptides by the lysosomal protease legumain (LGMN), also known as asparagine endopeptidase (AEP), and probably by various cathepsins, including cathepsin B and L[27-29]. An essential role of granulins in lysosomes is suggested, since lysosomal dysfunction caused by PGRN deficiency is ameliorated by granulin peptides[30]. Despite intense research, both the lysosomal function of PGRN / granulins and the mechanistic link between PGRN deficiency and TDP-43 aggregation remain unclear. A spatial paradox, namely PGRN expression primarily in microglia and TDP-43 pathology in neurons, makes the understanding of the link between PGRN loss and TDP-43 pathology even more challenging.

We have previously shown that loss of PGRN causes lysosomal dysfunction with altered cathepsin maturation[18]. To establish a functional link between PGRN deficiency and TDP-43 pathology, we hypothesize that lysosomal dysfunction contributes to disease-associated proteolytic TDP-43 processing. We therefore searched for a protease which plays a key role in processing of TDP-43 and lysosomal cathepsins. LGMN, a caspase-like cysteine protease of the C13 peptidase family emerged as a prime candidate[31], since it is involved in the proteolytic turnover of various cathepsins[32,33] and capable of cleaving TDP-43 *in vitro*[34]. Here, we provide a mechanistic link between PGRN deficiency and TDP-43 pathology *via* dysregulation of LGMN.

Results

PGRN deficiency results in elevated LGMN maturation and activity

To test our hypothesis, we investigated LGMN expression and activity in various model systems and in brain material from FTLD-*GRN* patients. Mature LGMN and its proteolytic activity were strongly elevated in *Grn* ko MEF compared to wt MEF (Fig. 1a,b). In line with that, knockdown of LGMN blunts the previously described increased maturation and accumulation of the heavy chain of cathepsins D and L in the *Grn* ko MEF (Extended Data Fig. 1a–c)[18]. *LGMN* ko mice further proved that LGMN is required for the generation of the heavy chain form of cathepsin L[35] and cathepsin D in mice

103

(Extended Data Fig. 1d). Moreover, elevated levels of mature LGMN were detected in the brain tissue of 6-month-old *Grn* ko mice (Fig. 1c) and increased proteolytic activity of LGMN was observed in all ages investigated between 3 and 24 months (Fig. 1d), indicating that LGMN dysfunction might be a driver of the disease and not a response. Increased LGMN expression and activity were not a result of transcriptional changes (Fig. 1e), suggesting posttranscriptional regulatory mechanisms. To test whether the increase in LGMN maturation and activity is directly caused by the loss of PGRN, we reintroduced PGRN in *Grn* ko MEF and *Grn* ko mice (Extended Data Fig. 2a-e). Restoration of PGRN in *Grn* ko MEF by stable transfection reduced mature LGMN and completely normalized LGMN hyperactivity (Extended Data Fig. 2a-b). To reintroduce PGRN *in vivo*, we used the previously described protein transport vehicle (PTV):PGRN, which shows enhanced brain penetrance due to its ability to bind to the transferrin receptor (TfR), to restore brain PGRN levels in *Grn* ko mice expressing chimeric humanized TfR (*Grn* ko; *TfR* ki) (Extended Data Fig. 2c)[16]. PTV:PGRN reduced maturation and activity of LGMN over time (Extended Data Fig. 2d-e). Thus, PGRN appears to directly affect LGMN maturation and consequently its proteolytic activity.

In the brain, PGRN is predominantly expressed by microglia[11,18]. In contrast, pathological TDP-43 inclusions observed in FTLD or amyotrophic lateral sclerosis (ALS) are mainly localized in neurons and are less abundant in glial cells[2,3]. Thus, we next investigated cell type-specific expression of LGMN. LGMN and PGRN were both strongly enriched in acutely isolated microglia (Fig. 1f; Extended Data Fig. 3). Moreover, microglia showed efficient LGMN maturation as well as the highest LGMN activity of all cell types investigated (Fig. 1f-g; Extended Data Fig. 3). Even though LGMN expression in neurons and astrocytes was much lower than in microglia, the relative change in LGMN activity between PGRN deficient and wt cells was highest in neurons with a 3-fold increase in *Grn* ko (Fig. 1g). In contrast to the LGMN activity, *Lgmn* mRNA levels were not increased in acutely isolated microglia (Fig. 1h), supporting the conclusion that LGMN is regulated at a posttranscriptional level. In addition, in primary cultures of *Grn* ko microglia LGMN activity was twice as high as in wt controls, mirroring the results obtained from the acutely isolated microglia (Fig. 1i). To investigate whether elevated LGMN levels are disease relevant, we assessed LGMN maturation and activity in the frontal cortex (Brodmann area 9 and 10) of patients suffering from FTLD-*GRN* (Extended Data Table 1). In line with our findings

104   4

in the model systems described above, we observed increased levels, maturation and proteolytic activity of LGMN in patient brains relative to age matched non-diseased controls (Fig. 1j,k).

Fig. 1: PGRN deficiency leads to enhanced LGMN maturation and elevated activity.
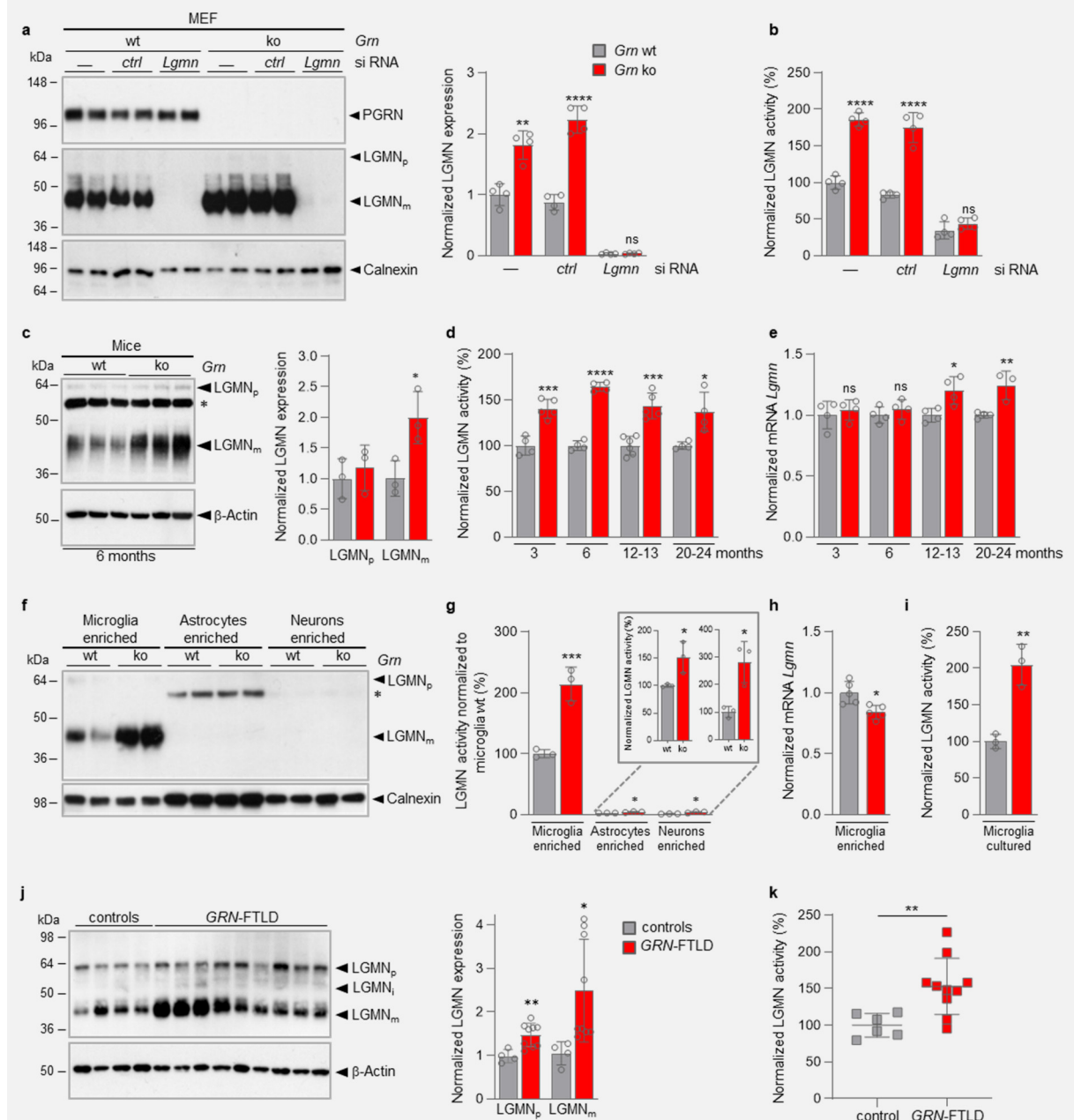
a, Representative immunoblots of mouse embryonic fibroblasts (MEF), isolated from wild-type (wt) and granulin knockout (*Grn* ko) mice, probed for progranulin (PGRN), legumain (LGMN), and calnexin as loading control. MEF are either non- (-), control- (*ctrl*) or *Lgmn* siRNA-transfected. Quantification of LGMN expression normalized to non-transfected wt levels (n=4). **b**, *In vitro* LGMN activity of non- (-), mock, *ctrl* and *Lgmn* siRNA-transfected *Grn* ko MEF

105

normalized to non-transfected wt MEF (n=4). **c**, Representative immunoblot for LGMN in total brain homogenates of 6-month-old wt and *Grn* ko mice. Proform (LGMN$_p$), mature form (LGMN$_m$), and non-specific band (*) are indicated, β-actin verified equal loading. Quantification of the immunoblot signals normalized to wt (n=3 mice per genotype). **d**, *In vitro* LGMN activity of brain homogenates from 3-, 6-, 12-13-, and 20-24-month-old wt and *Grn* ko mice (n=4-6 per genotype and age group). **e**, Total brain mRNA of 3-, 6-, 12-13-, and 20-24-month-old mice normalized to wt (n=4-5). **f**, Representative immunoblot for LGMN in MACS-sorted microglia-, astrocyte- and neuron-enriched brain cell fractions of 4-5-month-old wt and *Grn* ko mice. LGMN$_p$ and LGMN$_m$ are indicated, calnexin verified equal loading for each fraction. **g**, Microglia-, astrocyte- and neuron-enriched fractions from 4-5-month-old *Grn* ko and wt mice analyzed for LGMN activity either normalized to wt microglia or wt of the respective cell type (insert) (n=3 mice per cell type and genotype). **h**, *Lgmn* mRNA levels of microglia isolated from 6-month-old wt and *Grn* ko mice normalized to wt (n=5). **i,** LGMN *in vitro* activity in lysates of cultured primary mouse microglia (n=3 mice per genotype). **j**, **k**, LGMN expression (**j**) and activity (**k**) analyzed in brain lysates of frontal cortex from FTLD/*GRN* patients and pathology-negative control cases (see Extended Data Table 1). LGMN$_p$ and LGMN$_m$ are quantified in the immunoblot and normalized to the mean signal of control cases (**j**).

Data are mean ± s.d. of biologically independent experiments; unpaired two-tailed t-test: ns not significant; *P<0.05, **P<0.01, ***P<0.001, ****P<0.0001. *P* values and statistical source data are provided.

PGRN slows LGMN auto-activation

Next, we investigated whether PGRN directly affects LGMN catalytic activity or interferes with its proteolytic activation. With decreasing pH during lysosome maturation, LGMN is autoproteolytically activated in multiple steps and processed to its final mature form of approximately 43 kDa by unknown proteases (Fig. 2a)[36]. Autocatalytic *in vitro* maturation of the pro-form of LGMN (pro-LGMN) to an intermediate active form has been previously shown to be facilitated at an acidic pH[31]. To investigate whether PGRN directly affects LGMN activity, we measured the *in vitro* activity of autocatalytically pre-activated recombinant (r) LGMN in the presence and absence of rPGRN. PGRN did not affect the catalytic activity of rLGMN (Fig. 2b). Based on the increased LGMN maturation in various PGRN deficient model systems (Fig. 1), we next investigated whether the presence of rPGRN affects maturation of rLGMN.

Fig. 2: PGRN modulates LGMN activation and is proteolytically processed by LGMN.
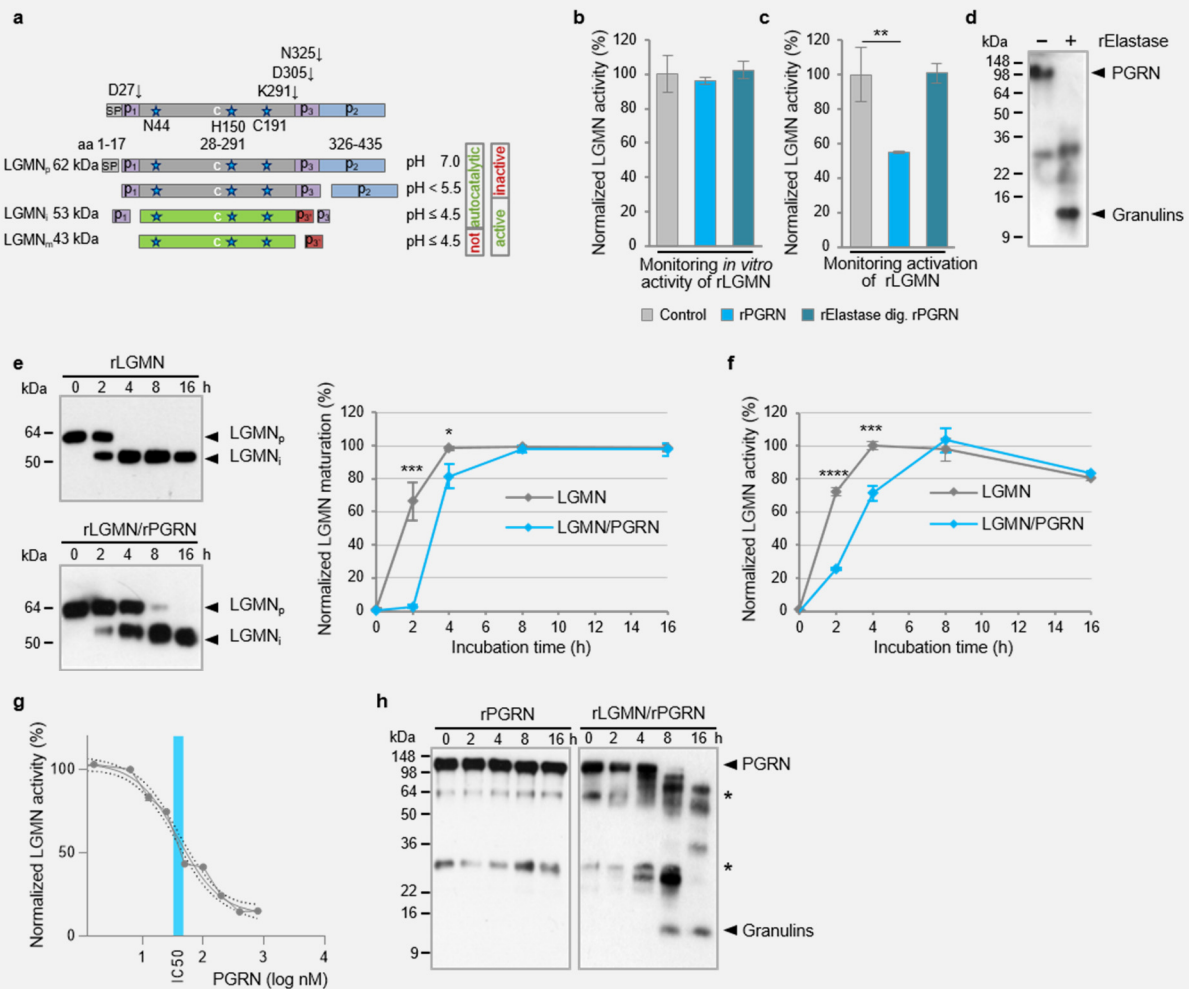
a, Schematic representation of pH-dependent auto- and not auto-catalytic LGMN maturation. N- and C-terminal pro-peptides (p1-p3) and the mature chain (c) with the active site residues (blue stars) are specified. Proform (LGMN$_p$), intermediate-form (LGMN$_i$) and mature-form (LGMN$_m$) are indicated. **b**, **c**, Activity analysis of *in vitro* auto-catalytically matured recombinant (r) LGMN incubated for 4 h at acidic pH. Either rPGRN or elastase-digested PGRN were added after (**b**) or before the 4 h activation step (**c**) (n=3). **d**, PGRN digest with elastase controlled by immunoblotting. **e**, **f**, Activation of rLGMN with/without rPGRN at acidic pH for indicated time points, monitored by immunoblotting. Quantification of the relative LGMN$_i$ level (% of total LGMN) (**e**) or activity (**f**) for each timepoint (n=3). **g**, LGMN activity after 2 h incubation with different concentrations of rPGRN at pH 4. The IC$_{50}$ was calculated using a non-linear curve fit, 95% confidence intervals (CI) are indicated (n=3). **h**, Immunoblot analysis of rPGRN turnover and granulin peptide generation by rLGMN. Stars indicate rLGMN independent bands. Data are mean ± s.d. of independent technical replicates, unpaired two-tailed t-test: ns,

107

not significant; *$P<0.05$, **$P<0.01$, ***$P<0.001$, ****$P<0.0001$. P values and statistical source data are provided.

Strikingly, rLGMN activity was reduced by more than 50 % when rPGRN was added to pro-rLGMN during the activation step at acidic pH 4 (Fig. 2c), while elastase-digested rPGRN did not reduce rLGMN activation (Fig. 2c,d), suggesting that rPGRN, but not granulins, regulate the maturation of rLGMN. Autocatalytic maturation of pro-rLGMN was then monitored longitudinally at pH 4.0 with and without rPGRN. Proteolytic *in vitro* maturation and enzymatic activation of rLGMN under acidic conditions was significantly slowed in the presence of rPGRN (Fig. 2e,f). Moreover, rPGRN reduced autocatalytic activation of rLGMN in a dose-dependent manner with an IC_{50} of 39.28 nM (Fig. 2g). However, after full autocatalytic maturation (Fig. 2e), the catalytic activity of rLGMN was identical in the presence and absence of rPGRN (Fig. 2f). Thus, PGRN does not affect the catalytic activity of LGMN *per se*, but rather slows its autocatalytic maturation. Intriguingly, as suggested before[29], rLGMN efficiently generates granulin peptides *in vitro* (Fig. 2h). After 8 h of co-incubation of rPGRN with rLGMN, full length rPGRN was completely converted into single or multiple granulin peptides. At this time point also full conversion of rLGMN to the intermediate form was observed (Fig. 2e), further indicating that full length PGRN is needed to slow LGMN activation and that LGMN regulates its own maturation by processing of PGRN in a negative feedback loop. *In vivo*, the interaction of LGMN with PGRN is supported by reduced generation of granulins in *Lgmn* ko mice. Granulin peptides are readily detected within purified liver lysosomes of wt mice, but are substantially reduced in *Lgmn* ko mice (Extended Data Fig. 4a,b). Thus, LGMN regulates its own maturation by processing of PGRN in a negative feedback loop.

Increased LGMN activity promotes pathological processing of TDP-43

Since TDP-43 is known to undergo pathological proteolytic processing[2,37,38] and contains several potential cleavage sites for LGMN[34] (Fig. 3a), we investigated if the lack of PGRN affects processing of TDP-43 *via* enhanced LGMN activity. In *Grn* ko MEF we observed a reduction of full-length TDP-43 accompanied by the enhanced formation of TDP-43 fragments (TDP-43F) which were enriched in the urea solubilized fraction (Fig. 3b). Furthermore, C-terminal fragments of TDP-43 (TDP-43CTF) with an approximate molecular weight of 25 kDa, reminiscent of those observed in FTLD cases[34], were observed in lysates of *Grn* ko MEF (Fig. 3b,c). Abnormal proteolytic

108   8

processing of TDP-43 was completely blocked upon knockdown of LGMN in *Grn* ko MEF (Fig. 3b,c), proving that disease-defining TDP-43 fragments are generated in a LGMN-dependent manner. Moreover, even in the presence of PGRN, reduction of LGMN was sufficient to reduce TDP-43 processing (Fig. 3b). Immunofluorescence staining of TDP-43 revealed significant cytoplasmic mis-localization of TDP-43 in *Grn* ko MEF (Fig. 3d, upper panels). MEF *Grn* ko show enhanced co-localization of TDP-43 with LGMN- and LAMP1-positive compartments, indicating that TDP-43 processing by LGMN occurs in the lysosome (Fig. 3d, lower panels).

Taken together, our findings suggest that reduced PGRN results in enhanced LGMN activation, which in turn mediates pathological processing and mis-localization of TDP-43.

Fig. 3: Enhanced LGMN activity results in accelerated TDP-43 processing.
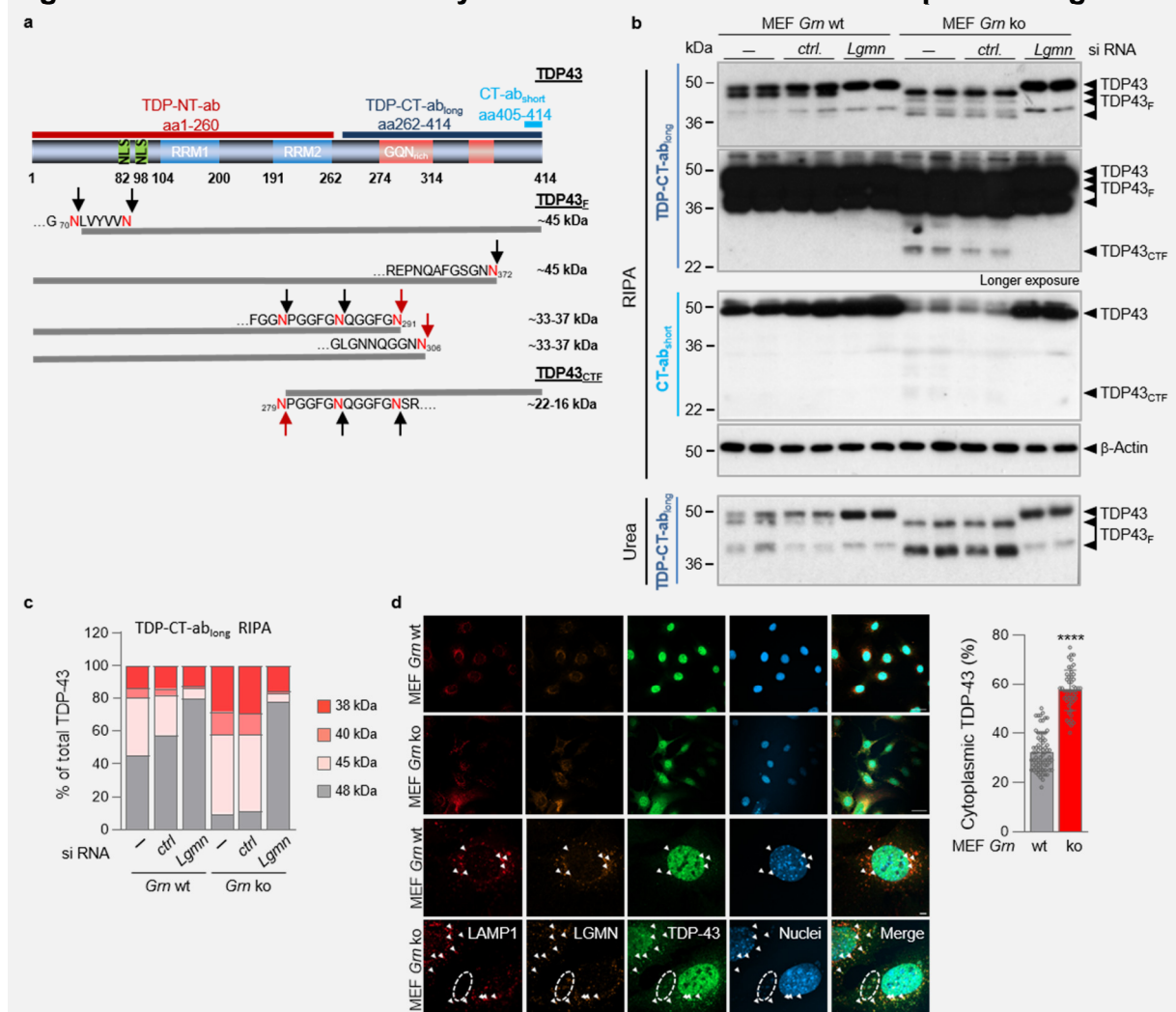
a, Schematic representation of the TDP-43 protein indicates the nuclear localization sequence (NLS, green), the RNA-recognition motifs (RRM1 / 2, blue), and the G-, Q-, N-rich hnRNP-interacting domains (red). Epitopes of different N-terminal (NT) and C-terminal (CT) antibodies

are indicated. Confirmed LGMN cleavage sites (black arrows) and putative fragments are indicated below. Red arrows indicate LGMN cleaved fragments identified in patient material (Herskowitz *et al*, 2012; Kametani *et al*, 2016). **b**, Immunoblot analysis of TDP-43, TDP-43 fragments (TDP43$_F$) and C-terminal fragments (TDP43$_{CTF}$) in MEF *Grn* wt and ko with and without *Lgmn* siRNA-mediated knockdown. **c**, Quantification of TDP-43 processing; holoprotein (48 kDa) and fragments (45 kDa, 40 kDa and 38 kDa) were normalized to total TDP-43 (n=4). **d**, Immunofluorescence staining of the lysosomal protein LAMP1 (deep red), LGMN (orange), TDP-43 (green) and nuclear DAPI staining (blue) of *Grn* wt and ko MEF (top panels scale-bar 10 μm, lower panels 20 μm). Arrowheads indicate co-localization of LAMP1, LGMN and TDP-43, encircled is a cytoplasmic DAPI, LGMN and TDP-43 positive area. Quantification of % cytoplasmic vs. total TDP-43. Data are mean ± s.d. (n=48-69 cells / genotype from 6-8 images), unpaired two-tailed t-test, ****$P<0.0001$. P values and statistical source data are provided

Shuttling of LGMN from microglia to neurons

TDP-43 deposits are predominantly found in neurons, however compared to microglia, neurons express substantially less PGRN and LGMN and therefore show much less LGMN activity (Fig. 1f,g, Extended Data Fig. 3). Since pro-LGMN was found to be secreted in peripheral immune cells[36], we hypothesized that PGRN-deficient hyperactivated microglia also release pro-LGMN, which could be internalized by neurons, where it then mediates pathological TDP-43 processing. To provide evidence that catalytically inactive pro-LGMN can be taken up and activated by neurons, we incubated primary mouse hippocampal neurons with conditioned media from wt, inactive mutant (mt) LGMN-, or mock-transfected HeLa cells (Fig. 4a). Robust levels of overexpressed wt and mt LGMN were detected in HeLa cells. Autocatalytic processing occurred in wt, but was altered in mt LGMN expressing cells, suggesting bimolecular processing by endogenous LGMN or alternative processing (Fig. 4b)[39,40]. Upon transfection, conditioned media contained significant amounts of secreted wt or mt pro-LGMN (Fig. 4c). Only secreted wt LGMN was autocatalytically activated upon incubation under acidic conditions while no activity was observed in conditioned media of mt LGMN or non-transfected HeLa cells (Fig. 4d). Both, wt and mt LGMN were internalized and either autocatalytically or alternatively processed in primary neurons (Fig. 4e). Noticeably, processed mt LGMN accumulated in lysates (Fig. 4e). Only neurons incubated with wt LGMN-containing conditioned media show increased LGMN activity (Fig. 4f). Strikingly, we observed enhanced TDP-43 processing relative

110   10

to total TDP-43 levels and even the formation of pathological TDP-43$_{CTF}$ upon uptake of wt LGMN, but not of the catalytically inactive variant (Fig. 4g). This demonstrates that proteolytically active LGMN is sufficient to generate disease-relevant TDP-43 fragments and that neurons can internalize and activate LGMN.

Fig. 4: LGMN internalized by neurons results in accelerated TDP-43 processing.
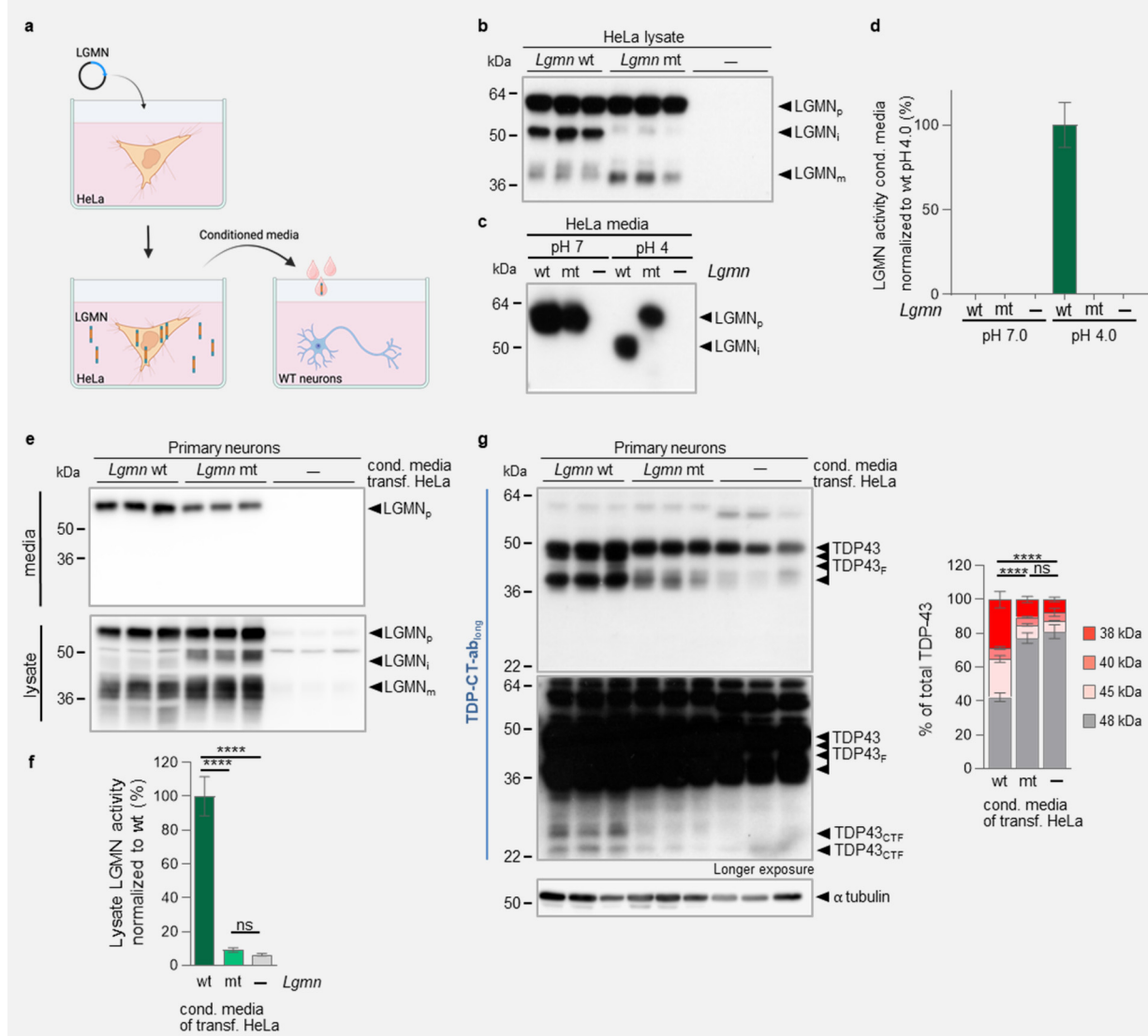
a, Schematic representation of the media transfer experiment. HeLa cells were transfected with wt mouse LGMN, the proteolytically inactive LGMN C191A variant (mt) or mock (-) and 25% conditioned media supplemented to primary hippocampal mouse neurons for 24 h. (**b,c**), LGMN expression (LGMN$_p$, LGMN$_i$, and LGMN$_m$) (**b**) and secretion of LGMN$_p$ (**c**) by HeLa cells was verified by immunoblotting (n=3 independent experiments). (**c,d**) To monitor autocatalytic processing of LGMN, conditioned media was incubated at pH 7 or pH 4 for 4 h. **d**, LGMN activity of conditioned media incubated at pH 7 and pH 4 (n=3 independent experiments). (**e-g**), Primary neurons were analyzed after 24 h incubation with conditioned media. Presence of the LGMN proform was confirmed in culture media (**e**). LGMN uptake by neurons (**e**) and TDP-

43 processing (**g**) in neuron lysates was detected by immunoblot and activity assay (**f**) (n=3 independent experiments). TDP-43 processing was quantified as percentage of holoprotein or fragment of total TDP-43 level for each treatment condition (n=3 independent experiments). Statistical significance for the activity assay (**f**) and TDP-43 processing (**g**) was determined by one-way ANOVA and Tukey's post-hoc test: ****P<0.0001. P values and statistical source data are provided.

To provide evidence for a pathological link between PGRN reduction, LGMN activation, and enhanced TDP-43 processing in a human disease-relevant system, we generated human iPSC lacking PGRN (*GRN* ko iPSC)[22] and differentiated them into human induced pluripotent stem cell-derived microglia (hiMGL) and neurons (hiNE). *GRN* ko hiMGL showed a 3-4-fold increased expression and activity of LGMN compared to wt hiMGL (Fig. 5a,b) but only a 1.5-fold increase of *LGMN* mRNA levels (Fig. 5c). Thus, the difference in LGMN mRNA levels between wt and *GRN* ko hiMGL was less pronounced than on LGMN protein or activity levels, further supporting a post-transcriptional regulation of LGMN activity upon PGRN deficiency. In line with our findings in mice (Fig. 1f,g), hiNE had almost no LGMN protein expression or activity (Fig. 5a,b) and showed lower transcript levels than hiMGL (Fig. 5c). Furthermore, *GRN* ko hiNE did not show an increase of LGMN activity in contrast to *Grn* ko mouse neurons (Fig. 1g). To investigate a potential cross-talk between microglia and neurons upon PGRN deficiency, we co-cultured *GRN* wt hiNE with either *GRN* wt or ko hiMGL (Fig. 5d). In co-cultures of wt hiNE with GRN ko hiMGL, we observed increased mature and active LGMN in lysates (Fig. 5f,g). As a consequence, co-culture of *GRN* ko hiMGL with *GRN* wt hiNE showed enhanced TDP-43 processing, indicated by reduced TDP-43 full length and enhanced TDP-43 fragments (Fig. 5h). To investigate if TDP-43 processing in the co-culture occurs predominantly within neurons, we selectively blocked neuronal LGMN activity by AAV9 (AAV-hSyn-Cst7) mediated neuronal expression of cystatin F (CSTF) prior to co-culturing with hiMGL (Fig. 5d). CSTF and CSTC are brain expressed[41,42] effective inhibitors of LGMN (Extended Data Fig. 5a-c) and other cysteine-proteases[43]. Since CTSF showed stronger inhibitory effects in cell culture, we decided to use AAV-hSyn-Cst7. Immunofluorescence confirmed neuronal CTSF expression (Fig. 5e), which resulted in reduced LGMN maturation and strongly reduced activity (Fig. 5f,g). Furthermore, as a consequence of the inhibition of LGMN activity, TDP-43 processing was also reduced to levels seen in wt co-culture (Fig. 5h).

112   12

Fig. 5: Elevated LGMN maturation and activity in human induced pluripotent stem cells (hiPSC)-derived microglia results in enhanced TDP-43 processing.
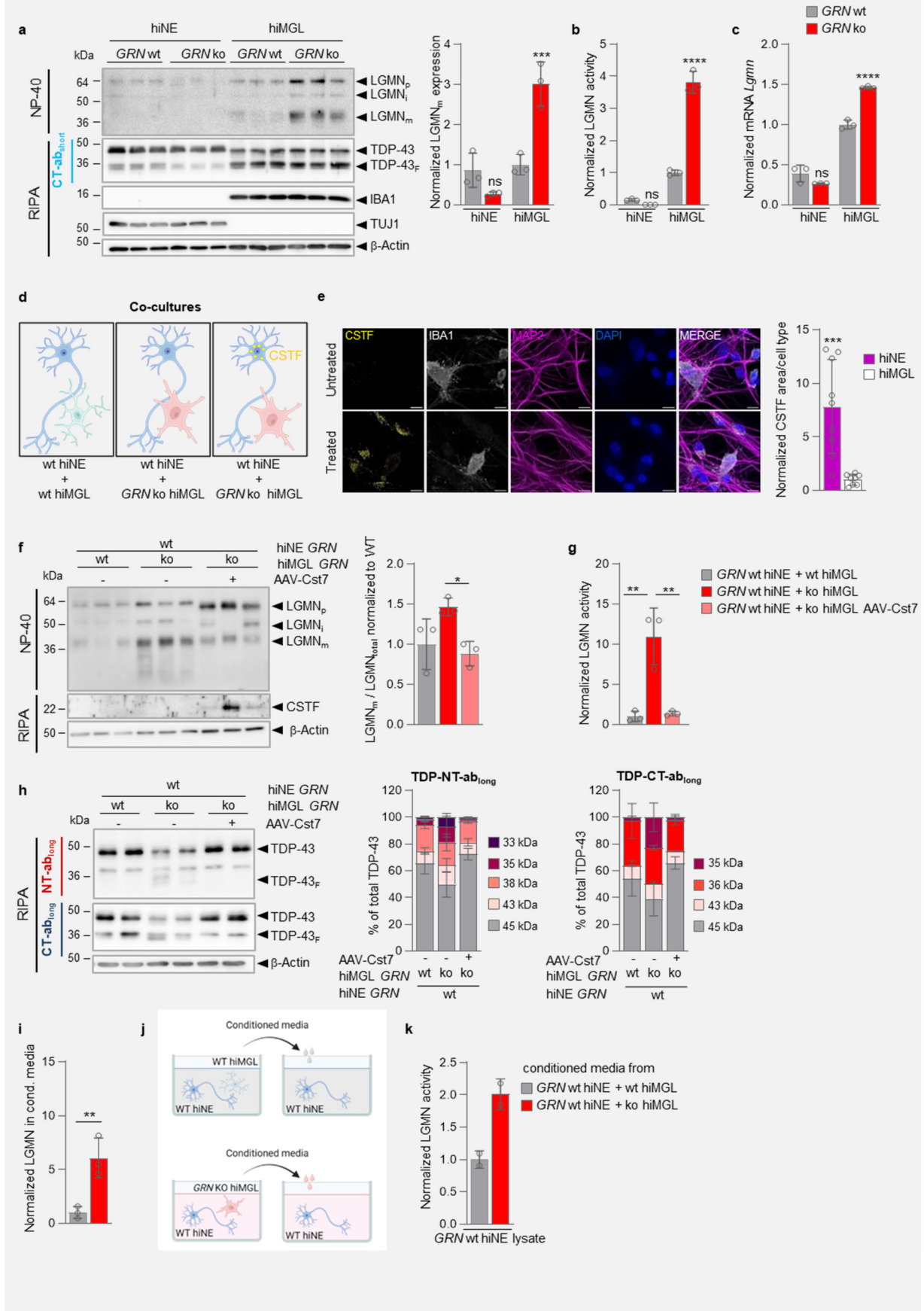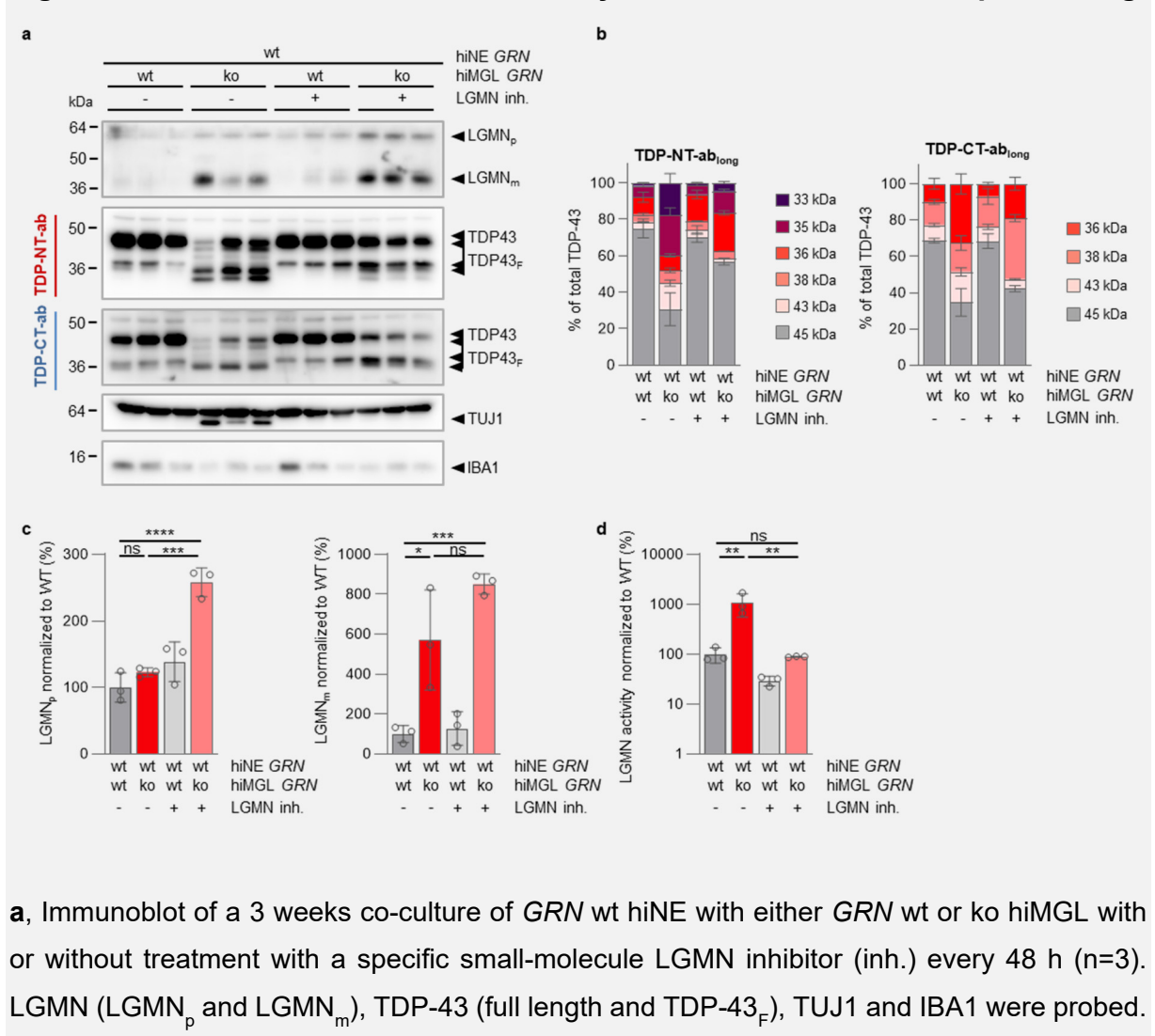
a, Representative immunoblot for LGMN, TDP-43, IBA1, TUJ1, and β-actin of *GRN* wt and ko hiPSC-derived microglia (hiMG) or neurons (hiNE). LGMN$_p$, LGMN$_m$, full-length TDP-43, and TDP-43 fragments (TDP-43$_F$) are indicated. Quantification of LGMN$_m$ from the immunoblot shown as mean normalized to wt hiMGL ± s.d. (n=3). **b,** *In vitro* LGMN activity of lysates from monocultured wt and *GRN* ko hiMGL and hiNE; mean normalized to wt hiMGL ± s.d. (n=3). **c,** qPCR of *LGMN* mRNA expression in wt and *GRN*-deficient (*GRN* ko) hiMGL or hiNE normalized to wt hiMGL, mean ± s.d. (n=3). **D**, Scheme for **e-i**: 3-week co-culture of wt hiNE with *GRN* wt hiMGL, ko hiMGL, or ko hiMGL and AAV-Cst7 (cystatin F expressing (CSTF)) transduction. **e**, Immunofluorescence of CSTF (yellow), neurons (MAP2, magenta), and microglia (IBA1, white) with nuclear staining (DAPI, blue) upon AAV transduction (scale bar 15 µm). Quantification of CSTF area normalized over MAP2 area (hiNE) or IBA1 area (hiMGL). Data are mean ± s.d. of image replicates (n=9). **f**, Immunoblotting of LGMN, CSTF, and β-actin to verify equal loading. Quantification of LGMN$_m$ over total LGMN; mean normalized to wt hiMGL co-culture ± s.d. (n=3). **g**, LGMN activity normalized to hiNE co-cultured with wt hiMGL shown as mean ± s.d. (n=3). **h**, Immunoblotting of TDP-43, using N-terminal (NT-ab$_{long}$) or C-terminal (CT-ab$_{long}$) anti-TDP-43 antibodies, and β-actin. Quantification of indicated TDP-43 fragments (TDP-43$_F$) and TDP-43 holoprotein for both antibodies; mean normalized to wt hiMGL co-culture (n=2). **i**, ELISA of LGMN detected in the media; mean normalized to wt hiMGL co-culture ± s.d. (n=3). **j**, Scheme for (**k**); monocultured *GRN* wt hiNE treated for 24 h with conditioned media from either 3 weeks *GRN* wt hiNE and wt hiMGL co-cultures or *GRN* wt hiNE and ko hiMGL co-cultures. **k**, LGMN activity of treated monocultured *GRN* wt hiNE, normalized to *GRN* wt hiNE treated with conditioned media from wt co-cultures (n=2). Statistical significance was determined using one-way ANOVA and Tukey's post hoc test: ns, not significant; *P<0.05, **P<0.01, ***P<0.001, ****P<0.0001. *P* values and statistical source data are provided.

To investigate potential shuttling of LGMN from microglia to neurons, we initially investigated whether LGMN can be secreted and found enhanced LGMN secretion in *GRN* ko hiMGL compared to wt hiMGL both co-cultured with wt hiNE (Fig. 5i). Conditioned media from these co-cultures were added to *GRN* wt hiNE monocultures (Fig. 5j). Transfer of conditioned media derived from co-cultured ko hiMGL and wt hiNE led to increased LGMN proteolytic activity in lysates of mono-cultured wt hiNE (Fig. 5j,k). This indicates that human neurons can internalize secreted LGMN further supporting our findings that secreted LGMN from microglia can lead to enhanced TDP-43 processing in neurons.

114   14

To further validate the unique role of microglia-derived LGMN in TDP-43 processing, we treated the co-culture with a highly selective small molecule LGMN inhibitor (Extended Data Fig. 6). Upon three weeks of treatment, full-length TDP-43 was increased and TDP-43 fragments were significantly reduced. The remaining TDP-43 processing product of slightly higher molecular weight appears to be generated in a LGMN independent pathway (Fig. 6a,b). Pro-LGMN and mature LGMN were both strongly increased upon inhibitor treatment (Fig. 6a,c). Together with an approximately 90% reduction of the proteolytic activity (Fig. 6d), this suggests reduced self-degradation of LGMN. Taken together, these findings indicate that ko hiMGL release LGMN, which is taken up by neurons, where it then mediates pathological processing of TDP-43.

Fig. 6: Inhibition of LGMN activity diminishes TDP-43 processing.

a, Immunoblot of a 3 weeks co-culture of *GRN* wt hiNE with either *GRN* wt or ko hiMGL with or without treatment with a specific small-molecule LGMN inhibitor (inh.) every 48 h (n=3). LGMN (LGMN$_p$ and LGMN$_m$), TDP-43 (full length and TDP-43$_F$), TUJ1 and IBA1 were probed.

b, Quantification of full-length TDP-43 and fragments in (**a**) shown as mean normalized to untreated *GRN* wt hiNE/ *GRN* wt hiMGL co-cultures ± s.d. (n=3). **c**, Quantification of LGMN$_p$ and LGMN$_m$ in (**a**) shown as mean normalized to untreated *GRN* wt hiNE/ *GRN* wt hiMGL co-cultures ± s.d. (n=3). **d**, LGMN activity of the co-cultures in % (log scale) normalized to untreated *GRN* wt hiNE/ *GRN* wt hiMGL co-cultures ± s.d. (n=3). Statistical significance was determined using one-way ANOVA and Tukey's post hoc test: ns, not significant; *$P<0.05$, **$P<0.01$, ***$P<0.001$, ****$P<0.0001$. P values and statistical source data are provided.

LGMN overexpression in mice results in TDP-43 pathology and motor deficits

As inhibition of LGMN activity in neurons reduced pathological processing of TDP-43, we assumed that TDP-43 pathology could be conversely enhanced *in vivo* by overexpressing LGMN. To prove if increased hLGMN expression in the brain is sufficient to induce FTLD-related pathology, 6-7-month-old *Grn* ko mice were treated *via* tail vein injection with AAV-PhP.eB-CAG-h*LGMN*, a serotype that was shown to have high brain penetrance as well as transduction of neurons and astrocytes[44]. Three months post injection, we observed substantial overexpression of hLGMN (Fig. 7a) as well as a 13-fold increase of LGMN activity in total brain lysates (Fig. 7b). hLGMN was expressed in all brain areas (Extended Data Fig. 7a). hLGMN expression was predominantly found in neurons, and to a lesser extent in astrocytes and microglia (Extended Data Fig. 7b). In line with our *ex vivo* findings, upon hLGMN overexpression in *Grn* ko mice, we detected enhanced generation of TDP-43 fragments (Fig. 7c) and a strong accumulation of insoluble abnormally phosphorylated TDP-43 (pTDP-43) (Fig, 7c). Abnormal processing and pathological phosphorylation of TDP-43 was accompanied by motor deficits as shown by increased hind limb clasping (Fig. 7d) as well as progressing deficits in rotarod performance over time (Fig. 7e). These phenotypes resembled the phenotypes observed in the previously described *Tmem106b* ko/ *Grn* ko FTLD model[45], suggesting that LGMN overexpression in *Grn* ko can induce an FTLD-like pathology. Finally, LGMN overexpression led to a 10-fold increase in plasma neurofilament light chain (NfL) (Fig. 7f), a biomarker for neuronal damage also used in clinical studies[46,47]. Taken together, these results suggest that LGMN is a main driver of TDP-43 pathology *in vivo*.

116   16

Fig. 7: Overexpression of hLGMN in *Grn* ko mice leads to TDP-43 pathology, motor deficits and increased plasma NfL levels.
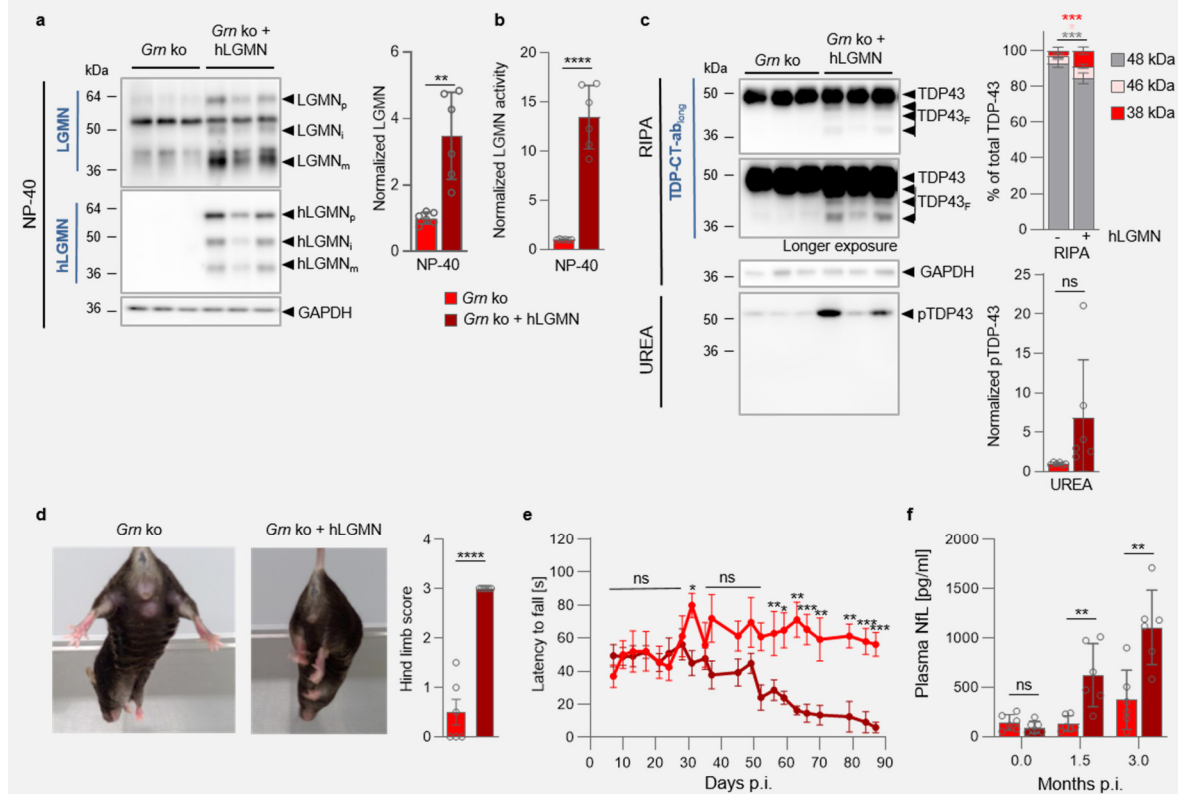
a, Representative immunoblots for total LGMN and human LGMN (hLGMN) in total brain homogenate (NP40) of *Grn* KO mice, three months p.i. and age-matched non-injected controls, GAPDH verified equal loading. LGMN expression is quantified and normalized to *Grn* ko (n=3 mice per condition, mean ± s.d) **b**, *In vitro* LGMN activity assay of total brain homogenate of AAV-injected *Grn* ko mice and age-matched non-injected controls (n=6 mice per condition, mean ± s.d). **c**, Representative immunoblot of TDP-43 in the RIPA soluble fraction of total brain lysates and pTDP-43 in the urea-soluble fraction, GAPDH verified equal loading. For quantification of TDP-43 processing in the RIPA fraction, the signal of indicated TDP-43 fragments was normalized to the total TDP-43 signal (n=6 mice per condition, mean ± s.d., multiple t-tests with FDR correction). pTDP-43 accumulation in the urea fraction was quantified and normalized to *Grn* ko (n=6 mice per condition, mean ± s.d.), **d**, Representative images show assessment of hind-limb clasping phenotype in hLGMN overexpressing mice and age-matched non-injected *Grn* ko mice (n=6 mice per condition). The clasping phenotype was quantified (n=6 mice per condition, mean ± s.e.m.). **e**, Longitudinal rotarod performance of *Grn* ko mice overexpressing hLGMN and age-matched controls (n=6 for *Grn* ko + hLGMN, n=6 for *Grn* ko control mice, mean ± s.e.m., multiple t-tests with FDR correction). **f**, Plasma NfL levels were measured before injection,1.5 months p.i and terminally. (n=6, mean ± s.d.).

Unpaired two-tailed Student t-test or multiple t-tests with FDR correction, if indicated, were used to assign significance (two-stage step-up, Benjamini, Krieger and Yekulti): ns, not significant; $*P<0.05$, $**P<0.01$, $***P<0.001$, $****P<0.0001$. P values and statistical source data are provided.

Discussion

Our findings demonstrate that enhanced LGMN activity provides a direct link between *GRN* haploinsufficiency and TDP-43 pathology. In various model systems, including two independent PGRN-deficient mouse lines, MEF, primary mouse- and hiPSC-derived microglia, and finally FTLD-G*RN* patient brains, we consistently found elevated LGMN maturation and activity. Upon co-incubation of LGMN and PGRN *in vitro*, we observed that PGRN, but not granulin peptides, delays LGMN maturation in a dose-dependent manner. Thus, PGRN slows LGMN maturation, presumably in a chaperone-like manner during trafficking to lysosomes. The inhibitory effect is balanced by LGMN itself, as it hydrolyses PGRN into non-inhibitory granulin peptides. We found that granulin peptides are reduced in *Lgmn* ko mice, thus LGMN is involved in granulin peptide generation *in vivo*. This is further supported by recent *in vitro* data by Mohan et al., who investigated the role of various lysosomal proteases in the differential processing of PGRN[29].

In addition, pathologically enhanced LGMN activity leads to increased processing of lysosomal cathepsins, which, consistent with previous findings[15,18,48], may result in dysregulation and malfunction of microglial lysosomes. Considering the potential of several lysosomal cathepsins to process PGRN as well[27-29,49], this could further accelerate the pathology. Based on our findings that both, knockdown of LGMN or selective inhibition of LGMN activity ameliorates pathological TDP-43 processing, whereas overexpression accelerates TDP-43 pathology, LGMN might be a main driver of FTLD-*GRN* pathology. Fragment formation is disease relevant, since proteolytically cleaved TDP-43 fragments are not only enriched in TDP-43 deposits, but such fragments are also known to be required for seeding and spreading of pathological TDP-43[50]. A contribution of other proteases activated by LGMN cannot be excluded though, as the overexpression of the more general protease inhibitor CSTF showed a stronger rescue than the selective small molecule LGMN inhibitor in our hiPSC co-culture system.

118   18

Strikingly, overexpression of LGMN in *Grn* ko mice caused a severe worsening of disease phenotypes, including processing, phosphorylation and aggregation of TDP-43. Similar effects of overexpressed LGMN have been proposed for tau processing and phosphorylation in Alzheimer's disease[51,52]. Phosphorylation of tau might be affected by elevated LGMN levels which results in reduced protein phosphatase 2a (PP2A) stability and as a consequence in hyperphosphorylated tau[51]. Whether this mechanism plays a role for TDP-43 phosphorylation needs to be further investigated. In addition, in *Grn* ko mice, overexpressed LGMN resulted in increased plasma NfL levels and worsened rotarod performance. Elevated NfL levels in serum and CSF of FTLD patients correlate with disease severity and brain atrophy, with particular high levels in symptomatic FTLD-*GRN* patients[53,54]. TDP-43 pathology results in motor deficits in amyotrophic lateral sclerosis, but also FTLD and specifically FTLD-*GRN* patients can present with motor neuron disease-like syndromes[55]. Since TDP-43 cleavage removes the nuclear localization signal from the C-terminal fragments, it will further enhance cytoplasmic accumulation and aggregation of TDP-43. LGMN secretion has already been described in the periphery[36]. Here, LGMN is mainly expressed by immune cells and upregulated upon stress or in tumor microenvironment. In these conditions its pro-form was also found to be secreted[36]. The secretion of LGMN by activated microglia and further functional consequences need to be studied in more detail in the future. Together, our findings strongly suggest that the pro-LGMN is released by PGRN deficient microglia and internalized by neurons, where it is activated and capable of processing TDP-43, thus resolving the spatial paradox of the differential expression of LGMN and PGRN predominantly in microglia, and TDP-43 pathology primarily occurring in neurons[3] (Fig. 8). In which cellular compartment LGMN gains access to TDP-43 remains to be discovered. To reach cytoplasmic TDP-43 mature LGMN might be released by damaged lysosomes[16]. Although active LGMN is unstable at the neutral pH of the cytosol, it might be stabilized by active center interacting proteins[36]. One could speculate that re-activation occurs by release of the binding partner in an acidic microenvironment. A more likely mechanism might be the direction of cytoplasmic TDP-43 towards autophagic degradation[56,57] and cleavage by LGMN in autolysosomes. TDP-43 fragments might then escape damaged, leaky lysosomes[16] and accumulate in the cytoplasm.

PGRN-deficiency can cause microglial hyperactivation[10-12] and triggers the complement cascade[58] resulting in neuronal loss. How aberrantly elevated LGMN

activity is linked to these processes remains to be investigated. As FTLD-*GRN* patients also present with co-pathology of other LGMN substrates, namely tau and α-synuclein[52,59,60], it is conceivable that their accumulation and deposition may also be facilitated by aberrantly enhanced LGMN activity. In addition, LGMN activity was also found to be upregulated in the brains of patients with other neurodegenerative diseases, such as Alzheimer's and Parkinson's disease[52,61]. Monitoring LGMN activity in patient brains or the increase of LGMN specific cleavage products in the CSF could be useful biomarkers in the future to monitor disease progression and lysosomal dysfunction. Finally, since TDP-43 pathology and lysosomal dysfunction co-exist in other neurodegenerative diseases such as Alzheimer's disease, Parkinson's disease, limbic-predominant age-related TDP-43 encephalopathy (LATE), Lewy Body dementia and hippocampal sclerosis, our findings may reveal a disease overarching pathway, which could be modulated by LGMN inhibitors[62-66].

Fig. 8: Increased legumain activity caused by progranulin deficiency drives TDP-43 pathology.

120   20
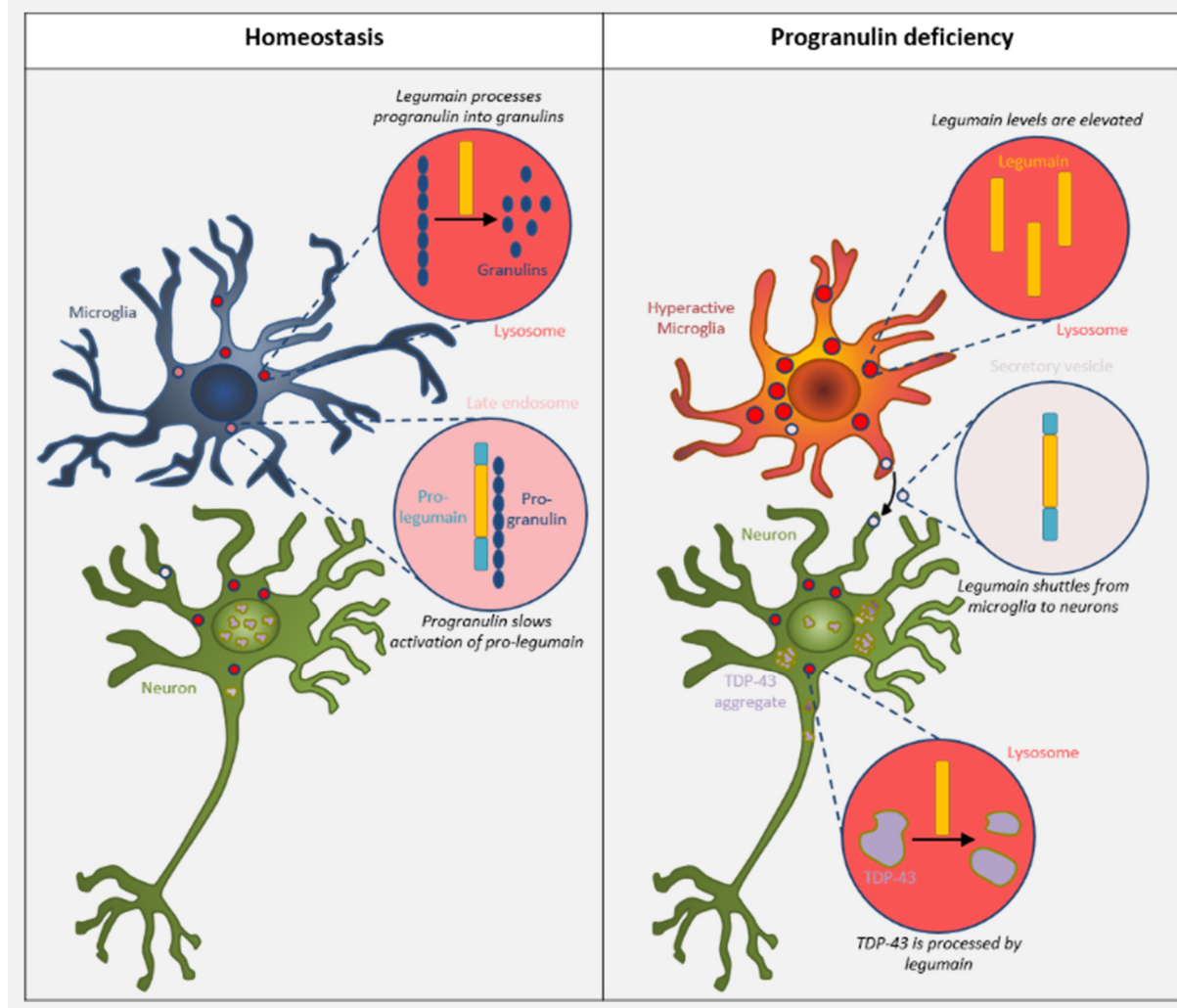
Suggested pathomechanism: In homeostasis, PGRN slows the maturation of LGMN, which is regulated in a negative feed-back loop *via* processing of PGRN into single granulins by LGMN. Upon PGRN loss-of-function, lysosomal function is impaired and microglia become hyperactivated. In this context, LGMN is not regulated by PGRN anymore and its protein levels and activity increase. The pro-form of LGMN is secreted by activated microglia and taken up by neurons (mechanism unknown), where it hyperprocesses TDP-43 and thereby drives TDP-43 pathology.

Methods

Data reporting

No statistical methods were used to predetermine sample size. The investigators were not blinded to allocation during experiments and outcome assessment, except for animal motor function assessment tests.

Ethical approval

All the work involving human tissues or mice was carried out in accordance with the Code of Ethics of the World Medical Association (Declaration of Helsinki). The use of human brain material was approved by the local ethic commission of the Ludwig-Maximilian's-University, Munich. All animal experiments were performed in compliance with the national guidelines for animal protection in Germany and with the approval of the regional animal committee (Regierung von Oberbayern) directed by a veterinarian. Mice were kept in small groups under standard housing conditions at constant temperature of 21 ± 2°C, on a 12 h light / dark cycle, providing standard pellet food and water *ad libitum*. At Denali Therapeutics Inc. all mouse procedures adhered to regulations and protocols approved by Denali Therapeutics Institutional Animal Care and Use Committee. Mice were housed under a 12 h light / dark cycle and group housed when possible.

Experimental mouse models

The *Grn* ko mouse line was provided by Dr. M. Nishihara (Department of Veterinary Physiology, The University of Tokyo)[67], backcrossed to the C57BL/6J strain and published before[10,17,18,22,45]. Animal ages / sexes for each experiment are indicated in the source data tables.

Overexpression of hLGMN in *Grn* ko mice

100 µl of AAV-PhP.eB-CAG-h*LGMN* with a titer of c=$5*10^{12}$ vg/ml was applied *via* tail vein injection at an age of 6-7 months in male *Grn* ko mice. Non-injected age-matched male *Grn* ko mice were used as controls.

Motor function assessment

Rotarod test

A rotarod (# 3376O4R, TSE Systems) was used to assess motor function. The speed was accelerated stepwise from 4-40 rpm within 300 s as previously described[45]. Mice were trained twice within one week before starting longitudinal rotarod measurements. The average latency to fall off the rotarod of three consecutive tests was calculated for each recording day.

Hind limb clasping test

Mice were recorded for 10 seconds while being lifted by their tail as previously described[63]. Mice were scored based on the degree of cramping of their hind limbs recorded on two different days at 3 months p.i.. Mice showing no cramping obtained a score of 0, cramping for less than 25% of recording time a score of 1, more than 25% of recording time a score of 2, or more than 50% of the recording time a score of 3.

Mouse brain dissection and blood collection

Mice were sacrificed by CO_2 inhalation or by deep/lethal anesthesia and perfused with ice cold PBS. Brain tissue dissected from adult mice was either snap frozen in liquid nitrogen, mechanically pulverized and stored at -80°C for biochemical analysis, fixed in PFA for immunofluorescence staining or directly used for cell isolation.

Blood was collected 1 day before virus injection and at 1.5 months p.i. by facial vein puncture. Terminally, blood was collected before perfusion via cardiac puncture in EDTA-coated tubes and centrifuged (15,500 x g, 7 min, 4°C). For analysis the plasma fraction was used.

Mouse brain cell isolation

Mice were sacrificed by CO_2 inhalation or by deep/lethal anesthesia and perfused with ice cold PBS and directly subjected to microglia and astrocyte or neuron isolation. Neural cells were acutely isolated from adult mouse brain using MACS technology (Miltenyi Biotec). Brain tissue was dissociated into a single-cell suspension by

122   22

enzymatic digestion using the Adult Brain Dissociation Kit P (# 130-107-677, Miltenyi Biotec) and the gentleMACS™ Octo Dissociator (# 614 130-096-427, Miltenyi Biotec) according to manufacturer´s instructions. Microglia and astrocyte isolation were performed from the same mouse brain. Briefly, the dissociated cell suspension was applied to a pre-wetted 100 µm cell strainer, cells were pelleted at 300 x g, 4°C, 10 min, pellets were washed twice and resuspended in 1 ml 0,5% (w/v) BSA/PBS. CD11b-positive microglia were magnetically labelled with 20 µl anti-CD11b MicroBeads (# 130-049-601, Miltenyi Biotec) and incubated for 20 min in the dark at 4°C with gentle shaking. Cells were washed by adding 1−2 ml of BSA/PBS. The cell pellets were resuspended in 1 ml BSA/PBS and applied together with 1 ml BSA/PBS onto the prepared LS columns (# 130-042-401, Miltenyi Biotec) placed into a QuadroMACS™ Separator (# 130-091-051, Miltenyi Biotec). The columns were washed with 3 × 3 ml BSA/PBS. The flow-through and the first wash containing the unlabeled cells was collected for astrocyte isolation. The columns were removed from the magnetic field, and microglia were flushed out using 5 ml BSA/PBS. To obtain a higher purity, the microglia containing eluate was applied onto pre-wetted MS columns (# 130-042-201, Miltenyi Biotec) placed into an OctoMACS™ Separator (# 130-042-108, Miltenyi Biotec), washed 3 x 0.5 ml and eluted with 1 ml BSA/PBS, then immediately stored on ice. For astrocyte isolation the microglia-depleted fraction including the first wash was pelleted and resuspended in 1 ml BSA/PBS, then 10 µl of FcR blocking reagent was added and incubated for 20 min, gentle shaking in the dark at 4°C, followed by adding 10 µl of anti-ACSA-2 MicroBeads (Anti-ACSA-2 MicroBead Kit, # 130-097-678, Miltenyi Biotec) and an additional incubation for 30 min. Cells were washed and astrocytes were magnetically separated as described for microglia. Neurons were isolated (Adult Neuron Isolation Kit mouse, # 130-126-603, Miltenyi Biotec) according to the manufacturer's instructions including a red blood cell removal and a debris removal step (Adult Brain Dissociation Kit P, # 130-107-677, Miltenyi Biotec). Isolated cells were washed twice with D-PBS (# 14040-133, Thermo Fisher Scientific) to remove BSA, pellets were snap frozen in liquid nitrogen and stored at -80°C until further biochemical analysis.

Mouse embryonic fibroblasts (MEF), HeLa and HEK293T cell culture

All MEF were generated as described before[4]. MEF, HeLa, and HEK293T were cultured in Dulbecco's modified Eagle's medium (DMEM) with GlutaMAX™-I (# 10566016, Thermo Fisher Scientific) supplemented with 10% (v/v) heat inactivated

FBS (# F7524, Sigma-Aldrich), 100 U/ml penicillin, and 100 µg/ml streptomycin (# 15140148, Thermo Fisher Scientific), and if required 1% non-essential amino acids (# 11140050, Thermo Fisher Scientific).

Primary culture of mouse microglia

Microglia were isolated from P11 pups using the MACS Technology (Miltenyi Biotec) as described above. Isolation was carried out under sterile conditions. 60,000 cells were plated in DMEM/F-12, HEPES (# 11594426, Thermo Fisher Scientific) supplemented with 10% (v/v) heat inactivated FBS (# F7524, Sigma-Aldrich), 100 U/ml penicillin, and 100 µg/ml streptomycin (# 15140148, Thermo Fisher Scientific).

Primary culture of mouse hippocampal neurons

Mouse hippocampal neurons were generated as described previously[45]. In brief, E18 embryos were collected from CO_2-euthanized C57BL/6J wildtype mice. The hippocampi were isolated and dissected in ice-cold dissection buffer (HBSS, 1 mM sodium pyruvate, 10 mM HEPES pH 7.2, all from Thermo Fisher Scientific). Single cell suspension was obtained by pelleting the tissue (300 x g, 3 min, RT) and incubating it for 15 min at 37°C with 0.125% trypsin (# 25200-072, Thermo Fisher Scientific) and 25 U/ml benzonase (# E1014-25KU, Sigma-Aldrich) in DMEM with GlutaMAX™-I. After centrifugation (300 x g, 3 min, RT), tissue was washed in DMEM with GlutaMAX™-I and pelleted again (300 x g, 3 min, RT) before trituration in culture media (neurobasal media, # 21103-049, Thermo Fisher Scientific) with 100 U/ml penicillin, 100 µg/ml streptomycin, 0.5 mM L-glutamine (# 25030-024, Thermo Fisher Scientific) and 1x B-27 supplement (# 17504-044, Thermo Fisher Scientific) with 25 U/ml benzonase and subsequent centrifugation (300 x g, 3 min, RT). The single cells were plated onto poly-D-lysine- (10 µg/ml, # P7280-5MG, Sigma-Aldrich) and laminin- (10 µg/ml, # L2020-1MG, Sigma-Aldrich) coated plates in culture media. On DIV 7, 20% media was added and on DIV 14, cells were used for experiments.

Gene expression analysis

For quantitative real time PCR (qRT-PCR) approximately 10-20 mg of powdered mouse brain homogenates or between 400,000 and 2 million hiPSC -derived MGL or hNE were subjected to total RNA preparation using the QIAshredder and RNeasy Mini Kit (# 79656, Qiagen) according to manufacturer's instructions. 0.1-1 µg of RNA was reverse transcribed into cDNA using M-MLV reverse transcriptase (Promega) and oligo(dT) primers (Life Technologies). The following primer sets from Integrated DNA

124

Technologies were used: mouse *Lgmn* Mm.PT.58.5122210 (Exon boundary 10 to 11), mouse *Gapdh* Mm.PT.39a.1 (Exon boundary 2 to 3), human *LGMN* Hs.PT.58.21235685 (Exon boundary 3 to 4) and human *RPL22* Hs.PT.58.41088691(Exon boundary 3 to 4).

For quantification, cDNA levels were normalized to mouse *Gapdh* or human *RPL22* cDNA and relative transcription levels were analyzed using the comparative ΔΔCt method (7500 Software V2.0.5, Applied Biosystems, Life Technologies). The *Lgmn* mRNA level of the microglia-enriched fraction was obtained from a NanoString dataset (Omnibus   GSE129709 https://www.ncbi.nlm.nih.gov/geo/query/acc.cgi?acc=GSE129709)[10].

Cloning of m*Lgmn*

The mouse *Lgmn* cDNA was amplified from MEF cDNA prepared as described for "gene expression analysis", following primers were used: *Lgmn* (XhoI) forward 5'-CCCGCTCGAGGCCACCATGACCTGGAGAGTGG-3' *Lgmn* (EcoRV) reverse 5'-AGCTTTGATATCTCAGTAGTGACTAAGAC-3'. The amplified *Lgmn* cDNA was sub-cloned into the XhoI/EcoRV sites of pcDNA3.1/Zeo(-). The *Lgmn* mutation leading to an inactive LGMN C191A variant[40,68] was introduced by site-directed mutagenesis using the QuickChange Site-Directed Mutagenesis Kit (# 200519, Agilent Technologies) according to manufacturer's instruction. The Cys coding base triplet TGT was exchanged to GCT coding for Ala using following primers: *Lgmn*(mt)F 5'-GGTGTTCTACATTGAAGCTGCTGAGTCTGGCTCCATGATGAACC-3'-*Lgmn*(mt)R 5'-GGTTCATCATGGAGCCAGACTCAGCAGCTTCAATGTAGAACACC-3'.

Design and production of adeno-associated virus.

AAV-hSyn-Cst7. A 603 bp long nucleotide encoding for cystatin-7 was cloned into the BamHI/EcoRI sites of pAAV-hSyn-EGFP (# 50465, Addgene) to receive the plasmid pAAV-hSyn-*Cst7*. To generate double-stranded adeno-associated virus of serotype 9 (AAV9), the plasmid and helper plasmid were transfected into HEK293T cells using polyethylenimine (# 24765, Polysciences). The virus was harvested after 72 h and purified from benzonase-treated cell lysates via an iodixanol density gradient (OptiPrep, Fresenius Kabi Norge). After rebuffering in lactose AAV titers were determined by real-time PCS on vector genomes using the SYBR Green Master Mix (Roche Molecular Systems).

AAV-PhP.eB-CAG-hLGMN. The AAV-PhP.eB-CAG-*hLGMN* vector used in this study was produced under research-grade conditions at SignaGen by triple transfection of adherent HEK293T cells. Briefly, HEK293T were transiently transfected after 48 h of culture using the corresponding Gene of Interest (GOI) plasmid, the corresponding capsid plasmid (AAV-PHP.eB), and the helper plasmid and PolyJet DNA transfection reagent (SignaGen) as transfection reagent. 72 h after transfection, cells were detached and harvested using sterile PBS. Harvested cells were lysed by three freeze/thaw cycles before an overnight benzonase treatment at 37 °C to digest residual DNA followed by high salt treatment for 1 h at 37°C. The crude lysate was further clarified by low-speed centrifugation. Full capsid AAVs were purified by ultracentrifugation in a cesium chloride (CsCl) gradient. A diafiltration step was then performed to concentrate the purified AAVs and reformulate them into PBS + 0.005% poloxamer 188 (# 13-901-CI, Corning) using Amicon Ultra-4 filter units (# UFC8100, Merck) with a 100 kDa MWCO membrane. Finally, a sterile filtration through a 0.22 µm membrane filter was performed. Vector genome titer was determined by qPCR using an ITR-specific primer-probe set. The final purified products were characterized with assays to measure identity, potency, and purity.

Lipofectamine 2000 mediated cDNA transfection

For transfection of HeLa and HEK293T cells Lipofectamine 2000 (# 11668030, Thermo Fisher Scientific) was used according to the manufacture's instruction. Briefly, 500 µl of 4 µg/ml plasmid solution in media was mixed with 500 µl DMEM with GlutaMAX™-I containing 20 µl Lipofectamine 2000 and incubated for 20 min at RT before dropwise addition onto HeLa cells at 50-70% confluency. After 6 h, the media was exchanged and after 36 h the media was replaced with 4 ml Opti-MEM® with GlutaMAX™-I media (# 51985-026, Thermo Fisher Scientific). Media and cells were collected 48 h after transfection.

siRNA Transfection

Lgmn siRNA (# M-044015-01-0005, siGENOME SMART pool, Dharmacon), control siRNA (#D-001210-04-20, siGenome non-targetting pool 4, Dharmacon) and mock reverse transfections were carried out with Lipofectamine™ RNAiMAX (# 13778030, Thermo Fisher Scientific). For each 10 cm dish 3 µl siRNA (20 µM), were diluted in 600 µl Opti-MEM™ (# 31985-062, Thermo Fisher Scientific) before adding 30 µl Lipofectamine™ RNAiMAX and then for complex formation incubated for 15 min at RT.

126   26

Trypsinized and washed MEF cells were added to reach a final volume of 6 ml culture media without antibiotics and a final siRNA concentration of 10 nM. The next day, media were exchanged to fresh culture media and 96 h after transfection cells were harvested and pellets were washed in PBS, snap frozen in liquid nitrogen and stored at -80°C.

Human iPSC culture

HiPSC experiments were performed in accordance with relevant guidelines and regulations. The female iPSC line A18944 was purchased from Thermo Fisher (# A18945), grown in Essential 8 Flex Medium (# A2858501, Thermo Fisher Scientific) on VTN-coated (# A14700, Thermo Fisher Scientific) cell culture plates with 5% CO_2 at 37°C, and split as small clumps twice a week after a 5 min incubation in PBS/EDTA. The *GRN* ko iPSC line was described before[22].

Differentiation of human iPSC-derived to cortical hiMGL, hiNE, co-culture of hiNE with hiMGL and treatment with AAV-Cst7 or LGMN inhibitor.

HiPSC-derived hiMGL were differentiated as previously described[22] following the protocol by Abud et al.[69] with modifications to improve yield and efficiency. HiMGL were used for monoculture experiments on day 16 of the differentiation. HiPSC-derived hiNE were differentiated as previously published[70] and used following day 60 of differentiation. HiNE were transduced with AAV-Cst7 at 500,000 gc/cell one week before co-culture with microglia. For co-culture experiments, hiMGL were added to differentiated neurons on day 12 of hiMGL differentiation and co-cultured for three weeks before collection for analysis. For LGMN inhibitor treatments, co-cultures were treated every 48 h from the start of co-culture with either 1 μM LGMN inhibitor (Roche) or a DMSO control for three weeks.

Conditioned media treatment of monocultured hiNE

Monocultured hiNE were maintained along with co-cultures, as described above. Half of the media was taken out of the monocultured hiNE and media from the co-cultures was added before collecting the monocultured hiNE 24 h later.

LGMN *in vitro* activity assay

A fluorescence-based activity assay was used to assess LGMN proteolytic activity of recombinant LGMN, or LGMN activity in lysates and media of the respective cells. Cell pellets or aliquots of powdered brain tissues were homogenized in LGMN-lysis buffer

(50 mM sodium citrate pH 5.0, 0.8% NP-40, 1 mM DTT), incubated 15 min (cell lysates) or 20 min (brain lysates) on ice, followed by a 15 min centrifugation at 15,000 x g, 4°C. Protein concentration was determined using the BCA protein assay (Pierce, Thermo Scientific) and indicated amounts of protein in 50 µl LGMN-lysis buffer were pre-incubated in black 96-well plates (FluoroNunc) at 37°C for 10 min, then 50 µl LGMN assay buffer (50 mM sodium citrate pH 5.0, 1 mM EDTA pH 8.0, 1 mM DTT and 200 µM substrate (Z-Ala-Ala-Asn-AMC (# I-1865.0050, BACHEM))) prewarmed at 37°C was added. Cleavage of the quenched fluorescence substrate was continuously measured for 30 min following the increase of the fluorescence signal (excitation, 390 nm; emission, 460 nm) using the Fluoroskan Ascent FL plate reader (Labsystems). The relative enzyme activity was calculated for a period of time with linear substrate turnover.

In vitro activation assays of recombinant pro-LGMN (rLGMN) or of the secreted pro-LGMN (sLGMN)

Prior to LGMN activity assays mouse rLGMN (# 2058-CY-010, R&D Systems) or sLGMN proform needs to be autocatalytically activated at acidic pH. 50 ng rLGMN or 25 µl of the collected media of transfected HeLa cells or hiMGL/hiNE co-cultures was preincubated in 10 µl or 25 µl acidic activation buffer (100 mM sodium citrate pH 4.0 or 3.5, 1 mM EDTA, 50 mM NaCl) for 4 h or as indicated at 37°C. For the activity assay 40 µl LGMN-lysis buffer was added and LGMN activity was measured as described above. To investigate the inhibitory effect of PGRN on LGMN activity, 200 ng or the indicated amount of human recombinant PGRN (rPGRN, # 10826-H08H, Sino Biological Inc.) was either added to the activation assay or to the activity assay.

hLGMN ELISA

hLGMN was measured by an ELISA protocol previously established for PGRN by our group using the MSD Platform[71]. The ELISA consists of streptavidin-coated 96-well plates (streptavidin Gold Plates, # L15SA, MSD), a biotinylated polyclonal goat anti-human LGMN capture antibody (0.5 µg/ml, # BAF2199, R&D Systems), a polyclonal rabbit anti-human LGMN detection antibody (0.25 µg/ml, # NBP1-87793, Novusbio) and a SULFO-TAG-labelled goat polyclonal anti-rabbit IgG secondary antibody (0.5 µg/ml, # R32AB, MSD). All antibodies were diluted in 0.5% bovine serum albumin (BSA) and 0.05% Tween 20 in PBS (pH = 7.4) buffer. Recombinant human legumain/asparginyl endopeptidase (# 2199-CY-010, R&D Systems) was used as a

128   28

standard (18.31 to 2343.75 pg/ml). In brief, streptavidin-coated 96-well plates were blocked overnight at 4°C in blocking buffer, then capture antibody (25 µl per well) was incubated for 1 h at RT, followed by four times washing (0.05% Tween 20 in PBS) and incubation for 2 h at RT with the samples diluted 1:2.5 in assay buffer (0.25% BSA and 0.05% Tween 20 in PBS (pH7.4)) or the recombinant human LGMN standard dilution. Plates were again washed four times with washing buffer before incubation for 1 hour at RT with the detector antibody. After four additional washing steps, plates were incubated with the secondary antibody for 1 h in the dark. Last, plates were washed four times with wash buffer followed by two washing steps in PBS. The electrochemical signal was developed by adding MSD Read buffer T (# R-92TC) and the light emission measured using the MSD MESO QuickPlex SQ120. The ELISA showed accurate results in spike recovery experiments (98%) and minimal measurement variation (CV = 4%) between replicates. For calculation of the sample concentration the MSD software Workbench v4 was used.

Plasma Neurofilament light-chain (NfL) analysis

Plasma Nfl levels were measured with the Quanterix Simoa® NF-light™ Reagent Kit (# 103186, Quanterix) following the manufacturer's instructions as previously described (Reifschneider, 2022). Plasma NfL levels were run on a Simoa HDX instrument (Quanterix) and interpolated against a calibration curve included in the Quanterix assay kit.

Generation of granulin peptides

Elastase generated granulin peptides were obtained by incubation of rPGRN with human neutrophil elastase (# RP-77526, Invitrogen). 50 ng/µl PGRN and 80 ng/µl elastase were incubated in 100 mM sodium citrate pH 6.0 overnight at 37°C, followed by buffer exchange to LGMN activation buffer. Aliquots were stored at -80°C.

Antibodies

Antibodies	Dilution		Source
	IB	IF	
Mouse anti-β-actin	1:5,000	--	# A 5316, Sigma-Aldrich
Rabbit anti-calnexin	1:5,000	--	# SPA-860, Stressgene
Rabbit anti-cystatin-7	1:2,500	1:250	# 50236, SinoBiological
Mouse anti-GAPDH	1:10,000	--	# AM4300, Invitrogen
Goat anti-human IBA1	--	1:250	# ab5076, Abcam

Rabbit anti-human IBA1	1:500	--	# PA5-27436, Thermo Fisher Scientific
Rat anti-mouse LAMP1	--	1:500	# sc-19992, Santa Cruz
Sheep anti-mouse LGMN	1:2,500	1:250	# AF2058, R&D Systems
Goat anti-human LGMN	1:1,000	1:250	# AF2199, R&D Systems
Chicken anti- MAP2	--	1:1,000	# NB300-213, Novus Biologicals
Rat anti-mouse PGRN, (clone 8H10)	1:50	--	generated[72]
Rabbit anti-human PGRN	1:1,000	--	# 40-3400, Thermo Fisher Scientific
Rabbit anti-human PGRN / granulin-peptides	1:1,000	--	# HPA008763, Atlas Antibodies
Rabbit anti-TDP-NTlong	1:4,000	1:600	# 10782-2-AP, Proteintech
Rabbit anti-TDP-CTlong	1:1,000	--	# 12892-1-AP, Proteintech
Rabbit anti-TDP-CTshort	1:1,000	--	# TIP-TD-P09, Cosmo Bio
Rabbit anti-pTDP-43	1:5,000	--	# 80007-1-RR, Proteintech
Mouse anti-tubulin α	1:500	--	# T5168, Sigma-Aldrich
Mouse anti-tubulin β3 (TUJ)	1:1,000	--	# 801201, BioLegend

The following secondary antibodies were used for immunoblots: horseradish peroxidase-conjugated donkey anti-goat IgG (H+L) (Dianova, 1:5,000), donkey anti-sheep IgG goat (Jackson Immuno Research, 1:10,000), goat anti-mouse IgG (Promega, 1:10,000), goat anti-rabbit IgG (Promega, 1:20,000), goat anti-rat IgG + IgM (L+M) (Dianova, 1:5,000), and generated mouse anti-rat IgG2c (1:1,000).

Immunohistochemistry

Cells seeded on coverslips in 24-well dish were fixed for 15 min in 4% paraformaldehyde and washed with PBS, then permeabilized for 10 min at room temperature in (0.1% Triton-X-100 in PBS for MEF and iPSCs, 0.1% Triton-X-100 and 0.1% saponin in PBS for *Cst7*-transduced hiN) and then washed with PBS again. SuperBlock (# 37515, Thermo Fisher Scientific) was used to block the coverslips for 1-2 h at RT. Primary antibodies were diluted in SuperBlock added overnight (iPSC) or for 2 h at 37°C (MEF). The coverslips were washed again in PBS and incubated in secondary antibodies (donkey anti-chicken Alexa 647 1:500, donkey anit-rat Alexa 647 1:500, donkey anti-sheep Alexa 555 1:500, donkey anti-rabbit Alexa 488 1:500, DAPI 1:5,000) diluted in SuperBlock for 90 min at RT in the dark. They were washed in PBS again and mounted with Fluoromount G (# 00-4958-02, Thermo Fisher Scientific).

130

Protein analysis and immunoblotting

Snap frozen cell pellets or powdered brain homogenate were lysed in NP-40 LGMN-lysis buffer (50 mM sodium citrate pH 5.0, 0.8% NP-40, 1 mM DTT), NP-40 STEN-lysis buffer (150 mM NaCl, 50 mM Tris–HCl pH 7.6, 2.5 mM ETDA, 1 % NP40) or RIPA-lysis buffer (150 mM NaCl, 20 mM Tris–HCl pH 7.6, 2.5 mM ETDA, 1% NP-40, 0.1% sodium dodecyl sulfate (SDS), 0.5% sodium-desoxycholate) as indicated. NP-40 STEN- and RIPA-lysis buffer were supplemented with protease inhibitor cocktail (# P8340, Sigma-Aldrich) and phosphatase inhibitor (# 4906845001 PhosStop™, Sigma-Aldrich). Lysates were centrifuged for 20 min, 17,000 x g, 4°C. The protein concentration of the soluble fraction was determined using the BCA protein assay (Pierce, Thermo Fisher Scientific) and equal amount of protein were separated by SDS-PAGE and transferred to polyvinylidene difluoride membranes (Immobilon-P, Merck Millipore). Membranes were blocked for one hour in I-Block™ (# T2015, Thermo Fisher Scientific). Proteins of interest were detected by the indicated primary antibodies followed by horseradish peroxidase-conjugated secondary antibodies detected by ECL Plus (# 32132X3, Pierce™ ECL Plus Western Blotting Substrate, Thermo Fisher Scientific). For the quantitatively analysis, images were taken by a Luminescent Image Analyzer LAS-4000 (Fujifilm Life Science, Tokyo, Japan) and evaluated with the Multi GaugeV3.0 software (Fujifilm Life Science, Tokyo, Japan).

Statistical analysis

Data are presented as mean ± s.d. or mean ± s.e.m. Statistical significance was calculated for comparison of two sample groups by unpaired, two-tailed Student's t-test, and for multiple comparison by one-way ANOVA with Tukey's or Dunnett's post hoc test and indicated as ns, not significant; $P>0.05$; *$P<0.05$; **$P<0.01$; ***$P<0.001$; ****$P< 0.0001$. All data were analyzed using GraphPad Prism 7 (GraphPad Software Inc.).

Data availability

All data and information are included in the manuscript. Supplementary information and source data are provided with this article. Data are available from corresponding authors upon reasonable request.

References

1   Russell, L. L. & Rohrer, J. D. Defining the presymptomatic phase of frontotemporal dementia. *Curr Opin Neurol* **36**, 276-282 (2023). https://doi.org:10.1097/WCO.0000000000001174

2   Neumann, M. *et al.* Ubiquitinated TDP-43 in frontotemporal lobar degeneration and amyotrophic lateral sclerosis. *Science* **314**, 130-133 (2006). https://doi.org:10.1126/science.1134108

3   Mackenzie, I. R. The neuropathology and clinical phenotype of FTD with progranulin mutations. *Acta Neuropathol* **114**, 49-54 (2007). https://doi.org:10.1007/s00401-007-0223-8

4   Baker, M. *et al.* Mutations in progranulin cause tau-negative frontotemporal dementia linked to chromosome 17. *Nature* **442**, 916-919 (2006). https://doi.org:nature05016 [pii] 10.1038/nature05016

5   Cruts, M. *et al.* Null mutations in progranulin cause ubiquitin-positive frontotemporal dementia linked to chromosome 17q21. *Nature* **442**, 920-924 (2006). https://doi.org:nature05017 [pii] 10.1038/nature05017

6   Almeida, M. R. *et al.* Portuguese family with the co-occurrence of frontotemporal lobar degeneration and neuronal ceroid lipofuscinosis phenotypes due to progranulin gene mutation. *Neurobiol Aging* **41**, 200 e201-205 (2016). https://doi.org:10.1016/j.neurobiolaging.2016.02.019

7   Smith, K. R. *et al.* Strikingly different clinicopathological phenotypes determined by progranulin-mutation dosage. *Am J Hum Genet* **90**, 1102-1107 (2012). https://doi.org:10.1016/j.ajhg.2012.04.021

8   De Muynck, L. *et al.* The neurotrophic properties of progranulin depend on the granulin E domain but do not require sortilin binding. *Neurobiol Aging* **34**, 2541-2547 (2013). https://doi.org:10.1016/j.neurobiolaging.2013.04.022

9   Tanaka, Y., Matsuwaki, T., Yamanouchi, K. & Nishihara, M. Increased lysosomal biogenesis in activated microglia and exacerbated neuronal damage after traumatic brain injury in progranulin-deficient mice. *Neuroscience* **250**, 8-19 (2013). https://doi.org:10.1016/j.neuroscience.2013.06.049

10   Gotzl, J. K. *et al.* Opposite microglial activation stages upon loss of PGRN or TREM2 result in reduced cerebral glucose metabolism. *EMBO Mol Med* **11** (2019). https://doi.org:10.15252/emmm.201809711

11   Lui, H. *et al.* Progranulin Deficiency Promotes Circuit-Specific Synaptic Pruning by Microglia via Complement Activation. *Cell* **165**, 921-935 (2016). https://doi.org:10.1016/j.cell.2016.04.001

12   Huang, M. *et al.* Network analysis of the progranulin-deficient mouse brain proteome reveals pathogenic mechanisms shared in human frontotemporal dementia caused by GRN mutations. *Acta Neuropathol Commun* **8**, 163 (2020). https://doi.org:10.1186/s40478-020-01037-x

13   Simon, M. J., Logan, T., DeVos, S. L. & Di Paolo, G. Lysosomal functions of progranulin and implications for treatment of frontotemporal dementia. *Trends Cell Biol* **33**, 324-339 (2023). https://doi.org:10.1016/j.tcb.2022.09.006

14   Zhou, X. *et al.* Regulation of cathepsin D activity by the FTLD protein progranulin. *Acta Neuropathol* **134**, 151-153 (2017). https://doi.org:10.1007/s00401-017-1719-5

15   Tanaka, Y. *et al.* Progranulin regulates lysosomal function and biogenesis through acidification of lysosomes. *Hum Mol Genet* **26**, 969-988 (2017). https://doi.org:10.1093/hmg/ddx011

16   Logan, T. *et al.* Rescue of a lysosomal storage disorder caused by Grn loss of function with a brain penetrant progranulin biologic. *Cell* **184**, 4651-4668 e4625 (2021). https://doi.org:10.1016/j.cell.2021.08.002

17   Gotzl, J. K. *et al.* Common pathobiochemical hallmarks of progranulin-associated frontotemporal lobar degeneration and neuronal ceroid lipofuscinosis. *Acta Neuropathol* **127**, 845-860 (2014). https://doi.org:10.1007/s00401-014-1262-6

18   Gotzl, J. K. *et al.* Early lysosomal maturation deficits in microglia triggers enhanced lysosomal activity in other brain cells of progranulin knockout mice. *Mol Neurodegener* **13**, 48 (2018). https://doi.org:10.1186/s13024-018-0281-5

19   Beel, S. *et al.* Progranulin functions as a cathepsin D chaperone to stimulate axonal outgrowth in vivo. *Hum Mol Genet* **26**, 2850-2863 (2017). https://doi.org:10.1093/hmg/ddx162

20   Hasan, S. *et al.* Multi-modal Proteomic Characterization of Lysosomal Function and Proteostasis in Progranulin-Deficient Neurons. *bioRxiv* (2023). https://doi.org:10.1101/2023.02.24.529955

21   Zhou, X. *et al.* Progranulin deficiency leads to reduced glucocerebrosidase activity. *PLoS One* **14**, e0212382 (2019). https://doi.org:10.1371/journal.pone.0212382

22   Reifschneider, A. *et al.* Loss of TREM2 rescues hyperactivation of microglia, but not lysosomal deficits and neurotoxicity in models of progranulin deficiency. *EMBO J* **41**, e109108 (2022). https://doi.org:10.15252/embj.2021109108

23   Marschallinger, J. *et al.* Lipid-droplet-accumulating microglia represent a dysfunctional and proinflammatory state in the aging brain. *Nat Neurosci* **23**, 194-208 (2020). https://doi.org:10.1038/s41593-019-0566-1

24   Evers, B. M. *et al.* Lipidomic and Transcriptomic Basis of Lysosomal Dysfunction in Progranulin Deficiency. *Cell Rep* **20**, 2565-2574 (2017). https://doi.org:10.1016/j.celrep.2017.08.056

25   Boland, S. *et al.* Deficiency of the frontotemporal dementia gene GRN results in gangliosidosis. *Nat Commun* **13**, 5924 (2022). https://doi.org:10.1038/s41467-022-33500-9

26   Paushter, D. H., Du, H., Feng, T. & Hu, F. The lysosomal function of progranulin, a guardian against neurodegeneration. *Acta Neuropathol* **136**, 1-17 (2018). https://doi.org:10.1007/s00401-018-1861-8

27   Holler, C. J., Taylor, G., Deng, Q. & Kukar, T. Intracellular Proteolysis of Progranulin Generates Stable, Lysosomal Granulins that Are Haploinsufficient in Patients with Frontotemporal Dementia Caused by GRN Mutations. *eNeuro* **4** (2017). https://doi.org:10.1523/ENEURO.0100-17.2017

28   Lee, C. W. *et al.* The lysosomal protein cathepsin L is a progranulin protease. *Mol Neurodegener* **12**, 55 (2017). https://doi.org:10.1186/s13024-017-0196-6

29   Mohan, S. *et al.* Processing of progranulin into granulins involves multiple lysosomal proteases and is affected in frontotemporal lobar degeneration. *Mol Neurodegener* **16**, 51 (2021). https://doi.org:10.1186/s13024-021-00472-1

30   Root, J. *et al.* Granulins rescue inflammation, lysosome dysfunction, and neuropathology in a mouse model of progranulin deficiency. *bioRxiv* (2023). https://doi.org:10.1101/2023.04.17.536004

31   Dall, E. & Brandstetter, H. Mechanistic and structural studies on legumain explain its zymogenicity, distinct activation pathways, and regulation. *Proc Natl Acad Sci U S A* **110**, 10940-10945 (2013). https://doi.org:10.1073/pnas.1300686110

32   Maehr, R. *et al.* Asparagine endopeptidase is not essential for class II MHC antigen presentation but is required for processing of cathepsin L in mice. *J Immunol* **174**, 7066-7074 (2005). https://doi.org:10.4049/jimmunol.174.11.7066

33   Shirahama-Noda, K. *et al.* Biosynthetic processing of cathepsins and lysosomal degradation are abolished in asparaginyl endopeptidase-deficient mice. *J Biol Chem* **278**, 33194-33199 (2003). https://doi.org:10.1074/jbc.M302742200

34   Herskowitz, J. H. *et al.* Asparaginyl endopeptidase cleaves TDP-43 in brain. *Proteomics* **12**, 2455-2463 (2012). https://doi.org:10.1002/pmic.201200006

35   Gieselmann, V., Hasilik, A. & von Figura, K. Processing of human cathepsin D in lysosomes in vitro. *J Biol Chem* **260**, 3215-3220 (1985).

36   Dall, E. & Brandstetter, H. Structure and function of legumain in health and disease. *Biochimie* **122**, 126-150 (2016). https://doi.org:10.1016/j.biochi.2015.09.022

37   Igaz, L. M. *et al.* Enrichment of C-terminal fragments in TAR DNA-binding protein-43 cytoplasmic inclusions in brain but not in spinal cord of frontotemporal lobar degeneration and amyotrophic lateral sclerosis. *Am J Pathol* **173**, 182-194 (2008). https://doi.org:10.2353/ajpath.2008.080003

38   Buratti, E. TDP-43 post-translational modifications in health and disease. *Expert Opin Ther Targets* **22**, 279-293 (2018). https://doi.org:10.1080/14728222.2018.1439923

39   Zhao, L. *et al.* Structural analysis of asparaginyl endopeptidase reveals the activation mechanism and a reversible intermediate maturation stage. *Cell Res* **24**, 344-358 (2014). https://doi.org:10.1038/cr.2014.4

40   Li, D. N., Matthews, S. P., Antoniou, A. N., Mazzeo, D. & Watts, C. Multistep autoactivation of asparaginyl endopeptidase in vitro and in vivo. *J Biol Chem* **278**, 38980-38990 (2003). https://doi.org:10.1074/jbc.M305930200

41   Sjostedt, E. *et al.* An atlas of the protein-coding genes in the human, pig, and mouse brain. *Science* **367** (2020). https://doi.org:10.1126/science.aay5947

42   Human Protein Atlas. *https://www.proteinatlas.org/ENSG00000101439-CST3/tissue/primary+data*, 2023).

43   Breznik, B., Mitrovic, A., T, T. L. & Kos, J. Cystatins in cancer progression: More than just cathepsin inhibitors. *Biochimie* **166**, 233-250 (2019). https://doi.org:10.1016/j.biochi.2019.05.002

44   Chan, K. Y. *et al.* Engineered AAVs for efficient noninvasive gene delivery to the central and peripheral nervous systems. *Nat Neurosci* **20**, 1172-1179 (2017). https://doi.org:10.1038/nn.4593

45   Werner, G. *et al.* Loss of TMEM106B potentiates lysosomal and FTLD-like pathology in progranulin-deficient mice. *EMBO Rep* **21**, e50241 (2020). https://doi.org:10.15252/embr.202050241

46   Bacioglu, M. *et al.* Neurofilament Light Chain in Blood and CSF as Marker of Disease Progression in Mouse Models and in Neurodegenerative Diseases. *Neuron* **91**, 494-496 (2016). https://doi.org:10.1016/j.neuron.2016.07.007

47   Zetterberg, H. *et al.* The role of neurofilament light in genetic frontotemporal lobar degeneration. *Brain Commun* **5**, fcac310 (2023). https://doi.org:10.1093/braincomms/fcac310

48   Klein, Z. A. *et al.* Loss of TMEM106B Ameliorates Lysosomal and Frontotemporal Dementia-Related Phenotypes in Progranulin-Deficient Mice. *Neuron* **95**, 281-296 e286 (2017). https://doi.org:10.1016/j.neuron.2017.06.026

49   Zhou, X. *et al.* Lysosomal processing of progranulin. *Mol Neurodegener* **12**, 62 (2017). https://doi.org:10.1186/s13024-017-0205-9

50   Kumar, S. T. *et al.* Seeding the aggregation of TDP-43 requires post-fibrillization proteolytic cleavage. *Nat Neurosci* **26**, 983-996 (2023). https://doi.org:10.1038/s41593-023-01341-4

51   Basurto-Islas, G., Grundke-Iqbal, I., Tung, Y. C., Liu, F. & Iqbal, K. Activation of asparaginyl endopeptidase leads to Tau hyperphosphorylation in Alzheimer disease. *J Biol Chem* **288**, 17495-17507 (2013). https://doi.org:10.1074/jbc.M112.446070

52   Zhang, Z. *et al.* Cleavage of tau by asparagine endopeptidase mediates the neurofibrillary pathology in Alzheimer's disease. *Nat Med* **20**, 1254-1262 (2014). https://doi.org:10.1038/nm.3700

53   Meeter, L. H. *et al.* Neurofilament light chain: a biomarker for genetic frontotemporal dementia. *Ann Clin Transl Neurol* **3**, 623-636 (2016). https://doi.org:10.1002/acn3.325

54   Rohrer, J. D. *et al.* Serum neurofilament light chain protein is a measure of disease intensity in frontotemporal dementia. *Neurology* **87**, 1329-1336 (2016). https://doi.org:10.1212/WNL.0000000000003154

55   Woollacott, I. O. & Rohrer, J. D. The clinical spectrum of sporadic and familial forms of frontotemporal dementia. *J Neurochem* **138 Suppl 1**, 6-31 (2016). https://doi.org:10.1111/jnc.13654

56   Barmada, S. J. *et al.* Autophagy induction enhances TDP43 turnover and survival in neuronal ALS models. *Nat Chem Biol* **10**, 677-685 (2014). https://doi.org:10.1038/nchembio.1563

57   Root, J., Merino, P., Nuckols, A., Johnson, M. & Kukar, T. Lysosome dysfunction as a cause of neurodegenerative diseases: Lessons from frontotemporal dementia and amyotrophic lateral sclerosis. *Neurobiol Dis* **154**, 105360 (2021). https://doi.org:10.1016/j.nbd.2021.105360

58   Zhang, J. *et al.* Neurotoxic microglia promote TDP-43 proteinopathy in progranulin deficiency. *Nature* **588**, 459-465 (2020). https://doi.org:10.1038/s41586-020-2709-7 Zhang,

59   Z. *et al.* Asparagine endopeptidase cleaves alpha-synuclein and mediates pathologic activities in Parkinson's disease. *Nat Struct Mol Biol* **24**, 632-642 (2017). https://doi.org:10.1038/nsmb.3433

60   Hosokawa, M. *et al.* Accumulation of multiple neurodegenerative disease-related proteins in familial frontotemporal lobar degeneration associated with granulin mutation. *Sci Rep* **7**, 1513 (2017). https://doi.org:10.1038/s41598-017-01587-6

61   Wang, H. *et al.* C/EBPbeta/AEP is age-dependently activated in Parkinson's disease and mediates alpha-synuclein in the gut and brain. *NPJ Parkinsons Dis* **9**, 1 (2023). https://doi.org:10.1038/s41531-022-00430-8

62   Xu, H. M. *et al.* PGRN Is Associated with Late-Onset Alzheimer's Disease: a Case-Control Replication Study and Meta-analysis. *Mol Neurobiol* **54**, 1187-1195 (2017). https://doi.org:10.1007/s12035-016-9698-4

63   Katsumata, Y. *et al.* Multiple gene variants linked to Alzheimer's-type clinical dementia via GWAS are also associated with non-Alzheimer's neuropathologic entities. *Neurobiol Dis* **174**, 105880 (2022). https://doi.org:10.1016/j.nbd.2022.105880

64   Rhinn, H., Tatton, N., McCaughey, S., Kurnellas, M. & Rosenthal, A. Progranulin as a therapeutic target in neurodegenerative diseases. *Trends Pharmacol Sci* **43**, 641-652 (2022). https://doi.org:10.1016/j.tips.2021.11.015

65   Cook, C., Zhang, Y. J., Xu, Y. F., Dickson, D. W. & Petrucelli, L. TDP-43 in neurodegenerative disorders. *Expert Opin Biol Ther* **8**, 969-978 (2008). https://doi.org:10.1517/14712598.8.7.969

66   Huang, W. *et al.* TDP-43: From Alzheimer's Disease to Limbic-Predominant Age-Related TDP-43 Encephalopathy. *Front Mol Neurosci* **13**, 26 (2020). https://doi.org:10.3389/fnmol.2020.00026

67   Kayasuga, Y. *et al.* Alteration of behavioural phenotype in mice by targeted disruption of the progranulin gene. *Behavioural Brain Research* **185**, 110-118 (2007). https://doi.org:S0166-4328(07)00369-5 [pii]10.1016/j.bbr.2007.07.020

68   Chen, J. M., Rawlings, N. D., Stevens, R. A. & Barrett, A. J. Identification of the active site of legumain links it to caspases, clostripain and gingipains in a new clan of cysteine endopeptidases. *FEBS Lett* **441**, 361-365 (1998). https://doi.org:10.1016/s0014-5793(98)01574-9

69   Abud, E. M. *et al.* iPSC-Derived Human Microglia-like Cells to Study Neurological Diseases. *Neuron* **94**, 278-293 e279 (2017). https://doi.org:10.1016/j.neuron.2017.03.042

70   Dannert, A., Klimmt, J., Cardoso Goncalves, C., Crusius, D. & Paquet, D. Reproducible and scalable differentiation of highly pure cortical neurons from human induced pluripotent stem cells. *STAR Protoc* **4**, 102266 (2023). https://doi.org:10.1016/j.xpro.2023.102266

71   Capell, A. *et al.* Rescue of progranulin deficiency associated with frontotemporal lobar degeneration by alkalizing reagents and inhibition of vacuolar ATPase. *J Neurosci* **31**, 1885-1894 (2011). https://doi.org:10.1523/JNEUROSCI.5757-10.2011

72   Wils, H. *et al.* Cellular ageing, increased mortality and FTLD-TDP-associated neuropathology in progranulin knockout mice. *J Pathol* **228**, 67-76 (2012). https://doi.org:10.1002/path.4043

Acknowledgement

Author information

Authors and Affiliations

Present address:

Sophie Robinson, Cure Ventures, Boston, MA, USA.

Todd Logan, BioMarin Pharmaceutical Inc., San Rafael, CA, USA.

Anika Reifschneider, Bristol Myers Squibb, Munich, Germany.

Author contributions

AC and CH conceived and designed the study and wrote the manuscript with the help of MTM, MR and SR. SR, MR and DP designed, performed and analyzed iPSC experiments. MR, DE, HR and AR performed and analyzed primary neuronal and microglial experiments. KB cloned LGMN constructs. MR performed and analyzed HeLa conditioned media-treated neuron experiments. KB and GW performed

experiments with MEF, mouse brain and FTLD-*GRN* patient material and recombinant LGMN. MTM and MR performed *in vivo* mouse experiments and MTM analyzed the AAV-overexpression study in *Grn* ko mice. MJS, TL and GDP generated, MR analyzed the PTV:PGRN study. QM conducted the cystatin experiments. AA and SE generated and purified the AAV9-Cst7. CVB and EW provided validated FTLD-*GRN* patients brain samples. MD co-initiated the study and performed liver lysosome isolation on mice provided by AC, MTM and TR. SG and BB discovered and characterized the legumain inhibitor (LGMN inh). All authors commented on the manuscript.

These authors contributed equally:

Sophie Robinson, Marvin Reich and Maria-Teresa Mühlhofer

Corresponding authors

Correspondence to Anja Capell or Christian Haass

Ethics declarations

CH collaborates with Denali Therapeutics, participated on one advisory board meeting of Biogen and is a member of the advisory board of AviadoBio. DP is a scientific advisor of ISAR Bioscience. MJS, TL and GDP are full time employees and/or shareholders of Denali Therapeutics Inc. SG and BB are full time employees and/or shareholders of F. Hoffmann - La Roche Ltd.

Additional Information

Extended data figures and tables

Extended Data Fig. 1: Elevated LGMN maturation and activity upon PGRN deficiency results in altered cathepsin processing.

Extended Data Fig. 2: Enhanced LGMN activity of *Grn* ko mice and MEF is rescued upon PGRN expression.

Extended Data Fig. 3: PGRN and LGMN are enriched in microglia.

Extended Data Fig. 4: LGMN deficiency results in reduced generation of single granulins in liver lysosomes.

Extended Data Fig. 5: LGMN inhibition by cystatin C and cystatin F.

Extended Data Fig. 6: Potency and selectivity of LGMN inhibitor.

Extended Data Fig. 7: Overexpressed hLGMN localizes predominantly to neurons, astrocytes and microglia.

Extended Data Table 1: Information on human brain tissue

Extended data methods

Experimental mouse models

The second *Grn* ko mouse model and the *Grn* ko/h*TfR*mu/hu ki were previously generated and characterized. *Grn* ko on a C57Bl6/J background were obtained from Jackson Laboratories (JAX strain 013175)[1]. *TfR*mu/hu ki mice (also on a C57Bl6/J background) expressing a chimeric TfR receptor (human TfR apical domain knocked into the mouse receptor) were developed by generating a knock-in of the human apical TfR mouse line using CRISPR, as described previously[2]. Homozygous *TfR*mu/hu male mice were bred to female *Grn*^{+/−} mice to generate *Grn*^{−/−} x *TfR*mu/hu mice. Constitutive *Lgmn* ko mice was generated on a C57Bl6/J background by CRISPR/Cas9 induced deletion of exon 3 of the *Lgmn* gene (842bp) leading to a frameshift knockout by an early stop codon.

Mouse handling and tissue collection at Denali Therapeutics

Animal weights were collected at the start and end of the study. Mice received therapeutic treatment *via* intravenous (IV) tail vein injection (~200 µl total injection volume). At indicated endpoints animals were anesthetized with tribromoethanol. Following plasma collection, mice were transcardially perfused with ice-cold PBS.

1

138

Tissues were then collected, weighed, frozen on dry ice and stored at -80ºC for subsequent analysis.

Isolation of liver lysosome

As described before[3] mice were injected with 4 µl/g bodyweight with 17% (w/v) tyloxapol in 0.9% NaCl four days prior to killing and organ removal. After the removal of the liver, the liver was homogenized in 5 ml ice-cold 0.25 M sucrose with four strokes at 1,000 rpm in a Potter-Elvehjem homogenizer. The homogenate was subsequently centrifuged for 10 min at 1,000 x g in a tabletop centrifuge, the supernatant was removed and the pellet re-extracted with another 2 ml of 0.25 M sucrose and centrifuged again. The pooled supernatants (postnuclear supernatant; PNS) were used for differential ultracentrifugation: 9 ml of the PNS were centrifuged at 56,000 x g for 7 min (70.1 Ti rotor, Beckmann, Coulter). The supernatant was removed, the pellet (mitochondria / lysosome fraction; ML) homogenized in 8 ml 0.25 M sucrose and centrifuged again at 56,000 x g for 7 min. The final pellet was resuspended in 3 ml of sucrose solution with a density of 1.21 g/ml. This fraction was overlaid with sucrose solutions with a density of 1.15 g/ml (3 ml), 1.14 g/ml (3 ml) and finally 1.06 g/ml to obtain a discontinuous sucrose gradient. The sucrose gradient was centrifuged at 110,000 x g for 150 min in a swinging bucket rotor (SW41 Ti rotor, Beckmann Coulter). Lysosomes were collected from the interphase between the sucrose solution with a density of 1.14 g/ml and 1.06 g/ml.

Treatment of mice with PTV:PGRN

PTV:PGRN was generated at DENALI Therapeuticas as previously described (Logan et al.). Mice received 10 mg/kg PTV:PGRN *via* intravenous (IV) tail vein injection (~200 µl total injection volume) and tissue collected either 7 or 14 days after treatment.

Transfection of MEF with *Grn* cDNA

MEF *Grn* ko were stably transfected with mouse *Grn* cDNA as described before[4].

Cloning of *Cst3* and *Cst7* constructs.

Mouse cystation-3 (# MR225378, OriGene) and cystatin-7 (# MR222507, OriGene) myc-tagged cDNA clones were subcloned into the BamHI/EcoRI sites of pcDNA3 using the following primers:

Cst3 (BamHI) forward 5'-CCCGGATCCCCAACCATGGCCAGCCCGCTGC-3'

Cst7 (BamHI) forward 5'- CCCGGATCCCCAGCCATGCCCTGGTCCTGG -3'

2

Cst3/7 (EcoRI) reverse 5'- CGGAATTCTTAAACCTTATCGTCGTCATCC -3'

Six hundred three base pairs (603 bp) encoding for cystatin-7 were cloned into the BamHI/EcoRI sites of pAAV-hSyn-EGFP (# 50465, Addgene). Serotype AAV9 (pAAV-GOI) virus particles were produced in HEK 293T cells by co-transfection with pAAV-RC, pHelper and pAAV-GOI using Lipofectamine 2000 (ThermoFisher Scientific). After 72 h cells were detached with 0.5 M EDTA and centrifuged for 5 min at 3000 rpm. The pellet was resuspended in 250 µl Neurobasal Medium (ThermoFisher Scientific) followed by 4 freeze-thaw cycles in a dry ice ethanol bath and a 37°C water bath for 2 min per bath and cycle. Centrifugation for 10 min at 10,000 x g generated the viral particles containing supernatant. AAV was stored at -80°C until further use.

In vitro determination of pIC$_{50}$ for the LGMN inhibitor

A modified fluorescence-based activity assay was used to assess the potency of the LGMN inhibitor to inhibit LGMN activity *in vitro*. Recombinant LGMN stored in 25 mM HEPES/NaOH pH 7, 300 mM NaCl, 200 mM trehalose was activated at a concentration of 0.1 mg/mL for 2 h at room temperature in 50 mM sodium actetate pH 4.0. Assay buffer was 20 mM Na-phosphate/citrate pH 5.8, 1 mM EDTA, 0.1% CHAPS. The pre-activated LGMN (c=0,1 nM) was incubated with10 µM of peptide Z-AAN-Rh110 and different doses of LGMN inhibitor. Excitation and emission wavelengths were 485 nm and 520 nm, respectively. Fluorescence was measured after 15 min and 30 min incubation.

Determination of pIC$_{50}$ for the LGMN inhibitor in HEK293A cells

HEK293A overexpressing LGMN were cultured using DMEM (Gibco 31966) supplemented with 10% FCS, 1% Penicillin/Streptomycin and 0.8 mg/ml Geneticin. On day before the assay 16.000 cells/well were plated in 384 well plates. At the assay day cells were treated with dose responses of LGMN inhibitor or DMSO control. Final DMSO concentration for all conditions was 0.6%, and compounds were tested in a 16-point-dose response starting at 60 µM. Cells were incubated with LGMN inhibitor for 2 h, prior to addition of fluorogenic substrate **S** (Roche, final concentration 60 µM)[5]. After addition of substrate cells were incubated for 5 h and the effect was detected by measuring fluorescence intensity at 460 nm after excitation at 380 nm in the living cells.

Protease selectivity screen

3

140

To test the selectivity of the LGMN inhibitor, pIC_{50} values for different proteases were determined using the Protease Assay Service from REACTION BIOLOGY (https://www.reactionbiology.com/services/target-specific-assays/protease-assays). pIC_{50} for LGMN was determined by Roche, Basel.

Immunofluorescence of mouse brain tissue

Freshly isolated brain hemispheres were post-fixed in 4% paraformaldehyde in PBS (Thermo Scientific, J19943-K2) for 24 h at 4°C. Brain hemispheres were transferred to PBS with 0.02% NaN_3 and stored at 4°C until further use. Brain hemispheres were cut in 40 µm sections using a vibratome (Leica VT1200S). Immunofluorescence was performed on free floating sections. Sections were blocked with blocking solution (4% bovine serum albumin (BSA, Sigma A8022-100G) and 0.1% fish skin gelatin (Sigma G7041) in PBS with 0.4% Triton-X) for 1 h at RT. Primary antibodies, hLGMN (R&D, AF 2199, c= 0.4 µg/ml), MAP2 (Novus Biologicals, 1:1000, NB300-213), IBA1 (GeneTex, 10042, c=0.06 ng/µl), GFAP (DAKO, Z0334, c=2.9 µg/ml) were diluted at the indicated concentration in blocking buffer and brain sections were incubated over night at 4°C in the primary antibody solutions. The next day the sections were washed three times with PBS with 0.1% Tween® 20 and subsequently incubated with fluorophore-coupled secondary antibodies (Thermo Fisher Scientific, donkey, c=4 µg/ml) diluted in secondary antibody buffer (4% bovine serum albumin (BSA, Sigma A8022-100G) and 0,1% fish skin gelatin (Sigma G7041) in PBS) with DAPI (c=1 µg/ml) for 2 h at RT. After three washing steps in PBS with 0.1% Tween 20 sections were mounted with Fluoromount-GTM (Invitrogen, 00-498-02).

Image acquisition

Full brain hemispheres were imaged at 4x with a Leica DMi-8 epifluorescence microscope with a DFC9000GT camera. Image mosaics were merged using the Leica LAS X software suite. Representative images were acquired on a Zeiss LSM800 Axio Observer 7 confocal microscope with a 40x oil immersion objective (NA 1.3). A z-stack was acquired and confocal images show an orthogonal projection of six images with a z-stack size of 0.4 µm. Post-processing (adjustment of brightness) of full brain scans was performed in ImageJ and brightness of confocal images was adjusted with the Zen 3.2 (blue edition) software in the same way for all conditions.

Additional antibodies used in figures

4

Antibodies	Dilution		Source
	IB	IF	
Goat anti-mouse CatD	1:1,000	--	# sc-6486, Santa Cruz
Goat anti-mouse CatL	1:1,000	--	# AF965, R&D Systems
Goat anti-cystatin-3	1:1,000	--	# AF1238, R&D Systems
Rabbit anti-GFAP	--	1:1,000	# Z0334, DAKO
Rabbit anti-mouse GFAP	1:5,000	--	# GA52461-2, DAKO
Rabbit anti-mouse IBA1	1:1,000	--	# GTX100042, GeneTex
Rat anti-mouse LAMP1	1:1,000	--	# sc-19992, Santa Cruz
Rabbit anti-mouse tubulin β3 (TUJ)	1:1,000	--	# 5568S, Cell Signaling

Extended data references

1   Yin, F. *et al.* Behavioral deficits and progressive neuropathology in progranulin-deficient mice: a mouse model of frontotemporal dementia. *FASEB J* **24**, 4639-4647 (2010). https://doi.org:10.1096/fj.10-161471

2   Kariolis, M. S. *et al.* Brain delivery of therapeutic proteins using an Fc fragment blood-brain barrier transport vehicle in mice and monkeys. *Sci Transl Med* **12** (2020). https://doi.org:10.1126/scitranslmed.aay1359

3   Markmann, S. *et al.* Quantitative Proteome Analysis of Mouse Liver Lysosomes Provides Evidence for Mannose 6-phosphate-independent Targeting Mechanisms of Acid Hydrolases in Mucolipidosis II. *Mol Cell Proteomics* **16**, 438-450 (2017). https://doi.org:10.1074/mcp.M116.063636

4   Gotzl, J. K. *et al.* Early lysosomal maturation deficits in microglia triggers enhanced lysosomal activity in other brain cells of progranulin knockout mice. *Mol Neurodegener* **13**, 48 (2018). https://doi.org:10.1186/s13024-018-0281-5

5   Krummenacher, D. *et al.* Discovery of Orally Available and Brain Penetrant AEP Inhibitors. *J Med Chem* (2023). https://doi.org:10.1021/acs.jmedchem.3c01804
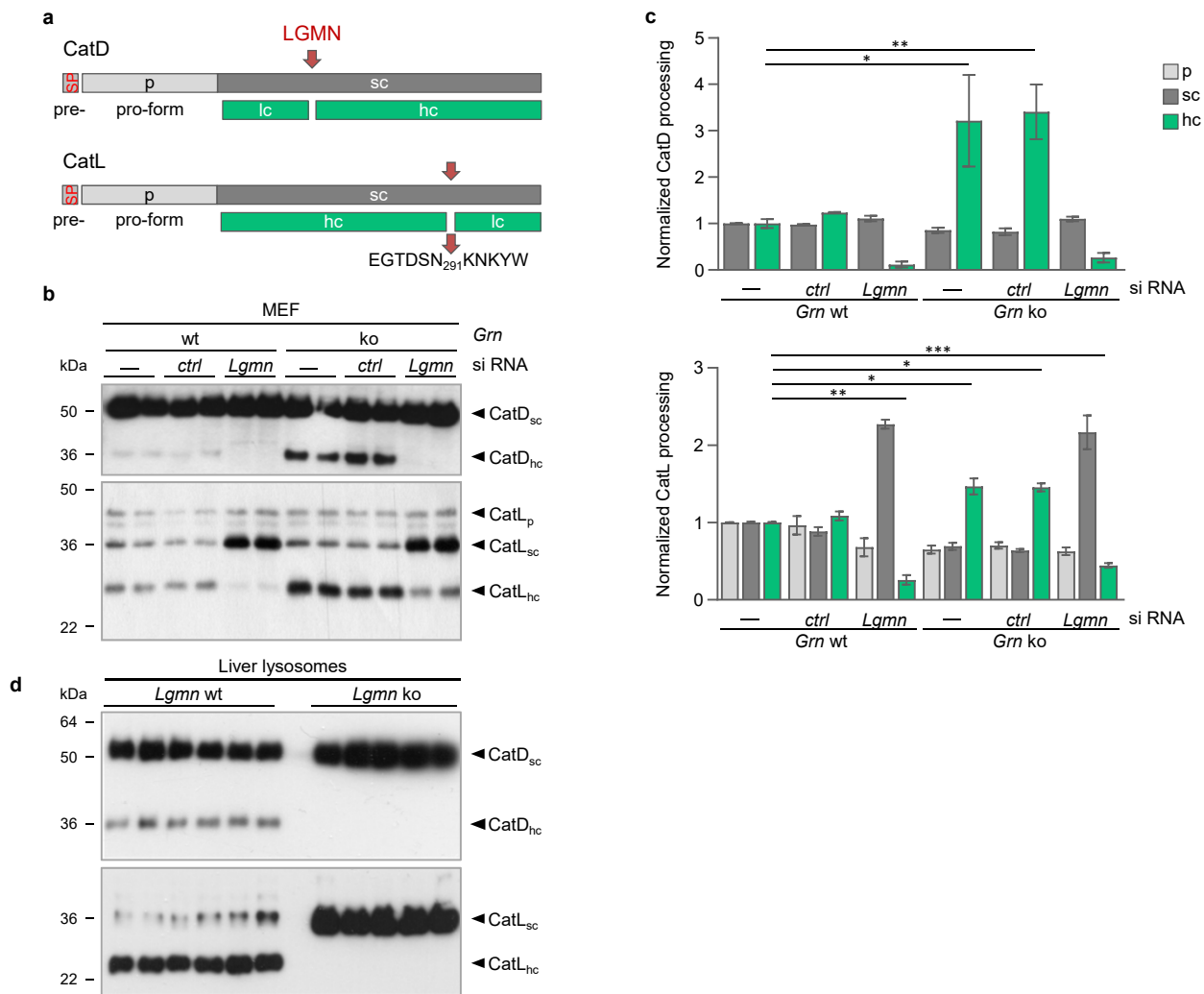
142

Extended Data Fig. 1: Elevated LGMN maturation and activity upon PGRN deficiency results in altered cathepsin processing.

a, Processing of cathepsin D (CatD) and L (CatL) by LGMN is shown schematically. **b**, Representative immunoblots of MEF isolated from wt and *Grn* ko mice probed for CatD and CatL. MEF were either non- (-), control (*ctrl*) or *Lgmn* siRNA-transfected. CatD, and CatL, proform (p), single chain (sc), heavy chain (hc) are indicated. **c,** CatD and CatL maturation are quantified and normalized to wt (n=4). **d**, Representative immunoblots of liver lysosomes isolated from 6 months old *Lgmn* ko and wt mice probed for CatD and CatL. Data are mean ± s.d; unpaired two-tailed t-test, *p<0.05, **p<0.01, ****p<0.0001.
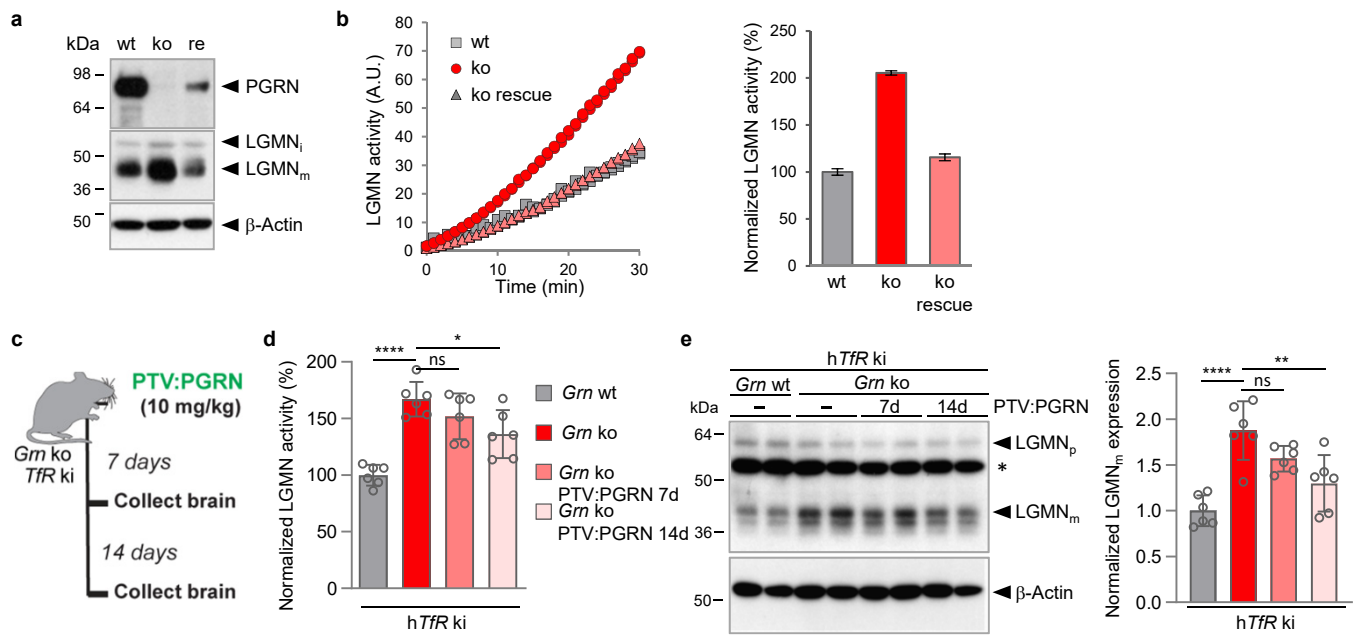
Extended Data Fig. 1.   143

Extended Data Fig. 2: Enhanced LGMN activity of *Grn* ko mice and MEF is rescued upon PGRN expression.

a, Representative immunoblots of MEF wt, *Grn* ko and *Grn* ko stably transfected with a mouse *Grn* cDNA probed for PGRN, LGMN, and β-actin to verify equal loading. **b**, LGMN substrate turnover and quantification of LGMN activity normalized to MEF wt of biologically independent duplicates is shown as mean ± s.d.. **c,** Schematic of PTV:PGRN single dosing study in *Grn* ko/h*TfR* ki. **d**, LGMN activity of a *Grn* wt, *Grn* ko, and *Grn* ko treated with a single 10 mg/kg i.v. dose of PTV:PGRN for 7 d and 14 d. Data indicate the mean normalized to wt. (n=6 mice per genotype and treatment, 3-4-month-old). **e**, Representative immunoblot for LGMN in total brain homogenate of wt and *Grn* ko non-treated and treated mice. Proform (LGMNp), mature form (LGMNm), unspecific band (asterisk) are indicated, β-actin verified equal loading. Quantification of LGMN immunoblot signals normalized to wt (n=6 mice per genotype and treatment).

Statistical significance was determined using one-way ANOVA and Tukey's post hoc test: ns, not significant; *$P<0.05$, **$P<0.01$, ****$P<0.0001$. P values and statistical source data are provided.
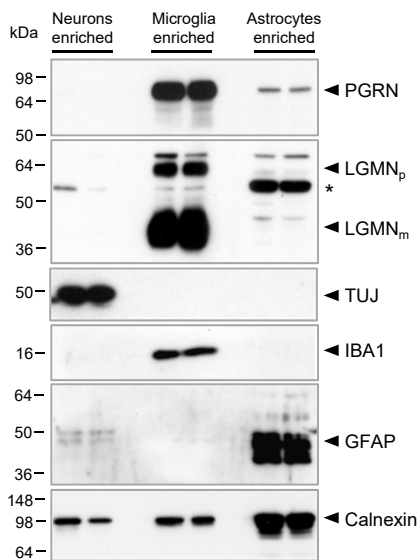
Extended Data Fig. 3: PGRN and LGMN are enriched in microglia.

Representative immunoblots for PGRN and LGMN in microglia-, astrocyte- and neuron-enriched brain cell fractions isolated from 10-month-old mice. Enrichment of each cell fraction is verified by immunoblotting for IBA1, GFAP and TUJ. Equal amounts of protein were loaded for all cell types, calnexin expression varies between cell types. n=2 mice per cell type and genotype.
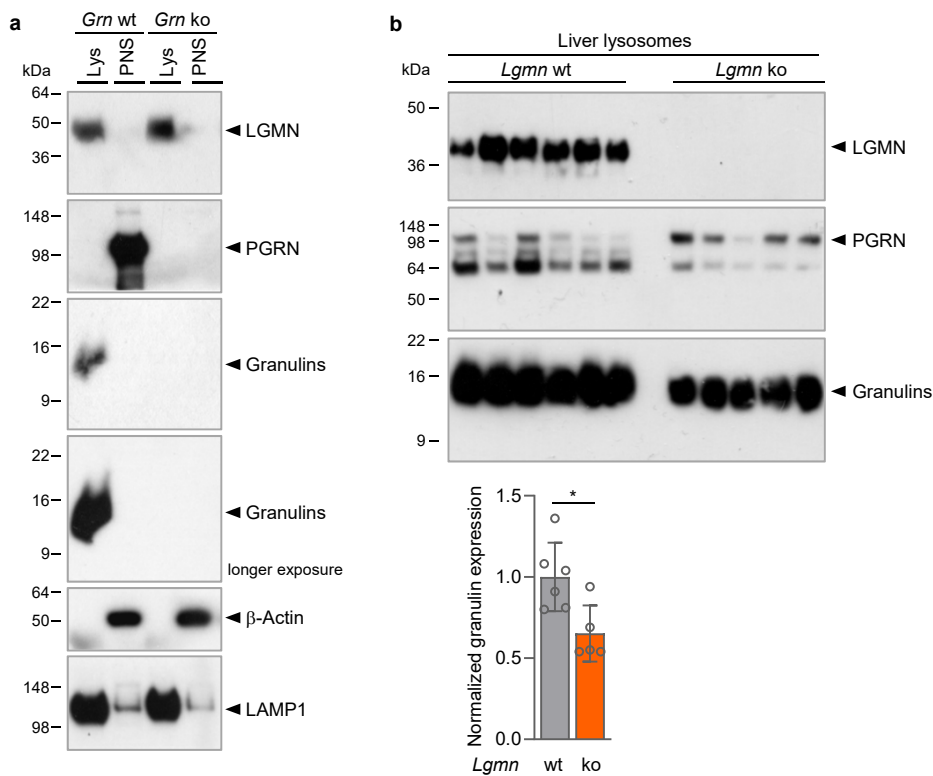
Extended Data Fig. 3   145

Extended Data Fig. 4: LGMN deficiency results in reduced generation of single granulins in liver lysosomes.

a, Representative immunoblot of liver lysosome preparation of wt and *Grn* ko mice probed for LGMN, PGRN, granulins, with β-actin and LAMP1 as loading control for post nuclear supernatant (PNS) and lysosomes (Lys). **b**, Immunoblot of liver lysosome preparation of Lgmn wt and ko mice, probed for LGMN, PGRN and granulins. Data are mean ± s.d. of granulins in lysosome preparation from individual mice (n=5-6); unpaired two-tailed t-test; *p<0.05, *P* values and statistical source data are provided.
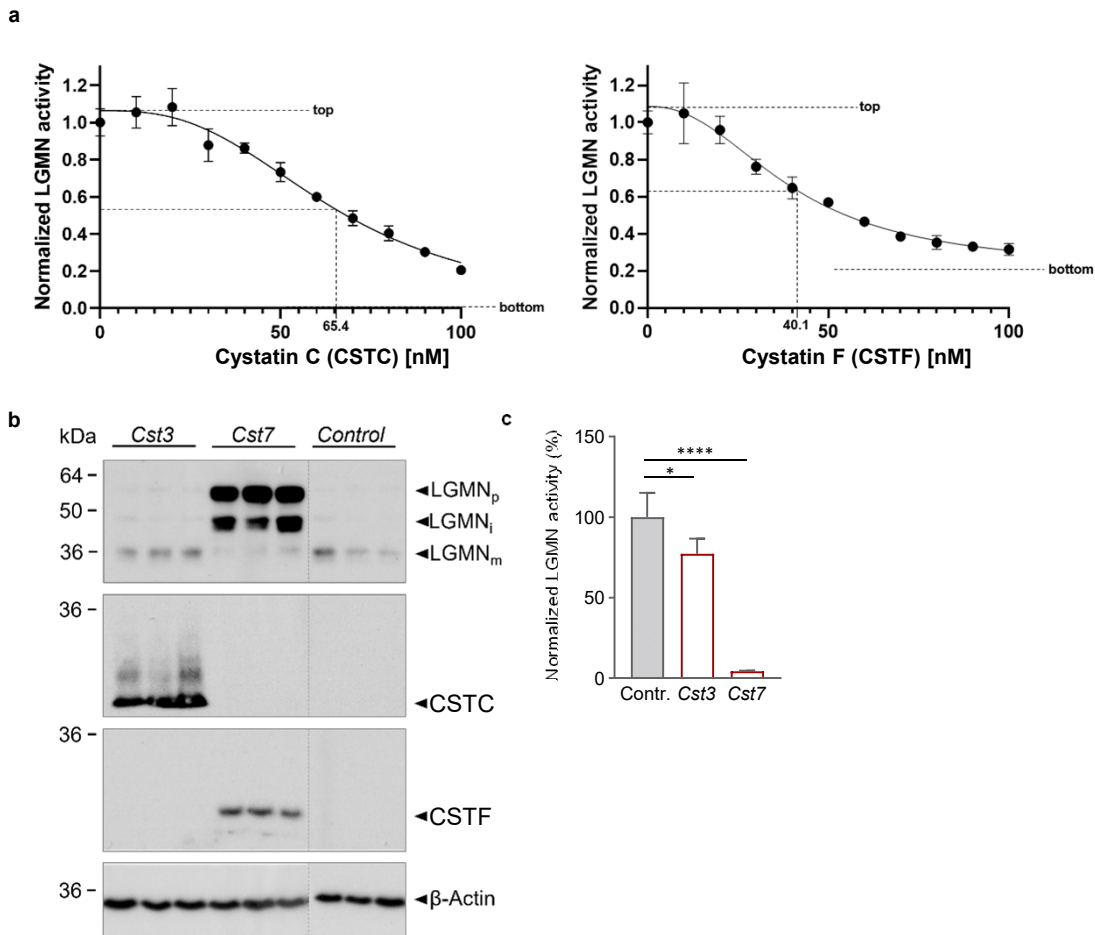
Extended Data Fig. 5: LGMN inhibition by cystatin C and cystatin F.

a, Dose-dependent inhibition of recombinant LGMN via recombinant cystatin C (CSTC) (left) and cystatin F (CSTF) (right). Nonlinear regression (curve fit; variable slope (4 parameters)), top, bottom and IC_{50} are indicated. Data points show the mean ± s.d. normalized to LGMN activity at 0 nM inhibitor (N=3 technical replicates). **b-c,** HEK 293T cells were transfected with *Cst3*, *Cst7* or pcDNA3 (Control). **b,** Immunoblotting indicates proform ($LGMN_p$), intermediate ($LGMN_i$) and mature form ($LGMN_m$) of LGMN, and CSTC and CSTF expression. β-Actin was probed to verify equal loading. **c,** In vitro LGMN activity assay of cell lysates. Data are mean ± s.d. of biologically independent experiments normalized to control (n=3). Statistical significance was determined by one-way ANOVA and Dunnett's multiple comparisons post-hoc test: *p<0.05, ****p<0.0001.
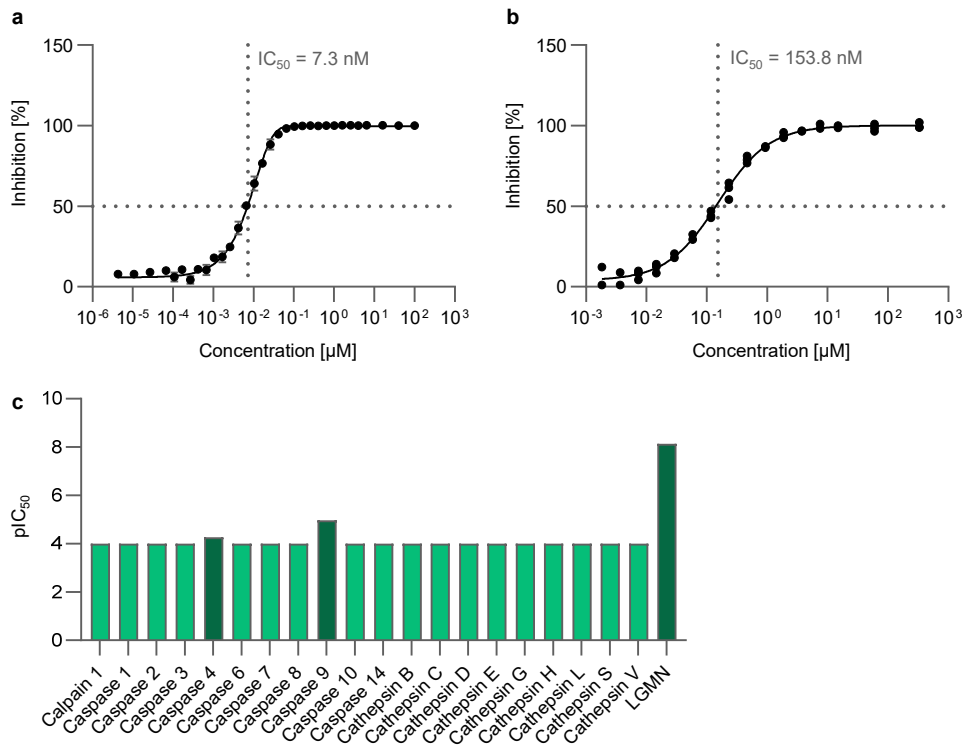
Extended Data Fig. 6: Potency and selectivity of LGMN inhibitor.

a, Dose-dependent inhibition of pre-activated recombinant LGMN by the LGMN inhibitor. An IC_{50} of 7.3 nM with a 95% confidence interval from 6.9-7.7 nM was determined (Nonlinear regression curve fit; variable slope (4 parameters)). Data points show the mean of six technical replicates ± s.d. **b**, Dose-dependent inhibition of LGMN in HEK293A cells by the LGMN inhibitor was determined using a cell permeable fluorogenic LGMN substrate. Effects of test compounds were normalized to effect of reference compound and DMSO control. An IC_{50} of 153.8 nM with a 95% confidence interval from 138.8-170.1 nM was determined (Nonlinear regression curve fit; variable slope (4 parameters)). Data points show the mean of four biological replicates ± s.d. **c**, *In vitro selectivity* screen for the LGMN inhibitor. Proteases with a pIC_{50} below the limit of detection of 4 are depicted in light green, proteases having a pIC_{50} >4 in dark green.

Extended Data Fig. 7: Overexpressed hLGMN localizes predominantly to neurons, astrocytes and microglia.

a, Immunofluorescence staining of sagittal brain sections 3 months post tail vein injection of AAV-PHP.eB.CAG-hLGMN (DAPI in blue, hLGMN in cyan, n=3 mice, scale bar = 1500 µm). **b**, Immunofluorescence staining for neuronal marker MAP2 (magenta), microglial marker IBA1 (orange) or astrocytic marker GFAP (yellow) and DAPI (blue). White arrowheads show co-localization of hLGMN with astrocytes, green arrowheads co-localization of hLGMN with microglia. (n=3 mice, scale bar = 20 µm).

Patient ID	Pathological diagnosis	Gender	Age at death	Mutation	Clinical diagnosis, subtype	Brain region	
P008	FTLD-TDP A	f	69	GRN IVS1+5G>C	FTD, bvFTD	FCx	BA9
P010	FTLD-TDP A	m	63	GRN IVS1+5G>C	FTD, PPA (nfvPPA)	FCx	BA9
P011	FTLD-TDP A	f	75	GRN IVS1+5G>C	FTD, bvFTD	FCx	BA9
P017	FTLD-TDP A	f	72	GRN IVS1+5G>C	FTD, PPA (nfvPPA)	FCx	BA9
P018	FTLD-TDP A	m	74	GRN IVS1+5G>C	Dementia, mixed phenotype	FCx	BA10
P025	FTLD-TDP A	f	72	pAla89Val fs*41	FTD, PPA	FCx	BA10
P035	FTLD-TDP A	f	79	GRN IVS1+5G>C	FTD, bvFTD	FCx	BA9
P036	FTLD-TDP A	m	71	pThr330Ala fs*6	FTD, unspecified	FCx	BA9
P037	FTLD-TDP A	f	67	GRN IVS1+5G>C	FTD, PPA (nfvPPA)	FCx	BA9
P038	FTLD-TDP A	m	60	GRN IVS1+5G>C	FTD, bvFTD	FCx	BA9
C001	Def Control	f	83			FCx	BA10
C002	Def Control	m	63			FCx	BA10
C004	Def Control	m	87			FCx	BA10
C011	Def Control	f	64			FCx	BA10
C012	Def Control	m	79			FCx	BA10
C013	Def Control	m	80			FCx	BA10

Extended Data Table 1: Information on human brain tissue.

Summary of clinical, pathological and genetic information of human brain tissue of FTLD-*GRN* and control cases. VIB Department of Molecular Genetics and Antwerp Brain Bank, Institute Born-Bunge: Antwerp, Belgium; m, male; f, female; FCx, frontal cortex.

4. DISCUSSION

4.1. AAV(L):bPGRN - AN ADVANCED PGRN REPLACEMENT THERAPY APPROACH

To date, there is no disease-modifying treatment available for FTD. As a monogenic disease, the subtype FTLD-*GRN* is ideally suited for the development of therapeutics and to study their effect on the hallmark FTD phenotypes. In this thesis a novel therapeutic approach was introduced and assessed for its potential as a potential treatment for FTLD-*GRN* (3.1.). A liver-targeting adenovirus-associated virus, AAV8[243,244], encapsulates a construct that expresses human PGRN fused to the single-chain variable fragment of an IgG engineered to bind to the murine TfR (AAV(L):bPGRN expressing 8D3:PGRN). Upon a single-dose *intravenous* administration in mice, robust expression was achieved in the liver and human PGRN could be detected in the plasma and brains of the treated animals. Treatment was well tolerated and the toxicological assessment of different tissues and blood parameters raised no safety concerns. In both *Grn* KO and *Grn* and *Tmem106b* DKO mice, FTLD-*GRN*-related phenotypes could be ameliorated or reversed by AAV(L):bPGRN treatment, showing that this approach is indeed promising for the treatment of FTLD-*GRN*.

4.1.1. AAV(L):bPGRN AND PTV:PGRN – NOVEL TREATMENT APPROACHES FOR FTLD-*GRN*

AAV(L):bPGRN is a potential alternative to the recently described PTV:PGRN – a recombinant human PGRN that contains a similarly engineered TfR-binding domain for facilitated transcytosis across the BBB[133]. This strategy was also successfully validated in *Grn* KO mice. Importantly, PGRN levels in the brain upon PTV:PGRN treatment were up to five-fold higher compared to the administration of PGRN without an engineered TfR-binding domain. Consequently, dysregulated lipids in the *Grn* KO brain, such as BMP and glucosylsphingosine, were fully normalized after PTV:PGRN treatment[133]. Whether the administration of AAV(L):bPGRN results in brain PGRN levels similar to those achieved *via* PTV:PGRN can't be concluded from these two studies alone, as the ELISA used in the PTV:PGRN study differed significantly from the one used in the AAV(L):bPGRN study. A side-by-side comparison of both therapeutic approaches would therefore be necessary to directly compare brain PGRN levels. Nevertheless, as in the PTV:PGRN study, the brain lipidome could be fully normalized with AAV(L):bPGRN[133]. Microglial activation, assessed by Cd68 and Trem2 levels, as well as lipofuscin accumulation and CSF NfL concentration were all completely rescued as well[133].

The main advantage of AAV(L):bPGRN is the single-dose treatment scheme, avoiding many injections over years, which would most likely be necessary in the case of a PTV:PGRN treatment paradigm. However, the repeated dosing of PTV:PGRN has the advantage of a better control over PGRN levels, allowing corrections, if and when needed. This is critical, as increased PGRN levels have also been associated with various forms of cancer[105,106]. Chronically elevated PGRN levels may therefore increase the risk of developing tumors. Furthermore, the use of the AAV8 serotype leads to the broad transduction of hepatocytes, which has been shown to trigger immune responses in the liver[245]. For these reasons, the chemical and microscopic pathological investigations of multiple tissues were performed after eight months of treatment in the AAV(L):bPGRN study and no abnormalities could be detected. Treatment in patients would of course greatly exceed this time frame and the potential development of tumors will therefore have to be monitored carefully in early clinical trials. Another potential issue with both approaches is the risk of anti-drug antibodies developing as a defense mechanism of the immune system directed against the therapeutic, which would result in its degradation[246]. This is a longstanding issue in the pharmaceutical industry and solutions exist, such as the administration of immunosuppressive drugs after screening for potentially reactive patients[246].

Taken together, the study by Logan *et. al* and the one presented here (3.1.) complement each other by presenting a variety of readouts relevant for FTLD-*GRN* that could be ameliorated by peripheral treatment with the brain-penetrant biotherapeutics PTV:PGRN and AAV(L):bPGRN. Both the sub-chronic treatment in the DKO mouse study and the chronic phase treatment in *Grn* KO mice were successful, establishing this as a viable therapeutic paradigm for both pre-symptomatic and symptomatic FTLD-*GRN* patients. This is particularly important for this disease, as pre-symptomatic patients can easily be identified based on their plasma PGRN levels[94-96]. Both treatment schemes also appeared to be safe in the assessed time frame and achieved a widespread biodistribution, raising PGRN levels extracellularly and intracellularly[133]. PTV:PGRN is currently in clinical development in a phase I/II study, its safety and efficacy in humans will therefore soon be known (clinical trial ID: NCT05262023).

4.1.2. BRAIN-PENETRANT PGRN REPLACEMENT IN COMPARISON WITH ALTERNATIVE FTLD-*GRN* TREATMENT APPROACHES

Besides PTV:PGRN, several other FTLD-*GRN* drugs are currently in clinical development, all aiming at raising PGRN levels to counteract the haploinsufficiency of PGRN that is causative of disease in FTLD-*GRN* patients[3].

One approach is PGRN replacement by AAV-based gene therapy[234,235]. Unlike AAV(L):bPGRN, in this case the virus is injected directly into the CNS *via cisterna magna*

injection. This approach rescued *Grn* KO phenotypes in early mouse studies, but a recent publication failed to show a rescue of brain phenotypes upon AAV-based PGRN expression in the CNS[234,235,239]. Biodistribution issues will most likely be even more pronounced in patients, considering the much larger size of the human brain. This was already shown by comparing AAV delivery in non-human primates and mice: AAV-driven transgene expression was mainly observed in the cortex and spinal cord in non-human primates[236,237]. PGRN expressed in these tissues, rather than in peripheral ones, might not be distributed as homogeneously as it would have to diffuse through the extracellular space, while PTV:PGRN and 8D3:PGRN reach the brain through the circulatory system and can therefore be uniformly delivered[238]. In the PTV:PGRN study by Logan *et al.*, uptake by both neurons and microglia was shown[133]. In the original AAV(L):bPGRN manuscript, as presented in this thesis (3.1.), biodistribution was not assessed beyond whole-brain PGRN concentrations. In the revision phase, however, its regional distribution was also investigated by immunofluorescence and the brain-wide distribution of 8D3:PGRN was confirmed, as well as its uptake by neurons, microglia, and astrocytes (data not shown). The PGRN signal was further strongly detected throughout the whole brain vasculature and in the choroid plexus, indicating the constant transcytosis of 8D3:PGRN into the brain. Lastly, a potential *caveat* related to a brain-directed AAV delivery strategy is the risk of puncturing the medulla, in addition to the neuroinflammation which was also previously shown to be caused by this administration route[236,240].

Another strategy, currently in phase III clinical trials, is to block the cellular uptake of PGRN using an anti-sortilin antibody. This approach successfully raised PGRN levels in the CSF and plasma of FTLD-*GRN* patients[232,233]. However, an issue with this paradigm is that PGRN is only targeted indirectly *via* the blocking of sortilin. This raises safety concerns, as sortilin performs a variety of functions in the brain. Its ligands include different neurotrophins and pro-neurotrophins, neurotensin, and ciliary neurotrophic factor, all critical to the maintenance of brain homeostasis[247]. In another study for example, the genetic ablation of sortilin resulted in a compromised BBB[248]. Besides the potential side effects arising from the impairment of the other functions of sortilin, this approach only raises PGRN levels extracellularly. As lysosomal dysfunction is a primary phenotype in PGRN deficiency, it is unlikely that this therapeutic approach will have a sustained effect on FTLD-*GRN* pathology[3,249].

Both of these therapeutics are in clinical trials, they might therefore still be suitable disease-modifying treatments for FTLD-*GRN* if the studies show positive results in their clinical outcomes.

4.2. GRN AND TMEM106B DKO MICE AND hiPSC-SYSTEMS AS *BONA FIDE* TRANSLATIONAL MODELS OF FTLD-*GRN*

To test the effect of AAV(L):bPGRN (3.1.), mice harboring a DKO of *Grn* and *Tmem106b* were used as a model of FTLD-*GRN*[169]. In addition, a newly developed hiPSC model with the same DKO was generated to study the effect of PGRN replacement in disease-relevant cell types and in a fully human system.

The DKO mouse model was originally described independently by three laboratories as a *bona fide* FTLD-*GRN* model exhibiting a number of disease-relevant phenotypes[162,169,170]. All the studies showed the impairment of lysosomal degradation and autophagy, as well as microglial and astrocytic hyperactivation. Additionally, demyelination and neurodegeneration were observed in both the spinal cord and the brain of DKO mice[162,169,250]. As a consequence, the transgenics used in Werner *et al.* and Feng *et al.* also presented with early-onset motor impairments and a premature death at around 4.5 months of age[162,169]. Most importantly, these mice showed TDP-43 pathology in the form of cytosolic aggregates positive for pTDP-43 and RIPA-insoluble pTDP-43[162,169,250].

It is important to keep in mind, that FTLD-*GRN* patients usually have a *GRN* mutation in only one allele that causes haploinsufficiency of the protein[74]. Homozygous *GRN* mutations, similar to the *Grn* KO, are ultra-rare and cause NCL[97,125]. However, animals heterozygous for *Grn*, did not show any obvious phenotypes[125,251,252]. The *Grn* KO mouse model, albeit rather being a model for NCL than FTLD-*GRN*, has robust phenotypes that replicate pathologies of both diseases[125]. These include lysosomal dysfunction, neuroinflammation, as well as weak TDP-43 pathology in aged mice[125,130,228]. Nevertheless, without pronounced neurodegeneration and TDP-43 pathology, as well as behavior phenotypes, *Grn* KO mice lack important FTLD-*GRN* hallmarks. Even though the KO of both *Grn* and *Tmem106b* does not recapitulate the genetic background of FTLD-*GRN*, the presence of multiple and robust disease-relevant phenotypes establishes DKO mice as an ideal model to study the efficacy of novel treatment approaches, such as AAV(L):bPGRN.

4.2.1. AAV(L):bPGRN PARTIALLY RESCUES DKO PHENOTYPES IN MICE

Because of their aggressive course of pathology and the premature death at 4.5 months of age, the choice was made to treat the DKO mice in a preventive fashion when evaluating the efficacy of AAV(L):bPGRN. Mice were therefore injected already at six weeks of age. Rescue of the phenotypes originally described in Werner et al. was assessed, namely motor impairment, dysfunctional protein degradation, accumulation of p62, TDP-43, and lipofuscin, and lastly neurodegeneration[169]. These readouts were complemented by the comprehensive omic analyses of global brain lipids and gene transcripts.

4.2.1.1. IMPROVEMENT OF MOTOR IMPAIRMENT AFTER AAV(L):bPGRN TREATMENT

Although motor impairment, caused by the loss of upper and lower motor neurons, is much more common in ALS patients, it has also been documented as happening sporadically in FTLD-*GRN* patients[23,253,254]. Following the observation that DKO mice present with severe motor deficits, rotarod performance was measured longitudinally in order to investigate their decline[162,169,170]. DKO mice rapidly worsened in their performance, while AAV(L):bPGRN-treated DKO mice showed a slower rate of decline and stabilized 4 weeks after treatment, at an age of 10 weeks. The improvement in motor performance was confirmed by testing hindlimb clasping and whether it was possible to flip the mice over. Our findings are in line with another study performed in DKO mice which tested direct CNS delivery of an AAV expressing PGRN[239]. AAV treatment almost completely rescued motor performance in the open field, another flipping test, and stride length. These phenotypes were rescued despite only modest brain PGRN expression levels post injection. Therefore the motor impairment was likely primarily caused by the loss of lower motor neurons, since the neurodegeneration, along with the other pathological phenotypes, could only be ameliorated in the spinal cord, where a robust PGRN expression was observed[239].

4.2.1.2. AAV(L):bPGRN TREATMENT RESTORES LYSOSOMAL FUNCTION

PGRN plays important roles within the lysosome and the KO of *Grn* alone was shown to dysregulate lysosomal homeostasis in mice (see 2.2.). This includes an enhanced lysosomal protease activity, lipidome alterations, lipofuscin accumulation, and the impairment of other protein degradation pathways, such as autophagy and the ubiquitin-proteasome system (reviewed in Simon *et al.*[3]). Other studies already showed, in part, that these pathologies can be rescued by PGRN replacement in *Grn* KO mice, either by AAV-mediated expression in the brain or by PTV:PGRN treatment[133,234]. Arrant *et al.* investigated lipofuscin accumulation and lysosomal enzyme activity, and their AAV treatment normalized both phenotypes[234]. Rescue of lipofuscin accumulation, lipidome alterations, and lysosomal membrane damage was also achieved by Logan *et al.* after PTV:PGRN treatment[133].

In the DKO mouse model the lysosomal dysfunction is strongly exacerbated[162,169,170]. It is therefore not trivial that PGRN replacement in DKO mice would be sufficient to also achieve a similar rescue. In the spinal cord of DKO mice, a CNS-delivered PGRN-expressing AAV successfully reduced lipofuscin and CTSD levels, but not in the brain[239]. In this study, the elevated protein levels of ubiquitin, saposin D, LC3, and p62 were analyzed as markers for impaired protein degradation pathways increased in DKO mice[169]. All of these proteins were at least partially renormalized after AAV(L):bPGRN treatment. In addition, brain

lipidomics and transcriptomics were also performed as part of this study. Lipidome alterations, previously uncharacterized in DKO mice, largely overlapped with those observed in *Grn* KO mice[133]. Consequently, lysosomal lipids such as various BMP species and glucosylsphingosine were rescued to the same extend[133]. Similarly, the gene expression levels of lysosomal proteases and general lysosomal markers, such as *Lamp1* and *Lamp2*, were strongly increased in DKO mice, as shown before[169]. AAV(L):bPGRN treatment fully reversed these expression changes as well. In conclusion, lysosomal dysfunction in DKO mice was rescued by AAV(L):bPGRN treatment. However, lipofuscin accumulation, an important phenotype that is also observed in patients, could not be analyzed conclusively, due to the high inter-animal variability observed[128,168].

4.2.1.3. NEUROINFLAMMATION IS SIGNIFICANTLY REDUCED AFTER AAV(L): bPGRN TREATMENT

The FTLD-*GRN* hallmark neuroinflammation is recapitulated already by *Grn* KO mice, as observed by microglial activation and astrogliosis, but strongly further enhanced in DKO mice[162,169,170,226,228,231]. In previous studies, microglial activation, as assessed by Cd68 immunofluorescence, could be successfully normalized by direct CNS delivery of an AAV expressing PGRN or by PTV:PGRN treatment[133,234]. In addition, PTV:PGRN treatment normalized astrocyte numbers and the brain concentrations of Trem2[133].

Here, bulk RNA sequencing of DKO mouse brains revealed a broad correction of microglial and astrocytic activation markers upon treatment with AAV(L):bPGRN. Validation by immunofluorescence confirmed a reduction in astrocyte numbers and Cd68 signal. However, the number of microglia was not affected as the signal of the microglial marker Iba1 was not reduced after treatment. Although the normalization of microglial activation markers in the whole-brain transcriptome analysis argues for a shift of microglial identity to a more homeostatic state, a detailed analysis using single-cell RNA sequencing of sorted microglia would be necessary to validate this statement.

4.2.1.4. RESCUE OF NEURODEGENERATION, BUT NOT DEMYELINATION, AFTER AAV(L): bPGRN TREATMENT

DKO mice present with severe neurodegeneration, as previously shown by the loss of motor neurons, a strong increase in plasma NfL levels, and demyelination[162,169-171]. Neurodegeneration was assessed in this study by measuring plasma NfL. NfL concentrations were mildly reduced four weeks after treatment and strongly reduced nine weeks after AAV(L):bPGRN treatment in treated DKO mice compared to saline-treated DKO mice. However, lipid alterations related to myelin degradation, such as increased cholesterol esters and reduced galactosylceramide levels, were left almost unaffected by AAV(L):bPGRN, probably because of the severe neuronal loss that is still

much higher in treated DKO mice compared to WT. In order to draw definitive conclusions, a thorough analysis of myelin deficits, as previously done in the DKO mice, would have to be performed[169,171].

4.2.1.5.   TDP-43 PATHOLOGY IS AMELIORATED BY AAV(L): bPGRN TREATMENT

A hallmark of FTLD-*GRN* is the presence of cytoplasmic TDP-43 and pTDP-43 inclusions[33]. This phenotype is recapitulated in the DKO mouse models, as shown by immunoblot and immunofluorescence[162,169,170]. In this study a robust increase of insoluble pTDP-43 was observed in DKO mice, which was reduced by 70% after AAV(L):bPGRN treatment. However, cytosolic TDP-43 inclusions, assessed *via* immunofluorescence against pTDP-43, were only observed sporadically in some animals and could therefore not be subjected to inferential statistics (data not shown). A potential explanation might be that the earlier endpoint of 15 weeks, chosen to avoid animal dropout, instead of terminating the animals at 18-20 weeks as done before, was too early to robustly detect pTDP-43 accumulation by immunofluorescence[169]. Alternatively, these aggregates could be too sparsely distributed across the brain to be picked up robustly by immunofluorescence and whole-brain lysate analysis is necessary for quantifiable assessments. It should be noted that another study using the same mouse model showed consistent and quantifiable pTDP-43 immunofluorescence in the spinal cord of the DKO animals[239]. It is possible that the disease kinetics of this particular phenotype differ across regions of the CNS and that, while the brain at 15 weeks is, histologically, clear of pTDP-43, the more severely affected spinal cord will, at the same age, exhibit clear cytosolic inclusions.

Another readout that could potentially be used to test the efficacy of AAV(L):bPGRN in DKO mice is the investigation of cryptic exons or peptides[64,65]. TDP-43 plays an important role in the post-transcriptional regulation of several proteins[41-43]. Its nuclear depletion and the formation of cytosolic aggregates, as observed in FTLD-*GRN*, can lead to the missplicing of target genes, with the formation of cryptic exons and, if translated, cryptic peptides[64,65]. The presence of insoluble pTDP-43 in the DKO model could already be indicative of TDP-43 mislocalization to the cytosol, which might in turn affect the splicing of its target genes. Preliminary experiments, however, could not identify splicing changes in the target gene *Sort1* (data not shown).

4.2.1.6.   LIMITATIONS OF THE AAV(L):bPGRN DKO MOUSE STUDY

DKO mice made it possible to model FTLD-*GRN* and investigate the effects of AAV(L):bPGRN on several disease-relevant phenotypes. Almost all of these could be ameliorated upon AAV(L):bPGRN treatment, providing supporting evidence for brain-

penetrant PGRN replacement as a treatment approach for FTLD-*GRN*. Nevertheless, this study also presents several limitations.

First of all, by definition, the DKO model cannot be used to study the effect of therapeutics aiming at modulating endogenous PGRN levels, such as the anti-sortilin antibody. At the same time, a full knockout in homozygosity is necessary to assess FTLD-*GRN*-related phenotypes, since these are not observed in heterozygous mice and even a small remnant of PGRN will significantly delay the pathology[125,127,170,251,252].

Another important point is that the AAV(L):bPGRN treatment fails to achieve a full rescue of the pathological phenotypes. The constitutive loss of TMEM106B is an unlikely explanation, as TMEM106B KO mice present with much milder phenotypes compared to the *Grn* KOs and the DKOs[160,162,169,170]. However, the timelines of treatment and tissue collection could explain these outcomes. An independent study, using direct CNS delivery of a PGRN-expressing AAV in DKO mice, compared two different treatment timepoints, six weeks of age – as in the study presented here – and also nine weeks of age[239]. While treatment at six weeks rescued most of the phenotypes in the spinal cord, treating nine-week-old mice resulted in consistently smaller beneficial effects. In fact, robust increases in CTSD, p62, and ubiquitin are already observed in two-month-old DKO mice, suggesting that deficits in protein degradation pathways arise early in disease[239]. Treatment as early as possible might therefore be necessary in order to prevent pathology altogether. Even so, plasma NfL levels, still roughly the same across treatment groups four weeks post injection, were robustly decreased at nine weeks in AAV(L):bPGRN-treated DKOs compared to untreated mice, suggesting a steep downward trajectory. AAV(L):bPGRN might thus not only slow down the progression of pathology, but even be able to revert it, to an extent. To validate this claim, however, later time points would also need to be analyzed in order to better trace the course of the disease.

4.2.2. A NOVEL hiPSC-DERIVED FTLD-*GRN* MODEL

Thanks to their modularity, hiPSCs are a useful tool to model disease and dissect pathomechanisms in a fully human *in vitro* system[255]. These cells can be differentiated into many different cell types and these can then be combined, as needed, to study specific cell-autonomous and intercellular interactions. This modularity is further expanded by the possibility to model the effect of disease-causing mutations. Patient-derived fibroblasts carrying pathogenic variants can be reprogrammed to hiPSCs, but also genome editing can be used to knock-in mutations or to generate a KO of disease-relevant genes[256]. Lastly, hiPSC models hold special significance in translational research, as their adaptability make them a perfect human *in vitro* system to test potential therapeutics. Given the therapeutic-oriented focus of the first study (3.1.), hiPSCs were a natural choice

to model FTLD-*GRN* and to test the efficacy of PGRN replacement therapy using the brain-penetrant biotherapeutic PTV:PGRN.

Initially, a hiPSC line harboring a DKO of both, *GRN* and *TMEM106B*, similar to the mouse model used in this study, was generated using CRISPR/Cas9 genome editing. Based on initial experiments and considering the central role of neuroinflammation in FTLD-*GRN*, hiPSC-derived DKO microglia and WT hiPSC-derived neurons were co-cultured for two weeks[257]. This co-culture model recapitulated multiple FTLD-*GRN*-related pathologies. The protein levels and activity of several cathepsins more than doubled compared to WT co-cultures, indicating lysosomal dysfunction most likely in microglia. Importantly, both the processing of TDP-43 down to its 36 kDa and 25 kDa fragments, as well as its phosphorylation, both also observed in patients, were strongly increased[31,45]. On top of that, this model exhibited neurodegeneration too, as the neuronal network was disrupted and the number of neurons decreased. All of these pathologies were ameliorated upon sustained treatment with PTV:PGRN.

4.2.2.1. LIMITATIONS OF THE hiPSC-DERIVED FTLD-*GRN* MODEL

The hiPSC co-culture model presented in this study not only recapitulates hallmarks of FTLD-*GRN* pathology, but it is further suitable for the assessment of the efficacy of novel therapeutics. However, this system also has some limitations.

TDP-43 mislocalization to the cytosol and the formation of aggregates could not be reliably observed by immunofluorescence or immunoblot. Longer co-cultures, aimed at enhancing TDP-43 pathology are also not possible, as in preliminary experiments this led to a complete neuronal loss. It could also not be ruled out that the processing of TDP-43 observed in co-cultures occurred in microglia after the engulfment of dead or dying neurons or neuronal processes. Excessive pruning was also observed both in *Grn* KO mice and, in the study presented in this thesis, the increased processing of the neuronal marker TUJ1 by DKO microglia is indicative of this[229]. In order to figure out whether TDP-43 processing and also the lysosomal hyperactivity take place in neurons or microglia, the co-cultures could have been sorted using magnetic activated cell sorting followed by the analysis of the two cellular fractions.

Furthermore, the rescue with PTV:PGRN was incomplete, similarly to the DKO mouse study. Cells were treated starting five days after the beginning of the co-cultures to mimic the treatment paradigm at six weeks of age, used in the DKO mouse model. In order to study whether PTV:PGRN might prevent altogether the FTLD-*GRN*-like phenotypes observed *in vitro*, treatment could be started right at the beginning of the co-cultures or microglia could even be pre-treated and then plated along with the neurons.

Whether this model presents with other pathological hallmarks phenocopied by DKO mice and relevant to FTLD-*GRN*, such as autophagic defects and other indicators of lysosomal dysfunction, also remains to be investigated. Likewise, the microglial activation state was not analyzed in this study. Nevertheless, several studies investigated the cell-autonomous effect of single *GRN* KO in hiPSC-derived microglia[133,231,258]. Transcriptome and proteome analysis showed, in these studies, a robust upregulation of lysosomal and microglial activation markers, such as lysosomal proteases, *CD68*, *APOE* or *TREM2*[231,258]. In addition, both an increased recruitment of the lysosomal damage marker Galectin-3 to the lysosomal membrane, as well as the increase of the general lysosomal marker LAMP1 were observed[133].

Lastly, this study highlights the central role of microglia in the pathogenesis of FTLD-*GRN*, as the genetic modification of microglia alone was necessary and sufficient to generate pathology in neurons[226,228,257]. However, as TDP-43 pathology primarily occurs in neurons, the cell-autonomous effect of a DKO in neurons should also be investigated. An intensive study of neuronal lysosomes in WT and *GRN* KO hiPSC-derived neurons described large-scale proteome alterations, increased lysosomal pH, and a decreased protease activity and overall protein turnover in *GRN*-deficient neurons[132]. Other studies showed very mildly increased levels of pTDP-43 and a minor cytosolic mislocalization of TDP-43 in *GRN* KO or in hiPSC-derived neurons from NCL patients[259,260].

4.3. LGMN – THE LINK BETWEEN *GRN* HAPLOINSUFFICIENCY AND TDP-43 PATHOLOGY?

In the second project presented in this thesis (3.2.), the hypothesis that LGMN is the link between *GRN* haploinsufficiency and TDP-43 pathology was investigated. Lysosomal dysfunction is a central hallmark of FTLD-*GRN*, especially since PGRN plays a variety of roles in lysosomal physiology[3,249]. Loss of PGRN was shown to increase the expression and activity of lysosomal proteases not only in microglia, but also in other brain cell types[125,126]. It thus seemed likely that a lysosomal protease might be involved in a downstream cascade resulting in TDP-43 processing and aggregation. This study focused on the lysosomal protease LGMN, as this enzyme was already shown to regulate the maturation of several cathepsins, as well as being capable of cleaving both PGRN and TDP-43[115,175,176,181].

LGMN protein levels and activity were shown to be increased in several biological systems that were analyzed in this study, including FTLD-*GRN* patient brains, hiPSC-derived *GRN* KO microglia, primary *Grn* KO murine microglia, and in the brain of *Grn* KO mice. Importantly, this increase was observed age-independently in *Grn* KO mice, while cathepsins only increased in aged animals, indicating that the higher LGMN levels are not just a byproduct of microgliosis-related lysosomal activation[125,126].

The reason for the increased LGMN levels might be a regulatory role of PGRN in LGMN activation, which is impaired by PGRN haploinsufficiency. This was assessed by co-incubation experiments of recombinant PGRN and LGMN. PGRN, but not the single granulins, was able to slow down autocatalytic LGMN maturation, but did not have an effect on already matured LGMN. Likewise, treatment of *Grn* KO mice with PTV:PGRN reduced LGMN protein levels and activity in the brain in a time-dependent manner. However, a direct interaction of the two proteins was not identified yet and it remains to be elucidated how exactly PGRN prevents the maturation of LGMN.

4.3.1. LGMN TRANSFER FROM MICROGLIA TO NEURONS

LGMN is highly expressed in microglia, but only very little is present in neurons (3.1.). However, TDP-43 pathology primarily occurs in neurons[33]. Excess LGMN, as observed in FTLD-*GRN*, might therefore be transferred from microglia to neurons. To investigate this hypothesis, primary mouse hippocampal neurons were incubated with conditioned media collected from HeLa cells overexpressing LGMN. Inactive pro-LGMN was detected in the media and could be taken up by neurons. This is of importance, as mature LGMN would be denatured and thereby inactivated at neutral pH[172]. After the uptake, LGMN was matured and activated, and subsequently caused enhanced TDP-43 processing. This transfer hypothesis was further supported by hiPSC experiments. In a co-culture of hiPSC-derived *GRN* KO microglia and WT neurons, enhanced TDP-43 processing could be prevented by LGMN inhibition only in neurons by AAV-mediated overexpression of the cysteine-protease inhibitor cystatin F[261]. This provided indirect evidence for a transfer of LGMN from microglia to neurons, as LGMN levels were much higher in microglia than in neurons and also *LGMN* transcripts were only upregulated in *GRN* KO microglia.

Nevertheless, the molecular details of the transfer mechanism were not addressed in this study. One possibility is the secretion of LGMN in exosomes. These small extracellular vesicles were shown to be important for intercellular communication in the brain and can contain various cargo proteins[262]. By proteomics of isolated exosomes, LGMN and other lysosomal proteins were already shown to be present in exosomes of hiPSC-derived microglia[263]. Additionally, a robust increase in the expression of the exosome markers CD9 and CD81 was also observed in *GRN* KO hiPSC-derived microglia[231].

Another possibility is the formation of tunneling nanotubes as postulated for the transfer of alpha-synuclein between microglia[264]. Even the transport of whole mitochondria between microglia and neurons was shown to be possible through this mechanism[265]. Similarly, lysosomes or early endosomes might be transported between microglia or to neurons.

However, LGMN could be detected in the media of hiPSC-derived microglia (3.2.) and in the periphery, LGMN release was shown through the secretory pathway, where it was also found in the microenvironment of tumors[172,266,267]. Taken together, a secretory mechanism, such as the transfer of exosomes, is a more likely scenario for the transfer of LGMN from microglia to neurons.

4.3.2. MODULATION OF LGMN INFLUENCES TDP-43 PATHOLOGY

TDP-43 pathology was described in form of enhanced TDP-43 processing in mouse embryonic fibroblasts (MEFs), hiPSC-derived microglia-neuron co-cultures, and in primary hippocampal mouse neurons incubated with LGMN-containing conditioned media (3.2.). As its nuclear localization sequence is lost during processing, cleaved TDP-43 is most likely mislocalized to the cytosol, enhances aggregation and is further found in intracellular neuronal aggregates in patients[33,44]. Cleavage of TDP-43 is further necessary for the propagation of aggregates from cell to cell, highlighting excessive TDP-43 processing as a key disease-relevant mechanism[268].

Whether LGMN is the protease responsible for the formation of TDP-43 fragments was first analyzed by KD in MEFs. The enhanced processing observed in *Grn* KO MEFs was diminished and there was even an enrichment of full-length TDP-43. Furthermore, Cystatin F-mediated blockage of neuronal cysteine proteases rescued the TDP-43 processing phenotype in hiPSC-derived neuron-microglia co-cultures. In addition, the specific inhibition of LGMN with a small molecule inhibitor in co-cultures of hiPSC-derived WT neurons with *GRN* KO microglia led to a size shift in the generated TDP-43 fragments, including an enrichment of the full-length form. However, this rescue was incomplete, as fragments were still formed, potentially by another lysosomal protease. In contrast, AAV-mediated overexpression of LGMN in the brain of *Grn* KO mice, led to the formation of aggregates containing processed and pTDP-43. Elevated LGMN further strongly raised plasma NfL levels and caused motor impairments similar to the ones observed in the *Grn* and *Tmem106b* DKO mouse model[169].

These findings strongly support a central role of LGMN in the pathological processing of TDP-43. This is further supported by the results of Herskowitz *et al.*, showing the presence of TDP-43 fragments with C-terminal asparagine residues in FTLD-*GRN* patient brains, as these would appear after cleavage by LGMN[181]. However, as LGMN directly influences the maturation of other lysosomal proteases, such as CTSL and CTSB, their downstream involvement in the pathogenesis cannot be excluded[175,176]. Additionally, caspases were shown in the past to be able to cleave TDP-43 as well, but this was only shown *in vitro*[269].

How LGMN-mediated processing of TDP-43 affects further downstream events, such as its nuclear depletion and the formation of cytosolic aggregates could not be addressed in this study, as the *Grn* KO models do not robustly have this phenotype. *Grn* KO mice only

show sparse and small aggregates at older ages[125,130,228]. An alternative option to investigate the effect of LGMN inhibition on insoluble TDP-43 aggregates containing pTDP-43 *in vivo* could be the treatment of the DKO mouse line with the small molecule LGMN inhibitor or the introduction of an additional KO of *Lgmn*. This would also enable the characterization of the effects of LGMN on other disease-relevant phenotypes, such as neurodegeneration, microglial hyperactivation, and motor impairment.

4.3.2.1. WHERE DO LGMN AND TDP-43 INTERACT?

Pro-LGMN, after being transferred from microglia to neurons, needs to be activated and then has to interact with TDP-43 to enable its processing. However, TDP-43 is a nuclear protein and LGMN a lysosomal protease that is only active at acidic pH, creating an apparent spatial paradox[172]. Despite its general localization to the nucleus, TDP-43 shuttles between the nucleus and the cytosol in homeostasis, as part of its RNA-regulating role[270]. Under stress conditions, such as enhanced oxidative stress, endoplasmic reticulum stress, or impaired protein degradation, TDP-43 was shown to be mislocalized to the cytosol and to form aggregates[271-273]. Excess amounts of TDP-43 could then be labeled by ubiquitin for proteasome-mediated degradation or directed towards the autophagic pathway and subsequently lysosomal degradation[33,274-276]. In the lysosome, TDP-43 could then be processed by LGMN and its fragments released into the cytosol, as the lysosomal membrane was reported to be damaged in PGRN deficiency[133]. Likewise, LGMN could escape from the lysosomes. As lysosomal pH is increased upon loss of PGRN, LGMN might not be able to undergo complete maturation and, while mature LGMN is unstable at neutral pH, its intermediate form was reported to be able to be stabilized at neutral pH[172,173]. Although stochastically unlikely, it could then process TDP-43 in the acidic microenvironment close to leaky lysosomes.

In this study, some evidence is provided for the direct interaction of LGMN and TDP-43 (3.2.). In *Grn* KO MEFs, cytosolic TDP-43 co-localized with LGMN and the lysosomal marker LAMP1, in close proximity to the nucleus. This supports the possibility of lysosomal processing of TDP-43 by LGMN. Additionally, patches positive for TDP-43, LGMN, and DAPI, but not LAMP1, were also observed in the close proximity of the nucleus. These might be stress granules or liquid-liquid-phase-separated membrane-less organelles, which would require additional investigation[54].

4.4. THE ROLE OF CELLULAR CROSSTALK IN FTLD-*GRN*

The pronounced role of LGMN in FTLD-*GRN* pathogenesis highlights the importance of cellular crosstalk as a fundamental mechanism underlying FTLD-*GRN* and neurodegeneration in general. In this study, it is shown that LGMN, highly expressed in

microglia and upregulated upon PGRN deficiency, can potentially be shuttled from microglia to neurons, where it contributes to TDP-43 pathology by enhanced processing of the protein (3.2.). Similarly, the DKO of *GRN* and *TMEM106B* in hiPSC-derived microglia was necessary and sufficient to induce TDP-43 pathology and neurodegeneration in WT neurons in a co-culture setting (3.1.). Both findings position microglia at the center of pathobiology. Microglia are highly dynamic cells which rapidly react to changes in their environment[1]. An internal disruption of their lysosomal function might therefore trigger their transition to the DAM state, as described in aged *Grn* KO mice and hiPSC-derived *GRN* KO microglia[226,228,231]. It was further shown that an initial lysosomal dysfunction in microglia eventually induces similar effects in other CNS cell types[126].

Microglial activation also leads to the release of pro-inflammatory cytokines, such as TNF and IL-6, which can create a toxic environment for neurons, which was also observed in PGRN-deficient mice[230]. Lui *et al.* further demonstrated that microglia in *Grn* KO mice and FTLD-*GRN* patients have increased expression of the complement factors C1q and C3, resulting in enhanced synaptic pruning[229]. These complement factors have been shown before to be critical for the removal of excess synapses during development[193]. However, a follow-up study by Zhang *et al.* investigated mechanistically the consequences of complement upregulation upon PGRN deficiency by incubating primary neurons with conditioned media from either WT or *Grn* KO microglia[228]. The increase of C1q and C3 in *Grn* KO primary microglia and their media was confirmed and resulted in increased cytosolic accumulation of TDP-43 and neuronal cell death, which could be reversed by the genetic ablation of these complement factors. Whether LGMN can directly contribute to the microglial release of complement components could be analyzed by studying the secretome of *GRN* and *LGMN* DKO microglia or *GRN* KO microglia treated with a LGMN inhibitor. Evidence supporting an indirect contribution of LGMN was shown in the context of T-cell activation, where CTSL, a lysosomal protease regulated by LGMN, was involved in the processing of C3 into its active fragments C3a and C3b[277]. Alternatively, it is also likely that complement activation is a direct consequence of the lysosomal dysfunction, as increased complement levels were also reported in the lysosomal storage disorders Gaucher disease and Niemann-Pick disease[278,279].

Another recent publication postulates a direct involvement of astrocytes in the pathogenesis of FTLD-*GRN*[259]. De Majo *et al.* analyzed three-dimensional hiPSC-derived neuronal WT and *GRN* KO cultures with or without WT or *GRN* KO hiPSC-derived astrocytes. Culturing neurons in the presence of *GRN* KO astrocytes resulted in increased levels of cytosolic TDP-43, as well as an increased expression of cryptic STMN2, which could be reversed by supplementation of recombinant PGRN. Even though the study remains descriptive, astrocytes may have an impact on neuronal pathology in FTLD-*GRN*. Whether these effects could be potentiated by using a tri-culture system, including microglia, would be an interesting question to address.

Taken together, cellular cross-talk, especially between microglia and neurons, plays a critical role in the pathogenesis of FTLD-*GRN*. However, the modulation of microglial hyperactivation, for example by inhibition of TREM2 signaling using antagonistic antibodies, might be a double-edged sword, as it was shown to mitigate the expression of DAM genes in *GRN* KO models, but at the same time it failed to rescue lysosomal pathology and even strongly increased neurodegeneration[231].

4.5. SUMMARY

In summary, the two studies presented in this thesis aimed at deepening the understanding of the molecular mechanisms underlying FTLD-*GRN* and leveraging this knowledge for the development of potential disease-modifying therapeutics.

In the first study, AAV(L):bPGRN was assessed as a complementary treatment approach to recombinant PTV:PGRN, combining the advantages of gene therapy and the ease of the peripheral administration of a brain-penetrant biotherapeutic. Using this treatment paradigm, PGRN levels in the brain could be increased after a single injection without any toxic side effects. All the phenotypes characteristic of the DKO mice were corrected or ameliorated by AAV(L):bPGRN administration, including their brain lipidomic and transcriptomic profiles, which were characterized *de novo* in this study. This also strengthens the applicability of DKO mice as a model of FTLD-*GRN* and their use for the evaluation of therapeutic strategies. Using hiPSC-derived co-cultures of WT neurons and DKO microglia, a novel cellular model of FTLD-*GRN* pathology was established and characterized. Neuron-microglia co-cultures recapitulate the cellular phenotypes of the DKO mice *in vitro*, showing lysosomal hyperactivation, TDP-43 pathology, and neurodegeneration. Once again, these phenotypes could be ameliorated by PGRN replacement making it a useful system for the investigation of FTLD-*GRN*-associated disease mechanisms and to screen therapeutic approaches. In conclusion, both the *in vitro* and *in vivo* DKO are *bona fide* FTLD-*GRN* models, which not only present with disease-relevant phenotypes, but can also be valuable in translational research. In addition, PGRN replacement therapy using brain-penetrant biotherapeutics, such as AAV(L):bPGRN or PTV:PGRN, is a promising approach for the treatment of FTLD-*GRN*.

The second, more mechanistic, study investigated LGMN as the potential link between PGRN haploinsufficiency and TDP-43 pathology. PGRN was shown to regulate the maturation of LGMN and consequently, LGMN levels were found to be increased in various models of PGRN deficiency and in FTLD-*GRN* patient brains. The study further provides evidence for a transfer of LGMN from microglia to neurons, where it could be activated and ultimately process TDP-43 into its disease-associated fragments. The specific role of LGMN in this cascade of events was confirmed by using a combination of

Discussion

Lgmn KD, a cysteine-protease inhibitor, a specific small molecule LGMN inhibitor, and AAV-mediated LGMN overexpression in the mouse brain. Taken together, these results prove that LGMN is an important link between loss of PGRN and TDP-43 pathology, however, both its transfer mechanism from microglia to neurons and the subcellular compartment in which its interaction with TDP-43 occurs still need further investigation.

5. OUTLOOK

The studies presented in this thesis investigate both the feasibility of PGRN replacement therapy as a treatment strategy for FTLD-*GRN* as well as the role of LGMN as a link between PGRN deficiency and TDP-43 pathology. Nevertheless, some related open questions remain, which will be briefly discussed here.

Could additional readouts for TDP-43 pathology be assessed to evaluate the efficacy of PGRN replacement in the DKO mouse model?
TDP-43 pathology was robustly detected as insoluble pTDP-43-positive aggregates by immunoblot. However, the presence of cytosolic mislocalization could not be demonstrated by immunofluorescence, due to a sparse fluorescent signal distribution and a high variability across animals. As this readout was shown to be robust in the spinal cord of DKO mice in an independent study[239], characterizing the pathology in the spinal cords of the AAV(L):bPGRN-treated mice would provide insights into the potential effects of PGRN replacement therapy on TDP-43 mislocalization. In addition, it could also be tested whether cryptic exons, a functional consequence of the nuclear loss of TDP-43, are present in this model.

What is the pathological sequence in FTLD-GRN?
Several studies have already aimed at addressing this question in cellular systems, *Grn* KO mice, and FTLD-*GRN* patient cohorts and lysosomal dysfunction was reliably identified as a trigger of pathology. For a more detailed analysis of the order in which the different pathological manifestations arise, the DKO mouse model is ideally suited. It presents with a lot of strong disease-relevant phenotypes and has a fast disease progression. To answer this question, different timepoints could be analyzed to dissect the dynamic nature of pathology, as it was done in the first study presented in this thesis for rotarod performance and plasma NfL levels.

What is the effect of the single or combinatorial loss of PGRN and TMEM106B on the crosstalk between microglia and neurons?
In the projects presented in this thesis it was shown how *GRN* KO and DKO hiPSC-derived microglia can cause different pathologies in neurons. By applying hiPSCs, the possibility exists to investigate all different kinds of genetic and cell type combinations. In order to shed light on the interaction of PGRN and TMEM106B, the proteome and secretome of WT, *GRN* KO, *TMEM106B* KO, and DKO hiPSC-derived microglia and neurons in either monoculture or co-culture could be analyzed by proteomics. This would make it possible to elucidate the cell-autonomous and non-cell-autonomous contributions of the respective loss of the two proteins and their consequences on the global protein expression and secretion profiles. Potential hits could then be validated in targeted mechanistic studies.

How is LGMN shuttled from microglia to neurons?

This question was partly addressed in the second project presented in this thesis. LGMN from conditioned media could be taken up by neurons and *GRN* KO hiPSC-derived co-cultures released more LGMN into the media. A transfer through vesicles, most likely exosomes, is likely, but should be verified experimentally. Exosomes from WT and *GRN* KO hiPSC-derived microglia may be purified and their cargo analyzed by LGMN ELISA or immunoblot. If LGMN was to be found in exosomes, purified exosomes could also be fluorescently labeled and supplemented to neuronal cultures in order to study potential uptake mechanisms. Another possibility is the generation of a hiPSC line expressing endogenously tagged LGMN. Microglia differentiated from such a hiPSC line could then be co-cultured with WT neurons to investigate the transfer mechanism. In addition, to confirm that LGMN is indeed shuttled from microglia to neurons, *LGMN* KO hiPSC lines could also be generated to exclude the possibility that the enhanced TDP-43 pathology in neurons results from an upregulation of neuronal LGMN upon co-culture with microglia.

Where do LGMN and TDP-43 meet in neurons?

The lysosomal protease LGMN and the nuclear protein TDP-43 have to meet in some subcellular compartment in order for LGMN to process TDP-43. In MEFs, the co-localization of LGMN and TDP-43 in LAMP1-positive lysosomes could already be shown, as well as in LGMN-, TDP-43-, and DAPI-positive patches in the cell. The exact localization should be further confirmed and detailed *via* super resolution microscopy, also to address whether TDP-43 and LGMN co-localize outside of lysosomes, at their membrane or in their lumen. Ideally, this would then be translated to neurons, where neurons from the experiments discussed in the previous question could be analyzed for co-localization of internalized LGMN and TDP-43.

6. ACKNOWLEDGEMENTS

At this point, I would like to thank everyone who helped me during my PhD journey.

First, I want to thank **Prof. Christian Haass** for welcoming me into his laboratory and giving me the opportunity to work on such intriguing projects during my PhD. I am grateful for his continuous support and guidance. Most importantly I want to thank him for his mentorship and professional advice, and for providing many opportunities to develop as a person and scientist.

I would like to further thank **Dr. Anja Capell** for providing direct supervision in the laboratory. I truly appreciate our many discussions, the experimental advice and that she was always available when I needed help.

Furthermore, I want to thank **Prof. Dominik Paquet**, not only for hosting me in his laboratory for the hiPSC work, but also for welcoming me as a part of his team and providing valuable scientific input and support.

I want to thank the members of my thesis advisory committee, namely **Prof. Christian Haass**, **Prof. Dominik Paquet**, **Prof. Paul Saftig** and **Dr. Anja Capell,** for the many good discussions we had and all the valuable input and help that I received.

Besides, I am very grateful to all the people that taught me new methods and always had the necessary patience. Here, I want to especially thank **Dr. Anja Capell**, **Dr. Georg Werner**, **Dr. Anika Reifschneider**, **Katrin Buschmann**, **Dr. Sophie Robinson**, **Dennis Crusius**, **Dr. Xianyuan Xiang**, **Dr. Jane Hettinger**, **Dr. Ida Pesämaa**, **Dr. Astrid Feiten**, **Dr. Iñaki Paris**, **Dr. Lena Spieth**, **Dr. Stefan Berghoff** and **Lennart Schlaphoff**.

I also want to thank all the people that continuously supported me with my projects through technical support. This especially includes **Katrin Buschmann**, **Ramona Rodde** and **Claudia Thiel**.

A special thanks goes to my students **Christian Schrader**, **Bea Polke** and **Kyle Brandon**. It was a pleasure working with them and I greatly enjoyed supervising them and to see them grow as scientists. I also want to thank my HiWi **Mariana Martins** for her great support in the last stretches of the PhD.

I further want to thank all the people that were involved in the work that led to the two manuscripts presented in this thesis. Without them, this would not have been possible. A special thanks goes to my co-starred authors **Dr. Matt Simon**, **Dr. Sophie Robinson** and **Maria Mühlhofer** for greatly contributing to the work as well as to **Prof. Christian Haass**, **Dr. Anja Capell**, **Dr. Gil Di Paolo** and **Prof. Dominik Paquet** for their supervision.

I would like to thank all the **collaborators at Denali** for this very fruitful collaboration, and for providing the opportunity to visit for an internship. Particularly, I would like to thank **Dr. Jung Suh and his team** for being great and fun teachers and colleagues and **Dr. Gil Di Paolo** for welcoming me into his team as well. I would also like to thank **Dr. Joe Lewcock** for making the internship possible and **all Denalians** for being so welcoming.

On top of that, I want to thank all the people at the **institute and my labs** for creating an inspiring environment with many good discussions, seminars and fun events. Importantly, I want to thank all the people in the lab and at the institute who welcomed me with kindness and continuously provided moral support throughout this not always smooth journey. They were not only **great colleagues**, but also became friends along the way.

Lastly, I want to thank **all my friends and my brother**, who supported me throughout the whole PhD journey and made every setback and issue more bearable and the successes worth celebrating.

7. LITERATURE

1   Paolicelli, R. C. *et al.* Microglia states and nomenclature: A field at its crossroads. *Neuron* **110**, 3458-3483, doi:https://doi.org/10.1016/j.neuron.2022.10.020 (2022).
2   Terryn, J., Verfaillie, C. M. & Van Damme, P. Tweaking Progranulin Expression: Therapeutic Avenues and Opportunities. *Front Mol Neurosci* **14**, 713031, doi:10.3389/fnmol.2021.713031 (2021).
3   Simon, M. J., Logan, T., DeVos, S. L. & Di Paolo, G. Lysosomal functions of progranulin and implications for treatment of frontotemporal dementia. *Trends Cell Biol* **33**, 324-339, doi:10.1016/j.tcb.2022.09.006 (2023).
4   Feng, T., Lacrampe, A. & Hu, F. Physiological and pathological functions of TMEM106B: a gene associated with brain aging and multiple brain disorders. *Acta Neuropathologica* **141**, 327-339, doi:10.1007/s00401-020-02246-3 (2021).
5   Ling, S.-C., Polymenidou, M. & Cleveland, Don W. Converging Mechanisms in ALS and FTD: Disrupted RNA and Protein Homeostasis. *Neuron* **79**, 416-438, doi:https://doi.org/10.1016/j.neuron.2013.07.033 (2013).
6   Daviglus, M. L. *et al.* NIH state-of-the-science conference statement: Preventing Alzheimer's disease and cognitive decline. *NIH Consens State Sci Statements* **27**, 1-30 (2010).
7   Nilsson, C., Landqvist Waldö, M., Nilsson, K., Santillo, A. & Vestberg, S. Age-related incidence and family history in frontotemporal dementia: data from the Swedish Dementia Registry. *PLoS One* **9**, e94901, doi:10.1371/journal.pone.0094901 (2014).
8   Onyike, C. U. & Diehl-Schmid, J. The epidemiology of frontotemporal dementia. *Int Rev Psychiatry* **25**, 130-137, doi:10.3109/09540261.2013.776523 (2013).
9   Knopman, D. S. & Roberts, R. O. Estimating the number of persons with frontotemporal lobar degeneration in the US population. *J Mol Neurosci* **45**, 330-335, doi:10.1007/s12031-011-9538-y (2011).
10   Magrath Guimet, N., Zapata-Restrepo, L. M. & Miller, B. L. Advances in Treatment of Frontotemporal Dementia. *J Neuropsychiatry Clin Neurosci* **34**, 316-327, doi:10.1176/appi.neuropsych.21060166 (2022).
11   Pick, A. Uber die Beziehungen der senilen Hirnatrophie zur Aphasie. *Prag Med Wchnschr* **17**, 165-167 (1892).
12   Alzheimer, A. Über eigenartige Krankheitsfälle des späteren Alters. *Zeitschrift für die gesamte Neurologie und Psychiatrie* **4**, 356-385 (1911).
13   Ingvar, D. H. & Gustafson, L. Regional cerebral blood flow in organic dementia with early onset. *Acta Neurol Scand* **46**, 42-73, doi:10.1111/j.1600-0404.1970.tb02156.x (1970).
14   Mesulam, M. M. Primary progressive aphasia. *Ann Neurol* **49**, 425-432 (2001).
15   Neary, D. *et al.* Frontotemporal lobar degeneration: a consensus on clinical diagnostic criteria. *Neurology* **51**, 1546-1554, doi:10.1212/wnl.51.6.1546 (1998).
16   Johnson, J. K. *et al.* Frontotemporal lobar degeneration: demographic characteristics of 353 patients. *Arch Neurol* **62**, 925-930, doi:10.1001/archneur.62.6.925 (2005).
17   Rascovsky, K. *et al.* Sensitivity of revised diagnostic criteria for the behavioural variant of frontotemporal dementia. *Brain* **134**, 2456-2477, doi:10.1093/brain/awr179 (2011).
18   Chow, T. W. *et al.* Apathy symptom profile and behavioral associations in frontotemporal dementia vs dementia of Alzheimer type. *Arch Neurol* **66**, 888-893, doi:10.1001/archneurol.2009.92 (2009).
19   Piguet, O. *et al.* Eating and hypothalamus changes in behavioral-variant frontotemporal dementia. *Ann Neurol* **69**, 312-319, doi:10.1002/ana.22244 (2011).
20   Lant, S. B. *et al.* Patterns of microglial cell activation in frontotemporal lobar degeneration. *Neuropathol Appl Neurobiol* **40**, 686-696, doi:10.1111/nan.12092 (2014).

21   Oeckl, P. *et al.* Different neuroinflammatory profile in amyotrophic lateral sclerosis and frontotemporal dementia is linked to the clinical phase. *J Neurol Neurosurg Psychiatry* **90**, 4-10, doi:10.1136/jnnp-2018-318868 (2019).

22   Burrell, J. R., Kiernan, M. C., Vucic, S. & Hodges, J. R. Motor Neuron dysfunction in frontotemporal dementia. *Brain* **134**, 2582-2594, doi:10.1093/brain/awr195 (2011).

23   De Silva, D. *et al.* Motor function and behaviour across the ALS-FTD spectrum. *Acta Neurol Scand* **133**, 367-372, doi:10.1111/ane.12471 (2016).

24   Lillo, P. & Hodges, J. R. Frontotemporal dementia and motor neurone disease: overlapping clinic-pathological disorders. *J Clin Neurosci* **16**, 1131-1135, doi:10.1016/j.jocn.2009.03.005 (2009).

25   Kertesz, A. & Munoz, D. Relationship between frontotemporal dementia and corticobasal degeneration/progressive supranuclear palsy. *Dement Geriatr Cogn Disord* **17**, 282-286, doi:10.1159/000077155 (2004).

26   Mackenzie, I. R. *et al.* Nomenclature for neuropathologic subtypes of frontotemporal lobar degeneration: consensus recommendations. *Acta Neuropathol* **117**, 15-18, doi:10.1007/s00401-008-0460-5 (2009).

27   McGeer, P. L., Schwab, C., McGeer, E. G., Haddock, R. L. & Steele, J. C. Familial nature and continuing morbidity of the amyotrophic lateral sclerosis-parkinsonism dementia complex of Guam. *Neurology* **49**, 400-409, doi:10.1212/wnl.49.2.400 (1997).

28   Masrori, P. & Van Damme, P. Amyotrophic lateral sclerosis: a clinical review. *Eur J Neurol* **27**, 1918-1929, doi:10.1111/ene.14393 (2020).

29   Couratier, P., Corcia, P., Lautrette, G., Nicol, M. & Marin, B. ALS and frontotemporal dementia belong to a common disease spectrum. *Revue Neurologique* **173**, 273-279, doi:https://doi.org/10.1016/j.neurol.2017.04.001 (2017).

30   Olney, N. T., Spina, S. & Miller, B. L. Frontotemporal Dementia. *Neurol Clin* **35**, 339-374, doi:10.1016/j.ncl.2017.01.008 (2017).

31   Mackenzie, I. R. & Neumann, M. Molecular neuropathology of frontotemporal dementia: insights into disease mechanisms from postmortem studies. *J Neurochem* **138 Suppl 1**, 54-70, doi:10.1111/jnc.13588 (2016).

32   Saberi, S., Stauffer, J. E., Schulte, D. J. & Ravits, J. Neuropathology of Amyotrophic Lateral Sclerosis and Its Variants. *Neurol Clin* **33**, 855-876, doi:10.1016/j.ncl.2015.07.012 (2015).

33   Neumann, M. *et al.* Ubiquitinated TDP-43 in frontotemporal lobar degeneration and amyotrophic lateral sclerosis. *Science* **314**, 130-133, doi:10.1126/science.1134108 (2006).

34   Mann, D. M. A. & Snowden, J. S. Frontotemporal lobar degeneration: Pathogenesis, pathology and pathways to phenotype. *Brain Pathol* **27**, 723-736, doi:10.1111/bpa.12486 (2017).

35   Lee, V. M., Goedert, M. & Trojanowski, J. Q. Neurodegenerative tauopathies. *Annu Rev Neurosci* **24**, 1121-1159, doi:10.1146/annurev.neuro.24.1.1121 (2001).

36   Mackenzie, I. R. *et al.* Nomenclature and nosology for neuropathologic subtypes of frontotemporal lobar degeneration: an update. *Acta Neuropathol* **119**, 1-4, doi:10.1007/s00401-009-0612-2 (2010).

37   Neumann, M. *et al.* A new subtype of frontotemporal lobar degeneration with FUS pathology. *Brain* **132**, 2922-2931, doi:10.1093/brain/awp214 (2009).

38   Johnson, B. S. *et al.* TDP-43 is intrinsically aggregation-prone, and amyotrophic lateral sclerosis-linked mutations accelerate aggregation and increase toxicity. *J Biol Chem* **284**, 20329-20339, doi:10.1074/jbc.M109.010264 (2009).

39   Sreedharan, J. *et al.* TDP-43 mutations in familial and sporadic amyotrophic lateral sclerosis. *Science* **319**, 1668-1672, doi:10.1126/science.1154584 (2008).

40   Borroni, B. *et al.* TARDBP mutations in frontotemporal lobar degeneration: frequency, clinical features, and disease course. *Rejuvenation Res* **13**, 509-517, doi:10.1089/rej.2010.1017 (2010).

41   Buratti, E. & Baralle, F. E. Characterization and Functional Implications of the RNA Binding Properties of Nuclear Factor TDP-43, a Novel Splicing Regulator ofCFTR Exon 9*. *Journal of Biological Chemistry* **276**, 36337-36343, doi:https://doi.org/10.1074/jbc.M104236200 (2001).

42   Tollervey, J. R. *et al.* Characterizing the RNA targets and position-dependent splicing regulation by TDP-43. *Nature Neuroscience* **14**, 452-458, doi:10.1038/nn.2778 (2011).

43   Ou, S. H., Wu, F., Harrich, D., García-Martínez, L. F. & Gaynor, R. B. Cloning and characterization of a novel cellular protein, TDP-43, that binds to human immunodeficiency virus type 1 TAR DNA sequence motifs. *Journal of Virology* **69**, 3584-3596, doi:10.1128/jvi.69.6.3584-3596.1995 (1995).

44   Zhang, Y. J. *et al.* Aberrant cleavage of TDP-43 enhances aggregation and cellular toxicity. *Proc Natl Acad Sci U S A* **106**, 7607-7612, doi:10.1073/pnas.0900688106 (2009).

45   Neumann, M. *et al.* Phosphorylation of S409/410 of TDP-43 is a consistent feature in all sporadic and familial forms of TDP-43 proteinopathies. *Acta Neuropathol* **117**, 137-149, doi:10.1007/s00401-008-0477-9 (2009).

46   Hasegawa, M. *et al.* Phosphorylated TDP-43 in frontotemporal lobar degeneration and amyotrophic lateral sclerosis. *Ann Neurol* **64**, 60-70, doi:10.1002/ana.21425 (2008).

47   Lee, E. B., Lee, V. M. & Trojanowski, J. Q. Gains or losses: molecular mechanisms of TDP43-mediated neurodegeneration. *Nat Rev Neurosci* **13**, 38-50, doi:10.1038/nrn3121 (2011).

48   Buratti, E. TDP-43 post-translational modifications in health and disease. *Expert Opinion on Therapeutic Targets* **22**, 279-293, doi:10.1080/14728222.2018.1439923 (2018).

49   Mackenzie, I. R. *et al.* A harmonized classification system for FTLD-TDP pathology. *Acta Neuropathol* **122**, 111-113, doi:10.1007/s00401-011-0845-8 (2011).

50   Arseni, D. *et al.* Structure of pathological TDP-43 filaments from ALS with FTLD. *Nature* **601**, 139-143, doi:10.1038/s41586-021-04199-3 (2022).

51   Arseni, D. *et al.* TDP-43 forms amyloid filaments with a distinct fold in type A FTLD-TDP. *Nature* **620**, 898-903, doi:10.1038/s41586-023-06405-w (2023).

52   Maharana, S. *et al.* RNA buffers the phase separation behavior of prion-like RNA binding proteins. *Science* **360**, 918-921, doi:10.1126/science.aar7366 (2018).

53   Mann, J. R. *et al.* RNA Binding Antagonizes Neurotoxic Phase Transitions of TDP-43. *Neuron* **102**, 321-338.e328, doi:10.1016/j.neuron.2019.01.048 (2019).

54   Molliex, A. *et al.* Phase separation by low complexity domains promotes stress granule assembly and drives pathological fibrillization. *Cell* **163**, 123-133, doi:10.1016/j.cell.2015.09.015 (2015).

55   Gasset-Rosa, F. *et al.* Cytoplasmic TDP-43 De-mixing Independent of Stress Granules Drives Inhibition of Nuclear Import, Loss of Nuclear TDP-43, and Cell Death. *Neuron* **102**, 339-357.e337, doi:10.1016/j.neuron.2019.02.038 (2019).

56   Keating, S. S., Bademosi, A. T., San Gil, R. & Walker, A. K. Aggregation-prone TDP-43 sequesters and drives pathological transitions of free nuclear TDP-43. *Cell Mol Life Sci* **80**, 95, doi:10.1007/s00018-023-04739-2 (2023).

57   Neumann, M. *et al.* Antibody against TDP-43 phosphorylated at serine 375 suggests conformational differences of TDP-43 aggregates among FTLD-TDP subtypes. *Acta Neuropathol* **140**, 645-658, doi:10.1007/s00401-020-02207-w (2020).

58   Farina, S., Esposito, F., Battistoni, M., Biamonti, G. & Francia, S. Post-Translational Modifications Modulate Proteinopathies of TDP-43, FUS and hnRNP-A/B in Amyotrophic Lateral Sclerosis. *Front Mol Biosci* **8**, 693325, doi:10.3389/fmolb.2021.693325 (2021).

59   Wils, H. *et al.* TDP-43 transgenic mice develop spastic paralysis and neuronal inclusions characteristic of ALS and frontotemporal lobar degeneration. *Proc Natl Acad Sci U S A* **107**, 3858-3863, doi:10.1073/pnas.0912417107 (2010).

60   Winton, M. J. *et al.* Disturbance of Nuclear and Cytoplasmic TAR DNA-binding Protein (TDP-43) Induces Disease-like Redistribution, Sequestration, and Aggregate Formation **. *Journal of Biological Chemistry* **283**, 13302-13309, doi:10.1074/jbc.M800342200 (2008).

61   Janssens, J. *et al.* Overexpression of ALS-associated p.M337V human TDP-43 in mice worsens disease features compared to wild-type human TDP-43 mice. *Mol Neurobiol* **48**, 22-35, doi:10.1007/s12035-013-8427-5 (2013).

62   Polymenidou, M. *et al.* Long pre-mRNA depletion and RNA missplicing contribute to neuronal vulnerability from loss of TDP-43. *Nat Neurosci* **14**, 459-468, doi:10.1038/nn.2779 (2011).

63   Fiesel, F. C., Schurr, C., Weber, S. S. & Kahle, P. J. TDP-43 knockdown impairs neurite outgrowth dependent on its target histone deacetylase 6. *Molecular Neurodegeneration* **6**, 64, doi:10.1186/1750-1326-6-64 (2011).

64   Brown, A.-L. *et al.* TDP-43 loss and ALS-risk SNPs drive mis-splicing and depletion of UNC13A. *Nature* **603**, 131-137, doi:10.1038/s41586-022-04436-3 (2022).

65   Seddighi, S. *et al.* Mis-spliced transcripts generate de novo proteins in TDP-43-related ALS/FTD. *Sci Transl Med* **16**, eadg7162, doi:10.1126/scitranslmed.adg7162 (2024).

66   Baughn, M. W. *et al.* Mechanism of STMN2 cryptic splice-polyadenylation and its correction for TDP-43 proteinopathies. *Science* **379**, 1140-1149, doi:10.1126/science.abq5622 (2023).

67   Hruska-Plochan, M. *et al.* A model of human neural networks reveals NPTX2 pathology in ALS and FTLD. *Nature* **626**, 1073-1083, doi:10.1038/s41586-024-07042-7 (2024).

68   Josephs, K. A. *et al.* TDP-43 is a key player in the clinical features associated with Alzheimer's disease. *Acta Neuropathol* **127**, 811-824, doi:10.1007/s00401-014-1269-z (2014).

69   Rohrer, J. D. *et al.* The heritability and genetics of frontotemporal lobar degeneration. *Neurology* **73**, 1451-1456, doi:10.1212/WNL.0b013e3181bf997a (2009).

70   Greaves, C. V. & Rohrer, J. D. An update on genetic frontotemporal dementia. *Journal of Neurology* **266**, 2075-2086, doi:10.1007/s00415-019-09363-4 (2019).

71   Baker, M. *et al.* Mutations in progranulin cause tau-negative frontotemporal dementia linked to chromosome 17. *Nature* **442**, 916-919, doi:10.1038/nature05016 (2006).

72   DeJesus-Hernandez, M. *et al.* Expanded GGGGCC Hexanucleotide Repeat in Noncoding Region of C9ORF72 Causes Chromosome 9p-Linked FTD and ALS. *Neuron* **72**, 245-256, doi:https://doi.org/10.1016/j.neuron.2011.09.011 (2011).

73   Hutton, M. *et al.* Association of missense and 5'-splice-site mutations in tau with the inherited dementia FTDP-17. *Nature* **393**, 702-705, doi:10.1038/31508 (1998).

74   Cruts, M. *et al.* Null mutations in progranulin cause ubiquitin-positive frontotemporal dementia linked to chromosome 17q21. *Nature* **442**, 920-924, doi:10.1038/nature05017 (2006).

75   Poorkaj, P. *et al.* Tau is a candidate gene for chromosome 17 frontotemporal dementia. *Ann Neurol* **43**, 815-825, doi:10.1002/ana.410430617 (1998).

76   Spillantini, M. G. *et al.* Mutation in the tau gene in familial multiple system tauopathy with presenile dementia. *Proc Natl Acad Sci U S A* **95**, 7737-7741, doi:10.1073/pnas.95.13.7737 (1998).

77   Renton, Alan E. *et al.* A Hexanucleotide Repeat Expansion in C9ORF72 Is the Cause of Chromosome 9p21-Linked ALS-FTD. *Neuron* **72**, 257-268, doi:https://doi.org/10.1016/j.neuron.2011.09.010 (2011).

78   Mackenzie, I. R. The neuropathology and clinical phenotype of FTD with progranulin mutations. *Acta Neuropathol* **114**, 49-54, doi:10.1007/s00401-007-0223-8 (2007).

79   Bellenguez, C. *et al.* New insights into the genetic etiology of Alzheimer's disease and related dementias. *Nat Genet* **54**, 412-436, doi:10.1038/s41588-022-01024-z (2022).

80   Nalls, M. A. *et al.* Identification of novel risk loci, causal insights, and heritable risk for Parkinson's disease: a meta-analysis of genome-wide association studies. *Lancet Neurol* **18**, 1091-1102, doi:10.1016/s1474-4422(19)30320-5 (2019).

81   Brouwers, N. *et al.* Genetic variability in progranulin contributes to risk for clinically diagnosed Alzheimer disease. *Neurology* **71**, 656-664, doi:10.1212/01.wnl.0000319688.89790.7a (2008).

82   Watts, G. D. *et al.* Inclusion body myopathy associated with Paget disease of bone and frontotemporal dementia is caused by mutant valosin-containing protein. *Nat Genet* **36**, 377-381, doi:10.1038/ng1332 (2004).

83   Skibinski, G. *et al.* Mutations in the endosomal ESCRTIII-complex subunit CHMP2B in frontotemporal dementia. *Nat Genet* **37**, 806-808, doi:10.1038/ng1609 (2005).

84   Freischmidt, A. *et al.* Haploinsufficiency of TBK1 causes familial ALS and fronto-temporal dementia. *Nat Neurosci* **18**, 631-636, doi:10.1038/nn.4000 (2015).

85   Gijselinck, I. *et al.* Loss of TBK1 is a frequent cause of frontotemporal dementia in a Belgian cohort. *Neurology* **85**, 2116-2125, doi:10.1212/wnl.0000000000002220 (2015).

86   Pottier, C. *et al.* Whole-genome sequencing reveals important role for TBK1 and OPTN mutations in frontotemporal lobar degeneration without motor neuron disease. *Acta Neuropathol* **130**, 77-92, doi:10.1007/s00401-015-1436-x (2015).

87   Gendron, T. F., Rademakers, R. & Petrucelli, L. TARDBP mutation analysis in TDP-43 proteinopathies and deciphering the toxicity of mutant TDP-43. *J Alzheimers Dis* **33 Suppl 1**, S35-45, doi:10.3233/jad-2012-129036 (2013).

88   Brenner, D. *et al.* FUS mutations dominate TBK1 mutations in FUS/TBK1 double-mutant ALS/FTD pedigrees. *Neurogenetics* **23**, 59-65, doi:10.1007/s10048-021-00671-4 (2022).

89   Deng, H. X. *et al.* Mutations in UBQLN2 cause dominant X-linked juvenile and adult-onset ALS and ALS/dementia. *Nature* **477**, 211-215, doi:10.1038/nature10353 (2011).

90   Vance, C. *et al.* Mutations in FUS, an RNA processing protein, cause familial amyotrophic lateral sclerosis type 6. *Science* **323**, 1208-1211, doi:10.1126/science.1165942 (2009).

91   Shankaran, S. S. *et al.* Missense mutations in the progranulin gene linked to frontotemporal lobar degeneration with ubiquitin-immunoreactive inclusions reduce progranulin production and secretion. *J Biol Chem* **283**, 1744-1753, doi:10.1074/jbc.M705115200 (2008).

92   Kleinberger, G., Capell, A., Haass, C. & Van Broeckhoven, C. Mechanisms of Granulin Deficiency: Lessons from Cellular and Animal Models. *Molecular Neurobiology* **47**, 337-360, doi:10.1007/s12035-012-8380-8 (2013).

93   Capell, A., Fellerer, K. & Haass, C. Progranulin transcripts with short and long 5' untranslated regions (UTRs) are differentially expressed via posttranscriptional and translational repression. *J Biol Chem* **289**, 25879-25889, doi:10.1074/jbc.M114.560128 (2014).

94   Finch, N. *et al.* Plasma progranulin levels predict progranulin mutation status in frontotemporal dementia patients and asymptomatic family members. *Brain* **132**, 583-591, doi:10.1093/brain/awn352 (2009).

95   Ghidoni, R., Benussi, L., Glionna, M., Franzoni, M. & Binetti, G. Low plasma progranulin levels predict progranulin mutations in frontotemporal lobar degeneration. *Neurology* **71**, 1235-1239, doi:10.1212/01.wnl.0000325058.10218.fc (2008).

96   Sleegers, K. *et al.* Serum biomarker for progranulin-associated frontotemporal lobar degeneration. *Ann Neurol* **65**, 603-609, doi:10.1002/ana.21621 (2009).

97   Smith, K. R. *et al.* Strikingly different clinicopathological phenotypes determined by progranulin-mutation dosage. *Am J Hum Genet* **90**, 1102-1107, doi:10.1016/j.ajhg.2012.04.021 (2012).

98   Almeida, M. R. *et al.* Portuguese family with the co-occurrence of frontotemporal lobar degeneration and neuronal ceroid lipofuscinosis phenotypes due to progranulin gene mutation. *Neurobiol Aging* **41**, 200.e201-200.e205, doi:10.1016/j.neurobiolaging.2016.02.019 (2016).

99   Bhandari, V. & Bateman, A. Structure and chromosomal location of the human granulin gene. *Biochem Biophys Res Commun* **188**, 57-63, doi:10.1016/0006-291x(92)92349-3 (1992).

100   Daniel, R., He, Z., Carmichael, K. P., Halper, J. & Bateman, A. Cellular localization of gene expression for progranulin. *J Histochem Cytochem* **48**, 999-1009, doi:10.1177/002215540004800713 (2000).

101   Petkau, T. L. *et al.* Progranulin expression in the developing and adult murine brain. *J Comp Neurol* **518**, 3931-3947, doi:10.1002/cne.22430 (2010).

102   Bateman, A. & Bennett, H. P. Granulins: the structure and function of an emerging family of growth factors. *J Endocrinol* **158**, 145-151, doi:10.1677/joe.0.1580145 (1998).

103   Xu, S. Q. *et al.* The granulin/epithelin precursor abrogates the requirement for the insulin-like growth factor 1 receptor for growth in vitro. *J Biol Chem* **273**, 20078-20083, doi:10.1074/jbc.273.32.20078 (1998).

104   He, Z., Ong, C. H., Halper, J. & Bateman, A. Progranulin is a mediator of the wound response. *Nat Med* **9**, 225-229, doi:10.1038/nm816 (2003).

105   Bateman, A. & Bennett, H. P. The granulin gene family: from cancer to dementia. *Bioessays* **31**, 1245-1254, doi:10.1002/bies.200900086 (2009).

106   Arechavaleta-Velasco, F., Perez-Juarez, C. E., Gerton, G. L. & Diaz-Cueto, L. Progranulin and its biological effects in cancer. *Med Oncol* **34**, 194, doi:10.1007/s12032-017-1054-7 (2017).

107   Tang, W. *et al.* The growth factor progranulin binds to TNF receptors and is therapeutic against inflammatory arthritis in mice. *Science* **332**, 478-484, doi:10.1126/science.1199214 (2011).

108   Van Damme, P. *et al.* Progranulin functions as a neurotrophic factor to regulate neurite outgrowth and enhance neuronal survival. *J Cell Biol* **181**, 37-41, doi:10.1083/jcb.200712039 (2008).

109   Hu, F. *et al.* Sortilin-Mediated Endocytosis Determines Levels of the Frontotemporal Dementia Protein, Progranulin. *Neuron* **68**, 654-667, doi:https://doi.org/10.1016/j.neuron.2010.09.034 (2010).

110   Zhou, X. *et al.* Prosaposin facilitates sortilin-independent lysosomal trafficking of progranulin. *Journal of Cell Biology* **210**, 991-1002, doi:10.1083/jcb.201502029 (2015).

111   Holler, C. J., Taylor, G., Deng, Q. & Kukar, T. Intracellular Proteolysis of Progranulin Generates Stable, Lysosomal Granulins that Are Haploinsufficient in Patients with Frontotemporal Dementia Caused by GRN Mutations. *eNeuro* **4**, doi:10.1523/eneuro.0100-17.2017 (2017).

112   Zhou, X. *et al.* Lysosomal processing of progranulin. *Mol Neurodegener* **12**, 62, doi:10.1186/s13024-017-0205-9 (2017).

113   Tolkatchev, D. *et al.* Structure dissection of human progranulin identifies well-folded granulin/epithelin modules with unique functional activities. *Protein Sci* **17**, 711-724, doi:10.1110/ps.073295308 (2008).

114   Lee, C. W. *et al.* The lysosomal protein cathepsin L is a progranulin protease. *Mol Neurodegener* **12**, 55, doi:10.1186/s13024-017-0196-6 (2017).

115   Mohan, S. *et al.* Processing of progranulin into granulins involves multiple lysosomal proteases and is affected in frontotemporal lobar degeneration. *Mol Neurodegener* **16**, 51, doi:10.1186/s13024-021-00472-1 (2021).

116   Kessenbrock, K. *et al.* Proteinase 3 and neutrophil elastase enhance inflammation in mice by inactivating antiinflammatory progranulin. *J Clin Invest* **118**, 2438-2447, doi:10.1172/jci34694 (2008).

117   Suh, H. S., Choi, N., Tarassishin, L. & Lee, S. C. Regulation of progranulin expression in human microglia and proteolysis of progranulin by matrix metalloproteinase-12 (MMP-12). *PLoS One* **7**, e35115, doi:10.1371/journal.pone.0035115 (2012).

118   Du, H., Zhou, X., Feng, T. & Hu, F. Regulation of lysosomal trafficking of progranulin by sortilin and prosaposin. *Brain Commun* **4**, fcab310, doi:10.1093/braincomms/fcab310 (2022).

119   Salazar, D. A. *et al.* The Progranulin Cleavage Products, Granulins, Exacerbate TDP-43 Toxicity and Increase TDP-43 Levels. *J Neurosci* **35**, 9315-9328, doi:10.1523/jneurosci.4808-14.2015 (2015).

120   Thurner, L. *et al.* The molecular basis for development of proinflammatory autoantibodies to progranulin. *J Autoimmun* **61**, 17-28, doi:10.1016/j.jaut.2015.05.002 (2015).

121   Butler, V. J. *et al.* Multi-Granulin Domain Peptides Bind to Pro-Cathepsin D and Stimulate Its Enzymatic Activity More Effectively Than Progranulin in Vitro. *Biochemistry* **58**, 2670-2674, doi:10.1021/acs.biochem.9b00275 (2019).

122   Root, J. *et al.* Granulins rescue inflammation, lysosome dysfunction, and neuropathology in a mouse model of progranulin deficiency. *bioRxiv*, doi:10.1101/2023.04.17.536004 (2023).

123   Butler, V. J. *et al.* Progranulin Stimulates the In Vitro Maturation of Pro-Cathepsin D at Acidic pH. *J Mol Biol* **431**, 1038-1047, doi:10.1016/j.jmb.2019.01.027 (2019).

124   Beel, S. *et al.* Progranulin functions as a cathepsin D chaperone to stimulate axonal outgrowth in vivo. *Hum Mol Genet* **26**, 2850-2863, doi:10.1093/hmg/ddx162 (2017).

125   Götzl, J. K. *et al.* Common pathobiochemical hallmarks of progranulin-associated frontotemporal lobar degeneration and neuronal ceroid lipofuscinosis. *Acta Neuropathol* **127**, 845-860, doi:10.1007/s00401-014-1262-6 (2014).

126   Götzl, J. K. *et al.* Early lysosomal maturation deficits in microglia triggers enhanced lysosomal activity in other brain cells of progranulin knockout mice. *Mol Neurodegener* **13**, 48, doi:10.1186/s13024-018-0281-5 (2018).

127   Klein, Z. A. *et al.* Loss of TMEM106B Ameliorates Lysosomal and Frontotemporal Dementia-Related Phenotypes in Progranulin-Deficient Mice. *Neuron* **95**, 281-296.e286, doi:10.1016/j.neuron.2017.06.026 (2017).

128   Ward, M. E. *et al.* Individuals with progranulin haploinsufficiency exhibit features of neuronal ceroid lipofuscinosis. *Sci Transl Med* **9**, doi:10.1126/scitranslmed.aah5642 (2017).

129   Valdez, C. *et al.* Progranulin-mediated deficiency of cathepsin D results in FTD and NCL-like phenotypes in neurons derived from FTD patients. *Hum Mol Genet* **26**, 4861-4872, doi:10.1093/hmg/ddx364 (2017).

130   Tanaka, Y., Chambers, J. K., Matsuwaki, T., Yamanouchi, K. & Nishihara, M. Possible involvement of lysosomal dysfunction in pathological changes of the brain in aged progranulin-deficient mice. *Acta Neuropathol Commun* **2**, 78, doi:10.1186/s40478-014-0078-x (2014).

131   Tanaka, Y. *et al.* Progranulin regulates lysosomal function and biogenesis through acidification of lysosomes. *Hum Mol Genet* **26**, 969-988, doi:10.1093/hmg/ddx011 (2017).

132   Hasan, S. *et al.* Multi-modal proteomic characterization of lysosomal function and proteostasis in progranulin-deficient neurons. *Molecular Neurodegeneration* **18**, 87, doi:10.1186/s13024-023-00673-w (2023).

133   Logan, T. *et al.* Rescue of a lysosomal storage disorder caused by Grn loss of function with a brain penetrant progranulin biologic. *Cell* **184**, 4651-4668.e4625, doi:10.1016/j.cell.2021.08.002 (2021).

134   Papadopoulos, C., Kravic, B. & Meyer, H. Repair or Lysophagy: Dealing with Damaged Lysosomes. *J Mol Biol* **432**, 231-239, doi:10.1016/j.jmb.2019.08.010 (2020).

135   Thelen, A. M. & Zoncu, R. Emerging Roles for the Lysosome in Lipid Metabolism. *Trends Cell Biol* **27**, 833-850, doi:10.1016/j.tcb.2017.07.006 (2017).

136   Wenger, D. A., Sattler, M. & Roth, S. A protein activator of galactosylceramide beta-galactosidase. *Biochim Biophys Acta* **712**, 639-649, doi:10.1016/0005-2760(82)90293-4 (1982).

137   Li, S. C., Sonnino, S., Tettamanti, G. & Li, Y. T. Characterization of a nonspecific activator protein for the enzymatic hydrolysis of glycolipids. *J Biol Chem* **263**, 6588-6591 (1988).

138   Breiden, B. & Sandhoff, K. Lysosomal Glycosphingolipid Storage Diseases. *Annu Rev Biochem* **88**, 461-485, doi:10.1146/annurev-biochem-013118-111518 (2019).

139   Jian, J. *et al.* Progranulin Recruits HSP70 to β-Glucocerebrosidase and Is Therapeutic Against Gaucher Disease. *EBioMedicine* **13**, 212-224, doi:10.1016/j.ebiom.2016.10.010 (2016).

140   Zhou, X. *et al.* Progranulin deficiency leads to reduced glucocerebrosidase activity. *PLoS One* **14**, e0212382 (2019).

141   Hruska, K. S., LaMarca, M. E., Scott, C. R. & Sidransky, E. Gaucher disease: mutation and polymorphism spectrum in the glucocerebrosidase gene (GBA). *Hum Mutat* **29**, 567-583, doi:10.1002/humu.20676 (2008).

142   Gegg, M. E. & Schapira, A. H. V. The role of glucocerebrosidase in Parkinson disease pathogenesis. *Febs j* **285**, 3591-3603, doi:10.1111/febs.14393 (2018).

143   Arrant, A. E. *et al.* Impaired β-glucocerebrosidase activity and processing in frontotemporal dementia due to progranulin mutations. *Acta Neuropathol Commun* **7**, 218, doi:10.1186/s40478-019-0872-6 (2019).

144   Boland, S. *et al.* Deficiency of the frontotemporal dementia gene GRN results in gangliosidosis. *Nature Communications* **13**, 5924, doi:10.1038/s41467-022-33500-9 (2022).

145   Showalter, M. R. *et al.* The Emerging and Diverse Roles of Bis(monoacylglycero) Phosphate Lipids in Cellular Physiology and Disease. *Int J Mol Sci* **21**, doi:10.3390/ijms21218067 (2020).

146   Van Deerlin, V. M. *et al.* Common variants at 7p21 are associated with frontotemporal lobar degeneration with TDP-43 inclusions. *Nat Genet* **42**, 234-239, doi:10.1038/ng.536 (2010).

147   Finch, N. *et al.* TMEM106B regulates progranulin levels and the penetrance of FTLD in GRN mutation carriers. *Neurology* **76**, 467-474 (2011).

148   van der Zee, J. *et al.* TMEM106B is associated with frontotemporal lobar degeneration in a clinically diagnosed patient cohort. *Brain* **134**, 808-815, doi:10.1093/brain/awr007 (2011).

149   Nicholson, A. M. *et al.* TMEM106B p.T185S regulates TMEM106B protein levels: implications for frontotemporal dementia. *J Neurochem* **126**, 781-791, doi:10.1111/jnc.12329 (2013).

150   Rutherford, N. J. *et al.* TMEM106B risk variant is implicated in the pathologic presentation of Alzheimer disease. *Neurology* **79**, 717-718, doi:10.1212/WNL.0b013e318264e3ac (2012).

151   Tropea, T. F. *et al.* TMEM106B Effect on cognition in Parkinson disease and frontotemporal dementia. *Ann Neurol* **85**, 801-811, doi:10.1002/ana.25486 (2019).

152   Lattante, S. *et al.* Defining the association of TMEM106B variants among frontotemporal lobar degeneration patients with GRN mutations and C9orf72 repeat expansions. *Neurobiol Aging* **35**, 2658.e2651-2658.e2655, doi:10.1016/j.neurobiolaging.2014.06.023 (2014).

153   Rollinson, S. *et al.* Frontotemporal lobar degeneration genome wide association study replication confirms a risk locus shared with amyotrophic lateral sclerosis. *Neurobiol Aging* **32**, 758.e751-757, doi:10.1016/j.neurobiolaging.2010.12.005 (2011).

154   Lang, C. M. *et al.* Membrane orientation and subcellular localization of transmembrane protein 106B (TMEM106B), a major risk factor for frontotemporal lobar degeneration. *J Biol Chem* **287**, 19355-19365, doi:10.1074/jbc.M112.365098 (2012).

155   Brady, O. A., Zheng, Y., Murphy, K., Huang, M. & Hu, F. The frontotemporal lobar degeneration risk factor, TMEM106B, regulates lysosomal morphology and function. *Hum Mol Genet* **22**, 685-695, doi:10.1093/hmg/dds475 (2013).

156   Chen-Plotkin, A. S. *et al.* TMEM106B, the risk gene for frontotemporal dementia, is regulated by the microRNA-132/212 cluster and affects progranulin pathways. *J Neurosci* **32**, 11213-11227, doi:10.1523/jneurosci.0521-12.2012 (2012).

157   Suzuki, H. & Matsuoka, M. The Lysosomal Trafficking Transmembrane Protein 106B Is Linked to Cell Death. *J Biol Chem* **291**, 21448-21460, doi:10.1074/jbc.M116.737171 (2016).

158   Stagi, M., Klein, Z. A., Gould, T. J., Bewersdorf, J. & Strittmatter, S. M. Lysosome size, motility and stress response regulated by fronto-temporal dementia modifier TMEM106B. *Mol Cell Neurosci* **61**, 226-240, doi:10.1016/j.mcn.2014.07.006 (2014).

159   Schwenk, B. M. *et al.* The FTLD risk factor TMEM 106B and MAP 6 control dendritic trafficking of lysosomes. *The EMBO journal* **33**, 450-467 (2014).

160   Lüningschrör, P. *et al.* The FTLD Risk Factor TMEM106B Regulates the Transport of Lysosomes at the Axon Initial Segment of Motoneurons. *Cell Rep* **30**, 3506-3519.e3506, doi:10.1016/j.celrep.2020.02.060 (2020).

161   Stroobants, S., D'Hooge, R. & Damme, M. Aged Tmem106b knockout mice display gait deficits in coincidence with Purkinje cell loss and only limited signs of non-motor dysfunction. *Brain Pathol* **31**, 223-238, doi:10.1111/bpa.12903 (2021).

162   Feng, T. *et al.* Loss of TMEM106B and PGRN leads to severe lysosomal abnormalities and neurodegeneration in mice. *EMBO Rep* **21**, e50219, doi:10.15252/embr.202050219 (2020).

163   Schweighauser, M. *et al.* Age-dependent formation of TMEM106B amyloid filaments in human brains. *Nature* **605**, 310-314, doi:10.1038/s41586-022-04650-z (2022).

164   Chang, A. *et al.* Homotypic fibrillization of TMEM106B across diverse neurodegenerative diseases. *Cell* **185**, 1346-1355.e1315, doi:10.1016/j.cell.2022.02.026 (2022).

165   Jiang, Y. X. *et al.* Amyloid fibrils in FTLD-TDP are composed of TMEM106B and not TDP-43. *Nature* **605**, 304-309, doi:10.1038/s41586-022-04670-9 (2022).

166   Marks, J. D. *et al.* TMEM106B core deposition associates with TDP-43 pathology and is increased in risk SNP carriers for frontotemporal dementia. *Sci Transl Med* **16**, eadf9735, doi:10.1126/scitranslmed.adf9735 (2024).

167   Cruchaga, C. *et al.* Association of TMEM106B gene polymorphism with age at onset in granulin mutation carriers and plasma granulin protein levels. *Arch Neurol* **68**, 581-586, doi:10.1001/archneurol.2010.350 (2011).

168   Zhou, X., Sun, L., Brady, O. A., Murphy, K. A. & Hu, F. Elevated TMEM106B levels exaggerate lipofuscin accumulation and lysosomal dysfunction in aged mice with progranulin deficiency. *Acta Neuropathol Commun* **5**, 9, doi:10.1186/s40478-017-0412-1 (2017).

169   Werner, G. *et al.* Loss of TMEM106B potentiates lysosomal and FTLD-like pathology in progranulin-deficient mice. *EMBO Rep* **21**, e50241, doi:10.15252/embr.202050241 (2020).

170   Zhou, X. *et al.* Loss of Tmem106b exacerbates FTLD pathologies and causes motor deficits in progranulin-deficient mice. *EMBO Rep* **21**, e50197, doi:10.15252/embr.202050197 (2020).

171   Feng, T. *et al.* TMEM106B deficiency impairs cerebellar myelination and synaptic integrity with Purkinje cell loss. *Acta Neuropathol Commun* **10**, 33, doi:10.1186/s40478-022-01334-7 (2022).

172   Dall, E. & Brandstetter, H. Mechanistic and structural studies on legumain explain its zymogenicity, distinct activation pathways, and regulation. *Proc Natl Acad Sci U S A* **110**, 10940-10945, doi:10.1073/pnas.1300686110 (2013).

173   Zhao, L. *et al.* Structural analysis of asparaginyl endopeptidase reveals the activation mechanism and a reversible intermediate maturation stage. *Cell Res* **24**, 344-358, doi:10.1038/cr.2014.4 (2014).

174   Li, D. N., Matthews, S. P., Antoniou, A. N., Mazzeo, D. & Watts, C. Multistep autoactivation of asparaginyl endopeptidase in vitro and in vivo. *J Biol Chem* **278**, 38980-38990, doi:10.1074/jbc.M305930200 (2003).

175   Maehr, R. *et al.* Asparagine endopeptidase is not essential for class II MHC antigen presentation but is required for processing of cathepsin L in mice. *J Immunol* **174**, 7066-7074, doi:10.4049/jimmunol.174.11.7066 (2005).

176   Shirahama-Noda, K. *et al.* Biosynthetic processing of cathepsins and lysosomal degradation are abolished in asparaginyl endopeptidase-deficient mice. *J Biol Chem* **278**, 33194-33199, doi:10.1074/jbc.M302742200 (2003).

177   Zhang, Z. *et al.* Delta-secretase cleaves amyloid precursor protein and regulates the pathogenesis in Alzheimer's disease. *Nat Commun* **6**, 8762, doi:10.1038/ncomms9762 (2015).

178   Zhang, Z. *et al.* Cleavage of tau by asparagine endopeptidase mediates the neurofibrillary pathology in Alzheimer's disease. *Nat Med* **20**, 1254-1262, doi:10.1038/nm.3700 (2014).

179   Zhang, Z. *et al.* Asparagine endopeptidase cleaves α -synuclein and mediates pathologic activities in Parkinson's disease. *Nat Struct Mol Biol* **24**, 632-642, doi:10.1038/nsmb.3433 (2017).

180   Wang, J. *et al.* Pharmacological inhibition of asparaginyl endopeptidase by δ -secretase inhibitor 11 mitigates Alzheimer's disease-related pathologies in a senescence-accelerated mouse model. *Transl Neurodegener* **10**, 12, doi:10.1186/s40035-021-00235-4 (2021).

181   Herskowitz, J. H. *et al.* Asparaginyl endopeptidase cleaves TDP-43 in brain. *Proteomics* **12**, 2455-2463, doi:10.1002/pmic.201200006 (2012).

182   Sierra, A. *et al.* The "Big-Bang" for modern glial biology: Translation and comments on Pío del Río-Hortega 1919 series of papers on microglia. *Glia* **64**, 1801-1840, doi:10.1002/glia.23046 (2016).

183   Lambert, J. C. *et al.* Meta-analysis of 74,046 individuals identifies 11 new susceptibility loci for Alzheimer's disease. *Nat Genet* **45**, 1452-1458, doi:10.1038/ng.2802 (2013).

184   Andrews, S. J., Fulton-Howard, B. & Goate, A. Interpretation of risk loci from genome-wide association studies of Alzheimer's disease. *Lancet Neurol* **19**, 326-335, doi:10.1016/s1474-4422(19)30435-1 (2020).

185   Wainberg, M., Andrews, S. J. & Tripathy, S. J. Shared genetic risk loci between Alzheimer's disease and related dementias, Parkinson's disease, and amyotrophic lateral sclerosis. *Alzheimer's Research & Therapy* **15**, 113, doi:10.1186/s13195-023-01244-3 (2023).

186   Broce, I. *et al.* Immune-related genetic enrichment in frontotemporal dementia: An analysis of genome-wide association studies. *PLoS Med* **15**, e1002487, doi:10.1371/journal.pmed.1002487 (2018).

187   Hashimoto, D. *et al.* Tissue-resident macrophages self-maintain locally throughout adult life with minimal contribution from circulating monocytes. *Immunity* **38**, 792-804, doi:10.1016/j.immuni.2013.04.004 (2013).

188   Bernier, L. P. *et al.* Nanoscale Surveillance of the Brain by Microglia via cAMP-Regulated Filopodia. *Cell Rep* **27**, 2895-2908.e2894, doi:10.1016/j.celrep.2019.05.010 (2019).

189   Nimmerjahn, A., Kirchhoff, F. & Helmchen, F. Resting microglial cells are highly dynamic surveillants of brain parenchyma in vivo. *Science* **308**, 1314-1318 (2005).

190   Hickman, S. E. *et al.* The microglial sensome revealed by direct RNA sequencing. *Nature neuroscience* **16**, 1896-1905 (2013).

191 Ginhoux, F. *et al.* Fate mapping analysis reveals that adult microglia derive from primitive macrophages. *Science* **330**, 841-845, doi:10.1126/science.1194637 (2010).

192 Schafer, D. P. *et al.* Microglia sculpt postnatal neural circuits in an activity and complement-dependent manner. *Neuron* **74**, 691-705, doi:10.1016/j.neuron.2012.03.026 (2012).

193 Stevens, B. *et al.* The Classical Complement Cascade Mediates CNS Synapse Elimination. *Cell* **131**, 1164-1178, doi:https://doi.org/10.1016/j.cell.2007.10.036 (2007).

194 Paolicelli, R. C. *et al.* Synaptic pruning by microglia is necessary for normal brain development. *Science* **333**, 1456-1458, doi:10.1126/science.1202529 (2011).

195 Sierra, A. *et al.* Microglia shape adult hippocampal neurogenesis through apoptosis-coupled phagocytosis. *Cell Stem Cell* **7**, 483-495, doi:10.1016/j.stem.2010.08.014 (2010).

196 Fourgeaud, L. *et al.* TAM receptors regulate multiple features of microglial physiology. *Nature* **532**, 240-244, doi:10.1038/nature17630 (2016).

197 Marín-Teva, J. L., Cuadros, M. A., Martín-Oliva, D. & Navascués, J. Microglia and neuronal cell death. *Neuron Glia Biol* **7**, 25-40, doi:10.1017/s1740925x12000014 (2011).

198 Parkhurst, Christopher N. *et al.* Microglia Promote Learning-Dependent Synapse Formation through Brain-Derived Neurotrophic Factor. *Cell* **155**, 1596-1609, doi:https://doi.org/10.1016/j.cell.2013.11.030 (2013).

199 Ueno, M. *et al.* Layer V cortical neurons require microglial support for survival during postnatal development. *Nature Neuroscience* **16**, 543-551, doi:10.1038/nn.3358 (2013).

200 Djannatian, M. *et al.* Myelination generates aberrant ultrastructure that is resolved by microglia. *J Cell Biol* **222**, doi:10.1083/jcb.202204010 (2023).

201 Li, Q. *et al.* Developmental Heterogeneity of Microglia and Brain Myeloid Cells Revealed by Deep Single-Cell RNA Sequencing. *Neuron* **101**, 207-223.e210, doi:10.1016/j.neuron.2018.12.006 (2019).

202 Jobling, A. I. *et al.* The role of the microglial Cx3cr1 pathway in the postnatal maturation of retinal photoreceptors. *Journal of Neuroscience* **38**, 4708-4723 (2018).

203 Foulquier, S. *et al.* The role of receptor MAS in microglia-driven retinal vascular development. *Angiogenesis* **22**, 481-489 (2019).

204 Dudiki, T. *et al.* Microglia control vascular architecture via a TGF β 1 dependent paracrine mechanism linked to tissue mechanics. *Nature communications* **11**, 986 (2020).

205 Ronaldson, P. T. & Davis, T. P. Regulation of blood–brain barrier integrity by microglia in health and disease: a therapeutic opportunity. *Journal of Cerebral Blood Flow & Metabolism* **40**, S6-S24 (2020).

206 Lou, N. *et al.* Purinergic receptor P2RY12-dependent microglial closure of the injured blood–brain barrier. *Proceedings of the National Academy of Sciences* **113**, 1074-1079 (2016).

207 Keren-Shaul, H. *et al.* A Unique Microglia Type Associated with Restricting Development of Alzheimer's Disease. *Cell* **169**, 1276-1290.e1217, doi:10.1016/j.cell.2017.05.018 (2017).

208 Krasemann, S. *et al.* The TREM2-APOE Pathway Drives the Transcriptional Phenotype of Dysfunctional Microglia in Neurodegenerative Diseases. *Immunity* **47**, 566-581.e569, doi:10.1016/j.immuni.2017.08.008 (2017).

209 Srinivasan, K. *et al.* Alzheimer's patient microglia exhibit enhanced aging and unique transcriptional activation. *Cell reports* **31** (2020).

210 Marschallinger, J. *et al.* Lipid-droplet-accumulating microglia represent a dysfunctional and proinflammatory state in the aging brain. *Nat Neurosci* **23**, 194-208, doi:10.1038/s41593-019-0566-1 (2020).

211   John, F. T. *et al.* A cross-disease human microglial framework identifies disease-enriched subsets and tool compounds for microglial polarization. *bioRxiv*, 2022.2006.2004.494709, doi:10.1101/2022.06.04.494709 (2022).

212   Weldon, D. T. *et al.* Fibrillar beta-amyloid induces microglial phagocytosis, expression of inducible nitric oxide synthase, and loss of a select population of neurons in the rat CNS in vivo. *J Neurosci* **18**, 2161-2173, doi:10.1523/jneurosci.18-06-02161.1998 (1998).

213   Condello, C., Yuan, P., Schain, A. & Grutzendler, J. Microglia constitute a barrier that prevents neurotoxic protofibrillar A β 42 hotspots around plaques. *Nature Communications* **6**, 6176, doi:10.1038/ncomms7176 (2015).

214   Heneka, M. T. *et al.* NLRP3 is activated in Alzheimer's disease and contributes to pathology in APP/PS1 mice. *Nature* **493**, 674-678, doi:10.1038/nature11729 (2013).

215   Hong, S. *et al.* Complement and microglia mediate early synapse loss in Alzheimer mouse models. *Science* **352**, 712-716, doi:10.1126/science.aad8373 (2016).

216   Liddelow, S. A. *et al.* Neurotoxic reactive astrocytes are induced by activated microglia. *Nature* **541**, 481-487, doi:10.1038/nature21029 (2017).

217   Aguzzi, A., Barres, B. A. & Bennett, M. L. Microglia: scapegoat, saboteur, or something else? *Science* **339**, 156-161, doi:10.1126/science.1227901 (2013).

218   Colonna, M. & Butovsky, O. Microglia Function in the Central Nervous System During Health and Neurodegeneration. *Annu Rev Immunol* **35**, 441-468, doi:10.1146/annurev-immunol-051116-052358 (2017).

219   Prinz, M. & Priller, J. Microglia and brain macrophages in the molecular age: from origin to neuropsychiatric disease. *Nature Reviews Neuroscience* **15**, 300-312, doi:10.1038/nrn3722 (2014).

220   Tejera, D. & Heneka, M. T. Microglia in Neurodegenerative Disorders. *Methods Mol Biol* **2034**, 57-67, doi:10.1007/978-1-4939-9658-2_5 (2019).

221   Lewcock, J. W. *et al.* Emerging Microglia Biology Defines Novel Therapeutic Approaches for Alzheimer's Disease. *Neuron* **108**, 801-821, doi:10.1016/j.neuron.2020.09.029 (2020).

222   Sierra, A., Paolicelli, R. C. & Kettenmann, H. Cien Años de Microglía: Milestones in a Century of Microglial Research. *Trends Neurosci* **42**, 778-792, doi:10.1016/j.tins.2019.09.004 (2019).

223   Marsan, E. *et al.* Astroglial toxicity promotes synaptic degeneration in the thalamocortical circuit in frontotemporal dementia with GRN mutations. *J Clin Invest* **133**, doi:10.1172/jci164919 (2023).

224   Sakae, N. *et al.* Microglia in frontotemporal lobar degeneration with progranulin or C9ORF72 mutations. *Ann Clin Transl Neurol* **6**, 1782-1796, doi:10.1002/acn3.50875 (2019).

225   Woollacott, I. O. C. *et al.* Microglial burden, activation and dystrophy patterns in frontotemporal lobar degeneration. *J Neuroinflammation* **17**, 234, doi:10.1186/s12974-020-01907-0 (2020).

226   Götzl, J. K. *et al.* Opposite microglial activation stages upon loss of PGRN or TREM2 result in reduced cerebral glucose metabolism. *EMBO Mol Med* **11**, doi:10.15252/emmm.201809711 (2019).

227   Liu, B. *et al.* In Vivo Detection of Age- and Disease-Related Increases in Neuroinflammation by 18F-GE180 TSPO MicroPET Imaging in Wild-Type and Alzheimer's Transgenic Mice. *J Neurosci* **35**, 15716-15730, doi:10.1523/jneurosci.0996-15.2015 (2015).

228   Zhang, J. *et al.* Neurotoxic microglia promote TDP-43 proteinopathy in progranulin deficiency. *Nature* **588**, 459-465, doi:10.1038/s41586-020-2709-7 (2020).

229   Lui, H. *et al.* Progranulin Deficiency Promotes Circuit-Specific Synaptic Pruning by Microglia via Complement Activation. *Cell* **165**, 921-935, doi:10.1016/j.cell.2016.04.001 (2016).

230   Martens, L. H. *et al.* Progranulin deficiency promotes neuroinflammation and neuron loss following toxin-induced injury. *J Clin Invest* **122**, 3955-3959, doi:10.1172/jci63113 (2012).

231   Reifschneider, A. *et al.* Loss of TREM2 rescues hyperactivation of microglia, but not lysosomal deficits and neurotoxicity in models of progranulin deficiency. *Embo j* **41**, e109108, doi:10.15252/embj.2021109108 (2022).

232   Miyakawa, S. *et al.* Anti-sortilin1 Antibody Up-Regulates Progranulin via Sortilin1 Down-Regulation. *Front Neurosci* **14**, 586107, doi:10.3389/fnins.2020.586107 (2020).

233   Kurnellas, M. *et al.* Latozinemab, a novel progranulin-elevating therapy for frontotemporal dementia. *J Transl Med* **21**, 387, doi:10.1186/s12967-023-04251-y (2023).

234   Arrant, A. E., Onyilo, V. C., Unger, D. E. & Roberson, E. D. Progranulin Gene Therapy Improves Lysosomal Dysfunction and Microglial Pathology Associated with Frontotemporal Dementia and Neuronal Ceroid Lipofuscinosis. *J Neurosci* **38**, 2341-2358, doi:10.1523/jneurosci.3081-17.2018 (2018).

235   Hinderer, C. *et al.* Adeno-associated virus serotype 1-based gene therapy for FTD caused by GRN mutations. *Ann Clin Transl Neurol* **7**, 1843-1853, doi:10.1002/acn3.51165 (2020).

236   Samaranch, L. *et al.* Cerebellomedullary Cistern Delivery for AAV-Based Gene Therapy: A Technical Note for Nonhuman Primates. *Hum Gene Ther Methods* **27**, 13-16, doi:10.1089/hgtb.2015.129 (2016).

237   Liguore, W. A. *et al.* AAV-PHP.B Administration Results in a Differential Pattern of CNS Biodistribution in Non-human Primates Compared with Mice. *Mol Ther* **27**, 2018-2037, doi:10.1016/j.ymthe.2019.07.017 (2019).

238   Wolak, D. J. & Thorne, R. G. Diffusion of macromolecules in the brain: implications for drug delivery. *Mol Pharm* **10**, 1492-1504, doi:10.1021/mp300495e (2013).

239   Feng, T. *et al.* AAV-GRN partially corrects motor deficits and ALS/FTLD-related pathology in Tmem106b(-/-)Grn(-/-) mice. *iScience* **26**, 107247, doi:10.1016/j.isci.2023.107247 (2023).

240   Amado, D. A. *et al.* AAV-Mediated Progranulin Delivery to a Mouse Model of Progranulin Deficiency Causes T Cell-Mediated Toxicity. *Mol Ther* **27**, 465-478, doi:10.1016/j.ymthe.2018.11.013 (2019).

241   St-Amour, I. *et al.* Brain bioavailability of human intravenous immunoglobulin and its transport through the murine blood-brain barrier. *J Cereb Blood Flow Metab* **33**, 1983-1992, doi:10.1038/jcbfm.2013.160 (2013).

242   Kariolis, M. S. *et al.* Brain delivery of therapeutic proteins using an Fc fragment blood-brain barrier transport vehicle in mice and monkeys. *Science translational medicine* **12**, eaay1359 (2020).

243   Gao, G. P. *et al.* Novel adeno-associated viruses from rhesus monkeys as vectors for human gene therapy. *Proc Natl Acad Sci U S A* **99**, 11854-11859, doi:10.1073/pnas.182412299 (2002).

244   Nakai, H. *et al.* Unrestricted hepatocyte transduction with adeno-associated virus serotype 8 vectors in mice. *J Virol* **79**, 214-224, doi:10.1128/jvi.79.1.214-224.2005 (2005).

245   Carestia, A. *et al.* Modulation of the liver immune microenvironment by the adeno-associated virus serotype 8 gene therapy vector. *Mol Ther Methods Clin Dev* **20**, 95-108, doi:10.1016/j.omtm.2020.10.023 (2021).

246   Vultaggio, A. *et al.* How to Prevent and Mitigate Hypersensitivity Reactions to Biologicals Induced by Anti-Drug Antibodies? *Front Immunol* **12**, 765747, doi:10.3389/fimmu.2021.765747 (2021).

247   Nykjaer, A. & Willnow, T. E. Sortilin: a receptor to regulate neuronal viability and function. *Trends in Neurosciences* **35**, 261-270, doi:https://doi.org/10.1016/j.tins.2012.01.003 (2012).

248   Toth, A. E. *et al.* Sortilin regulates blood–brain barrier integrity. *The FEBS Journal* **289**, 1062-1079, doi:https://doi.org/10.1111/febs.16225 (2022).

249   Paushter, D. H., Du, H., Feng, T. & Hu, F. The lysosomal function of progranulin, a guardian against neurodegeneration. *Acta Neuropathol* **136**, 1-17, doi:10.1007/s00401-018-1861-8 (2018).

250   Zhou, X. *et al.* Loss of TMEM106B leads to myelination deficits: implications for frontotemporal dementia treatment strategies. *Brain* **143**, 1905-1919, doi:10.1093/brain/awaa141 (2020).

251   Arrant, A. E., Nicholson, A. M., Zhou, X., Rademakers, R. & Roberson, E. D. Partial Tmem106b reduction does not correct abnormalities due to progranulin haploinsufficiency. *Molecular Neurodegeneration* **13**, 32, doi:10.1186/s13024-018-0264-6 (2018).

252   Filiano, A. J. *et al.* Dissociation of frontotemporal dementia-related deficits and neuroinflammation in progranulin haploinsufficient mice. *J Neurosci* **33**, 5352-5361, doi:10.1523/jneurosci.6103-11.2013 (2013).

253   Le Ber, I. *et al.* Phenotype variability in progranulin mutation carriers: a clinical, neuropsychological, imaging and genetic study. *Brain* **131**, 732-746, doi:10.1093/brain/awn012 (2008).

254   Burrell, J. R., Kiernan, M. C., Vucic, S. & Hodges, J. R. Motor neuron dysfunction in frontotemporal dementia. *Brain* **134**, 2582-2594, doi:10.1093/brain/awr195 (2011).

255   Li, J. & Fraenkel, E. Phenotyping Neurodegeneration in Human iPSCs. *Annu Rev Biomed Data Sci* **4**, 83-100, doi:10.1146/annurev-biodatasci-092820-025214 (2021).

256   Paquet, D. *et al.* Efficient introduction of specific homozygous and heterozygous mutations using CRISPR/Cas9. *Nature* **533**, 125-129, doi:10.1038/nature17664 (2016).

257   Lemprière, S. Neuroinflammation predicts cognitive decline in FTD. *Nature Reviews Neurology* **19**, 258-258, doi:10.1038/s41582-023-00804-3 (2023).

258   Pesämaa, I. *et al.* A microglial activity state biomarker panel differentiates FTD-granulin and Alzheimer's disease patients from controls. *Molecular Neurodegeneration* **18**, 70, doi:10.1186/s13024-023-00657-w (2023).

259   de Majo, M. *et al.* Granulin loss of function in human mature brain organoids implicates astrocytes in TDP-43 pathology. *Stem Cell Reports* **18**, 706-719, doi:10.1016/j.stemcr.2023.01.012 (2023).

260   Bossolasco, P. *et al.* GRN−/− iPSC-derived cortical neurons recapitulate the pathological findings of both frontotemporal lobar degeneration and neuronal ceroidolipofuscinosis. *Neurobiology of Disease* **175**, 105891, doi:https://doi.org/10.1016/j.nbd.2022.105891 (2022).

261   Breznik, B., Mitrović, A., T, T. L. & Kos, J. Cystatins in cancer progression: More than just cathepsin inhibitors. *Biochimie* **166**, 233-250, doi:10.1016/j.biochi.2019.05.002 (2019).

262   Soleymani, T., Chen, T. Y., Gonzalez-Kozlova, E. & Dogra, N. The human neurosecretome: extracellular vesicles and particles (EVPs) of the brain for intercellular communication, therapy, and liquid-biopsy applications. *Front Mol Biosci* **10**, 1156821, doi:10.3389/fmolb.2023.1156821 (2023).

263   Mallach, A. *et al.* Differential Stimulation of Pluripotent Stem Cell-Derived Human Microglia Leads to Exosomal Proteomic Changes Affecting Neurons. *Cells* **10**, doi:10.3390/cells10112866 (2021).

264   Scheiblich, H. *et al.* Microglia jointly degrade fibrillar alpha-synuclein cargo by distribution through tunneling nanotubes. *Cell* **184**, 5089-5106.e5021, doi:10.1016/j.cell.2021.09.007 (2021).

265   Chakraborty, R., Nonaka, T., Hasegawa, M. & Zurzolo, C. Tunnelling nanotubes between neuronal and microglial cells allow bi-directional transfer of α-Synuclein and mitochondria. *Cell Death & Disease* **14**, 329, doi:10.1038/s41419-023-05835-8 (2023).

266   Smith, R. *et al.* Intra-and extracellular regulation of activity and processing of legumain by cystatin E/M. *Biochimie* **94**, 2590-2599 (2012).

267   Dall, E. & Brandstetter, H. Structure and function of legumain in health and disease. *Biochimie* **122**, 126-150, doi:https://doi.org/10.1016/j.biochi.2015.09.022 (2016).

268   Kumar, S. T. *et al.* Seeding the aggregation of TDP-43 requires post-fibrillization proteolytic cleavage. *Nat Neurosci* **26**, 983-996, doi:10.1038/s41593-023-01341-4 (2023).

269   Li, Q., Yokoshi, M., Okada, H. & Kawahara, Y. The cleavage pattern of TDP-43 determines its rate of clearance and cytotoxicity. *Nature Communications* **6**, 6183, doi:10.1038/ncomms7183 (2015).

270   Ayala, Y. M. *et al.* Structural determinants of the cellular localization and shuttling of TDP-43. *Journal of Cell Science* **121**, 3778-3785, doi:10.1242/jcs.038950 (2008).

271   Ayala, V. *et al.* Cell stress induces TDP-43 pathological changes associated with ERK1/2 dysfunction: implications in ALS. *Acta Neuropathologica* **122**, 259-270, doi:10.1007/s00401-011-0850-y (2011).

272   Walker, A. K. *et al.* ALS-Associated TDP-43 Induces Endoplasmic Reticulum Stress, Which Drives Cytoplasmic TDP-43 Accumulation and Stress Granule Formation. *PLOS ONE* **8**, e81170, doi:10.1371/journal.pone.0081170 (2013).

273   Zuo, X. *et al.* TDP-43 aggregation induced by oxidative stress causes global mitochondrial imbalance in ALS. *Nature Structural & Molecular Biology* **28**, 132-142, doi:10.1038/s41594-020-00537-7 (2021).

274   Schmidt, M. F., Gan, Z. Y., Komander, D. & Dewson, G. Ubiquitin signalling in neurodegeneration: mechanisms and therapeutic opportunities. *Cell Death & Differentiation* **28**, 570-590, doi:10.1038/s41418-020-00706-7 (2021).

275   Pohl, C. & Dikic, I. Cellular quality control by the ubiquitin-proteasome system and autophagy. *Science* **366**, 818-822, doi:doi:10.1126/science.aax3769 (2019).

276   Scotter, E. L. *et al.* Differential roles of the ubiquitin proteasome system and autophagy in the clearance of soluble and aggregated TDP-43 species. *Journal of cell science* **127**, 1263-1278 (2014).

277   Freeley, S. *et al.* Asparaginyl Endopeptidase (Legumain) Supports Human Th1 Induction via Cathepsin L-Mediated Intracellular C3 Activation. *Front Immunol* **9**, 2449, doi:10.3389/fimmu.2018.02449 (2018).

278   Pandey, M. K., Grabowski, G. A. & Köhl, J. An unexpected player in Gaucher disease: The multiple roles of complement in disease development. *Semin Immunol* **37**, 30-42, doi:10.1016/j.smim.2018.02.006 (2018).

279   Klein, A. D., González de la Vega, J. & Zanlungo, S. Complement Component C3 Participates in Early Stages of Niemann-Pick C Mouse Liver Damage. *Int J Mol Sci* **21**, doi:10.3390/ijms21062127 (2020).

Literature

8. CURRICULUM VITAE

Marvin Reich

HIGHER EDUCATION

10/2020 – present	*Ludwig Maximilian University of Munich (Munich, Germany)* **PhD Student** at the Graduate School of Systemic Neurosciences
04/2016 – 01/2020	*University of Konstanz (Konstanz, Germany)* **Master of Science** (with distinction) Thesis: Characterization of hiPSC-derived microglia towards an application in compound testing and screening
08/2016 – 06/2017	*Uppsala University (Uppsala, Sweden)* **Erasmus+ scholarship**
10/2012 – 03/2016	*University of Konstanz (Konstanz, Germany)* **Bachelor of Science** Thesis: Engineering of the KOD DNA-Polymerase for epigenetic applications

RESEARCH EXPERIENCE

06/2023 – 07/2023	*Denali Therapeutics (South San Francisco, California, USA)* **PhD Internship in the OMX department** Project: Lipidomics cross-comparison of different lysosomal impairment models *General introduction to LC/MS planning, execution, and analysis – Comparison between datasets of different FTD and NPC models*
03/2020 – present	*German Center for Neurodegenerative Diseases & Ludwig Maximilian University of Munich (Munich, Germany)* **PhD Thesis in the laboratory of Prof. Dr. Dr. h.c. Christian Haass** Project: Rescue of FTD-*GRN* via a brain-penetrant biotherapeutic *Development of a hiPSC-based model for FTD-GRN – Testing a therapeutic approach to treat the hiPSC-based model and a mouse model for FTD-GRN – Investigating neuron-microglia crosstalk in the hiPSC-based model*
04/2019 – 12/2019	*F. Hoffmann - La Roche Ltd. (Basel, Switzerland)* **Master's Thesis in Neuroscience Discovery and the Stem Cell Group** Project: Characterization of hiPSC-derived microglia towards an application in compound testing and screening *Development of a protocol to generate hiPSC-derived microglia – Functional, genetic, and morphological characterization of the model – Application of the model to study the role of the microglial receptor TREM2*
11/2018 – 12/2018	*University of Konstanz (Konstanz, Germany)* **Intensive Course in Immunology in the laboratory of Prof. Dr. Marcus Groettrup** Project: 26S proteasome interaction partners and its specific activation by the ubiquitin-like protein family *Synthesis and purification of the 26S proteasome – Binding and activation analysis of potential interactors*
08/2018 – 10/2018	*Swiss Federal Institute of Technology Zurich (Basel, Switzerland)* **Internship in the Bio Engineering Laboratory of Prof. Dr. Andreas Hierlemann** Project: Investigation of the prenatal development of neuronal networks using murine cerebral organoids *Establishment of a multielectrode array setup for organoids – Longitudinal recordings of murine organoids*
11/2017 – 07/2018	*F. Hoffmann - La Roche Ltd. (Basel, Switzerland)* **Internship in Neuroscience Discovery and Mechanistic Safety** Project: Alpha-synuclein preformed fibril (PFF)-induced toxicity in a human neuronal cell model *Setup of LUHMES neuronal cell differentiation – Study of PFF-induced cellular and mitochondrial toxicity*
04/2016 – 06/2016	*University of Konstanz (Konstanz, Germany)* **Intensive Course in Biochemical Pharmacology in the laboratory of Prof. Dr. Thomas Brunner** Project: Investigation of kinetics and synergistic effects of mediators of different apoptosis pathways *Live-cell imaging and immunoblotting to dissect the time-resolved apoptosis induction by cisplatin and TRAIL*
07/2015 – 10/2015	*University of Konstanz (Konstanz, Germany)* **Bachelor's Thesis in the laboratory of Prof. Dr. Andreas Marx** Project: Engineering of the KOD DNA-Polymerase for epigenetic applications *KOD DNA-polymerase mutagenesis via error-prone PCR – Study of the effect of mutations on polymerase selectivity*

CONFERENCE PRESENTATIONS

Talks

Rescue of FTD-*GRN* Pathology via Peripheral AAV-mediated Delivery of a Brain-Penetrant PGRN Biologic
International Conference on Alzheimer's and Parkinson's Diseases and related neurological disorders in Lisbon, Portugal (03/2024)
Eibsee Meeting: Cellular Mechanisms of Neurodegeneration in Grainau, Germany (12/2023)
Keystone Symposium on Neuroimmune Interactions: From Basic Mechanisms to Novel Therapeutic Directions in Whistler, Canada (05/2023)

Neuron-microglia crosstalk in a human iPSC-based FTD model
Keystone Symposium on Neuro-Immune Interactions in the Central Nervous System in Keystone, Colorado, USA (06/2022)

Posters

Rescue of FTD-*GRN* Pathology via Peripheral AAV-mediated Delivery of a Brain-Penetrant PGRN Biologic
Eibsee Meeting: Cellular Mechanisms of Neurodegeneration in Grainau, Germany (12/2023)
Keystone Symposium on Neuroimmune Interactions: From Basic Mechanisms to Novel Therapeutic Directions in Whistler, Canada (05/2023)

Rescue of FTD-*GRN via* a brain penetrant biotherapeutic
Eibsee Meeting: Cellular Mechanisms of Neurodegeneration in Grainau, Germany (10/2022)
Retreat of the Graduate School of Systemic Neurosciences in Garmisch-Partenkirchen, Germany (10/2022)

Neuron-microglia crosstalk in a human iPSC-based FTD model
Retreat of the Institute for Stroke and Dementia Research in Herrsching, Germany (07/2022)
Keystone Symposium on Neuro-Immune Interactions in the Central Nervous System in Keystone, Colorado, USA (06/2022)

Human iPSC-derived microglia as a model system to investigate TREM2 biology
100 Years of Microglia Symposium in Lausanne, Switzerland (12/2019)
Eibsee Meeting: Cellular Mechanisms of Neurodegeneration in Grainau, Germany (11/2019)

GRANTS AND AWARDS

06/2022	Graduate School of Systemic Neurosciences Travel Grant
02/2022	NanoString nCounter Gene Expression Grant
12/2019	Honorable Mention: Poster Session of the 100 Years of Microglia Symposium in Lausanne, Switzerland

MEMBERSHIPS AND LEADERSHIP

05/2023 – present	Member of the German Stem Cell Network
04/2023 – present	PhD representative at the DZNE Munich
11/2021 – present	PhD representative at the Department of Metabolic Biochemistry (Head: Prof. Dr. Dr. h.c. Christian Haass)
08/2021 – present	Coordinator of the Haass lab hiPSC facility
01/2014 – present	Member of the German Association of Biochemistry and Molecular Biology

TEACHING

11/2022 – 10/2023	Supervision of a Master's student internship and thesis
06/2022	Medical student seminar on the biochemistry of Alzheimer's disease
02/2022 – 11/2022	Supervision of a Master's student internship and thesis
07/2021 – 09/2021	Supervision of a Master's student internship
04/2018	Supervision of a high school student for their practical internship

ADDITIONAL SKILLS

Languages
German (native); English (fluent); French, Swedish (moderate)

IT Skills
Microsoft Office (advanced); ImageJ, GraphPad Prism, Adobe Illustrator, LaTeX (proficient); MATLAB, Python (basic)

Soft Skill Trainings
Unconscious bias; Psychological safety; Efficiency; Leadership

9. LIST OF PUBLICATIONS

Robinson S*, **Reich M***, Mühlhofer M*, Buschmann K, Wauters E, Mühlhofer Q, Werner G, Ahles A, Engelhardt S, Krenner C, Bartels B, Gutbier S, Reifschneider A, Riemenschneider H, Reinheckel T, Edbauer D, Simon MJ, Kariolis MS, Logan T, Di Paolo G, van Broeckhoven C, Damme M, Paquet D, Haass C#, Capell A#. Enhanced legumain activity links progranulin deficiency to TDP-43 pathology in frontotemporal lobar degeneration. In revision at Nature Neuroscience.

Reich M*, Simon MJ*, Polke B, Werner G, Schrader C, Paris I, Robinson S, Suh JH, Sandmann T, Schlaphoff L, Spieth L, Berghoff S, Logan T, Nuscher B, Buschmann K, Simons M, Kariolis MS, DeVos SL, Lewcock JW, Paquet D#, Capell A#, Di Paolo G#, Haass C#. Rescue of FTLD-associated TDP-43 pathology and neurodegeneration by peripheral AAV-mediated expression of brain-penetrant progranulin. In revision at Science Translational Medicine.

Van Lengerich B*, Zhan L*, Xia D, Lianoglou S, Park JI, Bartos LM, Beumers P, Calvert M, Chan D, Davis SS, de Weerd L, Duque J, Gadkar K, Giese T, Gnorich J, Ha C, Huang F, Hummel S, Joy D, Kannuswamy M, Kim DJ, Kunte S, Kunze L, Lechtenberg K, Wing-Sze Leung A, Liang C-C, McQuade P, Modi A, Pesamaa I, Pizzo ME, Propson N, Prorok R, **Reich M**, Robles-Colmenares Y, Schlepckow K, Slemann L, Suh JH, Tatarakis D, Thomsen E, Thorne R, Vieira C, Wind K, Xiong K, Yu Zuchero YJ, Diaz D, Dennis MS, Scearce-Levie K, Watts RJ, Haass C, Lewcock JW, Di Paolo G, Brendel M, Sanchez PE#, Monroe KM#. A blood-brain barrier transport vehicle improves brain biodistribution of a TREM2 antibody and enhances microglial metabolism via receptor clustering. Nat Neurosci. 2023 Mar;26(3):416-429. doi: 10.1038/s41593-022-01240-0.

Reich M*, Paris I*, Ebeling M, Dahm N, Schweitzer C, Reinhardt D, Schmucki R, Prasad M, Köchl F, Leist M, Cowley SA, Zhang JD, Patsch C, Gutbier S#, Britschgi M#. Alzheimer's Risk Gene TREM2 Determines Functional Properties of New Type of Human iPSC-Derived Microglia. Front Immunol. 2021 Feb 3;11:617860. doi: 10.3389/fimmu.2020.617860.

Brüll M, Spreng AS, Gutbier S, Loser D, Krebs A, **Reich M**, Kraushaar U, Britschgi M, Patsch C, Leist M. Incorporation of stem cell-derived astrocytes into neuronal organoids to allow neuro-glial interactions in toxicological studies. ALTEX. 2020;37(3):409-428. doi: 10.14573/altex.1911111.

List of publications

10. EIDESSTATTLICHE VERSICHERUNG/AFFIDAVIT

_____ Marvin Reich _____

(Studierende / Student)

Hiermit versichere ich an Eides statt, dass ich die vorliegende Dissertation

Neuron-Microglia Crosstalk in FTLD-_GRN_ models

selbstständig angefertigt habe, mich außer der angegebenen keiner weiteren Hilfsmittel bedient und alle Erkenntnisse, die aus dem Schrifttum ganz oder annähernd übernommen sind, als solche kenntlich gemacht und nach ihrer Herkunft unter Bezeichnung der Fundstelle einzeln nachgewiesen habe.

I hereby confirm that the dissertation is the result of my own work and that I have only used sources or materials listed and specified in the dissertation.

München / Munich

_____ 07.05.2024 _____   _____ Marvin Reich _____

(Datum / Date)   (Unterschrift / Signature)

Eidesstattliche Versicherung/Affidavit

11.   DECLARATION OF AUTHOR CONTRIBUTIONS

Research article 1: (Reich, Simon *et al*.) "Rescue of FTLD-associated TDP-43 pathology and neurodegeneration by peripheral AAV-mediated expression of brain-penetrant progranulin"

Author contributions:
Conceptualization: MR, MJS, MSK, SLD, JWL, AC, GDP, CH
Methodology: MR, MJS, IP, GW, SR, SSD, GL, LSc, LSp, SB, TL, MS, MSK, JHS, TS, SLD, JWL, DP, AC, GDP, CH
Investigation: MR, MJS, BP, CS, IP, GW, SR, SSD, GL, LSc, LSp, SB, BN, KB, JHS, TS
Visualization: MR, MJS, IP, JHS, TS
Funding acquisition: DP, CH
Project administration: DE, MS, JWL, DP, AC, GDP, CH
Supervision: MR, MJS, GW, SR, JHS, TS, LSc, LSp, SB, DP, AC
Writing – original draft: MR, MJS, GDP, CH

Marvin Reich	Matthew J. Simon
(First authors)	

Dominik Paquet	Anja Capell	Gilbert Di Paolo	Christian Haass
	(Corresponding authors)		

Research article 2: (Robinson, Reich, Mühlhofer *et al*.) "Enhanced legumain activity links progranulin deficiency to TDP-43 pathology in frontotemporal lobar degeneration"

Author contributions:
Conceptualization: AC, CH
Methodology: AC, MR, MTM, SR, KB, EW, QM, GW, AA, CK, BB, SG, AR, HR, MJS
Investigation: AC, MR, MTM, SR, KB, EW, QM, GW, AA, CK, BB, SG, AR, HR, MJS
Visualization: AC, MR, MTM, SR
Funding acquisition: AC, CH, DP
Project administration: AC, CH, SE, BB, SG, TR, DE, MJS, MSK, TL, GDP, CVB, MD, DP
Supervision: AC, CH, SE, BB, SG, TR, DE, MJS, MSK, TL, GDP, CVB, MD, DP
Writing – original draft: AC, CH, MR, MTM, SR

Sophie Robinson	Marvin Reich	Maria T. Mühlhofer
	(First authors)	

Christian Haass	Anja Capell
(Corresponding authors)	

Declaration of author contributions